The nanomechanics of molecularly thin films studied by force spectroscopy AFM

Relat Goberna, Josep

Awarding institution:
King's College London

The nanomechanics of molecularly thin films studied by force spectroscopy AFM

A thesis

submitted for the degree of

DOCTOR OF PHILOSOPHY

in the University of London by

Josep Relat-Goberna

(King's College London)

September 2015

Abstract

Most materials break through the extension of their most prominent crack, as Griffith predicted over a century ago. Despite the fact that the extension of a crack occurs in the nanometre-sized area located at the crack tip end, we still know little about the crucial role that forces play at this scale. With the advent of the Atomic Force Microscopy (AFM), we have been able to apply small calibrated forces at the nanoscale. Until now, AFM has been most successful at unveiling the mechanical properties of biological materials while pulling. Investigating the mechanics of materials while pushing, however, has been less successful. Until now, most indentation experiments were performed at a constant pushing velocity, which precluded measuring the detailed rupture kinetics of the material. In this vein, we have developed an AFM capable of applying a more complex indentation protocol, called force-clamp, which expands the time window of experimentation and allows mapping out the energy landscape of the rupture mechanism. Then, we have investigated the rupture kinetics of an Angstrom-scale simple 2D material – confined solvation layers. By applying force-clamp, we have discovered that the rupture (and reformation) of these solid-like layers occurs through the disruption of a single molecule, contrary to currently accepted mechanical contact models. Secondly, we have investigated the more complex mechanism of lipid membrane rupture, which involves the displacement of tens to hundreds of molecules. In this case, we have developed a pore nucleation model to fit the complex rupture kinetics, which is far from the currently used two-state model. Finally, we have indented whole live cells. As a result, we have measured that lipid membrane lateral interactions ultimately define cell membrane integrity. Altogether, these experiments point out the key role that intermolecular forces play to define the mechanical strength of materials from a fraction of nanometre to several micrometres.

Acknowledgements

My supervisor Sergi Garcia-Manyes deserves the greatest thanks for his continued motivation and energy during these last four years. I also thank David Richards for his support and helpful supervision. This thesis is also indebted with William Luckhurst, John Wilkinson and Ernest Samuel whose help was fundamental to start up the laboratory. I would like to especially thank William for his outstanding patience and attention. Another part of this thesis would have been impossible without Eleonora Muro and Ulrike Eggert, who were outstanding journey companions during one of the most demanding parts of journey. I also thank all those who have shared this research adventure with me: Judit, Amy, Aisling, Ainhoa, David, and Justin; and those with whom I have shared the ship: Marco de Cesare, Marco Caccin, Federico, Dominic, Marcelo, Giovanni Doni, Giovanni Peralta, Spyros, Katy, and the rest of the friends and colleagues of the Physics department. Also, I want to thank 'La Caixa' foundation and EPRSC for their financial support.

I feel especially indebted with those who helped and supported me during the difficult times. I especially thank my parents, Josefina and Salvador, for their support and understanding; and my siblings, Claudina and Ferran, and my grandmother Teresa for their time and attention. I also want to mention my friends Alba, Marina, and Anna, who are like a second family to me. I must especially thank José Salvador for his helpful advice. This thesis would have been impossible without him.

Finally, I need to mention all those who brightened this journey. I especially want to thanks Josep Grau for his support, good humor, and for so many inspiring discussions about science, arts, and life. I also feel great gratitude to Magdalena and Natalia, who made me feel like home in London.

Manresa, 11th of September 2015

‘If it cannot break out of its shell, the
chick will die without ever being born.’

…

— *Toga Kiryuu*

(Revolutionary Girl Utena)

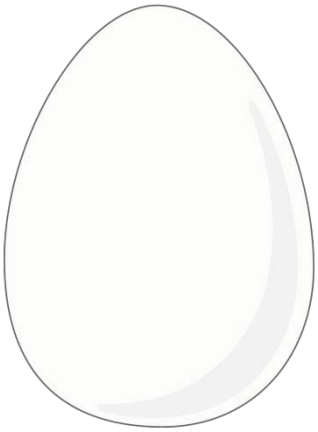

Table of Contents

Table of Figures

Chapter 2:

Chapter 3:

1 Introduction

1.1 Motivation

Most materials exhibit a mechanical strength several orders of magnitude lower than that predicted by the strength of their constituting individual atomic bonds. This apparent contradiction was firstly solved by Griffith over a century ago, who proposed that materials do not break as a whole, but through the expansion of the most prominent pre-existing crack in the material[1][2][3]. In this way, the applied stress concentrates in the end-tip area of the crack, which rapidly enlarges it, producing the large scale failure of the material. Despite Griffith theory only applies to purely brittle materials, later theories have confirmed that the same mechanism underpins the fracture of much broader range of materials[4][5][6]. Hence, the reliability of materials, a fundamental aspect of material engineering, mostly depends on the processes occurring at the end-tip area of cracks.

Despite the extensive research devoted to understanding fracture mechanics, we still know very little about the processes occurring at the end-tip of cracks. It is well known that the growth of the end-tip region is largely independent of the macroscopic sizes of the object and the current crack size[5]. Moreover, its dimensions are very small compared to the size of the crack, probably well into the nanometre realm[7][8]. In this sense, recent molecular dynamics simulation studies point out that the extension of cracks occurs at the single-bond rupture level[9]. As a consequence, nanoscale rupture experiments are required in order to unveil the molecular rupture dynamics responsible for maintaining (or destroying) the mechanical integrity.

During the last decades, the advent of micro- and nanotechnology has allowed us to measure (or apply) forces with ever-increasing accuracy. Pioneering force-sensing techniques, encompassing the micro aspiration technique[10] and the surface force apparatus[11], allowed to measure for the first time forces with great detail. Later techniques, such as the atomic force microscope, optical tweezers, and magnetic tweezers, achieved to study these processes in highly confined areas – up to (or almost) the molecular level[12]. Thus, these force-sensing techniques, also called force spectroscopy

techniques, provide an enticing opportunity to study for studying nanoscale rupture dynamics.

Regarding the crack formation dynamics, force spectroscopy studies have been mostly devoted to the indentation of 2D layered structures encompassing lipid membranes[13], confined liquids[14], graphene[15], graphite[16], and the first stages of indentation of ionic solids[16]. These 2D systems display a well-ordered alignment both in the vertical and in-plane axes with no pre-existing cracks. In this way, every new indentation corresponds to the creation of a completely new crack, which allows an unprecedented control of the indentation conditions that is unachievable at bigger length scales. Moreover, the force is directly transmitted to the in-plane atomic bonds in 2D layered materials, which prevents energy dissipation in form of plastic deformation. Therefore, most materials will exhibit a purely brittle behaviour at the nanoscale, which simplifies the analysis of the rupture mechanism. As a result, the indentation of 2D layered materials are great model systems to study crack formation at the molecular level.

Investigating the molecular rupture dynamics by AFM indentation, however, has produced limited results. The main drawback has been the constant velocity indentation protocol employed: due to the fast increasing load applied, the rupture of the molecular bonds happens at very high rates and in a history-dependent manner (see section 1.5 for a detailed description). In order to address this problem, we have applied a more complex indentation protocol, called force-clamp, in which a constant force is applied throughout the experiment. In this way, the time-window of experimentation is expanded and the energy landscape of the rupture pathway can be precisely mapped. This technique has been useful at investigating many processes while pulling such as the cleavage kinetics of single sulphide bonds[17], the unfolding of proteins[18], and their refolding[19] kinetics.

Translating force-clamp to the investigation of nanoscale crack formation poses several unresolved questions. For example, In single molecule pulling, the most well-established type of force spectroscopy experiment, it is easy to imagine that the force will be transmitted directly through the stretched molecular bonds. While pushing, however, we still have no previous

knowledge on the contact profile between the AFM tip and the sample at the molecular scale. In addition, force-clamp provides the distance from the initial unbroken state to the main energy barrier (the transition state), which in single bond pulling corresponds to about half of the bond length. In the case of pushing, however, we cannot easily identify what the reaction coordinate corresponds to, or even its direction in space, because we have no model that describes the fracture mechanism. In this sense, rupture processes have traditionally been assumed to occur in a single step fashion, which is a reasonable scenario when the motion of a handful of molecules is involved. We fail to know, however, if the same situation occurs when a greater number of atoms are involved. Consequently, we still lack a clear framework to correctly interpret indentation experiments at the nanometre realm.

For these reasons, we have revisited the indentation of materials using force-clamp in an attempt to build, in the long term, a unified viewpoint of the nanoscale rupture dynamics. In this vein, we have first assembled an AFM with force-clamp capabilities (chapter 2). Then, we have used it to first investigate the mechanical response of a seemingly small and simple 2D material: confined liquid layers (chapter 3). Liquid molecules self-assemble forming solid-like 2D layers when located between two surfaces in close vicinity due to their limited degrees of freedom[11]. Despite being mechanically stable, confined layers reversibly break and reform when pushed from a perpendicular direction thanks to their fast mobility in the horizontal axes. The resulting rupture/reformation equilibrium turns confined liquids in an appealing model for fracture mechanics because it allows gaining unprecedented insight in rupture energy landscape and the contact mechanics between the AFM tip and the sample. Furthermore, the molecular motions involved in the reaction coordinate are easier to identify because each Angstrom-sized layer corresponds to a single array of individual molecules. Hence, confined liquid layers are an enticing model from which to start building up a molecular model of material fracture. By the use of force-clamp, we have demonstrated for the first time that the rupture of confined layers occurs through the disruption of a single lateral interaction. In addition, we propose that the rupture of confined liquid layers involves the creation of

a molecular pore in the solid-like layer structure, likely though the lateral hop of a whole row of molecules.

Going a length scale up, we have then investigated the rupture of lipid membranes (chapter 4). Lipid membranes are the main constituent of the cell envelope and their integrity is crucial for cell survival. Lipids possess a polar headgroup and a long hydrophobic tail. In the presence of water, they self-assemble in bilayers, exposing the hydrophilic headgroups outwards while encapsulating the nonpolar tails to the inner region of the bilayer. Lipid membranes are about ten times thicker than confined liquid layers and sustain forces up to several orders of magnitude higher than confined liquids, which suggests that a larger number of molecular interactions are disrupted by the AFM tip. Lipid membranes also reform, providing at every indentation a newly formed test sample. In this case, however, the reformation occurs at time scales much slower than the reformation, which prevents us from completely map out the energy landscape of rupture. Lipid membranes, nonetheless, are a unique nanoscale-sized model system that has deep implications in biology. By applying force-clamp, we have measured the rupture kinetics of lipid membranes in a stacked configuration, which offers much more biologically relevant environment. To explain the resulting complex rupture kinetics in the absence of a dynamic equilibrium, we propose a novel pore (or crack) nucleation mechanism that encompasses hundreds of molecules to account for the measured complex kinetics of rupture. Thus, lipid membranes exhibit a rupture mechanism that is molecular in origin, but that requires displacements of molecules well into the nanometre range.

Finally, we proceed to investigate the mechanical properties of lipid membranes in whole living cells (chapter 5). In this case, the indentation range is expanded to the micrometre range, which greatly increases the contact area between the tip and the sample. As a result, the force is no longer transmitted just to the lipid-lipid lateral interaction, as in model lipid membranes. Instead, we discover that at low indentation depths the tip-cell mechanical interaction is dominated by the underlying cytoskeleton. When the cell is further indented, however, the in-plane nanoscale interactions dominate again the mechanical response, which eventually leads to the lipid membrane rupture.

Hence, even at micrometric indentation ranges the lipid-lipid lateral interactions define cell membrane integrity.

Altogether, these three distinct experimental systems point out the key role that intermolecular forces play to define the mechanical strength of materials from a fraction of nanometre to several micrometres. This novel outlook also highlights the key role of putative common mechanisms that might govern the properties at the nanoscale and which might likely differ from those following the mechanism underlying the Griffin theory. This is a new outlook that has not yet been used, to my knowledge, in the several decades of material fracture research and thus, might prove useful for the understanding of fracture mechanics at the nanoscale.

Additionally, this research effort also adds up to the current knowledge on each of the studied materials. For instance, the pore formation mechanism in lipid membranes has great implications in endocytosis and cell trafficking[20]. Thus, the conclusions of each chapter need to be placed also in the context of their research topic individually. For this reason, the introduction has been split up in various sections. The present section sets the outlook of the dissertation and its key concepts. The remaining sections of this chapter provide the general theoretical framework and an in-depth discussion on the working principles behind force spectroscopy AFM and the analysis protocols for the experimental data. Finally, each results chapter contains an introductory section to put the results in the context of their research field. I thought that this setup will make it easier for the reader to find the most crucial part of the introduction closest to the results section provided that each results chapter is aimed at different research fields. I hope the reader will find this layout useful too.

1.2 Forces at the nanoscale

All the forces in the universe arise from four different fundamental types of interaction: strong, weak, electromagnetic, and gravitational[21]. Strong and weak forces act in the very short scale comprising the atomic nucleus, and thus will have a negligible effect in the nanometre scale where bond rupture takes place. The gravitational force also will have a negligible effect as it acts in much larger distances – for instance, the orbit of planets around the sun. The forces acting in the nanoscale will hence have an electromagnetic origin.

1.2.1 Strong electrostatic interactions

All interatomic forces are originated when their respective atomic electron clouds interact. Depending on the type of interaction, the resulting atomic bond will display different characteristics (see Fig. 1-1 for an overview of the different types). The bonding properties are fundamental for almost any science, from physics to biology and particularly chemistry. But bonding properties also have a great impact in the mechanical properties of materials: each type of bond have different strength and bond cleavage properties, thus defining the possible fracture mechanisms[22].

In one of the stronger types of interaction, the electrons of two or more atomic orbitals join together to form covalent bonds[23]. This new electronic configuration allows both atoms to have closed electron shells, which is favoured energetically as quantum mechanics predicts. This type of bond is stoichiometric: it forms structures with a fixed number of atoms [see Fig. 1-2], which defines the basis of chemistry and also define the structure of molecules, from water to complex macromolecules such as proteins or polymers. The resulting bonds are very strong and the force required to break them is orders of magnitude higher than that of other interatomic interactions[24]. This notwithstanding, in many cases covalent bond might be cleaved by substitution, which is a reaction that can be activated at significantly lower forces[25].

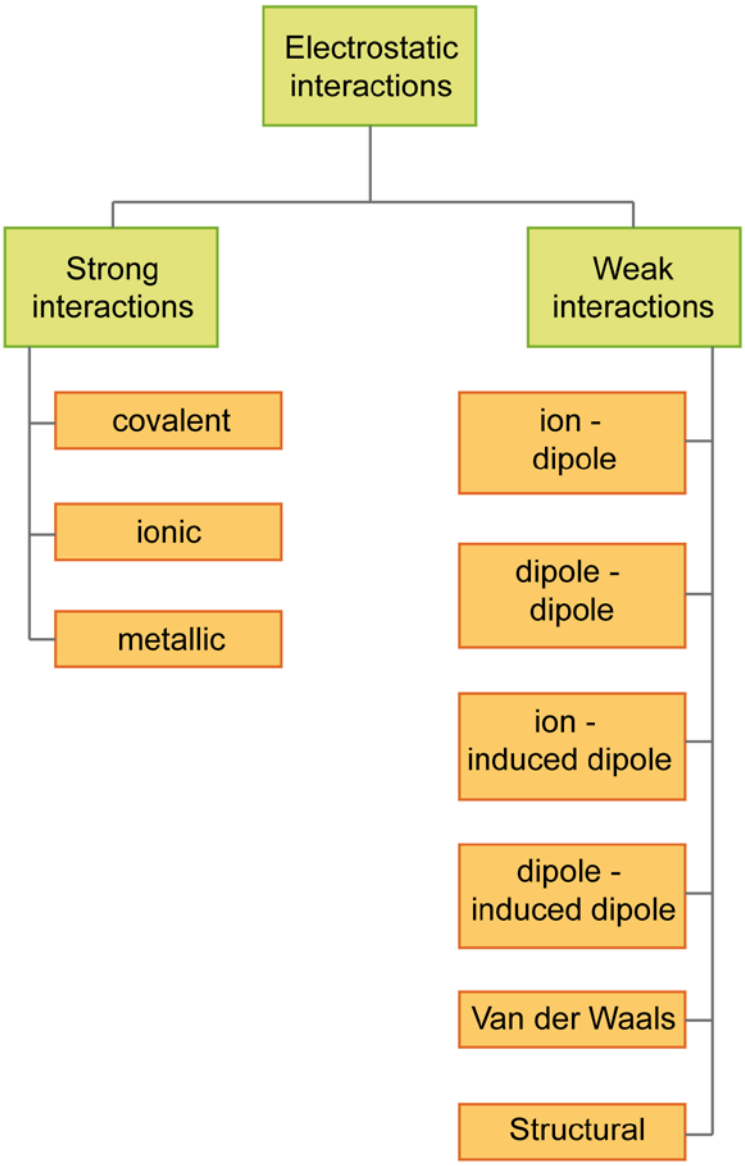

Fig. 1-1 Diagram of the types of electrostatic interactions.

Another important aspect of covalent bonds is that they are directional. Hence, their stability will depend on the direction of application of a pushing or pulling force. For example, carbon in its graphite form generates stacked hexagonal 2D layers of covalent bonds[23]. Breaking the covalent bonds bridging laterally contiguous carbon atoms requires high amounts of energy. Separating two layers, instead, requires cleaving more labile interatomic interactions. As a consequence of the directionality of bonds, graphite is a material easy to break at the macroscopic level despite possessing covalent bonds stronger than those of diamond. This picture dramatically changes when a single layer of carbon atoms is used. This allotrope of carbon – called graphene – misses inter-layer bonds and therefore the carbon-carbon bonds will have to be broken to create a hole in the graphene structure. The resulting mechanical stability is far greater than that predicted by Griffith theory and close to the theoretical limit. It is also the highest among known materials, among possessing many more enticing properties[26], [27].

Another type of strong interatomic interaction is the metallic bond [see Fig. 1-2]. This type of bond – typical of metals – is formed when the atoms overlap their electron clouds, thus delocalizing their electrons throughout the structure of the solid. Metallic bonds are similar in nature to covalent bonds, but have no directionality and no valence – no specific proportion of atoms is

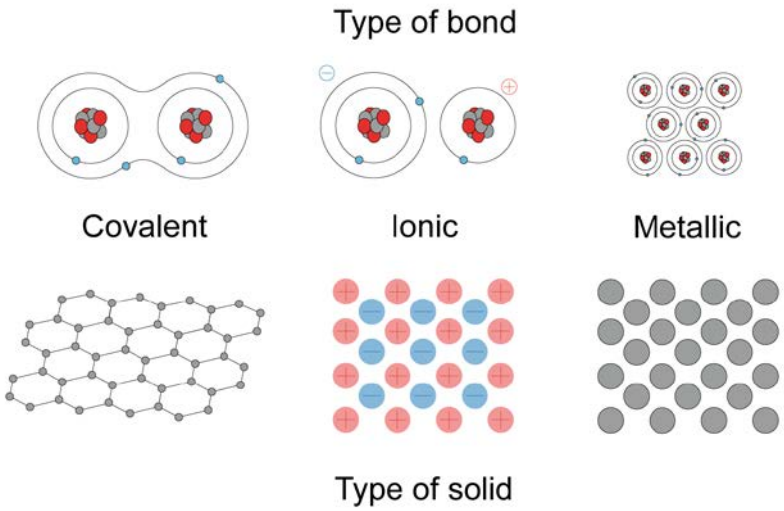

Fig. 1-2 The three types of electrostatic interactions (covalent, ionic, and metallic) and an example of the atomic lattice in each type of solid (graphene, ionic solid, and metal), respectively.

required. Because of the charge neutrality of metallic bonds, atoms can shift position easily, thus allowing atomic planes to move respective to each other easily when a force is applied. As a result, metals of high plasticity and lower stiffness. As they have no specific valence, metals can be easily doped with other elements to finely tune their properties. A simple example is the stiffening of iron by adding small proportions of carbon in order to form steel[28].

Instead of sharing the electrons between atoms, one of the atoms might capture them. This is the case of ionic bonds, where an electron is transferred from the cation to the anion [see Fig. 1-2]. The electron exchange is highly favoured because both atoms can close their electron shells as a result of the exchange. Due the charge separation, a strong electromagnetic field is generated between the two charged ions. Breaking an ionic bond, hence, will require separating the two charges to infinity, which involves a great amount of work[23]. As a consequence, ionic materials typically display crystal ordering in solid state and also a high melting temperature. In addition, ionic crystals can grow in the three dimensions while keeping their ion network because the non-directionality of their bonds.

Ionic materials, however, require that ions are intercalated. Because two ions of the same sign repel each other, an ion of opposite sign needs to be placed in between to shield them. As a result, ions need to overcome a high energy barrier while shifting to contiguous positions and hence the translation of atomic planes in an ionic crystal is hindered. As a result, ionic materials display high stiffness and fragility as they cannot absorb impacts as plastic deformation. This characteristic also makes ionic materials as a simple platform to study rupture mechanisms as complex atomic motions involved in plastic deformation are prevented[28].

Ionic materials can also display non-crystalline structure. For instance, disordered materials like silicon oxide (in glass form) display a molecular structure where the long range order is highly reduced, thus displaying a structure analogous to that of a ‘frozen’ solid[23]. Indeed, many disordered materials are obtained by quickly cooling them. But perhaps the simplest example is when ions are in the liquid state. In the liquid state, ions can

quickly diffuse and interchange their positions, thus highly deceasing their long scale ordering. Because of their strong ion-ion interactions, however, the order in short scale is conserved and ions form complex structures at the molecular scale[11].

Ionic liquids can be obtained by heating any ionic solid above its melting temperature. In the recent years, however, the term ionic liquid typically refers in the literature at ions which have non-conforming shapes, usually composed of alkyl organic groups. Organic ionic liquids display enticing surfactant and solvation properties, which makes them great candidates as solvents in organic chemistry[29]–[32]. They also form solid-like structured layers in the close vicinity of a flat substrate due to solvation forces, as it will be later explained.

1.2.2 Weak electrostatic interactions

Covalent bond, metallic bond, and ionic bond are the three types of strong interatomic interactions. Yet they describe the structure of most materials, the interactions between different solids or molecules are mostly ruled by weak interatomic interactions. These interactions originate when the charge and/or dipole of two electron clouds interact. They can be divided as ion-dipole, dipole-dipole, dipole-induced dipole, and spontaneous dipole-induced dipole interactions (see Fig. 1-3). These four categories give rise to many molecular and nanoscale phenomena ranging from inter-particle interactions to solubility.

Ion-dipole interactions have a strong influence in the hydration of ions. Water molecules, or any other polar solvents, will tend to align themselves in the presence of a strong electric field forming layers of structured solvent around the ion called hydration (or solvation). Generally, the hydration layers are weakly attached to the ion leading to short ion-water complex lifetimes ($<10^{-6}$s)[11]. But if the ions are smaller, such as with beryllium, or have several charges, such as with aluminium or calcium, these complexes can last up to minutes or even hours. Thus, ions-ion interactions in a solvated medium will have to go through their respective hydration layers.

In an analogous way, ion-dipole interactions also influence solid-liquid interfaces in aqueous medium by forming a layered network of ions on top of a flat ionic substrate. For instance, ions form a layered network of ions on top of the highly charged substrate muscovite mica, which was recently imaged by using the atomic force microscope[33]. Another example are lipid membranes, which exhibit such ion and water molecule network attached to its outer surfaces and which has been identified as critical for the mechanical properties of the lipid membrane[34]–[36]. Despite its confirmed existence, we still fail to fully comprehend how these ion networks tune the mechanical properties of materials at the nanoscale.

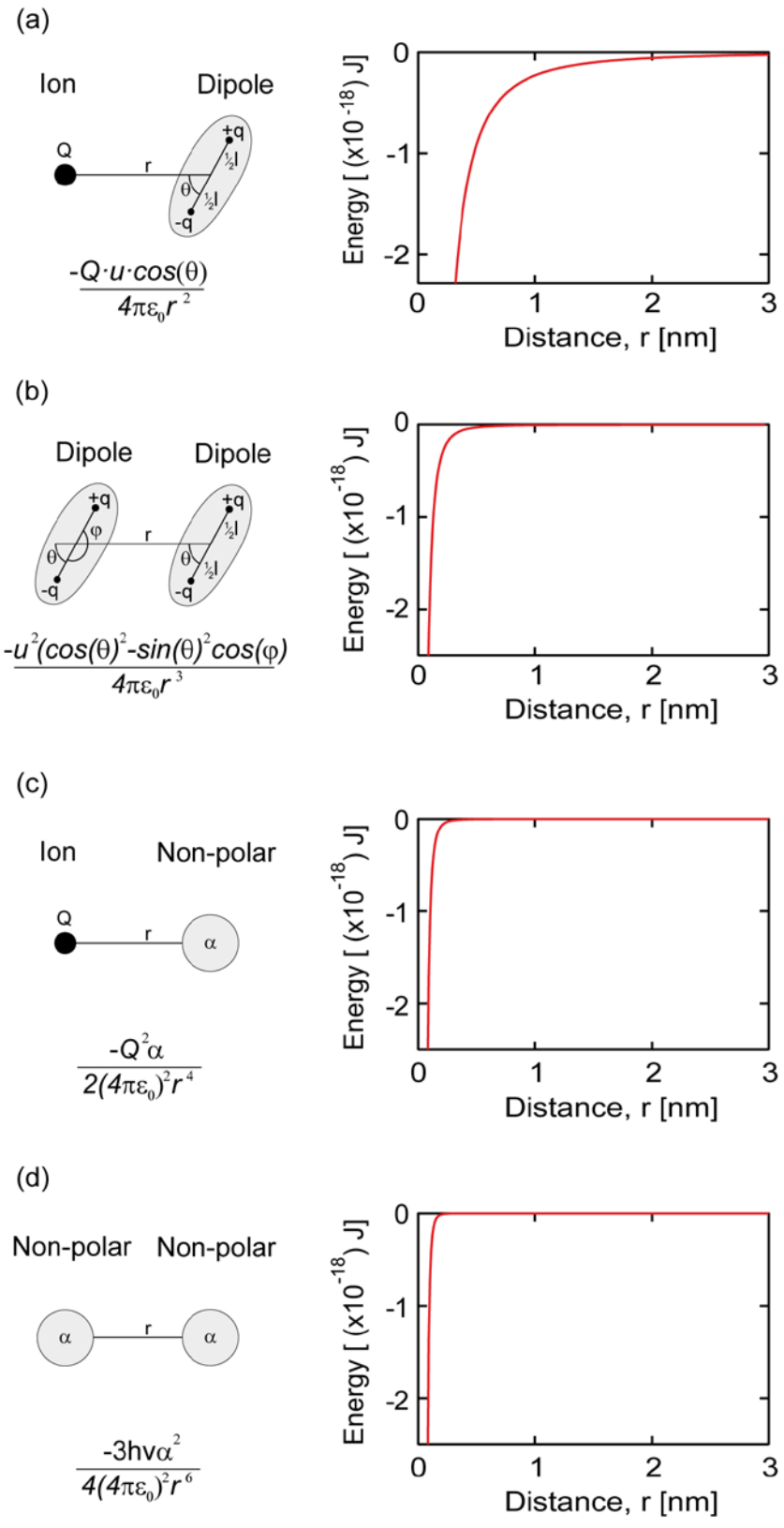

Fig. 1-3 Each type of weak electrostatic interaction leads to a distinct energy profile. (a) Ion-dipole, (b) dipole-dipole, (c) ion-non-polar, (d) non-polar-non-polar interatomic interactions are shown. (continues next page)

A schematic drawing showing the relevant variables that, as a first approximation, define the strength of the interaction has been drawn for each case together with the equation defining the energy profile. The following approximate values have been used to calculate the energy profiles: $Q = 1.6e^{-19}$ C, $u = q^*l$, $q = 1.6e^{-19}$ C, $l = 0.1$ nm, $\varepsilon_0 = 8.9e^{-12}$ Fm^{-1}, $\theta = \pi/8$, $\varphi = \pi/2$, $\alpha = 4\pi\varepsilon_0 R^3$, $R = 0.1$ nm, $hv = 1e^{-18}$ J.

Dipole-dipole interactions arise when two molecules with a dipole are in close proximity. The dipoles might arise either from a separation of charge in the molecular orbitals or from a cation and an anion being part of the same molecules (called zwitterions). Despite the widespread of dipole motifs, their low strength leads to the formation of just transient intermolecular complexes. A noticeable exception is the dipole in water molecules, which has a strong charge separation over a short distance thus producing exceptional dipole-dipole interactions. As a result, water molecules tend to align their hydrogen groups towards the oxygen groups of neighbouring molecules. Because of the tetrahedral symmetry of the hydrogen bonds, water molecules form complex 3D networks even in the liquid state. Recently, this theory is being contested by the hypothesis that water forms ring-like nanostructure that 'swim' in a fluid-like sea[37]. Hydrogen bonds are also crucial for almost any process occurring in aqueous environment encompassing ion solvation[11] (the solvated layers also need to align their hydrogen bonds), protein unfolding[37], lipid membrane rupture[38], and electrochemical reactions[23].

Molecules without an ionic charge or a permanent electric dipole might interact electrostatically too. The electronic orbitals surrounding the atomic nucleus can be deformed by an external electric field, generated i.e. by a nearby ion or dipole, which creates an induced dipole. The newly-created dipole can interact with existing charges or dipoles, thus creating a new type of weak interatomic interaction. The induced dipole will interact with other dipoles or ions in the same way that permanent dipoles do, but with a reduced intensity. For this reason, induced dipoles are important for the solubility of ionic and polar molecules in non-polar mediums as well as they will influence the net dielectric constant of such solutions. However, they have an unremarkable effect on the strength of materials[11].

Non-polar atoms can also interact electrostatically with each other even in the absence of an electric field. This interaction is best described by quantum electrodynamics. But to grasp the principles underpinning this counterintuitive effect, let's consider a helium atom as a model. Its time averaged dipole is zero, but at any given time, the specific location of its two electrons will likely not be exactly opposite to that of the other electron. The resulting instantaneous dipole will generate an electric field that will induce a short-lived induced dipole in a nearby molecule. Hence, an attractive force will arise between both atoms and its time average will be finite.

'Instantaneous dipole-induced dipole' forces are usually called dispersion forces and they are present in all materials – its working principle is valid even for ionic or polar molecules. They are generally attractive and have a range of several nanometres. Dispersion forces are typically considered together with the repulsive force that arises when the electron cloud of two atoms overlap due to the Pauli Exclusion Principle. Taken together, these two forces are called Van der Waals forces. The Van der Waals force profile is difficult to write down in a simple analytical expression and it is usually approximated by the Lennard-Jones potential[39]:

$$V_{LJ} = \varepsilon\left[\left(\frac{r_m}{r}\right)^{12} - 2\left(\frac{r_m}{r}\right)^{6}\right] \tag{1.1}$$

where ε is the depth potential, r_m is the distance at which the potential is minimum, and r is the distance between the particles. The Lennard-Jones potential is sown in Fig. 1-4.

Van der Waals forces are typically lower than ionic and polar interactions, and thus will be only predominant in the absence of permanent charges and dipoles. In such cases, Van der Waals forces crucially permit weakly-interacting, non-polar molecules to reach the liquid and solid states. But despite being a rather weak interatomic interaction, Van der Waals forces play a critical role in the interphase between materials. As Van der Waals forces are additive, their total value can add up to Newtons, which is well into the range of macroscopic forces. This is particularly the case when the contact area between materials is maximised, as it happens in gecko toe pads[40].

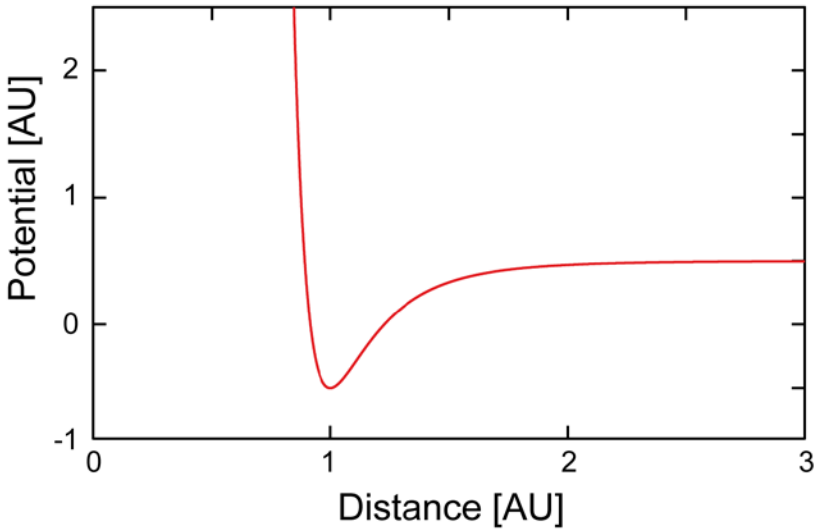

Fig. 1-4 The Lennard/Jones potential. All parameters have unity value.

Interestingly, Van der Waals forces are responsible for the force applied by an atomic force microscopy tip. Thanks to their ubiquity, the AFM can image virtually any surface. Thus, the force profile between an AFM tip and a surface, or between two surfaces, will follow a profile analogous to the Lennard-Jones one. In the attractive regime, the interaction potential can be roughly approximated to a flat surface and a sphere – the tip end. In this geometry, the (added-up) Van der Waals force is equal to[11]:

$$F = \frac{-AR}{6D^2} \tag{1.2}$$

where R is the tip radius, D the tip-sample separation, and A the Hamaker constant, which defines the strength of the Van der Waals interaction. The Hamaker constant depends on the properties of the material (or materials) and hence different materials will interact differently. This is an important factor for i.e. adhesion between materials. In order to increase the interacting between materials, however, it might be more effective to increase the contact

area (depending for this geometry on the radius R) – just as the gecko does to stick to virtually any surface.

But surfaces are seldom electrically neutral; they frequently become charged through a number of mechanisms. And when in a liquid environment, ions will stay close to the surface in order to compensate the electrical charge. Ions can neutralize surface charge through two different mechanisms[41], [42]. Firstly, they can directly absorb onto the surface. This is a mechanism found i.e. in lipid membranes. Secondly, ions will accumulate close to the surface without absorbing. At a long distance, the ionic concentration will increase exponentially with the proximity to the substrate. At a closer distance, near the hydrated ionic radius, a layer of atoms will form just in front of the surface (without direct absorption). The combination of these two forms of ion accumulation close to the substrate is commonly called the electrical double layer.

Molecules or solid particles close to the substrate will feel at the same time the electrical double layer and Van der Waals forces. The combined interaction was calculated independently by Derjaguin and Landau in Russia, and Verwey and Overbeek in the Netherlands. By combining the initials of their names, this theory is currently known as DLVO[23]. In short, this theory explains that if the Van der Waals force overcomes the electrical force, then the two surfaces will approach until they reach intimate contact (see Fig. 1-5). Instead, if the repulsive electrical force is bigger, then there will be an energy barrier that will kinetically prevent both surfaces to come into contact. The DLVO energy barrier is the foundation of colloidal science as it prevents solid particles to coagulate[41], [42].

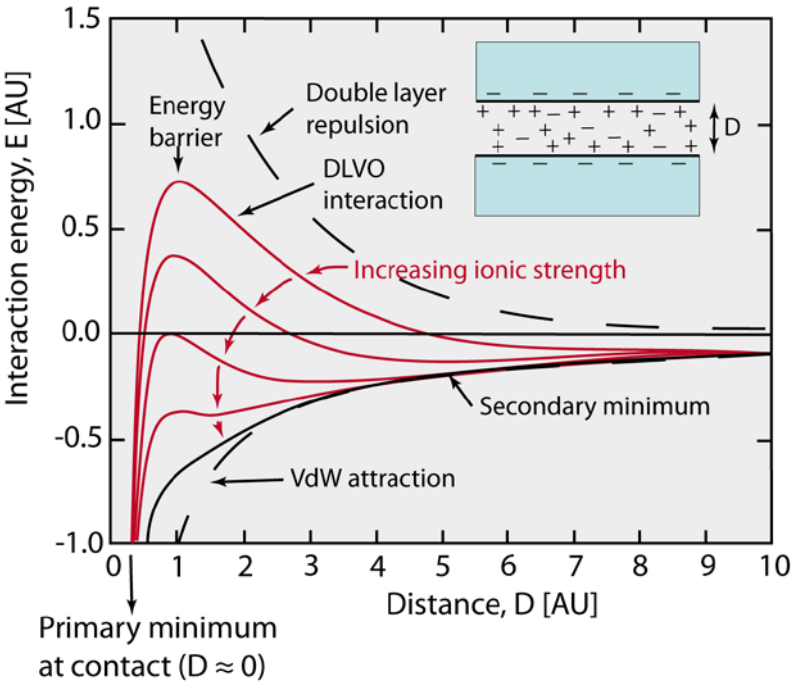

Fig. 1-5 The DLVO energy profile (red solid lines) results from summing the Van der Waals and double layer repulsion interactions (dashed black lines). The Van der Waals interaction only depend on the inter-surface distance, the geometry, and nature of the surfaces and medium, which are given for each case. (Inset) The double layer interaction, however, is screened by the amount of ions that are located between the two plates. Thus, the double layer interaction will decrease as the concentration of ions and their atomic charge increase (the ionic strength). As a result, the DLVO energy profile changes with an increasing ionic strength (red solid lines). For low ionic strengths, it exhibits one maximum (energy barrier) and a primary minimum at the contact point. When higher than the thermal vibrations, the energy barrier allows the particles to be suspended in solution without coagulating for long periods of times. As the ionic strength is increased, a secondary minimum appears at distances bigger than the energy barrier. As the ionic strength is increased even further, the energy barrier decreases as it becomes smaller than the thermal vibrations and ultimately it disappears.

1.2.3 Electromagnetic forces at play: the case of lipid membranes

Lipid membranes are a beautiful example of how the interaction of electromagnetic forces creates a 2D material. Lipids molecules are composed of two parts[43] [see Fig. 1-6(a-b)]. The first one is a long aliphatic chain that will interact with neighbouring molecules mostly through Van der Waals forces, thus preferring to stay close to other non-polar molecules. The second part is a short and strongly dipolar head. In many cases, the head-group dipole is generated by a zwitterion – or a cation and anion located in the same molecule. In other cases, the head might have a positive or negative net charge. Hence, the head-group will interact mostly through ion-ion, ion-dipole, and dipole-dipole interactions; thus preferring to stay close by to ionic and polar molecules.

In order to fulfil both polar and non-polar affinities at the same time, lipids self-assemble into complex macromolecular structures. Lipids can self-organize in a plethora of structures depending on their specific molecular geometry, solvent, and lipid concentration. They include spherical micelles, hexagonal phases, inverted micelles, and cubic phases[41], [42]. In the presence of a polar solvent and a lipid cylindrical geometry, they will form lipid bilayers (also called lipid membranes), a configuration with two lipid monolayers each facing their polar heads outwards, thus forming a 2D-layered material [see Fig. 1-6(c)].

In this geometry, the aliphatic chains stay secluded from the polar solvent inside the core of the lipid bilayer while fulfilling their bonds through dispersion forces. The polar heads, instead, will be in direct contact with the solvent, forming a complex network of polar bonds[35], [36]. These interactions encompass polar-polar bonds with contiguous lipid heads, hydrogen bonds with the aqueous solvent, and ion-ion interactions with solvated ions. Ions, in particular, play a key role in the stability of lipid membranes. Apart from forming an electrical double layer, molecular dynamics simulations show that ions directly bond to the lipid membrane surface[44], which has been confirmed by AFM imaging[35], [36]. Thus, both

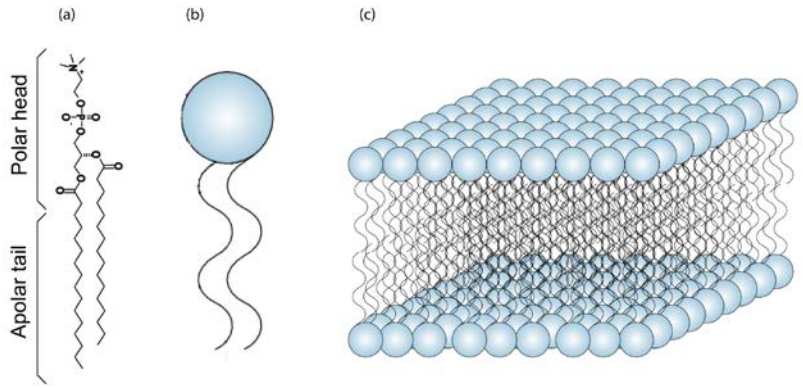

Fig. 1-6 The structure of lipid membranes. (a) Molecular structure of a typical lipid (Dipalmitoylphosphatidylcholine, DPPC). The phosphatidylcholine group is called the polar head (upper part), while the palmitoyl chains are called the apolar tail (lower part). (b) Schematic representation of the lipid molecule where the polar head is represented as a blue ball and the apolar tail as two solid lines. (c) Schematic representation of a lipid membrane composed of two opposing lipid monolayers.

the lipid moieties and the solvent properties will crucially influence the behaviour of a lipid membrane.

Lipid molecular composition is crucial for lipid membrane structure. Over the last fifty years, lipid membranes have been studied by using a plethora of experimental techniques. Until the two thousands, differential scanning calorimetry (DSC)[45], [46], nuclear magnetic resonance (NMR)[47], [48], and X-ray diffraction[49] were crucial to study lipid membranes in varying temperature, lipid mixture composition, and solvent composition conditions. They discovered that lipid membranes can exists in two different phases. In the first phase, called solid-ordered phase, lipids display low diffusion in the lateral directions, as well as very low diffusion in the vertical axis (flipping of lipids). Thus, the solid-ordered phase is like a two-dimensional solid. The second phase, called liquid-disordered, the lipids maintain the same low diffusion in the vertical axis, but now they quickly diffuse in the horizontal plane. Hence, the liquid-disordered phase is like a solid in the vertical direction, but like a liquid in the horizontal one (as in liquid crystals).

Interestingly, when a sterol (like cholesterol) is added to a binary mixture of a liquid-ordered and a solid-ordered lipid, the lipid membrane exhibits

intermediate properties: while lipids diffuse laterally as in a liquid-disordered phase, they also maintain the short-range correlation typical of the solid-ordered phase[50]–[53]. This intermediate phase is called liquid-ordered phase and it has been one of the main objects of study in lipid research for the last two decades because it is thought to be the origin of lipid rafts, nano-sized lipid domains existing in the lipid membrane of live cells whose role is to co-localize proteins with similar functions[54]–[56]. In vitro, sterol concentration have dramatically increased the mechanical stability of lipid membranes[57], thus confirming its key role in tuning lipid-lipid interactions.

The molecular structure also dictates the lipid membrane mechanical properties. During the last two decades, lipid membranes have been probed by force spectroscopy techniques – mostly the micropipette aspiration technique[10], [58] and AFM[13], [57]. These studies showed that both aliphatic tails and ionic heads crucially contribute to the lipid membrane mechanical properties. Longer and saturated lipid tails provide a higher mechanical strength because they provide better and larger contacts between neighbouring aliphatic tails, which maximizes the interacting dispersion forces. These factors also favour solid-ordered phases over liquid ones because a higher inter-particle interaction slows down molecular mobility. Unsaturations tend to decrease the mechanical strength. However, cis-unsaturations have a more disruptive effect than trans- ones because their looser configuration.

Ionic head-groups, however, fail to display any clear tendency on regarding their mechanical strength[57]. The solution ions, instead, have been found to dramatically increase the mechanical strength of phosphatidylcholine lipids[38], which is in agreement with the picture of ions incorporating in the lipid-ion network. A similar phenomenon has been observed for hydroxyl-containing lipid moieties when varying the pH[38]. In addition, calcium ions can induce phase segregation in a homogeneous lipid membrane[59]. Therefore, the lipid-ion network is a constituting part of the lipid membrane as important as the lipid themselves.

After more than four decades of lipid research, we have quite a detailed map of how the different parts of the lipid membrane affect its properties. Yet

we still face many unresolved questions. Regarding their mechanical properties, we still know little on the chemical and mechanical changes that lipid membranes undergo in vivo. In a more physical viewpoint, the current theoretical framework lacks clarity. Force spectroscopy data is analysed in terms of mechanical stability, which is generally related with the strength of the constituting bonds. This terminology, however, cannot be linked to any specific fracture mechanism, which ultimately is what defines the mechanical strength of a material. In this vein, here we have interpreted for the first time the lipid membrane mechanical rupture to a poration problem, which is a field that has been extensively studied over the last decades by electroporation experiments[60], [61]. In addition, lipid membrane poration is a key step in cellular endocytosis[20] and virus infection[62]. Hence, this new framework adds value to the current mechanical experiments. But most importantly, by developing a clearer theoretical framework we hope to gain a better understanding on the physical basis of lipid membrane poration, its mechanical properties, and ultimately its structure.

1.2.4 Solvation forces

Despite the DLVO theory describes well inter-surface forces at nanoscale separations, DLVO is a continuum theory and therefore it will fail to predict the force profile in those situations where matter displays its particulate nature. One such important case is solvation forces. They appear in solid-liquid interface because liquid molecules need to accommodate their position to the nearby 'hard' wall[11]. If the solid surface is molecularly flat, then the contiguous liquid molecules will self-assemble forming molecularly ordered solid-like layers (also called confined layers). These confined layers will possess a horizontal in-plane as well as a vertical 'out-of-plane' order (see Fig. 1-7).

When a second surface is used to indented the study substrate, then each of the ordered solid-like layers will have to be removed individually, hence generating an oscillatory force profile which is solely generated from the geometrical constraints (and not from the interactions between electrons clouds) unlike all aforementioned intermolecular interactions. Solvation forces also play a key role for non-flat geometries, such as molecular pores or cavities within proteins[63].

Solvation forces where first discovered using the surface force apparatus (SFA, described in detail in section 1.3). In these experiments, two mica plates are brought together with Angstrom-resolved motions while recording the resulting force. These experiments where initially recorded in OMCTS[64] and ethylammonium nitrate[65] and then subsequently expanded to other solvents[11]. The indented solvents displayed a different number of solid-like ordered layers and all of them displayed a rupture force several kT higher than the thermal energy. Also, the rupture force only varied slightly with the temperature. Together with the high contact area between the mica plates in the SFA experimental setup, these findings suggested that the removal of ordered solid-like layers required complex motions involving several steps (see Fig. 1-7).

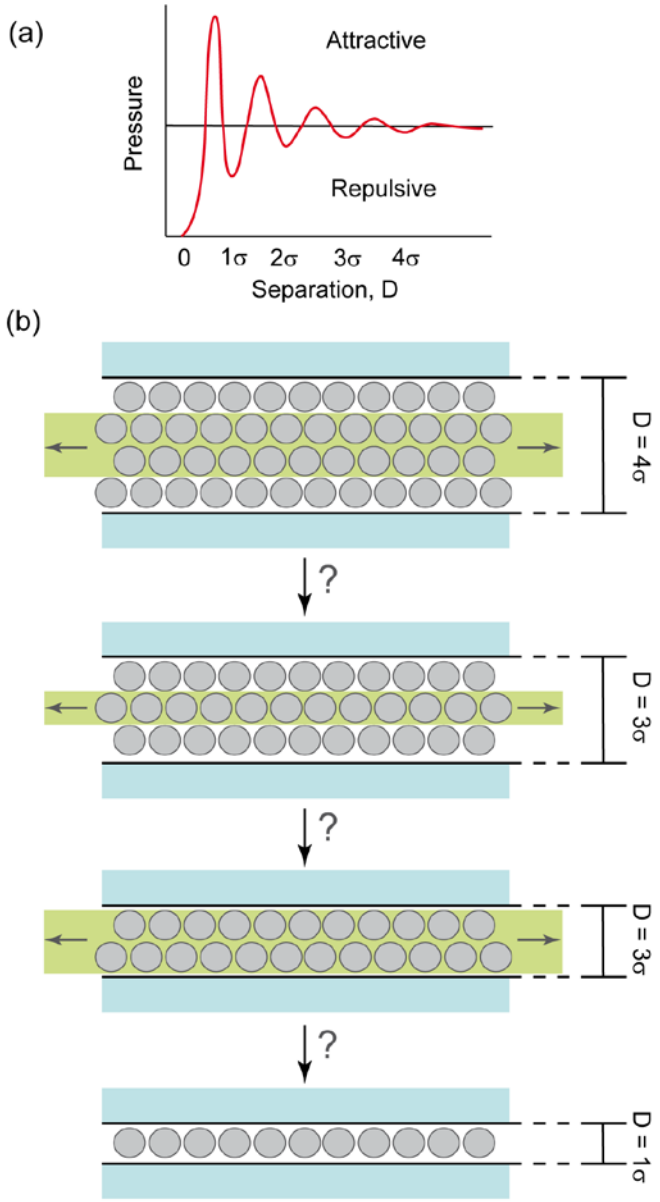

Fig. 1-7 When liquid molecules (grey circles) are confined between two surfaces (blue rectangles) separated by a few molecular radiuses, they self-assemble into discrete, solid-like structured molecular layers. (a) When the plates are brought together, the pressure will vary periodically with the molecular radius, σ. (b) When the pressure reaches a maximum, one layer at a time will squeeze out from between the plates. The molecular motions that are involved in each of these squeeze-out transitions are thought to require complex molecular motions that are still not well understood.

A decade later, solvation force experiments were revisited using the atomic force microscopy (detailed in section 1.4), where the contact area is orders of magnitude smaller. Initially, these experiments were aimed at replicating the number of ordered solid-like layers found in SFA in a plethora of solvents encompassing non-polar alkanes[66], [67], alcohols[68], ionic liquids[69], [70], and even water[71]. The number of layers recorded with AFM highly correlated well with previous measurements. Their rupture force, however, depended exponentially on the temperature. Taken together with other indirect findings, O'Shea[14] argues that the ordered solid-like layers break following different mechanisms on SFA and AFM. In the case of the AFM, the rupture would be initiated (almost) at the molecular layer following a single transition. In this vein, the work developed here provides data on the direct dynamics of ordered solid-like layers, which supports O'Shea's findings, thus pointing out the key role molecular motions play in the rupture of a 2D material at the nanoscale. In addition, these conclusions point out that solvation forces take place at a range much smaller than that proposed by SFA experiments, which links this research with the confinement in small non-flat cavities that area present in molecular pores or protein cavities. But in all cases, these experiments highlight the importance of solvation forces.

1.3 Force-sensing techniques

The first force measurements at the nanonscale date back to more than sixty years ago, when Derjaguin and co-workers[72] [73] measured for the first time the attractive Van der Waals forces between a convex lens and a flat glass surface in vacuum. An electro-torsion balance was used to monitor the force and the surface-to-surface distance was recorded using an optical technique. This experimental setup, however, only allowed to measure forces only in the range 100-1000 nm because of the roughness of the materials employed.

The first techniques capable of measuring forces at the molecular level were invented in the late 60s. The advent of the surface force apparatus allowed gaining an unprecedented knowledge on the precise forces that arise between two surfaces when they are in close proximity[74], [75]. Also during the same years, the micropipette aspiration technique permitted accessing the mechanical properties affecting of lipid vesicles. By expanding the technique to whole cells, micropipette aspiration provided a wealth of details on the mechanobiology of cells. Additionally, a variation of this technique achieved to monitor the rupture of single bonds for the first time. Despite being both techniques about half a century old, they are still employed in many laboratories worldwide, which highlight the versatility and robustness of the experimental setups.

By the end of the nineteen eighties and beginning of the nineties, the advent of nanotechnology revolutionized our knowledge of the nanoscale. The invention of the scanning tunnelling microscope (STM) allowed for the first time to directly visualize the surface of Silicon[76], the structure of which had subject of strong scientific debate. Silicon was shortly followed by many other metal and semiconductor structures, which greatly expanded our knowledge on surface science. STM records the topography of the surface by monitoring the tunnelling current that naturally occurs when a small gap separates a surface with the end of a metallic tip. Because the tunnelling current is exponentially proportional to the gap separation, sub-atomic

resolution can be easily achieved. STM, however, is limited to imaging conducting surfaces and, most importantly, it cannot measure forces.

But by using the same design idea, the creators of STM developed the atomic force microscope (AFM)[77], which measures Van der Waals forces. As Van der Waals interactions are ubiquitous, the AFM can visualize virtually any surface. And most importantly, they allow the AFM to directly apply, and sense, forces at the nanoscale. Thanks to this characteristic, the AFM is nowadays a versatile tool for imaging the topography and manipulating surfaces at the nanoscale. Despite that the AFM is less precise than the STM, state-of-the-art AFMs have atomic resolution and apply forces close to those occurring between single molecules.

The same decades saw the creation of another force-sensing technique: the optical tweezers[78]. This technique is based on trapping a micron-sized bead in a laser beam, which is subsequently used to pull from single molecule attached between its surface and the substrate (or a second bead). Optical tweezers offers greater force sensitivity and higher degrees of freedom in the three dimensions (unlike AFM, which lateral force-sensing ability is typically not possible). The optical tweezers soon became a powerful tool to investigate the motion kinetics of biomolecules at the single molecule level.

Finally, the magnetic tweezers are a force-sensing technique analogous to the optical tweezers, except that it uses magnetic force instead of optical pressure to trap a microparticle[79]. The magnetic tweezers are employed at the same single molecule fields of study as optical tweezers. Its main advantage is the lower trap stiffness, and thus higher force sensitivity. For this reason, magnetic tweezers are recently gaining interest for protein folding experiments[80]. It also permits to apply torque to single molecules, unlike any other single-molecule technique. An important drawback is the lower spatial and temporal resolution. Due to that it has never been used for pushing experiments and that its applications are very similar to those of the optical tweezers, magnetic tweezers have not been presented in more detail.

The following sections will introduce the working principle of each of these force-sensing techniques and their main applications will be shortly described. In addition, their suitability to be used for this project will be discussed. In this respect, indenting 2D materials at the nanoscale has two main requirements to be met. Firstly, the force-sensing technique must be able to perform indentation experiments. Hence, to measure forces while pushing. Secondly, the technique must be able to apply force in a very confined area in order to capture the first stages of molecular fracture.

1.3.1 Surface Force Apparatus

The first experimental approach capable of measuring forces with Angstrom resolution is the surface force apparatus (SFA). Tabor and Winterton[81]and Israelachvili and Tabor[82] developed a first SFA model to measure forces between two opposing mica plates in air or vacuum. These first results confirmed Lifshitz predictions[83], [84] up to 1.5 nm of separation between surfaces. Then, the SFA model was adapted to work in fluid medium, which greatly opened the window of experimentation.

The working principle of a surface force apparatus is shown in Fig. 1-8 [11], [85]. Two atomically-smooth mica plates (radius of ca. 1 cm) are placed in a crossed-cylinder geometry, which is the locally equivalent of two opposing spheres. The lower sits on top of a force-measuring adjustable cantilever. The distance between both plates is controlled by a complex

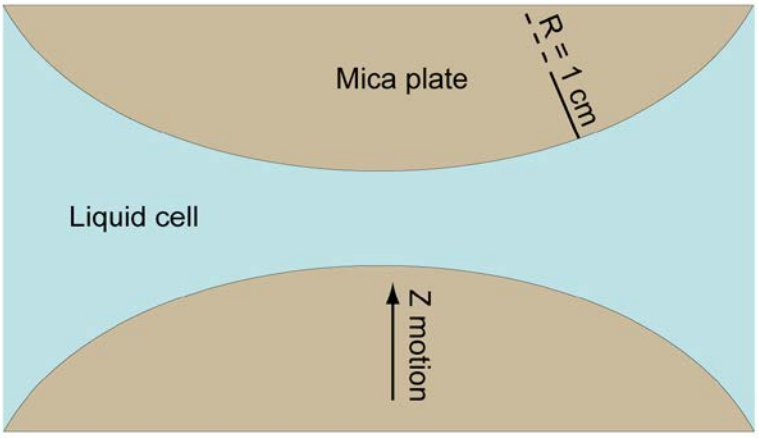

Fig. 1-8 Working principle of the surface force apparatus. Two mica plates of radius ca. 1 cm are brought in contact inside a liquid cell.

control system. For the coarse approach between the surfaces, the lower mica plate can be moved using a mechanical actuator. Then, the surfaces can be brought to close vicinity with a helical springs which control the position with about 1 nm resolution. Finally, the experiments are performed with a piezoelectric actuator. The piezoelectric actuator provides Angstrom resolution in the vertical axis, which allows to precisely measure any deformation in the gap area between plates. In the horizontal axes, however, the precision is much lower (in the micrometre level).

The position of the mica surfaces is visualized by multiple beam interferometry. The gap between the two mica plates generates an interference pattern and the size of the gap can be extracted by measuring the distance between two fringes of equal chromatic order. The pattern can also be used to extract the thickness of any absorbed layer on top of the mica plates and the refractive index of the gap. The two latter properties help identifying the degree of coverage of the mica plate in case it was functionalized – i.e. with a thin film or a self-assembled monolayer – and that no bubbles or other 'big' particles are present in the gap between the mica plates. Another main advantage of multiple beam interferometry is that thermal drifts can be directly monitored and controlled, thus allowing more long and stable experiments.

In a typical SFA experiment, the two plates are firstly approached in the absence of any absorbed layer to measure the initial separation between the plates. Subsequently, the mica plates are immersed in solution and, if desired, their surface covered with a molecular layer of interest. Then, the plates are approached at a constant velocity and the resulting force in function of the layer-to-layer distance is recorded in real time. Then, the experiment is repeated several times at varying loading rates, which allows accessing the mechanical properties of the absorbed layers. This protocol is the same one used for force spectroscopy and it will be explained in more detail in section 1.5.

By measuring the force against the distance between the two surfaces, the pressure or energy between both surfaces can be calculated by knowing the radius of each plate. In the same way, the adhesion energy can be easily

calculated knowing the area of contact between surfaces. Also, the surface radius crucially affects the force resolution of the surface force apparatus. For the same force sensitivity (ca. tens of nanoNewtons), a typical radius of 1 cm produces an average force per molecule much smaller than with the atomic force microscope. Conversely, pressures as high as 0.5 GPa can be applied with a much smaller plate radius (1 mm). In any case, the contact area and the applied pressure are calculated using mechanical contact models (explained in section 1.5 too)

The SFA was initially employed to investigate the Van der Waals forces between two mica plates in vacuum[81], [82]. Soon afterwards, it was adapted to work in liquid, which allowed to unveil many more surface interactions, including double layer forces[65], [86], [87], hydrophobic forces[88], structural hydration forces[64], lipid membrane rupture[89], [90], friction[91], and lubrication forces[92]. Even after more than three decades of research, the surface force apparatus is still producing relevant result in the field of surface science[85].

One of the main limitations of the surface force apparatus is its low lateral resolution: the diffraction-limited lateral resolution and the extended area of contact limit the SFA to capture vertical forces arising from the interaction of a large areas, which are assumed to be homogeneous. In addition, dust and suspended particles can easily interfere with the measurements if they get between the plates because of the extended area of contact. As a result, experiments can easily provide irreproducible experiments unless thorough cleaning procedures and high purity reactants are employed.

Additionally, the extended area of contact might also limit the type of processes that can be monitored. For instance, when certain liquids are confined in the nanometre scale between the two SFA plates, they produce solid-like structured layers. As the force is increased, the solid-like layers suddenly break one at a time. In SFA, these sudden transitions happen at a force that is independent of the temperature, which is a signature of many-molecules, cooperative processes[11]. Instead, when the same liquids are indented with AFM[14], or when rough surfaces are used for the SFA setup[11], then a completely different result is obtained. For AFM

measurements, the process occurs in a thermally activated manner[14]. Thus, different contact areas rule might crucially influence the rupture process of a material. This is an important parameter to consider for the goal of this project.

Another main limitation of SFA is the limited number of available surfaces. SFA substrates must be transparent because its positioning system relies on optical measurements. Additionally, atomically smooth surfaces are better suited to accurately calculate the contact area between both plates. Otherwise, the plates would make contact only through the last asperities of the surfaces and thus the pressure applied would become ill-defined. For these reasons, mica is the surface employed in most of the surface force apparatus literature as it exhibits both transparency and atomic-level flatness. Other substrates have been employed, such as sapphire[93], silica[94], and various polymer films[95]. But these requirements limit the applicability of the technique to many other substrates of interest, such as graphite or metals.

All in all, the surface force apparatus has provided invaluable information regarding the structure and the forces arising at the surface of materials ranging from the simple Van der Waals force profiles between two mica plates to the complex motions of confined liquids. This notwithstanding, the force applied in SFA experiments distributes over thousands or more molecules in a simple profile, which is far from the molecular scale that we aim to investigate here. In addition, as most surfaces are rough by nature – at least at the nanometre range – forces at this scale will likely distribute through a few contacts points, which will produce a force or pressure profile dramatically different than that obtained between two atomically smooth, perfectly aligned mica plates. Despite this difference might be unimportant for certain systems, it will likely be for others such as solid-like ordered layers.

1.3.2 Micropipette aspiration technique

Micropipette aspiration is considered the pioneering technique for capturing the mechanical properties of lipid vesicles or cells. In a typical setup, a vesicle is trapped at the end of a suctioning pipette [see Fig. 1-9(a)] and its shape is recorded in real time by a camera. Due to the suction, the lipid membrane is stretched and the vesicles exhibits a smoother, globular-like shape.

Initial micropipette aspiration technique studies were mostly conducted on lipid vesicles[10]. These are globular-like structures which are composed of a single lipid bilayer encapsulating buffer solution. Lipid vesicles are generally regarded as the simplest mechanical models of cells and, interestingly, they have been widely used to study the mechanics of lipid membranes, an example of a 2D layered material. At the low suction pressure regime, the lipid membrane is assumed to be incompressible[96], and thus its total area constant. However, the suction pressure reduces the ripples and undulations of the vesicles, thus decreasing its configurational entropy. As a result, an apparent increase of the optically resolvable change membrane area α[97]. It has been shown that α follows:

$$\alpha \cong \frac{1}{8\pi k_B \beta} \ln(\tau) \tag{1.3}$$

where k_B is the bending rigidity, τ is the lipid membrane tension, and β is $1/k_B T$. In this way, the bending rigidity can be obtained for different lipid compositions. At the high tension regime, the lipid membrane area changes as[98]:

$$\alpha \cong \frac{(\tau)}{K_A} \tag{1.4}$$

where K_A is the apparent area modulus. This approach has provided a wealth of information on how the lipid membrane composition affects the membrane elasticity and the rupture force[99], [100]. It has also been useful to investigate the effect of sterols on the lipid membrane mechanics or the effect on tension of the channel forming peptides[101]. These achievements

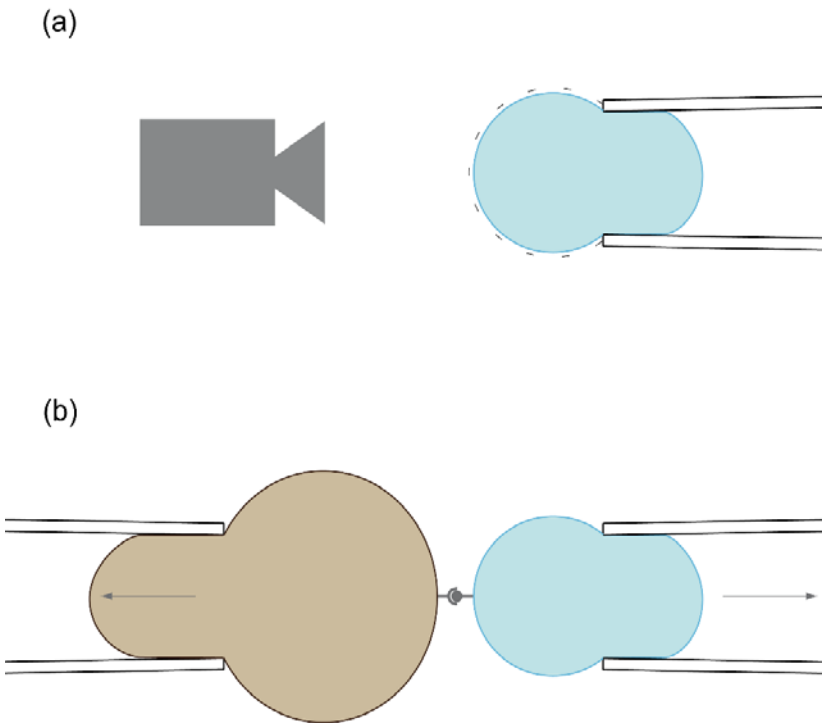

Fig. 1-9 Micropipette aspiration technique experimental setup. (a) A cells or lipid vesicle is trapped at the tip of a micropipette by maintaining a suction pressure. The mechanical properties of the trapped cell or lipid vesicles are measured by recording the morphology of the vesicle in real time. (b) Micropipette aspiration can also be used to perform single molecule pulling experiments. Two cells are trapped by micropipettes and brought into contact. After allowing a dwell time, the pipettes are withdrawn. As a result, any adhesive cell-to-cell bonds will sustain an increasing force until they break.

notwithstanding, the bending rigidity and the apparent area modulus are mesoscopic measurements arising from the average behaviours of vast numbers of molecules, which is orders of magnitude bigger than the scale at which the rupture of the lipid membrane will initiate.

To quantify the mechanical properties of cells, a commonly used approach is to consider that the cells deforms while maintaining its inner volume constant. As a first approximation, the cell can be considered as a completely elastic membrane holding a Newtonian liquids. When the cell is suctioned into the pipette – forming an almost perfect semi-sphere – its radius is equal to the pressure difference as[102]:

$$\Delta p = 2T_m\left(\frac{1}{R_P}-\frac{1}{R_C}\right) \tag{1.5}$$

where T_m is the membrane tension, R is the radius of the pipette, and R is the radius of the cell. This model fits well soft cells such as neutrophils, but fails to fit for solid-like cells such as chondrocytes[103]. For the former cases, alternative models are available[104]. In addition, cells can trigger active responses. For instance, Luo and co-workers showed that the cytoskeletal cortex generated oscillations in the lipid membrane shape during bleb formation[105]. However, the cytoplasm, cytoskeleton, and cell internal organelles are mostly responsible for the observed cell deformation. Thus, the contribution of the lipid membrane on cell mechanics cannot be isolated using these micropipette aspiration experiments. Instead, a more localized force should be applied, as with atomic force microscopy.

Micropippette aspiration is also suited to study molecular adhesion between ligands and receptors. In this modality, called biomembrane force probe (BFP), two cells are held in two separate micropipettes [see Fig. 1-9(b)]. As they are brought into contact, the ligands can bind to other ligands or receptors located in the opposite lipid membrane, thus generating molecular bonds binding both cells together. As the cells are pulled apart, these bonds will sustain the increasing pulling force until they break. This approach has been used i.e. to study the adhesion between Fc receptors and IgG at the single molecule level[106]. Or, for instance, the mechanism of adhesion based on "catch bonds" in leukocytes was investigated by substituting a cell by a functionalized glass microsphere[107].

All in all, micropipette aspiration technique has provided a wealth of information regarding cell and lipid membrane mechanics. On the other hand, it has pioneered the field of single-molecule bond rupture experiments. However, the micropipette aspiration technique cannot apply pushing forces in a highly confined area. Thus, it is not suited for the study of the molecular mechanisms underpinning material fracture.

1.3.3 Optical tweezers

Optical tweezers can apply up to hundreds of picoNewtons of force to nano- and microparticles while recording their position in the three dimensions with sub-nanometre resolution. In addition, optical tweezers can also record any external forces applied to the particle. These characteristics turn optical tweezers in one of the most versatile force spectroscopy and nanomanipulation tools currently available[12].

An optical trap is created by focusing a high NA laser on a dielectric particle(see Fig. 1-10). The optical trap creates a restoring force field in the three dimensions that keeps the particle at the centre of the laser focus. The restorative force is generated by the excess of photons in one of the sides of the particle when its moves out of focus[108]. The restorative force is linear for small displacements and its strength is proportional to the laser intensity. Thus, the 'stiffness' of the optical trap can be tuned at will by the operator. If high forces are required, the trap stiffness can be increased up to the limit, which is dictated by the laser power and/or the photobleaching of the sample. On the other end, the laser intensity can be decreased to perform experiments with higher accuracy. The accuracy, however, comes at the price of a higher noise because the Brownian shocks from the surrounding molecules will create higher displacements. In practical terms, the typical force range is 0.1-500 pN.

The first type of optical tweezers experiments were aimed at following the movement of a particle against a fixed object. Block and co-workers pioneered this field by tracking the movement of a kinesin-coated microparticle over a fixed microtubule[109]–[111]. The same type of experiment can measure the unbinding force of virus-coated bead when brought into contact with an erythrocyte[112], or the binding strength of a single fibrinogen-integrin pair in live cells[113].

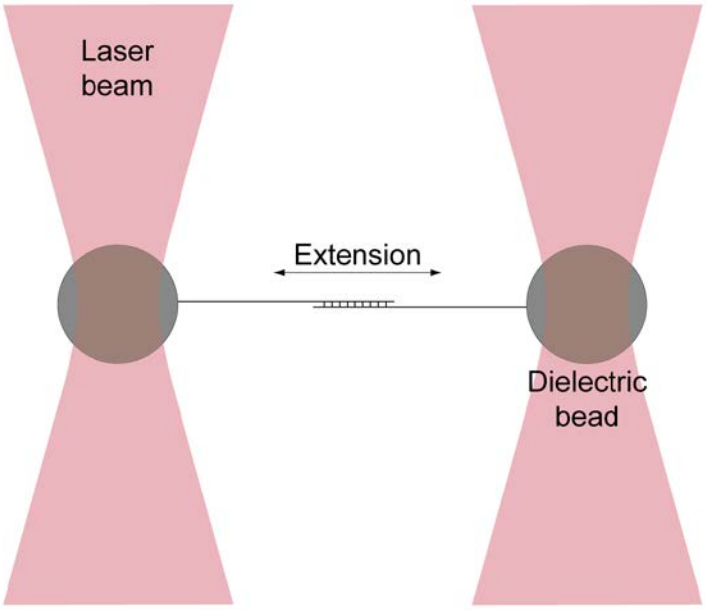

Fig. 1-10 Working principle of the optical tweezers. A dielectric bead is optically trapped at the focus plane of a laser beam (red coloured area). Optionally, a second bead can be trapped for the ease of manipulation. For force spectroscopy experiments, typically the beads are coated two complementary molecules. In this case, the straight line represents a DNA strand. When the beads are brought in close contact, the DNA strands will bind. Then, one optical trap can be moved away in order to study the single molecule kinetics under force.

In a second type of experiments, the optical trap is used as a force and displacement sensor of a trapped molecule. For instance, the optical trap can monitor the translocation and force generation of DNA transcription by RNA polymerase[114]. In this setup, the RNA polymerase reels in a bead attached to the end of a DNA strand. Every time a single step of the transcription occurs, the force stall can be measured[114], as well as the transcriptional pausing[115], [116], backtracking of DNA strand[117], and the mechanism of translocation[118].

A third type of optical trap experiment is force spectroscopy. In this case, the optical tweezers are used to apply a vector force to a molecule. As the main field of application of optical tweezers is biology, the goal of force spectroscopy experiments is to record the unfolding and folding trajectories of single molecules. The main limitation of optical tweezers is its low limit force, which in many occasions is below or about the unfolding force of many

proteins. Instead, optical tweezers is very well suited to study protein folding[119], [120]. But perhaps the most famous experiment is the unzipping of DNA, which has wield a precise knowledge of the phase behaviour of DNA under force[121].

Despite these are the three most common types of experiments, there are much more types of experiments that could be performed with optical tweezers. Especially since optical tweezers has become more widespread (there are even optical tweezers commercially available), the applications of optical tweezers has greatly increased. This notwithstanding, optical tweezers are difficult to fit to study the rupture of materials. The first limitation is that optical tweezers are designed for pulling, not pushing. Additionally, the low upper force limit is far below any of the applications mentioned here; for some cases up to several orders of magnitude. For these reasons, optical tweezers were not employed in this project.

1.3.4 Atomic force microscope

The atomic force microscopy (AFM) belongs to the family of experimental techniques called scanning probe microscopies (SPMs). Also comprising the scanning tunnelling microscope (STM) and the near-field scanning optical microscope (NSOM), this microscopy family employs a sharp tip to interact with the sample surface. AFM is most broadly known for imaging. In a typical experiment, the tip is maintained in gentle contact with the surface of the material and then its topography is scanned by moving the tip horizontally (see the next section for a more detailed explanation on the AFM working principles). Because the end of the tip has nanometre-sized dimensions, the surface topography can be imaged with great detail. Indeed, by using a highly precise positioning system, these techniques can achieve sub-nanometre resolution. Furthermore, because no light beam is used here, SPMs exceed the light wavelength resolution limit affecting traditional light microscopy.

In particular, the AFM monitors the mechanical forces. These forces arise from the intermolecular Van der Waals and electrostatic interactions occurring at the tip-sample interface. Thanks to their ubiquity, the AFM can successfully interact with virtually any material. Indeed, AFM imaging has been successfully employed to study a wide variety of materials in fields spanning from biology to engineering. Moreover, AFM precisely measures the vertical features of the surface profile, which is impossible with traditional light microscopy. All in all, AFM has become a standard imaging tool frequently employed in research laboratories within both companies and universities.

Atomic fore microscopy is not limited to imaging the surface topography; it can also measure the surface mechanical, chemical, and electrical properties[122]. The most basic procedure consists of measuring the phase lag during dynamic mode scanning (oscillating the tip close to the surface). In short, the phase lag is characteristic of each material and it thus serves to qualitatively compare chemically different surfaces that might display very similar topographic features. More specific properties can be also extracted by using more complex AFM tip motions or applying electric and magnetic fields. Indeed, the latter option has greatly developed during the last decades

producing a wide variety of AFM modes such as Kelvin probe microscopy, conductive AFM, or electric force microscopy. Currently, the top AFM developers commercialize turnkey modules to implement them, making them readily available for the scientific community if they can meet the budget.

All these modes of operation, however, cannot quantitatively measure the mechanical properties of the materials because the gentle contact with the surface precludes measuring the elastic and plastic (rupture) properties of materials that only arise when they are significantly deformed. This is particularly the case for the rupture mechanisms studied here. But even elastic deformations are difficult to grasp quantitatively by using gentle contact because the complex motions of the tip used in many of these AFM modes result in complex tip-sample interactions, which are difficult to describe analytically. Even if these equations are experimentally determined, in most of the cases the resulting parameters are complex mechanical measurements difficult to compare with other techniques. Hence, significant deformations are required to fully probe the mechanical properties of materials.

To perform force spectroscopy, the sampled material needs to be indented by the AFM tip, instead of scanned as in the previous modes. Thus, the tip is initially placed in a fixed position close to the surface. Then, it is approached to the material until significant deformation is produced. Finally, the tip is retracted, thus returning it to the original position. By calibrating the forces applied by the tip, we can monitor the mechanical properties and rupture processes occurring at a wide range of penetration depth regimes.

Perhaps the most widespread use of AFM indentation is to measure the stiffness of a material. For this experiment, the indentation trajectory is fitted with a contact model to obtain the Young modulus, a dimensionless estimate of the material stiffness (explained in detail in the next section). Using this approach, a wide range of materials encompassing ionic solids[122], polymers[123], [124], and live cells[124], [125] have been studied. Also, Moeendarbary et al. measured the viscoelastic properties of live cells by using tipless cantilevers[126].

The adhesive properties of materials can also be probed by AFM indentation. When the AFM tip retracts from the substrate, the tip necessitate

of an extra force, or 'pull-off' force, to disengage the surface. The pull-off force informs on the number and strength of the adhesive bonds formed between the tip and the substrate. This approach has been used mostly to study the surface free energy of self-assembled monolayers[127](and citation therein).

The AFM is not limited to probe the mechanical properties of materials while pushing: single molecules can also be pulled from a supporting substrate with the AFM tip. In this situation, the pulled molecules elastically stretch and then unfold (rupture) when their mechanically relevant bonds are disrupted. In this sense, pulling experiments provide analogous information to that obtained while pushing, and their theoretical models are easily interchangeable. Pulling experiments are most famous for investigating the unfolding kinetics of single proteins under force. Titin was the first protein pulled in 1997[128]. Since, then, the unfolding and folding kinetics of proteins have been thoroughly investigated both in protein constructs (polyproteins)[129], single proteins[130], or membrane proteins[131]. Also, the cleavage kinetics of disulphide bonds has been investigated using this approach[132] – just to cite a few studies.

But the goal of this project is to measure the fracture mechanics of materials at the nanoscale. For this purpose, the sample materials are indented until a crack is formed in their structure and the AFM tip can break through. By recording the rupture force, the mechanical properties have been measured for a number of solids encompassing lipid membranes[13], ordered solid-like layers[11], ionic solids[16], graphene[15], and graphite[16]. In the case of lipid membranes, the mechanical properties have been correlated to the ionic strength and pH[133], ion species[134], chemical structure[57], cholesterol concentration[135], temperature[136], and to the relative lipid concentration in lipid mixtures[137].

These indentation experiments cannot be performed any of the previous force-sensing techniques. Surface force apparatus has a contact radius in the order of microns, far above the molecular level that we are interested to investigate. Micropipette aspiration technique has the same problem. Optical tweezers and magnetic tweezers can apply very confined force when pulling molecules. The opposite motion, however, is not possible. In addition,

indenting materials requires applying forces much higher than those allowed by the stiffness of the optical trap. Therefore, we have chosen AFM to perform indentation experiments at the nanoscale.

1.4 The AFM working principle

Atomic force microscopes have a relatively simple working setup. As previously mentioned, the force is applied through the tip of a pyramidal probe, which sits at the end of a long micro-sized cantilever. Under experimental conditions, the end of the tip is pointed towards the sample, as shown in Fig. 1-11. When they make contact, the resulting force is transmitted to the cantilever, causing a deflection. In this manner, the cantilever acts as a linear force detector. The cantilever deflection is then converted to a measurable voltage by a laser optical system which monitors its deflection. It is composed of a laser beam, a mirror and a 4-quadrant photodiode. The laser is pointed at the end of the cantilever, and thanks to its reflective coating, the laser reflection is guided by the mirror to the middle of the 4-quadrant photodiode. In this configuration, any small deflection of the cantilever produces a shift in position of the laser spot at the quadrant photodiode. The shift then results in more photons hitting either the upper or lower photodiode panels, which generates a proportional voltage signal.

In order to apply small forces, the position of the tip must be precisely controlled. Otherwise, the AFM tip would contact the sample in an uncontrolled way causing major damage to the sample. Precise control of the tip is achieved by using a piezoelectric actuator. This type of actuator is made of a piezoelectric crystal that expands as a bias voltage is applied to its ends. With this type of positioning system we can achieve Angstrom resolution. Its

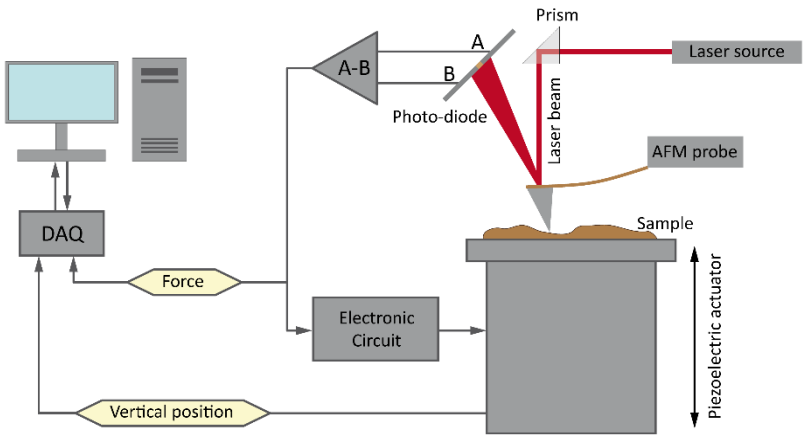

Fig. 1-11 Schematic drawing of the working setup of an atomic force microscope.

main drawback is its non-linearity. For this reason, the piezoelectric crystal is typically mounted between two capacitor plates, which measure the extension of the actuator. It is worth noting that the Luigs&Neumann AFM model that we tested does not require them: thanks to its high quality and small travel range, the piezoelectric expansion is highly linear with the applied biasing voltage. In any case, the position of the sample (or the tip) and the applied force are constantly monitored by a controlling computer (left side of Fig. 1-11). The controlling computer can also directly drive the actuator, which is the case in force-extension mode. Thanks to this setup, we can manipulate molecular-sized objects with sub-nanometre resolution.

1.4.1 The force-sensing principle of the AFM

The force-sensing principle of the cantilever can be explained by using classical mechanics. As a first approximation, the deflection of a cantilever beam by a point force exerted at its end can be described as[138]:

$$\delta = -\frac{l^3}{3EI}F \tag{1.6}$$

Where l is the length of the cantilever, E its bending modulus and I the area moment of inertia, whose value depends on the geometry of the cantilever. Hence, the force sensitivity of an AFM will depend on the effective spring constant of the cantilever k, by the relationship:

$$F = -\frac{3EI}{l^3}\delta \equiv -k\cdot\delta \tag{1.7}$$

By producing cantilevers with higher length/thickness ratio, manufacturers obtain smaller spring constants, and hence increase the force sensitivity of the AFM. Current manufacturers achieve spring constants as small as 10 pN/nm (i.e. the tip C from MLCT Bruker Probes (Karlsruhe, Germany)). Thus, the geometry of the cantilever effectively determines its sensitivity: the smaller the spring constant, the weaker the range of forces sensed. Conversely, harder materials can be probed just by using harder cantilevers, but at the cost of losing force resolution.

The geometry of a cantilever also determines the signal to noise ratio. If a cantilever has a bigger area, more surrounding particles will collide against the cantilever generating thermal noise. In a similar way, a damper medium will lead to higher noise. The force noise $\langle F \rangle$ caused by thermal fluctuations in a cantilever can be computed as a first approximation as[139]:

$$\langle F \rangle = \sqrt{\frac{2k_B T k b_w}{Q\omega_0}} \tag{1.8}$$

where k_B is the Boltzmann constant, T the absolute temperature, b_w the measurement bandwidth, Q the Q-factor of the cantilever, and ω_0 its resonant frequency. Thus, for the same spring constant, higher resonant

frequencies will produce more precise measurements. In addition, it will also increase the response time. Hence, the resonant frequency of the cantilever defines the time resolution of AFM force measurements (and also imaging).

The resonant frequency can be tuned for the same spring constant by building smaller cantilevers. The standard commercial cantilevers for force spectroscopy (10-1000 pN/nm) resonate at 1-10 kHz in liquid environment. This is a relatively low bandwidth and hence limits the time resolution of our measurements. Currently, a new line of small-factor cantilevers display resonant frequencies 3-5 times faster for the same spring constants (i.e. the Olympus BioLever Mini (Tokyo, Japan)). These cantilevers, however, are significantly more expensive, and thus were discarded for our experiments. Therefore, the time and force resolution of our technique depends on the manufacturing processes used to fabricate the AFM tips, which we cannot control.

1.4.2 Force calibration

Each specific cantilever displays a slightly different spring constant. As a result, the spring constant needs to be determined prior to every experiment. The calibration protocol is currently a standard procedure and all commercial AFMs already have built-in protocols to determine it. In all cases, it is based on acquiring the power spectral density of the freely standing cantilever via Fourier transform (Fig. 1-12). The first harmonic peak is equal to the total thermal vibrations of the cantilever and thus its shape and area will depend on its spring constant[140]:

$$k = \frac{k_b T}{\langle x_0 \rangle} \tag{1.9}$$

where $\langle x_0 \rangle$ is the average displacement of the cantilever when freely standing. In contrast to what is commonly thought, the resonant peaks observed at higher frequencies in the power spectrum do not contribute to the total energy computed in the equipartition theorem because they are higher vibration eigen-modes of the cantilever.

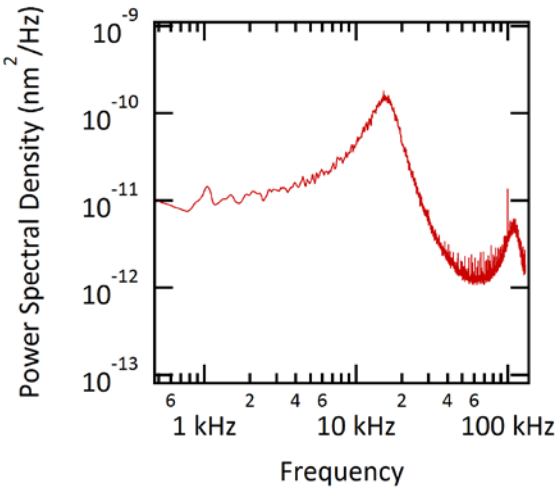

Fig. 1-12 Power spectral density of an AFM cantilever [SNL-10 tip A (Bruker Probes, Karlsruhe, Germany] performed in our AFM setup.

1.4.3 Force spectroscopy operation

Force spectroscopy AFM measures the mechanical response of a material when a calibrated force is applied. In this context, the force can be exerted in various manners — constant, freely varying, or a periodic function of time. Each way of applying force will produce a different interaction between the AFM tip and the substrate, which will allow accessing distinct mechanical properties. The way the tip is driven thus defines both the fore spectroscopy mode and the accessible mechanical properties.

We used here two force spectroscopy modes to investigate the kinetics of rupture of materials. On the one hand, in force-extension mode the AFM probe is driven at a constant velocity, thus allowing to capture the distinct rupture processes that occur at a wide range of forces. On the other hand, by applying a constant force, force-clamp provides an insight to the kinetics of each of these processes. We have not used dynamic force spectroscopy modes — whereby the tip is vibrated — because the obtained mechanical measurements produce experimental parameters that are difficult to interpret.

1.4.4 The force-extension mode

The basic mode of force spectroscopy consists of driving the AFM probe at a constant velocity against the substrate. A schematic drawing of a typical constant velocity indentation is depicted in Fig. 1-13(a). Firstly, the AFM tip is brought to the substrate from its initial position far apart from the substrate. When they come into contact, the AFM tip starts applying an increasing force. Subsequently, the piezoelectric actuator is retracted, thus decreasing the force applied by the AFM tip until. Eventually, it detaches from the substrate and returns to its initial position.

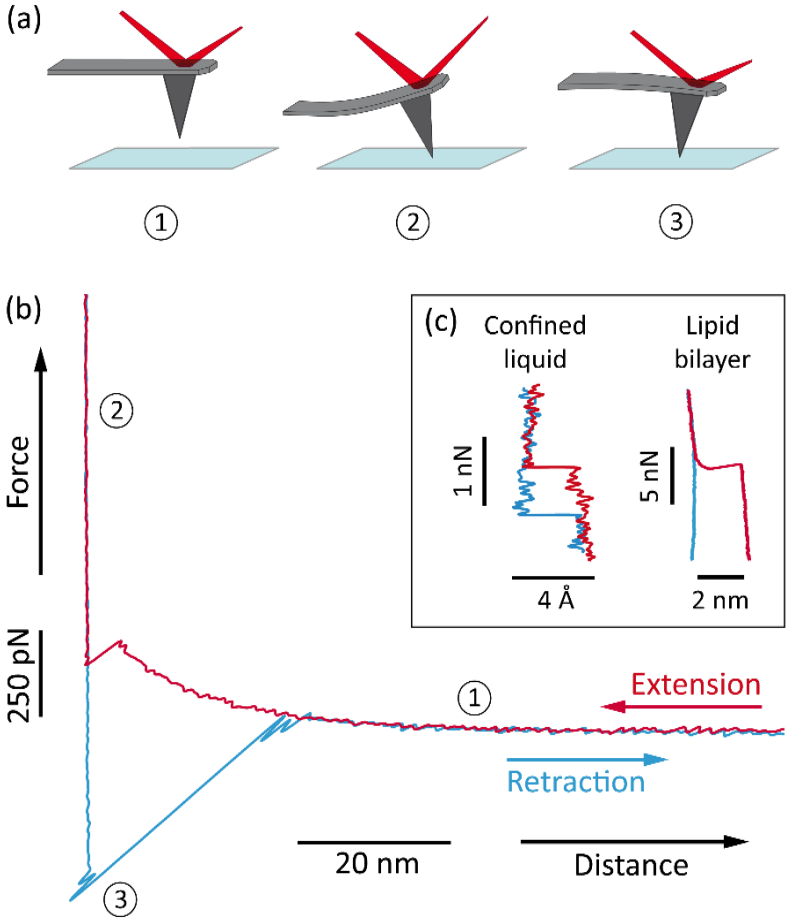

Fig. 1-13 Working principle of the force-extension mode. (a) Schematic drawing of the AFM cantilever in three different positions in respect to the substrate: far away (1), advancing against (2), and retracting from (3) the substrate. (b) A typical force vs distance curve obtained in water against a hard substrate. The red and blue traces correspond to the initial extension and subsequent retraction of the AFM tip, respectively. Each of the previously described positions of the tip are marked by their corresponding number. (c) Examples of rupture events occurring in a confined liquid (1-undecanol) and a lipid membrane (DPhPC lipid membrane).

This type of indentation produces typical force vs. distance plots like the one shown in Fig. 1-13(b). The flat plateau (on the right) corresponds to the non-contact region while the AFM tip is either approaching (red line) to or retracting from (blue line) the substrate. The vertical section corresponds to the contact region, where an increasing pushing force is applied by the AFM tip. This region provides information about the elastic mechanical properties of the substrate, which can be extracted by analysing its deformability. As the tension increases, plastic deformation in the form of sudden (fragile) rupture

events might occur. As an example, Fig. 1-13(c) displays the rupture of a single lipid bilayer and a confined liquid, which is hallmarked by a sudden drop in the position of the AFM tip. As the piezoelectric actuator is subsequently retracted, any reformation processes will be observed as sudden increases in the AFM tip position, just the opposite of rupture events. This is the case for confined liquids, but not for lipid membranes. As will be discussed in the following chapters, the size of each of these rupture events corresponds to the size of the objects indented. Most importantly, their rupture/reformation forces are a fingerprint of the mechanical stability of the sampled material.

Finally, the detachment of the AFM tip from the surface also provides useful information. The detachment or 'pull-off' force is proportional to the adhesion properties of the substrate material. In addition, if any molecule might have attached to the AFM tip, it will be pulled from the substrate as the AFM retracts, which constitutes the working principle of protein pulling experiments. All in all, the force-extension technique is an excellent platform to investigate a wide range of mechanical properties of materials. Due to this flexibility, force-extension constitutes the basic mode of force spectroscopy operation when indenting or pulling a material for the first time. However, as it will be discussed in the next section, the only limitation of force-extension is the quick change in the applied force during the indentation, which prevents obtaining the precise kinetics of plastic deformation processes.

1.4.5 The force-clamp mode

The force-clamp technique was developed to obtain more precise mechanical measurements than force-extension. By applying a constant force, the transition rate and the probability density function of the rupture/reformation processes can be precisely measured at each particular force. This presents many advantages, as it will be described below. A schematic of the setup used in force-clamp is shown in Fig. 1-14. In this case, instead of directly driving the AFM tip, a feedback loop is used to maintain the force constant. Thus, the AFM tip will remain 'stationary' until a rupture event spontaneously occurs. When this happens, the feedback loop will correct the extension of the piezoelectric actuator until the AFM tip applies the same average constant force.

A typical force-clamp trace is shown in Fig. 1-15. As can be observed in the upper panel, the AFM tip follows a series of steps. Like in force-extension, each sudden drop corresponds to a rupture event and its length equals the thickness of the object indented. The rupture events can also be observed in the force channel (lower panel) as spikes due to the non-instantaneous response time of the feedback loop. By repeatedly measuring the times-to-rupture, or dwell times, the transition rates can be calculated for a specific force. By repeating the operation over several forces, we can map out the energy landscape by using a rupture model (see section below).

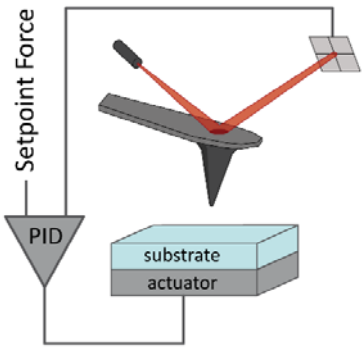

Fig. 1-14 In force-clamp mode, the resulting deflection is compared to a setpoint force value by a PID feedback loop. Its output is then fed to the piezoelectric actuator, which corrects its position in order to maintain the deflection constant through time.

Force-clamp can also perform more complex pulse experiments in which the setpoint force varies with time. A typical example are protein refolding pulse experiments[141], where a protein is allowed to refold at zero force after unfolding it at high pulling force; or single bond cleavage measurements [142], where the dissociation kinetics of a single bond are measured while the bond is stretched. Hence, force-clamp provides a versatile platform to capture the detailed kinetics of rupture.

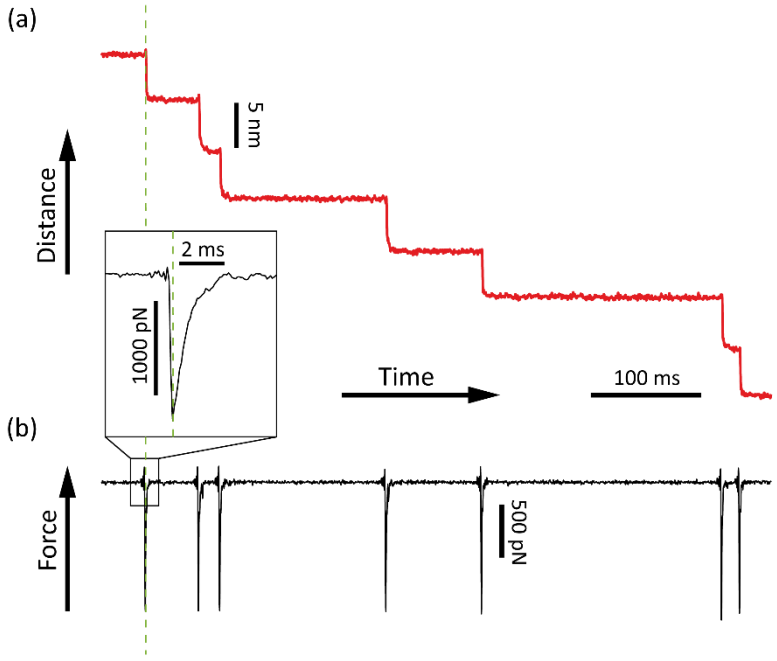

Fig. 1-15 A typical trace obtained in force-clamp mode when indenting a stack of DPhPC lipid membranes. (a) The position of the AFM tip follows a staircase-like trajectory where each step corresponds to the rupture of a layer of the material. These steps occur concurrently (green dashed line) with the appearance of spikes in the detected force. (b) Each step is caused by the non-instantaneous response time of the feedback loop, which typically is in the millisecond range (inset).

1.5 Interpreting force spectroscopy results

As we have just seen, force spectroscopy measures the deformability and rupture processes of materials at the nanoscale. These behaviours are broadly accepted as direct measurable properties of materials; for example, the rupture force of lipid membranes is widely used as a fingerprint of their mechanical stability[57]. These raw fingerprints, however, depend on many extrinsic parameters; in lipid membranes, for instance, the rupture forces are highly dependent on the lipid moiety but also on the buffer ionic strength[143], pH and AFM tip chemistry[133] among other parameters.

This problem is not limited to the plastic deformation: the elastic deformability of a material depends on the size and shape of the indenter, and hence the extrinsic geometrical factors must be considered before comparing different results. Therefore, theoretical models can be used to exclude the extrinsic factors from the raw experimental results, thus helping to unveil the molecular mechanism underpinning the mechanical properties of materials. In this section, we are going to introduce these theoretical models. First, we are going to critically present the theory to extract the Young modulus from force-extension plots. Then, we are going to explain and discuss the models used to interpret rupture forces in force-extension and force-clamp operation modes.

1.5.1 Young Modulus

The deformability of a material depends on its intrinsic mechanical properties as well as the sample and indenter dimensions. Its intrinsic (dimensionless) deformability, commonly known as the Young Modulus[144], can only be extracted by determining the area of contact and its pressure distribution. Unlike macroscopic indentation, the small areas involved in AFM nano-indentation are frequently difficult to access by imaging techniques. Moreover, biological or other soft materials might 'heal' after indentation, which prevents quantifying directly the area of contact by the mark left after indentation. As a result, the area of contact and the pressure distribution can only be accessed through the use of contact models.

The prototypical contact model for nanoscale indentation is the Hertz model[145]. In short, this model calculates the pressure distribution between two smooth objects in non-adhesive contact — the force only distributes through the areas strictly in contact. Specifically, this models assumes four non-trivial conditions:

a) The strains are small (within elastic regime)
b) The surfaces are continuous and non-conforming (the contact area is much smaller than the radius of the objects)
c) The bodies can be considered half-spaces (they are thicker than the length of the strains)
d) The surfaces are frictionless

Given these conditions, the area of contact between the indenter can be calculated for each geometry. The choice of geometry will mostly depend on the shape of the indenter and, crucially, on the depth range of indentation. Considering that the tip radius of an AFM is in the range of 10-100 nm, any indentation smaller than the tip radius can be approximated as a contact between a spherical punch and a flat surface [see Fig. 1-16(a)]. Instead, if the indentation is deeper than roughly the tip radius, the walls of the AFM tip will make contact with the substrate, and thus the area of contact will resemble more that of a conical or pyramidal indenter, as shown in Fig.

1-16(b). The force vs. indentation depth δ relationship for a spherical punch is[146]:

$$F = \frac{4}{3} E^* R^{1/2} \delta^{3/2} \tag{1.10}$$

and for a conical indenter is[146]:

$$F = \frac{2E^*}{\pi \tan \varphi} \delta^2 \tag{1.11}$$

where R is the tip radius, φ the angle between the surface and the side surface of the cone and E^* is the reduced Young modulus that can be approximated as[140]:

$$E^* = \frac{E}{(1-\nu^2)} \tag{1.12}$$

with E being the Young Modulus and ν the Poisson ratio. The values for R and φ are typically obtained by imaging the AFM tip with electron microscopy prior or post the indentation experiment.

Even though the four conditions aforementioned are fulfilled for large indentations depths such as the ones for living cells (chapter 5), these will be partially violated for small objects such as lipid membranes (chapter 4) and

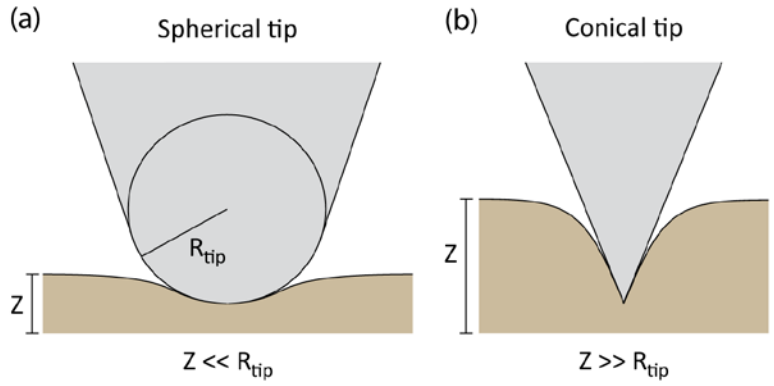

Fig. 1-16 Different indentation models depend on the indentation depth. (a) When the indentation depth Z is much smaller than the tip radius R_{tip}, the interaction can be modelled, in a first approximation, as a spherical punch contacting a semi-infinite solid. When the area of contact increases, the tip-substrate contact occurs predominantly through the tip walls and therefore the tip can be approximated to a conical (or pyramidal) indenter.

confined molecular liquids (chapter 3). In particular, condition b) will be difficult to hold for typical AFM tip radii (5-10 nm) where the area of contact will be the same range as the AFM tip. In addition, the stress will build up in a very confined space for these tips, thus contradicting condition a). An alternative for very small indentation ranges (a few nanometres) is to consider that the AFM tip is a punctual force, which turns the deformability of the material independent on the exact size of the tip. This will be a good approximation if the force is transmitted through the last asperities of the AFM tip, as it turned out to be for confined liquids. In this context, the substrate cannot be treated mathematically as a continuous material. A simple solution is to consider the surface as a network of springs, each one representing one (or a few) interatomic interactions in the surface plane. This model has been successfully fitted to the deformation of ionic solids[147], lipid bilayers[143][148], and graphene[149]. Its success notwithstanding, it is difficult to demonstrate quantitatively that the punctual force models fit significantly better the experimental data than continuous pressure distribution models; fitting such small indentation depths is highly dependent on the chosen range of fitting, and thus on the criteria of the operator.

Another source of deviation from the Hertz model is the size of one or more dimensions of the substrate, which will contradict condition c). Similarly, the pressure distribution will crucially change if the substrate is layered or if it possesses a non-homogeneous structure. In a general context, this category includes viscoelasticity and other velocity-dependent mechanical behaviours. These type of biases can be accounted by correcting the geometrical constraints of the current model. Because these types of biases also exist in macroscopic indentation, there is a significant literature from which we can draw solutions for each specific case. For example, Muller and co-workers used a poroelastic indentation model to model the velocity-dependent indentation profile of living cells[150]. Unfortunately, it is difficult to draw a general model that can include all the cited cases and therefore, specific solutions should be gathered when the basic Hertz elastic model fails to fit the experimental data.

Finally, the adhesion between the tip and the substrate — condition d) — might increase the effective area of contact. To account for it, various models have been developed, such as the well-known JKR[151] and DMT[152][153]. This effect, however, is the easiest to correct due to the extensive literature available and only requires the use of slightly more complex equations. This notwithstanding, these are slight corrections of the elastic model and thus will likely fail to model major deviations. In such case, it is more likely that one of the previous conditions has been violated.

Altogether, the Herz model constitutes a good starting point to fit experimental data. Its basic assumptions, however, might be strongly violated, especially when the indented objects are in the nanometre range. In this case, there is still no consensus on the way the force is distributed at the tip-sample region. Probably for this reason, most researchers choose to use the most accepted model — the Hertz model — when computing the Young modulus. Despite this is a reasonable compromise solution to draw comparisons between the stiffness in different experimental conditions (i.e. indentation speed, material composition, etc.), we should be cautious to extract conclusions from the absolute value of the measured Young modulus or to assume that it explains accurately how forces are transmitted in the tip-sample area.

1.5.2 The Bell model

The rupture and reformation events observed in force spectroscopy occur in clear steps which are function of the applied force (in force-extension) or time (in force-clamp). This type of rupture events have been observed in a myriad of processes encompassing mechanical protein unfolding[128], cell adhesion[154], and the rupture lipid bilayers[155], confined liquids[156], and ionic solids[147]. A simple theory to interpret the physics underlying these many different processes was presented by G. I. Bell in 1978[157]. The Bell model was originally created to understand the adhesion forces arising between two adjacent cells when pulled apart. Even though it is usually cited as an original model, the Bell model is a derivation of Kramers model, which was first presented in 1940[158] and further expanded during the following decades[159].

In the Bell model, the system is described by a 1D Gibbs free-energy profile with two states, [Broken] and [Unbroken], that are separated by a maxima — the transition state. A schematic of such an energy profile is shown in Fig. 1-17. For most of the time, the state of the system will remain within

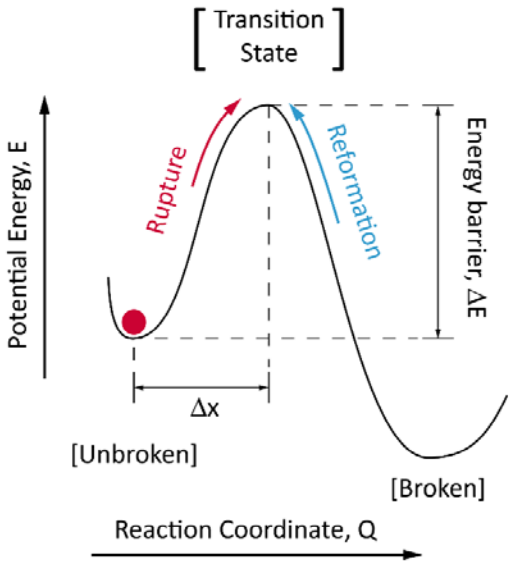

Fig. 1-17 Schematic drawing of the energy profile in the Bell model consisting of two minima states — [Broken] and [Unborken] — separated by a single energy barrier. The red particle represents the energy configuration of the material. The rupture or reformation will occur when the system crosses through the [Transition state] and falls in the opposing minima state.

the coordinates of its initial state ([Broken] or [Unbroken]), where it will freely diffuse due to thermal fluctuations. The majority of these fluctuations will be smaller than the height of the energy barrier, thus leaving the system unbroken. When a stronger fluctuation occurs, however, the system will unavoidably break. Given that these fluctuations need to be strong enough to overcome the energy barrier, the rate of transition α will exponentially depend on its height, following an Arrhenius relationship:

$$\alpha = A_0 \exp\left(\frac{-\Delta E}{k_B T}\right) \tag{1.13}$$

where ΔE is the height of the energy barrier and A_0 is its attempt frequency. If a force is applied, the energy of the transition state will decrease by an amount equal to the mechanical work exerted to overcome the transition state. Thus, the height of the energy barrier will become $\Delta E' = \Delta E - f \cdot \Delta x$, where Δx stands for the distance between the initial and the transition state and f the force applied at each of the disrupted bonds. If *N* bonds are disrupted in parallel, then total force applied by the tip follows that $F = f \cdot N$. In his seminal paper, for example, Bell divided the total force pulling apart two cells by the number of molecular bonds bridging them. In this sense, the pressure distribution of an indenter is crucial for the mechanical stability of a material because it reduces the effective force exerted to each individual bond or interaction responsible to maintain the mechanical stability. Hence, accounting for the number of disrupted bonds in the previous equation results in:

$$\alpha(F) = A_0 \exp\left(-\frac{\Delta E}{k_B T} + \frac{\Delta x}{N \cdot k_B T} F\right) \tag{1.14}$$

And a more compact expression can be obtained by adding the force-independent terms together:

$$\alpha(F) \equiv \alpha(0) \exp\left(\frac{\Delta x}{N \cdot k_B T} F\right) \tag{1.15}$$

where $\alpha(0)$ stands for the transition rate in absence of force.

Following the Bell model, the rate of rupture should depend exponentially on the applied force. This relationship has been experimentally validated for several cases such as protein unfolding[160], disulphide bond cleavage[161], and lipid membrane rupture[148]. These examples contain both pushing and pulling force spectroscopy experiments. In this sense, the Bell model can be applied to both experimental setups indistinguishably. The rupture rate, however, does not always follow an Arrhenius dependence. Perhaps the clearest case are catch-bonds, frequently present in adhesive proteins, whereby the bond lifetime increases when a tensile mechanical force is exerted to it[162]. This seemingly contradictory behaviour has been explained by considering the existence of two possible bound states that the bond might populate. One of the states is assumed to be more mechanically resistant, thus displaying longer lifetimes when pulled apart. When a stretching force is applied, the mechanically resistant state becomes more stable and populated, thus increasing the average lifetime of the bond.

Another cause for non-exponential force dependency is the shift in position of the transition state caused by the application of a force, which is not accounted for in the simple Bell model. As a result, a force-dependent distance to the transition state $\Delta x \equiv \Delta x(F)$ has to be introduced in the Bell model. Finally, by using more complex mathematical formulations, Dudko and co-workers reported a power-law force dependency. Except for adhesive proteins, however, these type of deviations are not frequently observed or happen in a range smaller than the experimental error. Consequently, the Bell model constitutes a good first approximation to explain the force dependency of rupture processes. Only if deviations from the model are encountered, then it would be advisable to use more complex theoretical models.

1.5.3 Rupture events in force-extension

In a force-extension experiment, the pushing force increases with time as the AFM tip is moved against to (or retracted from) the substrate. At low loading forces, the rupture rate will be much slower than the experiment time, and thus negligible. As a threshold force is reached, however, the rupture rate will become as fast as the time scale of the indentation. As the substrate is further deformed, the probability of rupture will increase exponentially causing the almost immediate rupture of the material. As a consequence, despite the fact that the Bell model is a stochastic one, the time-to-rupture in force-extension experiments will be narrowly distributed. This is indeed the origin of the observed average rupture forces in such a wide range of materials.

As a proof-of-concept example, we can use the previous Bell formulas to obtain the force distribution of rupture events in force-extension[157]. As a first approximation, we can assume that the force increases linearly with time as $F(t) = k \cdot V \cdot t + F_0$, where V stands for the extension velocity of the actuator (either in pushing or pulling), k is again the spring constant of the cantilever, and F_0 for the initial force. This is a good approximation for indentation experiments where the indentation area is roughly constant, but not for pulling experiments where the elasticity of the protein or DNA polymer depends on the extension of the molecule. By using this approximation, we can calculate the survival probability of the system as:

$$\frac{dS(t)}{dt} = \alpha(t) \cdot S(t) \tag{1.16}$$

By inserting equation (1.15) in this expression and changing the variables, the survival probability in terms of the pushing force is:

$$S(F) = \exp\left(-\frac{\alpha_0}{\eta k V} \left[\exp(\eta F) - e \exp(\eta F_0) \right] \right) \tag{1.17}$$

where the parameter η stands for:

$$\eta = \frac{\Delta x}{N \cdot k_B T}$$

The distribution of rupture times corresponds to the probability density function:

$$p(F) = -\frac{d}{dF} S(F)$$

$$p(F) = \frac{\alpha_0}{kV} \exp\left(\eta F - \frac{\alpha_0}{\eta k V} \left[\exp(\eta F) - \exp(\eta F_0) \right] \right) \qquad (1.18)$$

As can be observed in Fig. 1-18(a), the previous equation results in a distribution with a central maxima skewed to the left. Most importantly, the average rupture force of this distribution depends on the logarithm of the loading rate — the independent variable in this force spectroscopy mode. When the average rupture force is plotted against the logarithm of the loading rate, as shown in Fig. 1-18(b), the resulting slope is equal to η, which is directly proportional to the distance to the transition state. Also, the height of the energy barrier can be estimated by the origin coordinate, which is equal to α_0 / k. Therefore, by measuring the rupture forces at increasing loading rates, we can partially map out the energy landscape of the rupture process in force-extension.

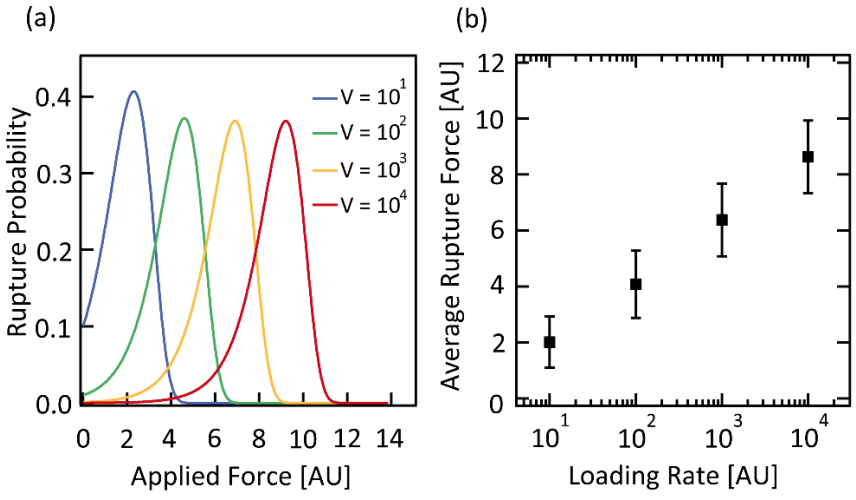

Fig. 1-18 Rupture force distributions in force-extension according to the Bell model for different loading speeds. Each peak has been calculated using equation (1.18). The initial force was set to zero and the rest of the parameters were set to arbitrary values of 1, except for the loading rate. (b) The average rupture force and is standard deviation for each loading rate

An analogous model was developed by H.J. Butt and co-workers[163] for lipid membrane rupture, which was then experimentally tested[164]. This model, however, does not apply to pulling experiments whereby the extension of a molecule does not occur linearly with the stretching force. By using WLC theory to describe the molecular extension and a more complex description of the energy landscape, Dudko and co-workers[165] found a similar force distribution that depended as a power-law from the pulling speed. Later, the same authors developed a more complex analytical approach which allowed them to extract information directly from the rupture force distributions[166]. Alternatively, Freund[167] directly solved the first passage distribution of the Kramers model for an increasing load, which yields an analogous loading rate dependence. Other approaches have included considering the multidimensionality of the energy landscape[168] or the direction of the applied force[169]. Even though these more complex models allow a deeper insight in the energy landscapes of rupture of materials, all of them reach similar rupture force distributions with weakly depends on the loading rate.

The weak dependency of the rupture force on the loading rate is precisely one of the two main drawbacks of the force-extension technique. State-of-the-art piezoelectric actuators extend in experimental conditions at a speed ranging 10-10000 nm/s in the best cases. If the fluid environment is viscous, for example, the surrounding molecules will drag the AFM tip motion, thus decreasing the upper bound of the loading rate range. Also, inherent temperature changes introduce drift to our measurements, limiting the lower bound of speeds achievable. Even if these limitations were partially removed by using high-speed AFM, the window of experimentation would still be limited because of the rupture kinetics would quickly move away from diffusive regime where Bell (or Kramers) model applies[170]. As a result, only a tiny variation in the average rupture force can be observed by varying the loading speed in real experimental conditions, usually in a range close to the experimental error. Thus, only rough estimates of the distance to the transition state can be obtained with force-extension.

The second main drawback of force-extension is that rupture forces depend on the past AFM tip trajectory. As shown in equation (1.18), the

rupture force depends on the initial force. If a material exhibits, for example, two or more modules or layers that have identical mechanical stability (the same energy barrier), the starting force for the second one will depend on the force applied to break the first module or layer. Precisely, it will depend on how much the tip can relax to zero force after rupture. If it relaxes well, this effect is negligible. If the remaining force is significant, however, the rupture force of the second event will be significantly different because F_0 will be close to the rupture force.

As a result, when several rupture processes occur in a material, their rupture force depends on the rupturing history. This is a common case for materials with tandem modules: the initial force for the N^{th} stacked lipid membrane is very close to the rupture force of the previous one due to their limited size (see chapter 4); the initial force applied to the N^{th} modules of a polyprotein depends on the extensibility of the polyprotein as a whole. These cases have also flagged another experimental complication: if the second rupture event has a lower energy barrier, it will likely rupture faster than the resolution of the AFM because of the high initial force, yielding it undetectable. All in all, the history dependency of the force-extension technique poses several problems towards analysing the complex rupture kinetics of materials.

1.5.4 Rupture events in force-clamp

Force-clamp applies a constant force. In this way, the mechanical stability is hallmarked only by the time-to-rupture for a specific force. If a higher force is applied, then the rupture time (or dwell time) will shorten. Since the rupture is a stochastic process, each rupture event will possess a different rupture time even if two objects display the same mechanical properties, as shown in Fig. 1-19(a). Oppositely to force-extension, the rupture times are broadly scattered in time, which allows to obtain more precise measurements of the rupture kinetics. By summing all the times-to-rupture, we can access the probability density function of the rupture process, which bears information of the kinetics of rupture. Interpreting this rupture time distribution requires a model. Like previously, we can use the Bell model to obtain the probability density function for a simple barrier-crossing process by considering equation (1.16) under constant force conditions:

$$S(t) = \exp\left(-\int_0^t \alpha_0 \exp\left(\frac{\Delta x}{N k_B T} F \right) dt \right) = \exp\left(-\alpha(F) t \right) \qquad (1.19)$$

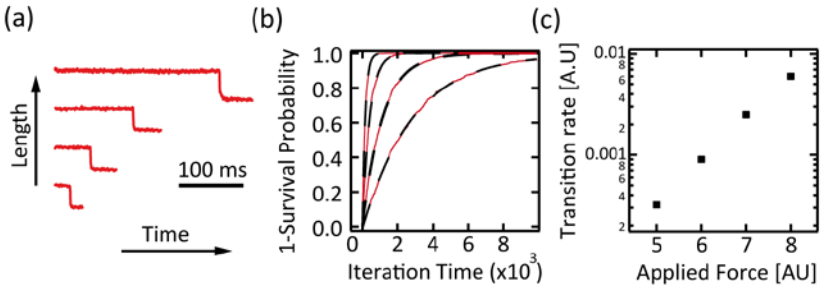

Fig. 1-19 (a) The rupture of a material is a stochastic process that yields different dwell times when the same experiment is repeated. The traces shown correspond to the rupture of four identical DPhPC lipid membranes at the same pushing force. (b) By adding several dwell times the probability of survival with time can be computed (red traces). In this case, the survival function has been computed for different applied forces using a Monte Carlo simulation (each simulation has 100 iterations. The defining parameters where set to arbitrary values). To obtain the rate, an exponential function has been fitted to each model survival function. (c) The fitted transition rates are plotted for each applied force displaying an exponential dependency.

In force-clamp, hence, the distribution of rupture times will exponentially decay with time. If we fit the rupture time distribution with an exponential function [Fig. 1-19(b)], the resulting decay time will equal the rupture rate. As shown in Fig. 1-19(c), the rupture rate depends exponentially on the force, as predicted by (1.15), and the slope will be equal to η and the origin coordinate to α_0. These are the same parameters that we previously obtained in force-extension. In this case, however, force-clamp allow us to measure them with precision.

Despite the apparent simplicity of the analytical solution, the probability density function experimentally measured here significantly differ from the simple Bell model in a wide range of cases. A noteworthy example is the model protein Ubiquitin, which unfolds faster than predicted. Even though this bias was initially explained as a feature of glassy dynamics of the energy profile[171], the non-exponential survival function was later interpreted using static disorder theory[172]. This model assumes that the bonds relevant to rupture are maintained in the same configuration for up to tens of seconds, which is more than a billion times slower than their barrier-crossing attempt frequency[173]. A different approach was followed by Lannon and co-workers[174], who used maximum likelihood estimation to rank different analytical models. The highest rank was for stretched-exponential models such as the Weibull model[175]. This approach, however, fails to provide an underlying molecular mechanism to justify the selection of model, as the NIST recommends[176].

Other examples might be found in a wide selection of fields encompassing DNA escape times[177] and ion channel gating[178], which display non-exponential residence times that are typically modelled using Markov chain dynamics[179][180] or fractal kinetics[181]. The same behaviour is encountered in the similar field of single molecule fluorescence[182]. These cases share the common feature that multiple intermediate states must be crossed before rupture. Therefore, it is likely that the complex rupture dynamics observed in all these nanoscale processes might originate in the multiple-step dynamics rather than the complexities of the shape of the energy barrier. In this sense, it would be interesting to compare Kramers

theory predictions against multiple step models to account for non-exponential kinetics. Unfortunately, no such solution is available in the literature to our knowledge. As a consequence, we are still far from understanding the rupture models underlying the probability density functions measured in force-clamp, and probably far too from understanding the molecular motions underlying them. In this sense, expanding force-clamp to new materials is an enticing opportunity to help construct a common and robust model for material rupture at the nanoscale.

2 Instrumentation

2.1 Selection of instrumentation

Unlike AFM imaging, force spectroscopy AFM is not yet a widespread, commercially available technique. Currently, commercial apparatuses typically allow only to use the simplest force spectroscopy mode, force-extension, whereby the AFM tip is displaced at a constant speed. As we will describe later, this force spectroscopy mode is useful to observe the distinct mechanical responses of a material but fails to capture the complex kinetics of fracture. Force-clamp mode, instead, monitors the fracture process with greater precision, but it is not yet available commercially for most cases. In addition, analysing and interpreting the experimental data is a complex procedure that requires a trained technician. The only exception is the new force spectrometer with force-clamp capabilities developed by Luigs&Neumann GmbH (Karlsruhe, Germany), which can be employed with little training. This apparatus, however, has a very limited actuator range and a set-up not suited for most samples. Therefore, except for protein pulling, a custom-made instrument is required to conduct force-clamp. Consequently, we assembled our own custom-made atomic force microscope. Our instrument (described below), exhibits millisecond response time and sub-nanometre resolution, which has been crucial to investigate the rupture kinetics of confined liquids (chapter 3) and lipid membranes (chapter 4).

For living cells, however, the actuator of our instrument has a travel range smaller than the size of the cells (chapter 5). This prevented us from using force-clamp. In this case, instead, we employed a commercial model with a longer actuator — the Bruker Dimension Icon — that allowed us to probe the cell mechanical properties by using force-extension mode. Performing this experiments with the Bruker Dimension Icon required overcoming two problems: the AFM lacked a temperature controller to maintain the cells at physiological temperature and the company could not provide a software program to analyse the data. As opposed to the previous cases, these two problems can be solved by using commercial instrumentation specifically designed for working with biological samples, such as the BioScience JPK and MFP-3D-Bio Asylum AFMs. Unfortunately, we could not access any of these AFMs or had the time and budget to acquire them. Instead, we tackled both

problems by developing our own hardware and software tools. Hence, even the force spectroscopy experiments performed in a commercial AFM required to developed custom-made instrumentation.

2.2 Construction of a custom-made AFM

The conceptual design of an atomic force microscope with force-clamp capabilities is almost identical to that of any commercial AFM. However, the technical requirements for imaging and for applying forces with high accuracy differ substantially. For instance, the study of the rupture mechanisms of both confined liquids (chapter 3) and lipid membranes (chapter 4) required measuring sub-nanometre displacements, far beyond the resolution of many commercial AFMs. Because of these greater demands, we decided to construct our own microscope.

Our model is based on the original design developed by Prof. Julio Fernandez in Columbia University, which has proved invaluable in studying the kinetics of protein unfolding[160][183] and refolding[184][185] by using force-clamp. Despite the ease of having the design of a working apparatus, the manufacture of a few key elements is still custom-made, which requires a

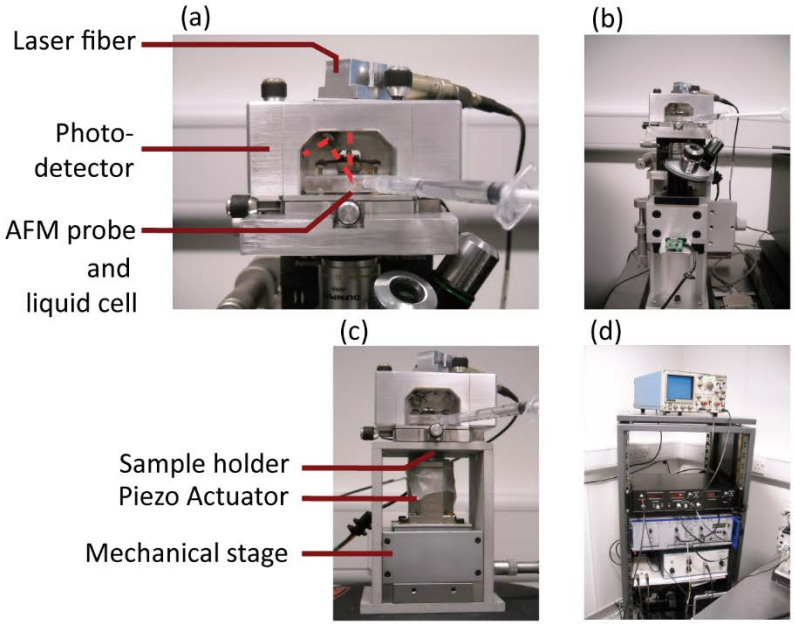

Fig. 2-1 Setup of our custom-made atomic force microscope. (a) A modified Bruker headstage. The AFM probe and the liquid cell are located at its bottom, with a syringe connected to it. The laser fibre is sitting on top of the headstage. The laser beam (red dashed light) is reflected by the AFM cantilever and re-directed by a mirror to the photodetector (left). (b) The headstage sitting on top of the inverted microscope, which is used to focus the laser beam on the microscopic AFM cantilever. (c) The AFM in the working setup sitting on top of the mechanical and piezoelectric actuators. (d) Photograph of the electronic peripherals.

thorough testing of the microscope during the assembly process. Furthermore, Prof. Fernandez's design is optimized for pulling experiments. Instead, we required to perform for the first time pushing protocols, which required to adapt a number of characteristics of the setup and the controlling software.

2.2.1 Description of the model

The force sensing module [Fig. 2-1(a)] of our AFM consists of a modified MultiMode Veeco headstage (Bruker, Karlsruhe, Germany). This commercial stage contains all the required components for force measurement: an AFM probe holder, a liquid cell, and the optical elements to guide the laser beam. At the start of every experiment, the laser beam is aligned by using the custom-built inverted optical microscope shown in Fig. 2-1(b).

During the experiment, the headstage is located on top of the sample, which is tightly held by a magnet [Fig. 2-1(c)]. Its position is controlled by the underlying mechanical actuator. The actuator is composed of two elements: the initial coarse movement required to bring into close proximity the sample and the force probe are performed by a mechanical translation stage; during measurements, the fine movements are controlled by a piezoelectric actuator.

The electronic peripherals are located in a contiguous rack [Fig. 2-1(d)]. The force sensing stage and the piezoelectric actuator are controlled by a custom-built electronic circuit (the black box), which also interfaces the controlling computer through a data acquisition card. Due to the high-voltage voltage input characteristics of the piezoelectric actuator, the output voltages from the custom-built circuit need to be amplified by two separate amplifiers for the vertical (Z) and horizontal (X,Y) axes of the piezoelectric actuator (modules below the black box). Finally, an oscilloscope was added for monitoring and diagnostics purposes

2.2.2 Description of the components

FORCE-SENSING STAGE. The force sensing stage is the most varying part among different atomic force microscope designs, both commercial and custom-made. This is because different setups will optimize different characteristics of the microscope. In our case, thermal and mechanical stability were the characteristics to optimize. Thermal stability can be easily minimized by a closed sample cell that avoids the surrounding fluid (liquid or air) convection. Working in a temperature-controlled room is also crucial to decrease thermal drift during the experiment hours. On the other hand, thermomechanical stability stems from the expansion of different pieces of the force-sensing stage; small independent temperature fluctuations in each part can generate an overall drift in the order of several nanometres. An effective way to reduce the mechanical drift is to tightly bind the different parts of the force sensing stage by strong springs, thus reducing the uncoordinated expansion of the separate parts. This technique, however, requires a very specific know-how that would have been very time-consuming to acquire. For this reason, we purchased a commercial headstage — from Bruker Multimode — which is well-known for its thermal stability.

In this force-sensing stage, the AFM probe is fixed in the quartz liquid cell facing downwards, towards the sample. Around the AFM probe, a silicone O-ring creates a closed space between the quartz cell and the sample which can be filled with buffering solution thanks to a channel connected to a syringe. The deflection of the cantilever is monitored by a laser beam focused at the end of the cantilever. The laser fibre is located on top of the stage and its reflection is directed to a 2-quadrant photodiode located at the top-left corner thanks to an adjustable mirror. The laser beam, the mirror and the photodiode need to be adjusted at the beginning of every experiment.

Despite its advantages, the Bruker Multimode headstage has as a main disadvantage: the low quality of its built-in laser beam. If the laser spot size is bigger than the area at the end of the AFM cantilever, as it is the case, the excess laser light might generate a varying interference pattern with the surface that significantly bias the force measurements. To address this

problem, the built-in laser was substituted by pigtail laser diode and power source (SK9733), both devices from Schäfter + Kirchhoff GmbH.

When the power spectrum of a cantilever was measured for the first time, it became evident that our particular headstage presented an unexpected problem: instead of the predicted resonant frequency peaks, the spectrum was flat above 1 kHz. After checking the serial number of our model, we discovered that our refurbished headstage dated back from 1992. Because it was manufactured prior to the invention of AFM dynamic modes, the headstage contained a low-band pass filter of 1 kHz that was limiting the bandwidth of the spectrum measurements — and the instrument as a whole. We solved the problem by removing the filter, which was redundant due to the existing filter of our electronic circuit.

AFM PROBES. The AFM probes were specifically selected for each experiment depending on the range of forces sensed. In all cases, cantilevers from Bruker Probes (Karlsruhe, Germany) designed for force spectroscopy mode (MLCT and SNL) were chosen because of their improved performance and thermal drift stability in liquid environment. The latter parameter is particularly scarce to find among commercially available tips because many of them either lack protective gold coatings or constantly deflect due to the high expansion index of the cantilevers.

INVERTED MICROSCOPE. The original hole of the headstage used to align the AFM cantilever became obstructed by the new laser beam. For this reason, we built an inverted microscope to align the laser. The AFM cantilever is positioned by a mechanical stage which can move independently in the three axes (ball bearing linear stage from NewPort, Irvine, CA). The image are then obtained by a camera (Logitech C270, Newark, CA) with a 10x magnification lens (Leica Microsystems, Wetzlar, Germany).

ACTUATOR. The mechanical translation stage from M-MVN-50 from NewPort (Irvine, CA) can travel up to 8 mm with a sensitivity of 0.5 μm. The piezoelectric actuator is a XY(Z) piezo scanning stage (P-363.3CD PicoCube) model from Physik Instrumente GmbH (Karlsruhe, Germany), featuring a

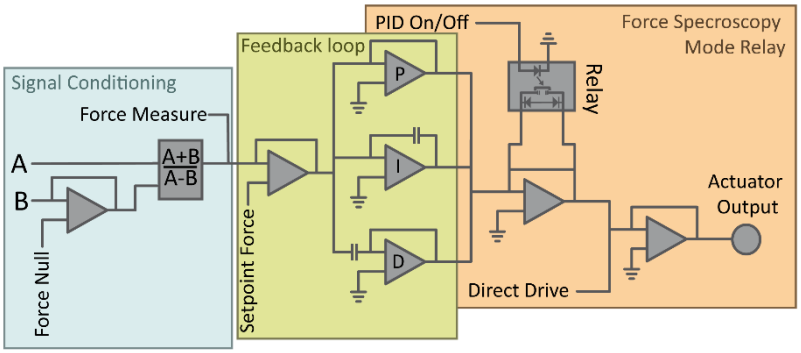

Fig. 2-2 Schematic representation of the design of the electronic circuit of our custom-made microscope. The circuit has three separate sections. Initially, the deflection signal from the upper and lower parts of the photodiode (*A* and *B* , respectively) are combined in the multiplier unit. The resulting signal is then compared to the setpoint force and the output is fed to the PID feedback loop. Finally, the output signal is controlled by an optomechanical relay. When it is closed, the microscope works in force-clamp mode. If it is open, then the feedback loop output is nulled and the piezo is directly controlled by a DAQ-generated signal.

maximum displacement of 3 μm at 250V and a nominal resonant frequency of 9,8 kHz. The PicoCube stage contains a capacitive sensor which measures the displacement of the actuator with 0.1 nm resolution in closed-loop. This constitutes a resolution that is far higher than most commercial atomic force microscopes.

ELECTRONIC CIRCUIT. The custom-made electronic circuit controls the microscope and interfaces it with the data acquisition card (DAQ). A schematic of the circuit is shown in Fig. 2-2. The deflection signal is initially calculated from the intensity voltage of the upper and lower quadrants of the photodiode (A and B , respectively) as $(A-B)/(A+B)$ by the multiplier unit. Instead of typically calculating the deflection as a simple difference, $(A-B)$, this more complex operation was introduced to cancel the effect of varying signal sums due to a reflective substrate — like it happens with the gold substrates used for protein pulling. The testing of the multiplier unit showed, however, that varying signal sums still affect the output voltage due to undesired voltage offsets. At the output of the multiplier, the resulting deflection is firstly measured by the DAQ and then compared to a setpoint signal by an operation amplifier. The setpoint signal is directly sent from the controlling computer and corresponds to the force at which the operator

wants to exert with the AFM tip. The resulting difference is then fed to the PID feedback loop, which produces the correction for the piezoelectric actuator position in force-clamp mode. The feedback loop is composed of three parallel operational amplifiers in the differential (Proportional), integrator (Integral), and differentiator (Derivative) configurations. The output from all three units is summed to provide the global correcting signal for the piezoelectric actuator in force-clamp mode. In force-extension mode, however, an optomechanical switch located between the summing operational amplifier and the actuator input pin disconnects the feedback loop from the piezoelectric actuator. In this configuration, the actuator can be directly controlled by the controlling computer through the DAQ card by an auxiliary input.

DATA ACQUISITION CARD. The data acquisition card (PCI 8281) from National Instruments (Austin, TX) was selected for its high-accuracy voltage outputs (for the setpoint signal and force-extension control). The input signals from the force and piezo extension are filtered using a selectable low-band pass filter from Frequency Devices (Ottawa, IL), which is controlled through a National Instruments PCI-6281 card. This filter was originally included because computers where too slow to digitally filter data in-line. With the current computing PC power, however, it has become redundant.

VOLTAGE AMPLIFIERS. Voltage amplifiers are required to match the low working voltage output from the electronic circuit with the high-voltage demands of the piezoelectric actuator. The main requirement for this component is a high linearity for the 500 V range in order to improve sensitivity and reduce the response time. The more demanding vertical (Z) axis of the actuator is controlled by a high-precision amplifier from Piezo Systems (Cambdrige, MA). The input signal is filtered by a 4-pole low-band pass filter from Frequency Devices (Ottawa, IL) to avoid spurious voltage spikes damaging the piezoelectric actuator. The horizontal (X,Y) axes are controlled by the default E-500.00 controller from Physik Instrumente. This controller also monitors the extension of the actuator axes through their capacitive sensors.

VIBRATION ISOLATION. The microscope is placed on top of a vibration isolation platform BM-4 from Minus K Technology (Inglewood, CA) sitting on top of a passive isolation table (63-500 from Scientifica, Uckfield, United Kingdom).

CONTROLLING SOFTWARE. The microscope was controlled using a custom-made routine programmed in IGOR PRO (Wavemetrics, Portland, OR).

2.2.3 Testing the electronic circuit

Due to the small forces applied, the accuracy of the force-clamp mode is very sensitive to small voltage offsets, especially if they originate in the electronic components of the circuit preceding the PID feedback loop. Just a small setpoint offset of 1 mV can correspond up to a 5% of bias in the force applied during a typical protein pulling experiment, a 2% for a confined liquids pushing experiment (chapter 3), and just a 0.1% for a lipid membrane one (chapter 4). The decreasing relative error is because of the increasing forces applied in these different systems. To minimize the voltage offsets, the electronic circuit was tested separately from the rest of the components. For testing purposes, the two deflection voltage inputs, A and B, were connected to the same constant voltage source. In this configuration, the expected deflection should be theoretically zero, and thus any spurious offset can be easily trimmed (reduced below < 1 mV) in all the relevant operational amplifiers.

Further testing, however, showed that the deflection setpoint signal was also affected by another offset bias. Due to the non-star configuration of the ground connections in the circuit, the setpoint signal coming from the DAQ suffered a voltage drop of several milliVolts. As a compromise solution, an extra, thicker ground cable was connected from the DAQ pins to the main circuit. In this way, the total setpoint bias at the applied force was reduced below 1 mV. The setpoint offsets have been further tested annually, yielding differences smaller than 1 mV over three years.

2.2.4 The PID feedback loop performance

The performance of the PID feedback loop was tested by pulling the well-known ubiquitin polyprotein. The response time of the PID feedback loop is shown in Fig. 2-3(a). An exponential function of the type $F = A - B\exp(-t/\tau)$ was fitted to the spike, which yielded a response time τ of 2.0 ± 0.1 ms.

The speed of our feedback loop will be limited by its slowest component. A block diagram of the feedback loop is shown in Fig. 2-4. The components with a lower bandwidth are the AFM cantilever and the piezoelectric actuator. In the case of the piezoelectric actuator, the limit comes from the maximum velocity at which the sample can be translated. Reducing the required torque can be achieved i.e. by placing the piezoelectric actuator upside down, as in the Luigs&Neumann AFM. Any modification of this kind in our microscope, however, would require a major and time-consuming re-arrangement of the AFM setup

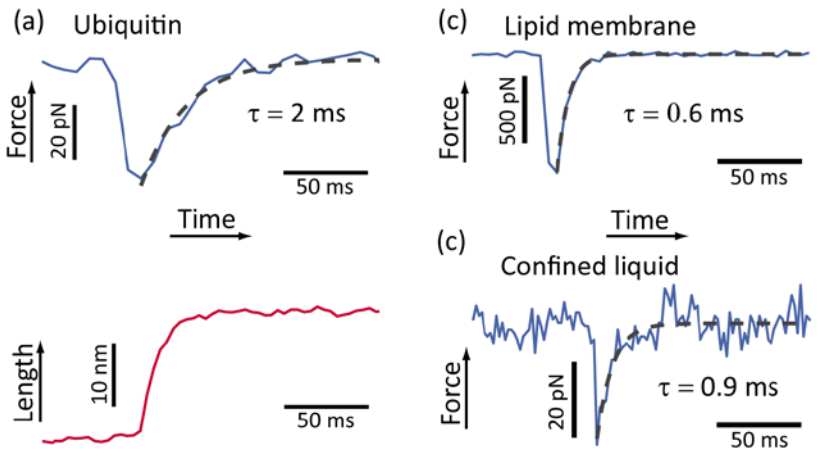

Fig. 2-3 The response time of the feedback loop in our system is tested in three distinct materials. (a) When one of the modules of the benchmark polyprotein ubiquitin is unfolded, the PID feedback loop of our AFM responds bringing the applied force back to its nominal value (blue line) by extending the position of the piezoelectric actuator (red trace). An exponential function has been fitted (grey dashed line) to the force reading and a decay time of 2 ± 0.1 ms was obtained. (b) Rupture of a DPhPC stacked lipid membrane displaying a recovery time of 0.6 ± 0.1 ms. (c) Rupture of a 1-undecanol confined liquid layer displaying a recovery time of 0.9 ± 0.1 ms.)

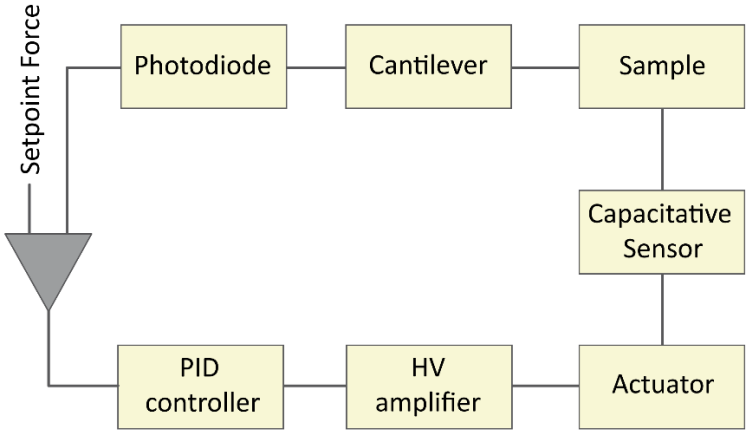

Fig. 2-4 Block diagram of the different step of the feedback loop.

In the second case, the feedback loop response speed can be improved by increasing the resonance frequency of the cantilevers. Since the resonant frequency increments with the spring constant, studying systems with a higher mechanical stability, such as lipid bilayers (chapter 4) and confined liquids (chapter 3), will naturally increase the performance of the feedback loop because of the higher resonance frequency of the stiffer cantilevers employed. Furthermore, the feedback response will be faster in thinner systems of study as the AFM tip needs to travel shorter distances to recover its original force. For these reasons, even though our setup is almost identical to that used to study protein unfolding, the recovery times measured when rupturing confined liquids or lipid bilayers are much shorter than for longer polyproteins, as shown in Fig. 2-3(b) and (c).

2.2.5 Software development

The controlling and analysis software for our AFM was designed by the original developers to perform pulling experiments. Pushing experiments, however, require different protocols. For example, force-clamp pushing pulses require a force ramp at their end to confirm the rupture events observed. Thus, the original code was modified to fulfil the pushing protocol needs.

The most work, however, originated in the analysis software. The unfolding of the modules of a polyprotein is a concurrent process — they happen in parallel. Thanks to this characteristic, the survival function can be easily computed just by averaging many force-clamp traces. This property allows many steps of the analysis process such as bootstrapping to become relatively simple. The rupture of a material while pushing, however, happens in a consecutive fashion — for example, a material layer cannot break until the previous one has. Thus, a whole new set of analysis tool were required to account for this process.

A screenshot of the program is shown in Fig. 2-5. Each rupture event can be captured by just clicking on it. Also, each of the rupture steps can be tagged with a number (1-9) that identifies, for instance, different intermediate steps of the rupturing process. The tags also allow to selectively analyse one type of intermediate or to find patterns in tag sequences. From the tags, the dwell times or any other measurable can be easily computed. The list containing all or a subset of rupture events is then used to perform the data analyses. This

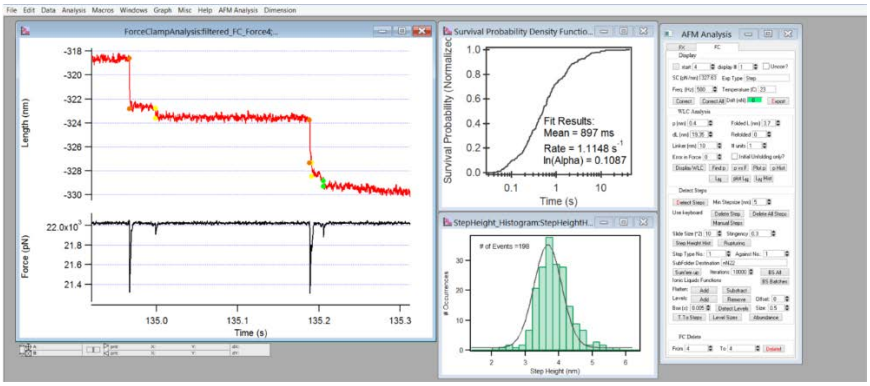

Fig. 2-5 Screenshot of the custom-made analysis software while analysing the rupture of DPhPC lipid membranes.

method of analysis also allows to reduce the amount of data managed by the software, and thus highly reduces the computing times. In the same way, an analogous program was developed to analyse the thicknesses and rupture forces in force-extension mode.

2.2.6 Benchmarking of the AFM

The performance of the AFM was benchmarked by pulling the well-studied polyprotein Ubiquitin. The polyprotein should display a maximum of eight unfolding events, each of them corresponding to the unfolding of a single modules of ubiquitin. The results are shown in Fig. 2-6. The measurement of several step yielded an average protein module length of 20 ± 1 nm, in very close agreement with the literature value of 20 nm[186]. The unfolding rate at 120 pN yielded 1.1 ± 0.1 s^{-1}, which is in close agreement with the reported result (1 ± 0.1 s^{-1}).

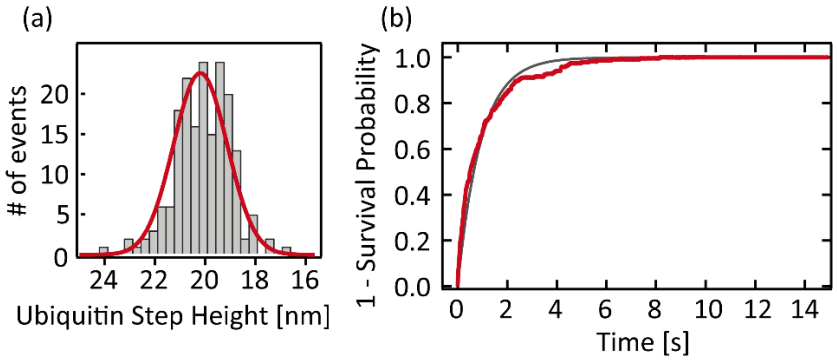

Fig. 2-6 Benchmarking of our AFM by unfolding the well-known polyprotein Ubiquitin. (a) The histogram of the ubiquitin step height has been fitted with a Gaussian function, yielding an average step size of 20 ± 1 nm. (b) The computed survival function (red trace) for the unfolding of ubiquitin at 120 pN has been fitted with an exponential function. The resulting unfolding rate is 1.1 ± 0.1 s^{-1}. The results correspond to 1832 unfolding events measured from 32 different unfolding trajectories.

2.3 Customizing a commercial AFM

The experiments in chapter 5 could not be performed with our custom-made AFM because the dimensions of a living cell are bigger than the extension range of the piezoelectric actuator (3 μm), as previously commented. Instead, we used a commercial AFM, the Bruker Dimension Icon, which exhibits a much longer piezo excursion size (80x80x9 um). This microscope, however, was (surprisingly) not suited to perform force spectroscopy and therefore a number of modifications had to be put in place.

2.3.1 Customization of the force spectroscopy protocol

In the default indentation mode with the Bruker Dimension Icon, the location of the substrate is initially measured by applying a high force against it. This method crucially affects any mechanical measurements performed afterwards because it plastically deforms the sample just before performing the mechanical measurements. Furthermore, the technical service has no knowledge of this misbehaviour (to our knowledge), thus posing a potential threat to unexperienced users. To overcome this limitation, the indentation curves were performed in by guessing the distance to the surface, which highly complicated the indentation protocol.

2.3.2 Development of the data analysis software

The built-in software from Bruker was not capable of performing complex analysis procedures. For this reason, an analysis routine was implemented in IGOR PRO, which also allowed to highly increase the analysis throughput. The routine consists of three independent modules specifically designed to satisfy the needs of our experiments. The first one converts the raw force vs. distance curves recorded in the original binaries to IGOR-compatible files. The second module extracts the Young modulus from indentation traces performed in N x N grids. The third program displays single indentation traces and allows the user to manually analyse the breakthrough forces of the cells lipid membranes.

A screenshot of the Young modulus analysis software is shown in Fig. 2-7(top image). The program initially performs an automatic analysis of all the traces, searching for the contact range and fitting an indentation model. The Young moduli obtained are displayed in the grey-scale top left image, which is a false colour reconstruction of the mechanical properties of the indented cell. For the example displayed, the false colour map shows the distinct mechanical properties of the nucleus and the cytoplasm of a single cell. Each single indentation trace can be inspected just by placing the cursor on any pixel of the image (top left plot). The quality of the fittings can be assessed by the rainbow-scale false colour image, which displays the Chi-square of each fitting. The aggregated results can be visualized in a histogram (right bottom plot), which can also be used to automatically filter the results by their Young modulus value.

The third module of the custom-made software analyses the rupture force of single indentation traces. The rupture events of the lipid envelope of a living cell can be measured at the end of the indentation trace, just as shown in Fig. 2-7 (bottom image). By pointing a cursor on any point of the curve, the program records their force and position values. It also attaches a tag containing information about the cell of origin. The results from several indentations are then visualized either in histograms or scatter plots. In the case of scatter plots, the original trace form each rupture force can be retrieved by clicking on them. This function proved invaluable for ensuring the quality of our data given the large amount of different experiments and attempts required to build a significant data set (at least > 20 indented cells per case).

Altogether, the routine allowed us to analyse more than hundreds of thousands of indentation traces in just a few days. This represents a leap in the accuracy in the measurement of mechanical properties. Moreover, the software is user-friendly: the analysis is performed just following simple actions that require no code typing or manual operation. The software has been recently used by another researcher to investigate the changes in mechanostability of cells when we interrupt proteins in the LINC complex – a multiplex of proteins connecting the cytoskeleton to the nucleoskeleton.

Therefore, designing a user-friendly interface has been key to add value to the

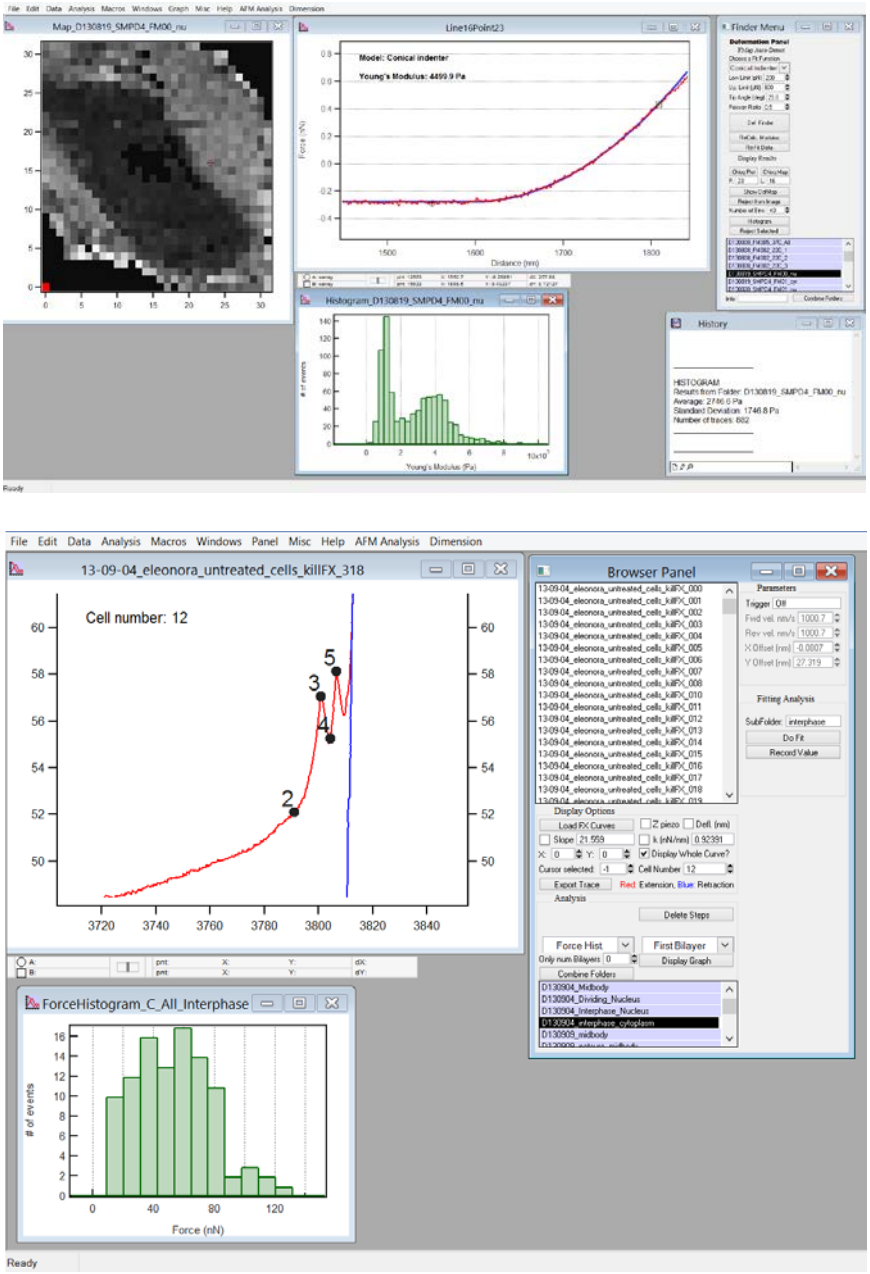

Fig. 2-7 Screenshots of the custom-made analysis software developed to process the data obtained in cell indentation experiments. The top screenshot corresponds to the modules that extracts the Young modulus (second module), whereas the bottom one corresponds to the program that analyses the rupture force of live cells (third module).

software.

2.3.3 Development of a temperature controller

Conducting experiments on live cells requires maintaining a constant temperature throughout the experiment of 37 ^{0}C. We decided to build our own controller because the AFM manufacturer failed to provide a commercial alternative at an affordable price. A temperature controller was developed to maintain the living cells at 37 ^{0}C during our indentation experiments. A photograph of the model is shown in Fig. 2-8. The sample containing the cells is placed on the centre of a custom-made aluminium stage, which is thermally isolated from the underlying support by a plastic layer. The sample is warmed by two heating mats (from Omega, Manchester, UK) located at each end of an aluminium plate. The temperature of the sample was monitored by a type K thermocouple wire (from Cole Parmer, Vernon Hills, IL) and the control was performed by an On/Off commercial temperature controller (E5GN-R1T-C AC100-240 from Omron, Kyoto, Japan). Despite its simplicity, this temperature controller achieved the target temperature accuracy and stability of ± 0.1 ^{0}C over the several hours of experimentation.

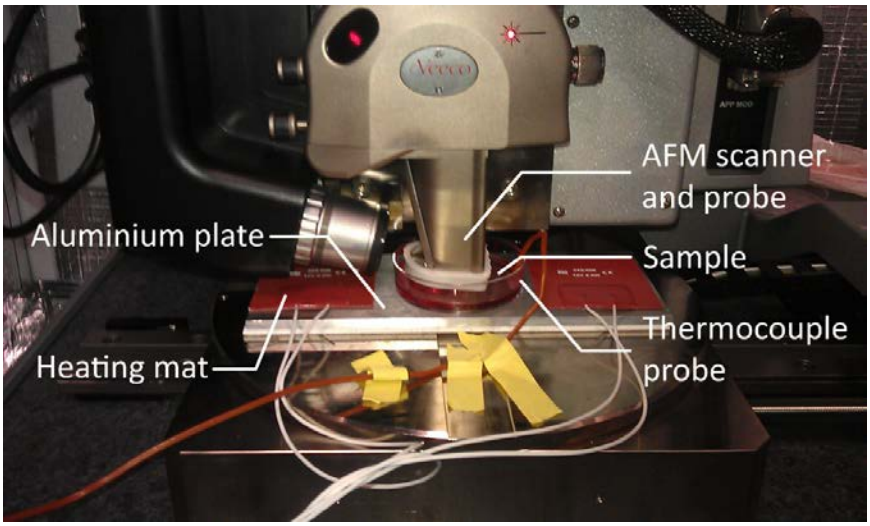

Fig. 2-8 Photograph of the custom-made temperature controller during an eperiment with licing cells.

2.4 Testing an AFM alpha model

Our laboratory actively collaborated with Luigs&Neumann GmbH (Ratingen, Germany) in testing the first commercially available AFM with force-clamp capabilities. A photograph of the new model is shown in Fig. 2-9. As previously commented, the main feature of this AFM is its inverted setup to optimize the feedback loop response time. Moreover, the photodiode and the actuator are automatically controlled by stepper motors, thus allowing the microscope to run for several hours — even days — without the intervention of the operator. Its main limitation, however, is the restriction in size and weight of the sample that can attached to the piezoelectric actuator without unsticking during experimentation.

After using it regularly for a few months, two main errors arose. The first one was a spurious force bias that typically appeared when polyproteins were pulled during short times. After testing its performance under various conditions, the bandwidth was found to be the only variable responsible for the bias. This information then helped the company technicians to identify an interference on the feedback loop originating in the clocking frequency of the data acquisition card. A second problem was encountered with the stepper motors controlling the photodiode and the piezoelectric actuator, which misbehaved moving forward or backwards without control. After testing the stepper motors independently, we located the source of the problem in the updated version of the stepper motor drivers, which were incorrectly translating the orders sent by the computer.

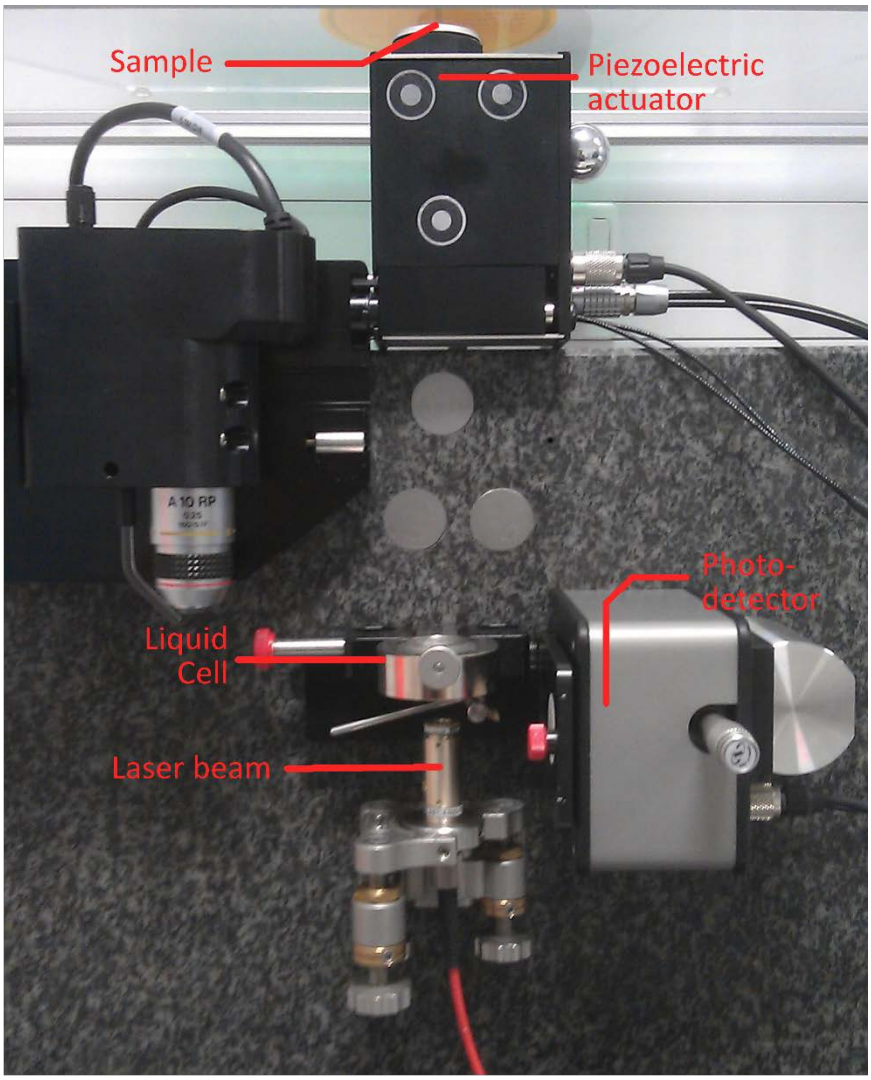

Fig. 2-9 Photograph of the Luigs&Neumann AFM setup.

3 The nanomechanics of solvation layers in confined liquids

Confined liquids organize in solid-like layers at the liquid-substrate interface. In this chapter, we use force-clamp spectroscopy AFM to capture the equilibrium dynamics between the broken and reformed states of an individual solvation layer in real time. Our results provide a first description of the energy landscape governing the fast molecular motions that drive the self-assembly of each individual liquid layer.

This chapter was published 25 June 2015 in Physical Review Letters[187] (attached in appendix III)

3.1 Introduction

Understanding the structural properties of liquids at the solid interface is fundamental to many applications in the fields of nanotribology, wetting or molecular biophysics[11]. When confined between two flat surfaces separated by a few nanometres, liquids exhibit properties that cannot be described by the continuum theories based on Van der Waals and electrostatic interactions characterizing the bulk properties. Instead, the molecules forming the liquid order into well-defined solvation layers, giving rise to oscillatory forces described by radial distribution functions with a periodicity of about one molecular diameter[11].

The discrete oscillation forces were first experimentally measured by pioneering Surface Force Apparatus (SFA) experiments, in which liquids are confined between two opposing macroscopic flat mica plates of $R = 10$ nm[64]. These observations were later complemented by AFM measurements, where the confined liquid is compressed by the AFM tip, with a much smaller contact radius ($R = 10$ nm)[188]. In the latter case, the deflection of the AFM cantilever is measured as it approaches a rigid, flat substrate (typically HOPG or Mica) at constant velocity. The layered nature of the probed liquids is hallmarked by the presence of discrete jumps in the resulting force-distance curves. Each discontinuity or jump occurs when an individual layer of confined liquid is suddenly squeezed out from below the AFM tip [189]. Crucially, the distance between two consecutive jumps informs on the precise orientation of each molecular layer with respect to the surface. This experimental approach has revealed invaluable information about the molecular packing properties of a variety of chemically distinct liquids, encompassing non-polar liquids with spherical structure such as octamethylcyclotetrasiloxane (OMCTS)[190], linear and branched alkanes [191][192], polar liquids such as short alcohols [193], a variety of ionic liquids [194][195] and even water [196][197], all exhibiting a priori similar force-induced rupture mechanisms. This progress notwithstanding, the reverse process encompassing the reversible reformation of each individual molecular layer remained completely elusive.

In this chapter, we make use of force-clamp spectroscopy AFM to directly capture the forced-induced rupture and reformation of each of the individual solid-like ordered layers populating the alcohol-HOPG and EAN-mica interface. These observations enable us to map out the complete energy landscape of a confined liquid, providing (sub)molecular insight into the mechanisms underpinning the rupture and reformation dynamics of self-assembly of an individual liquid layer according to its particular chemical structure.

3.2 Results

3.2.1 The case of molecular liquids

Using a home-made AFM spectrometer[198], we measured individual force distance curves [Fig. 3-1 (a)] on 1-undecanol whereby the cantilever was approached towards (red trace) and subsequently retracted from (blue trace) an HOPG surface at a constant velocity of 200 nm s^{-1} (for the detailed experimental procedure, see maerials and methods section at the end of this chapter). Upon approaching the surface, the cantilever penetrated 5 well-defined 1-undecanol layers (red arrows), each of them requiring an exponentially higher force to be indented [Fig. 3-1(b)]. As the cantilever was withdrawn from the sample, each previously broken layer was reversibly reformed (blue arrows). The distribution of breakthrough forces can be fitted with an exponentially decaying function [189],

$$F = F_0 \cos(2\pi d)\exp(-\tau d) \tag{3.1}$$

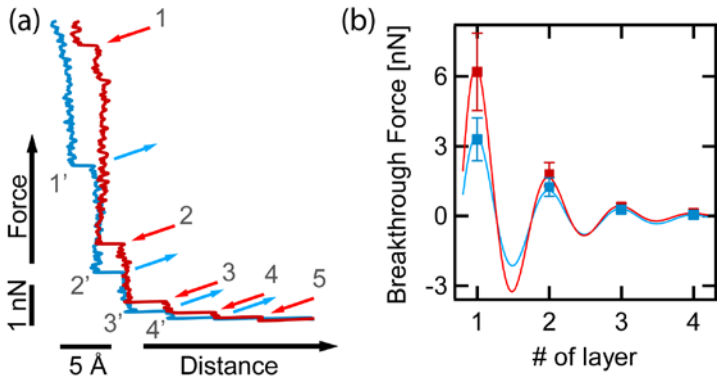

Fig. 3-1 Solvation layers in 1-undecanol revealed by constant velocity AFM. (a) Force vs. Distance plot of the AFM tip approaching towards (red line) and subsequently retracting from (blue line) the HOPG surface in 1-undecanol at constant velocity, showing the rupture and reversible reformation of a total of 5 confined layers. (b) Rupturing and reforming forces (n = 90 individual trajectories) for the first four measurable solvation layers.

(where d is the thickness of the confined layers and τ stands for the decay length), further confirming the periodic packing properties of 1-undecanol. The average jump-in distance (~3 Å) is significantly shorter than the 1-undecanol length (~14.7 Å)[14], thus suggesting an almost flat layering of the 1-undecanol layers on the HOPG surface. These results are in full agreement with previous X-ray[199], SFA[200], force[193] and imaging[201] AFM studies.

The direct observation of the discrete reformation events in the force extension traces [Fig. 3-1 (a), blue arrows] suggests that the rupturing process is reversible and that, by holding the applied force constant throughout the experiment at an 'average' set-point value between the rupturing and reformation force, the equilibrium dynamics between the broken and reformed states should be captured. In fact, applying a constant force of 430 pN with the force-clamp set-up displayed bistability [Fig. 3-2 (a), supplementary material for the detailed experimental procedure]; the layer #3 hopped between the broken and reformed states in real time, with a concomitant change in length Δl = 3.3 ± 2 Å, corresponding to the length of an individual layer (see supplementary material,). Changing the applied force to lower (410 pN) and higher (450 pN) values dramatically altered the equilibrium between the reformed and broken states. The thermodynamics of the Reformed/Ruptured transition can be evaluated by measuring the relative time abundance of the reformed state for each distinct constant force value according to the Boltzmann distribution:

$$\frac{N_{\text{ref}}}{N_{\text{total}}} = 1 - \frac{1}{1 + \exp\left(\frac{\Delta G - \Delta l F}{kT}\right)} \tag{3.2}$$

where ΔG is the difference in free energy between the broken and reformed states and Δl is the physical length distance separating them. Fitting this equation to the experimental data corresponding to the rupture/reformation of layer #3 [Fig. 3-2(b)] yields ΔG = 27 ± 2 kT and Δl = 2.6 ± 0.2 Å. Notably, the measured value of Δl is consistent with the thickness of one individual 1-undecanol layer and in agreement with the results obtained from force-extension [supplementary material, Fig. 3-5] and force-clamp [supplementary

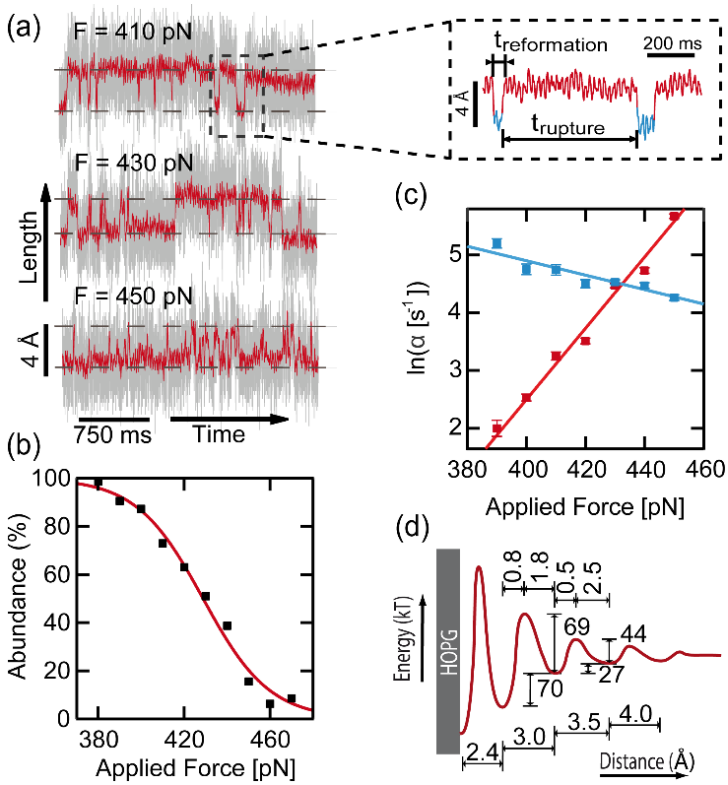

Fig. 3-2 The equilibrium dynamics of an individual solvation layer in 1-undecanol captured by force-clamp AFM. (a) Applying a constant force of 430 pN samples the rupture/reformation dynamics of layer #3. The equilibrium is readily displaced upon changing the applied force. (b) Plot of the abundance of the reformed state as a function of the applied force. (c) The dwell times of rupture and reformation [(a), inset] depend exponentially on the applied force (red and blue dots, respectively). The error has been calculated using the bootstrap method[21]. (d) Repeating the process for each individual layer (Fig. 3-10, Fig. 3-11, and Fig. 3-12 in supplementary material) allows the full 1D-reconstruction of the energy landscape of confined 1-undecanol. These results have been obtained reproducibly in three independent days of experiment (supplementary material, Fig. 3-9).

material, Fig. 3-6] measurements. The force dependent rates of breakthrough and reformation have been measured by extracting the dwell time for each individual transition occurring at a fixed force (Fig. 3-7 in supplementary material, and the methods and materials section), assuming that, as a first approximation, the distribution of dwell times at a particular force follows a single exponential (supplementary material, Fig. 3-8). Our observations demonstrate that, both for the rupturing and reformation processes, the measured rates depend exponentially on the applied force following a simple Bell formalism[202]:

$$\alpha(F) = A_0 \exp\left(-\frac{\Delta E}{kT} + \frac{\Delta x}{NkT} F\right) \tag{3.3}$$

where α is the rate of the process as a function of force, A_0 the pre-exponential factor, ΔE stands for the height of the energy barrier, Δx is the width of the energy barrier governing the process (normally known as 'distance to the transition state') and N is the number of bonds (or interactions) that withstand mechanical force. This approach has been used to interpret a wide variety of single molecule pulling experiments[198][203][204] for which $N = 1$. Fig. 3-2(c) shows the graph plotting the $\ln(\alpha)$ as a function of the pushing force, for both the rupturing (red) and reformation (blue) processes. Fitting eq. (3.3) for both processes results in $\Delta x_{,rupture}/N = 2.5 \pm 0.1$ Å for the rupturing process $\Delta x_{,reformation}/N = 0.5 \pm 0.1$ Å for the reverse reforming reaction. By assuming an arbitrary value $A_0 = 4 \cdot 10^9$ s^{-1} [205], we obtain $\Delta E = 44$ kT.

Dividing the expressions for the rates of rupturing and reformation and assuming that $A_{0,rup} \sim A_{0,ref}$ it follows that:

$$\ln\left(\frac{\alpha_{\text{rup}}}{\alpha_{\text{ref}}}\right) = \frac{\Delta G}{kT} + \frac{\Delta l}{NkT} F \tag{3.4}$$

Fitting eq. (3.4) to the experimental data, and using the previously obtained value of $\Delta l = 2.6 \pm 0.2$ Å, we obtain $\Delta G = 31 \pm 2$ kT and $N = 0.9 \pm 0.1$. Remarkably, the ΔG values obtained through kinetic and thermodynamic measurements are in close agreement, thus strongly suggesting that the hopping process occurs through a single barrier. Most importantly, our experiments revealed that $N = 1$ (by definition N must be an integer ≥ 1). This has fundamental implications, entailing that the applied force is transmitted through an 'individual' interaction within a very narrow space. These conclusions complement recent findings suggesting that the force does not distribute through the whole cantilever tip in contact with the liquid (which would imply that a larger number of bonds are effectively broken, yielding a large N) but rather through the last micro-asperities of the AFM cantilever tip[206]. The same approach used to uncover the kinetic and thermodynamic properties of layer #3 was extended and applied to layers #1 and #2 (Fig. 3-10,

Fig. 3-11, and Fig. 3-12 in supplementary material). Combined, these results allowed us to reconstruct the energy landscape of the first confined layers of 1-undecanol in the 1D-direction perpendicular to the graphite surface [Fig. 3-2 (d)]. Interestingly, and as expected in light of the large hysteresis between the breakthrough and reformation events observed in Fig. 3-1(a), the layer closer to the surface does not exhibit signatures of dynamic equilibrium between the ruptured and reformed states. Moreover, in this case, N is an order of magnitude bigger than in the rest of the confined layers (supplementary material, Table 3-1). The markedly different behaviour of this first layer suggests that the underlying solid substrate is likely to have a large effect on the conformation and dynamics of the layer.

3.2.2 The case of ionic liquids

The dynamic properties of a long, non-branched alcohol such as 1-undecanol lying flat on an HOPG surface sets the ground to study the molecular self-assembly mechanism of chemically more complex solvents. Due to their sterically-mismatched anion-cation pairs, ionic liquids exhibit fascinating properties that lie in-between those of a liquid and a solid[194][195]. In this context, ethylammonium nitrate (EAN) has revealed oscillatory forces in the vicinity of a flat mica substrate. Using constant velocity experiments [Fig. 3-3(a)], we recorded force-distance traces showing the initial 3 clear discontinuities hallmarking the rupture (red) and reformation (blue) processes. In this case, each jump measures 4.3 ± 0.4 Å in excellent agreement with the predicted ion pair diameter of EAN and with previous SFA [14] and AFM results [194][207]. This suggests that the EA^+ and the nitrate ions facing the bulk liquid are perpendicularly adsorbed onto the mica substrate. Due to the similar forces between consecutive solvation layers in EAN [Fig. 3-3 (a)], applying a constant pushing force of 50 pN to the EAN-mica interface results in an equilibrium situation where the system hops between three well-defined states (layers #1-2) in discrete jumps of ~5 ± 2 Å [Fig. 3-3 (b)]. Slightly changing the applied force to lower (40pN) or higher (70pN) values dramatically shifts the equilibrium properties of the system. The relative time abundance of each state as a function of the applied force is shown in Fig. 3-3(c). Fitting eq. (3.2) for each state provides a direct measurement of the associated ΔG and Δl values for the studied layers #1 and #2. Crucially, the obtained Δl values are ~5 Å, thus corresponding to the actual measurement obtained from force extension ([Fig. 3-3 (a)] and see supplemental Fig. 3-13]) and force-clamp [supplementary material, Fig. 3-14]. As before, the dwell times for each individual transition can be used to compute the cumulative probability density function for both rupturing and reformation processes, the time-course of which can be in both cases captured by a single exponential [Fig. 3-3 (d)]. The resulting rates at each particular force are fitted to eq. (3.4) yielding in this case $N = 2.0 \pm 0.8 \approx 2$ [Fig. 3-3 (e)]. The observed $N = 2$ indicates that 2 interactions are disrupted in parallel, most likely suggesting that the ions have to be dislocated in pairs in order to avoid configurations where two ions of the same sign are in close contact.

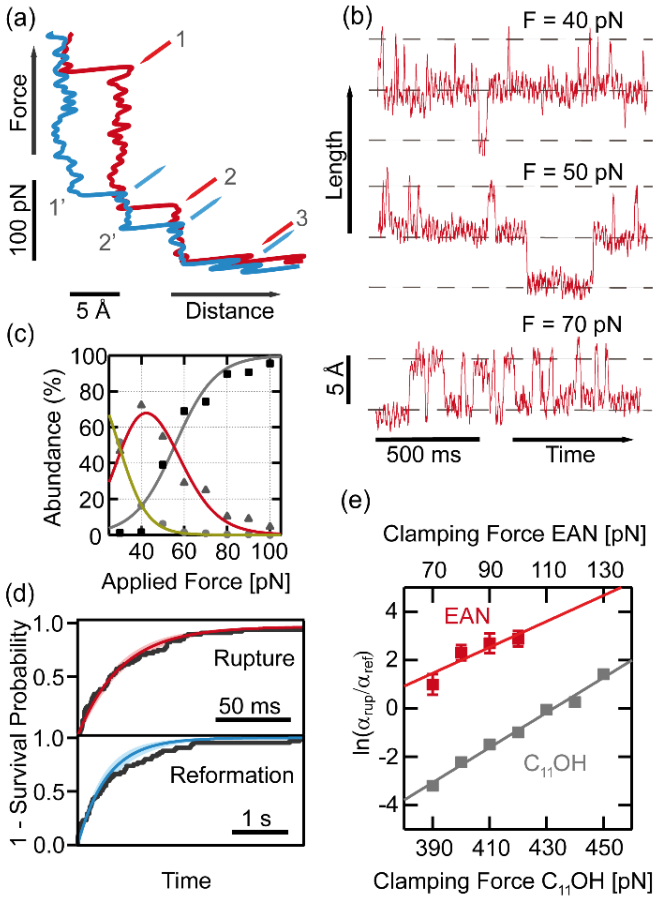

Fig. 3-3 The solvation dynamics of EAN. (a) Force extension trajectories showing the rupture and reformation of 3 confined EAN solvation layers. (b) The system hops between layers #1 and #2 as the applied constant force varies from 70pN-40pN. (c) Relative abundances of the reformed (green) and ruptured state (red) of layer #1 and the ruptured state of layer #2 as a function of the applied force. Global fit of eq. (3.2) yields Δl = 4.3 ± 0.4 Å and ΔG = 5.9 ± 0.6 kT (layer #2, red line); Δl = 6.2 ± 0.1 Å and ΔG = 4.5 ± 1 kT (layer #3, blue line). (d) The cumulative density function reconstructed from the transition dwell times is fitted, as a first approximation, to an exponential function to obtain the rates of rupture (red line, τ = 29 ± 4 ms) and reformation (blue line, τ = 500 ± 100 ms) for F = 100 pN. (e). Fitting of eq. (3.4) yields ΔG = 4.5 ± 1 kT and N = 2.0 ± 0.8 (EAN, red solid line). For comparison, the same equation was fitted to 1-undecanol results (grey solid line) yielding ΔG = 31 ± 2 kT and N = 0.9 ± 0.1.

3.3 Discussion and conclusions

While qualitatively similar, AFM solvation force measurements quantitatively differ from SFA results[206]. The main important difference lies in the massively different (~10^6 fold) contact radius, which affects the liquid confinement area and hence the mechanisms of liquid squeeze-out. Briefly, the nanometre confinement below the AFM tip has allowed measurement of solvation forces in branched liquid molecules lacking molecular symmetry[191], and the packing properties can be analysed even for surfaces that are not atomically flat (such as SAMs)[206], both being important prerequisites in SFA measurements[11]. Moreover, the large temperature effect of the solvation forces observed with AFM [208] and the lack of correlation between the measured forces and the tip radius[65] —indicating that the nanometre-scale micro-asperities of the tip dominate the short-range interaction— suggest novel molecular mechanisms underlying the squeezing out of liquids confined in the gap between the cantilever tip and the substrate[206]. These observations have been recently complemented by AFM and STM imaging[201][209][210], directly demonstrating the semi-solid behaviour of the liquid layers. Our results using force-clamp spectroscopy add a new dimension to the study of the solvation phenomena, providing precise quantification of the equilibrium rupture-reformation dynamics, which allow, for the first time, the reconstruction of the solvation free-energy landscape. Moreover, these experiments provide new insights into the (molecular) mechanisms underlying liquid disruption; (i) Using the Bell formalism, borrowed from antigen-antibody and single molecule mechanics pulling experiments, we gained access to the number of key 'interactions' disrupted (and reformed) under force. (ii) For 1-undecanol, molecules lie parallel to the HOPG surface. Our experiments reveal that a unique interaction (N = 1) needs to be broken to induce the rupture of the layer. We speculate that the pore created in the structure of the confined liquid induces the lateral shift of a whole row of molecules pushed to the sides [Fig. 3-4 (a)]. However, our experiments cannot tell whether the lateral displacement corresponds to 1 or more molecular positions. (iii) In the case of EAN, molecules are oriented up-right from the mica normal direction. The EA+

moiety measures 3 Å, while the nitrate measures 1.7 Å [211]. Since the barrier is highly symmetric (Δx = 2.5 Å), and probably located in the plane where electrostatic interactions take place, we speculate that there is a slight molecular mismatch between the position of contiguous ion pairs in order to better accommodate their charges. Our experiments show that in this case N = 2. Since N only corresponds to the number of molecules/interactions being disrupted in parallel with the tip, we hypothesise that individual anion-cation pairs need to be displaced together in tandem [Fig. 3-4 (b)], which is easy to rationalize due to their electrostatic nature. Altogether, our experiments directly capture the molecular motions involved in the rupturing and self-assembly processes of individual solid-like liquid layers and highlight the single molecule nature of the squeeze-out mechanism when the confinement area lies in the nanometre realm.

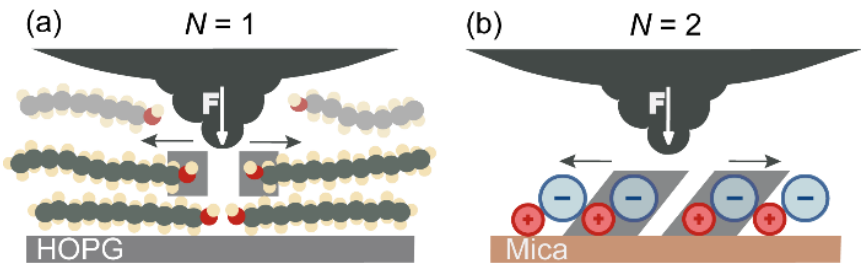

Fig. 3-4 Schematics of the rupturing process for (a) 1-undecanol (N = 1) and (b) EAN (N = 2).

3.4 Materials and methods

3.4.1 Sample preparation method

Freshly cleaved Highly Oriented Pyrolytic Graphite (HOPG, 3.5 ± 1.5° of mosaic angle, Agar Scientific, Stansted, UK) was placed into the chamber of our custom-built Atomic Force Spectrometer (the details of the apparatus are described elsewhere[198]). Then, a droplet of 1-undecanol (99%, Sigma-Aldrich, St. Louis, MO) was injected into the cell and left to equilibrate for ten minutes. The AFM cantilever was calibrated against the HOPG substrate using the equipartition theorem. Both MLCT Tip D (k = 0.03 nN/nm) and MLCT tip E (k = 0.1 nN/nm) from Bruker Probes (Karlsruhe, Germany) were used indistinctively in 1-undecanol experiments. Ethylammonium nitrate (EAN) experiments (>97%, Io-Li-Tec, Heilbronn, Germany) were performed on freshly cleaved Muscovite Mica (Ted Pella, Redding, CA) and MLCT tips B (k = 0.02 nN/nm) were used. In this case, due to the higher viscosity of EAN, the cantilevers were calibrated prior to the experiment in ultra-pure water. The AFM cantilevers were thoroughly rinsed and dried after calibration in order to avoid contamination. All experiments were performed at 22 ℃ in a temperature-controlled room with a stability of ± 1 ℃.

3.4.2 Force-extension experiments

The Force vs. distance plots were acquired by allowing the AFM tip approach the surface at a constant velocity (200 $nm \cdot s^{-1}$ for 1-undecanol and 50 $nm \cdot s^{-1}$ for EAN) until the substrate was encountered and all the confined layers were pierced. In the case that any signs of impurities attached either to the tip or the substrate appeared, such as an increased detachment force or the indentation of features with different shape than that of confined liquid layers, the experiment was aborted, the set-up thoroughly cleaned and the AFM tip discarded.

3.4.3 Force-clamp experiments

Force-clamp AFM experiments were performed by applying a constant force between the AFM tip and the surface. An external feedback mechanism was used to maintain a constant AFM cantilever deflection (force) by controlling the position of the surface with a piezoelectric actuator. The feedback loop consists of proportional, integral and derivative terms and displays a time response faster than 1ms. The unprecedented quick response of our feedback loop stems from the higher resonant frequency of the cantilevers used and the small distance (<0.5 nm) that the piezoelectric actuator has to travel in order to recover the set-point deflection. In order to capture the transitions with detail, the cantilever deflection and the piezo extension were recorded for all Force-Clamp pulses with a sampling rate higher than 2 kHz, usually in the 5-10 kHz range. After applying the Force-Clamp pulse (typically 10-20s), the applied force was steadily increased for a few hundreds of picoNewtons to confirm that the layer had been broken. This protocol helped us to unambiguously identify the confined layer being indented. Finally, the tip was retracted from the surface a few hundreds of nanometres and a new spot in the close vicinity was probed.

From all the force-clamp traces acquired, only those that displayed low drift were considered for analysis. The drift might come from either the displacement of the surface or from the uncontrolled deflection of the AFM cantilever. Whereas the displacement of the surface does not highly affect the measurement of the transition rates, the cantilever drift alters the applied force and therefore the rates measured. In order to minimize this bias from the calculated rates, the deflection drift between the beginning and the end of each trace was directly measured. If it was higher than the applied force steps (typically 10 pN) then the trace was discarded for further analysis. Moreover, those traces that showed surface drift higher than a few nanometres were also discarded to avoid any other sources of bias.

The initial analysis of 1-undecanol layers showed that the rates obtained for each applied force varied within different days and even within the same experimental day. This effect is due to the net rate of rupture and reformation depends bi-exponentially on the energy difference between the work applied

by the tip and the height of the energy barrier. Thus, any tiny environmental change that slightly shifts the stability of the confined layers will generate a great change in the rupture and reformation rates. Our Force-Clamp results show that even during the same day of experiment the mechanical stability of 1-undecanol layers decreases after the first 4-5 hours of experiments. Unfortunately, these time-dependant effects on the mechanical stability constrained us to only consider for analysis those traces that were obtained with sufficient drift stability and within the first hours of experiment. Thus, if the measurement of the rates for the whole range of applied forces, typically 8-12 points, could not be finished within a few hours, the experiment had to be started again from scratch and the acquired data discarded.

3.4.4 Force-clamp data analysis

Force-clamp traces were analysed using a purposely written code developed in our lab using Igor Pro (WaveMetrics, Portland, OR). Firstly, the traces were flattened using 10-parameter polynomial functions that were fitted to different parts of the trace [Fig. 3-7 (a)]. Then, the force channel was analysed in the search of rupture and reformation transitions. These transitions could be detected as a spike in the force channel [Fig. 3-7(a), bottom]. These spikes are due to the limited time-response of the PID feedback mechanism. Each spike occur concomitant to a transition observed in the length channel. Each downward spike corresponds to the rupture of a confined layer and each upward spike to its reformation. In all cases, a rupture event was followed by reformation transition and *vice-versa*. Each transition could be easily measured manually following the error (spikes) in the force channel (in most cases they were three times bigger than the standard deviation of the trace).

The rupture and reformation equilibrium of the confined layers was studied by calculating the relative abundance of the reformed state at different applied forces. The calculation of the abundances was computed by adding up the time spent in the reformed state, measured from the manual analysis of the force channel spikes, and dividing it by the total time of the whole trace spent at an applied force. Then, a sigmoidal function was fitted to the computed abundances vs. the applied force:

$$\frac{N_{\text{ref}}}{N_{\text{total}}} = 1 - \frac{1}{1 - \exp\left(\frac{\Delta G - \Delta l F}{kT}\right)} \tag{8.1}$$

where ΔG is the Gibbs free energy between the reformed and rupture states and Δl, its physical separation. In order to validate the method of analysis used, a second independent method of analysis that did not include any bias from the manual measurement of the transitions was employed. In this case, a histogram of the points of the flattened force-clamp traces was computed and the relative abundance of each state calculated by integrating the area below each peak. The results obtained from both methods yielded the same results.

The rates of rupture and reformation were calculated by first measuring the dwell times for each transition. Then, their cumulative distribution function (CDF) was reconstructed and an exponential function was fitted, as a first approximation, to obtain the rate [Fig. 3-7]. The bootstrap method[205] was used to find the most likely rate and its standard deviation. The rates of rupture and reformation were calculated for each applied force and its dependency was fitted with the Bell model[202]:

$$\alpha(F) = A_0 \exp\left(-\frac{\Delta E}{kT} \pm \frac{\Delta x}{NkT} F\right) = \alpha_0 \exp\left(\frac{\pm \Delta x}{NkT} F\right) \tag{8.2}$$

where $\alpha(F)$ is the rate of the process as a function of force, α_0 the rate in the absence of force, A_0 is the pre-exponential factor, ΔE stands for the height of the energy barrier, Δx is the width of the energy barrier governing the process (normally known as 'distance to the transition state') and N is the number of bonds (or interactions) which withstand mechanical force. The height of the energy barrier decreases with the applied force and hence, its exponential factor will be positive. Inversely, the variation of the height of the barrier for the reformation process will have a negative exponential factor. Also, the Gibbs free energy of the transition, ΔG, can be obtained by dividing the expressions for the rates of rupturing, α_{rup}, and reformation α_{ref}, and assuming that $A_{0,\text{rup}} \sim A_{0,\text{ref}}$:

$$\ln\left(\frac{\alpha_{\text{rup}}}{\alpha_{\text{ref}}}\right) = \frac{\Delta G}{kT} + \frac{\Delta l}{NkT} F \tag{8.3}$$

The calculated ΔG value obtained by measuring the relative abundances and by the ratio of the rupture/reformation rates are in good agreement for all the layers where dynamic equilibriums have been observed (Table 3-1). Thus, this strongly confirms that the measurement of the dwell times measured here does not introduce an important measurement bias to the results.

The analysis of the rupture and reformation transitions was more complex for the dynamic equilibrium of EAN, where up to 3 different processes coexist at the same time at low applied forces. Indeed, the rates of the transitions of layers #2 and #3 of EAN occurred at the limit of the time resolution of our technique. In order to circumvent this problem, the abundances were calculated by directly making a histogram of the points of the force-clamp traces and taking the abundance from the area below the different peaks.

3.5 Supplementary figures and tables

3.5.1 Layer thickness in 1-undecanol confined layers

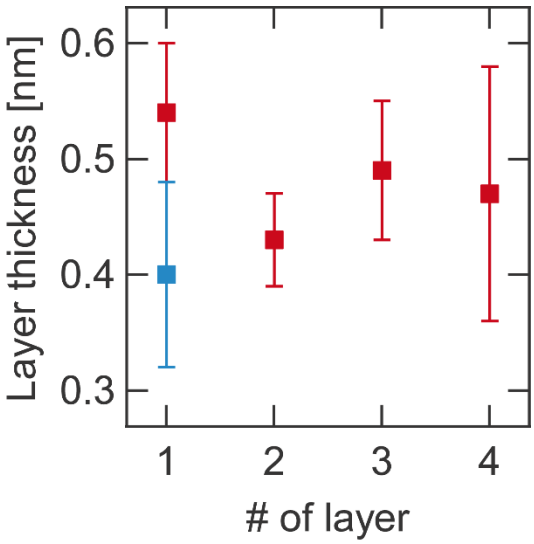

Fig. 3-5 The thickness of each solvation layer in 1-undecanol slightly depends on the surface proximity and demonstrate that molecules lie parallel to the substrate. Thickness of each layer for the rupturing (red) and reformation (blue) events (average ± s.d.). Statistical analysis of the jump distance corresponding to each independent layer reveals that the 'inner' (closest to the surface) layer is slightly shorter than the other layers, in accordance with previous studies using dynamic force spectroscopy[193].

3.5.2 Layer thickness of 1-undecanol measured in force-clamp

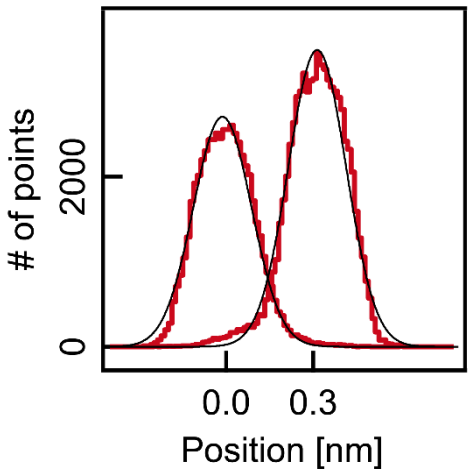

Fig. 3-6 The length of the hopping transition can be calculated by the distribution of points within the force-clamp trajectory. A histogram of the number of points for each force-clamp trace exhibiting hopping between two states results in two peaks, which correspond to the ruptured and reformed states, respectively. A Gaussian function was fitted to each of the peaks, and by taking the peak-to-peak distance, a layer thickness of $\Delta l = 3 \pm 1$ Å was measured. This value corresponds to the value obtained in constant velocity experiments. The relative abundance of each state can be calculated by integrating the area below the peaks.

3.5.3 Force-clamp event detection protocol

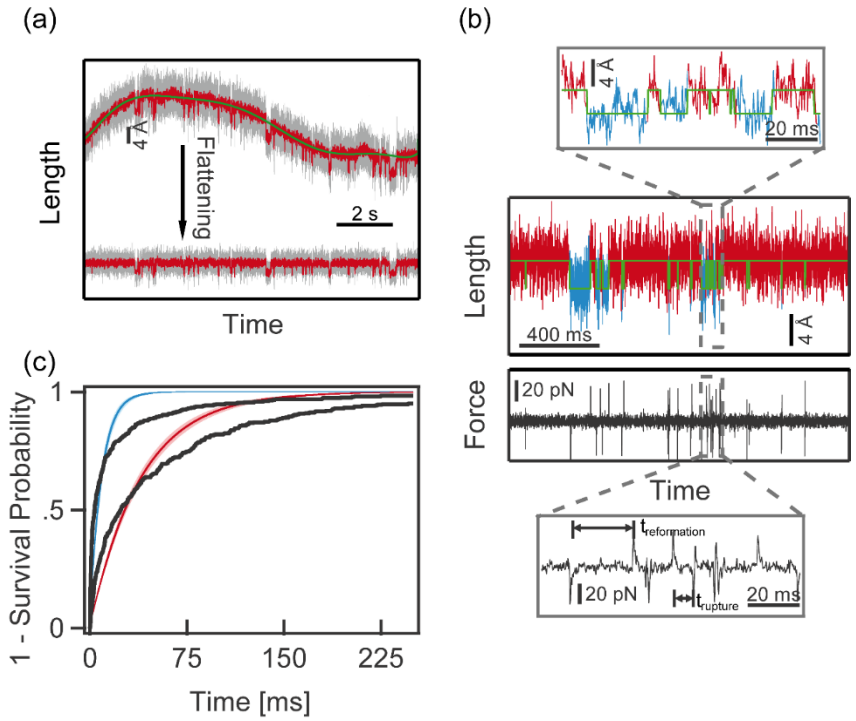

Fig. 3-7 Analysis of the force-clamp raw trajectories. (a) Length channel of a typical raw Force-Clamp trace of 1-undecanol acquired at an applied force of 410 pN (solid light grey). A low-band pass filter is applied to improve the visualization of rupture/reformation transitions (solid red). The original raw length trace (top) is flattened by subtracting the fitted polynomial function (solid green line). This process is repeated several times for various sections of the trace to obtain the flattened bottom trace. (b) The rupture/reformation transitions are manually detected by locating the spikes that appear on the force channel (bottom plot, solid dark line) due to the non-instantaneous time response of the feedback loop. (Bottom inset): Rupturing events generate spikes facing downwards (lower forces) due to the relaxation of the cantilever, whereas reforming events generate upward looking spikes (higher forces). By locating every transition, the dwell times of rupture and reformation can be measured, (Bottom inset). Then, the time the confined liquid spends in each state can be reconstructed (solid green line) and each point on the recorded trace assigned to either the ruptured (solid blue) or reformed states (solid red). The inset of the length channel (top inset) shows that the transitions detected in the force channel correspond to actual transitions between the ruptured and reformed states. (c) By taking the dwell times from several traces, the cumulative density functions (CDFs) of the rupture and reformation processes can be computed (solid dark lines). The CDFs have been fitted with an exponential function like in Fig. 3-8 (solid red (τ = 38 ± 3 ms) and solid blue lines (τ = 8.7 ± 1 ms) for the rupture and reformation processes, respectively). The light coloured areas surrounding the fitted exponential functions correspond to one standard deviation of the most-likely rates.

3.5.4 Rupture cumulative density function for 1-undecanol

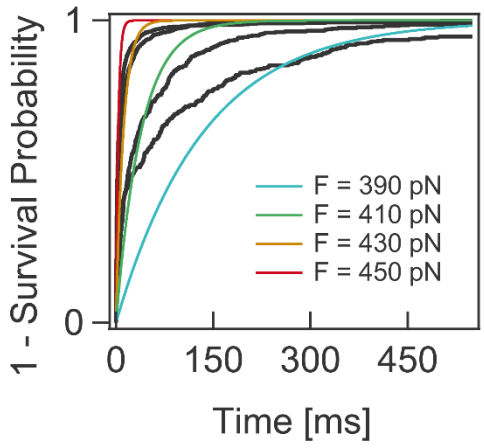

Fig. 3-8 The rate of rupture and reformation is calculated from a single exponential fit to the CDF. The cumulative density function (dark lines) is obtained from the computed transition dwell times. As a first approximation, the CDF is fitted by a single exponential fit to obtain the rate of rupture (or reformation). As higher loads are applied, the faster the rupture of the confined layer occurs (the measured half-lifes are τ = 135 ms for 390 pN (light blue line), τ = 39 ms for 410 pN (green line), τ = 12 ms for 430 pN (orange line) and τ = 4 ms for 450 pN (red line)).

3.5.5 1-undecanol layer #3 repeats

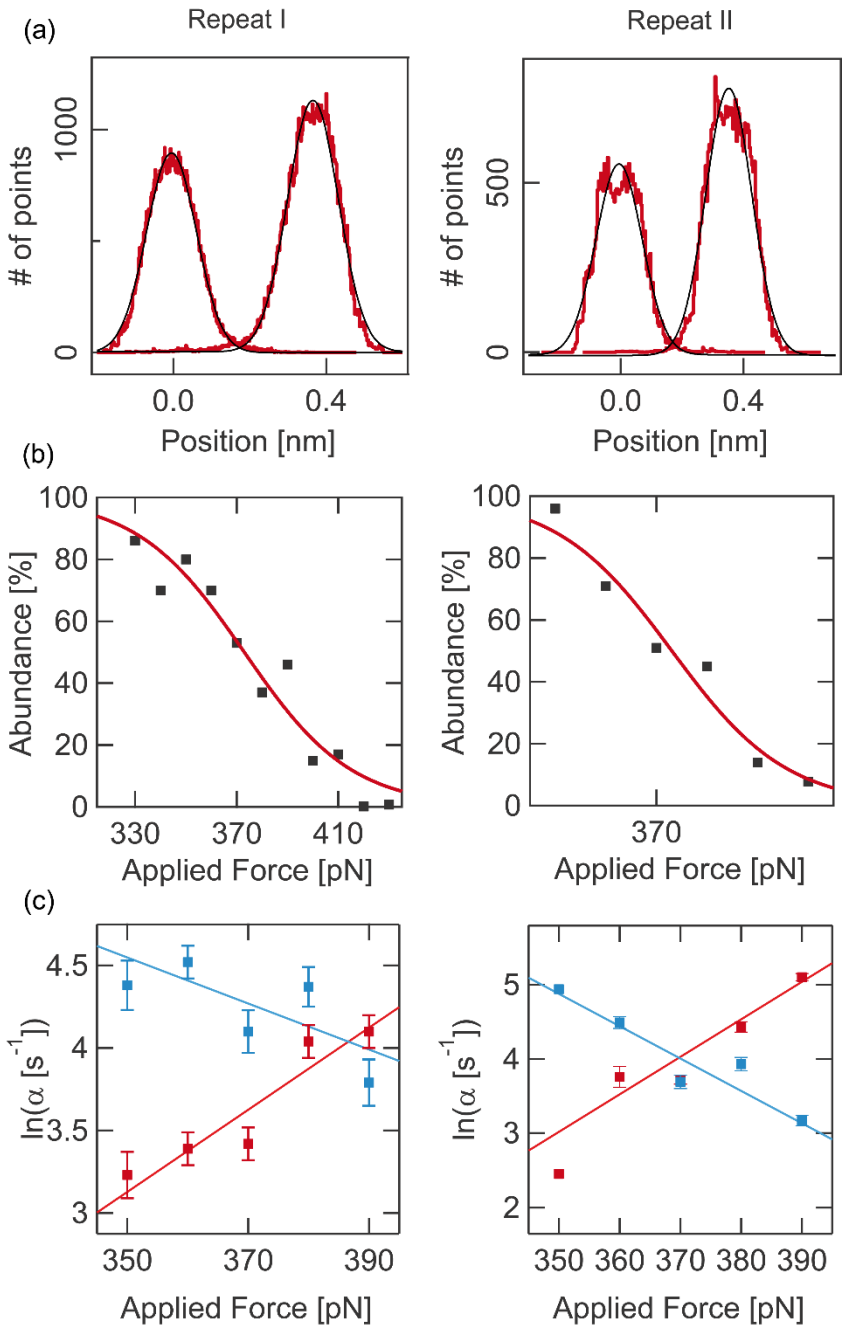

Fig. 3-9 Independent measurements of the rupture/reformation equilibrium dynamics of layer #3 of 1-undecanol on HOPG. Each column (left and right) corresponds to an individual, independent measuring experimental day. (a) The histogram of a single trace (low-band pass filter of 100 Hz) of the data set produces two clearly separated peaks corresponding to the ruptured and reformed states. Each of both peaks (dark lines) is fitted to a Gaussian. The peak-to-peak distance corresponds to the layer thickness, Δl. Layer thicknesses of 3.5 ± 1.4 Å and 3.7 ± 1.4 Å were measured for the Replicate I and II, respectively, conducted during two independent experimental day (new sample, new cantilever, etc.). (b) Plot of the abundance of the reformed state against the applied force for layer #3 in 1-undecanol (dark squares). Fitting a Boltzmann function, eq. (3.2) in the main text, (solid red line) yields a distance between

ruptured and reformed states, Δl = 1.9 ± 0.3 Å for the Replicate I and 3.6 ± 0.6 Å for Replicate II. The calculated ΔG was 18 ± 3 kT and 33 ± 6 kT for Replicates I and II, respectively. (c) The rates of rupture and reformation of the layer #3 in 1-undecanol depends exponentially on the applied force (red and blue dots, respectively). Replicate I consists of a total number of 2869 transitions and Replicate II consists of 2373. The Bell model has been fitted to the rates of rupture (red solid line) and reformation (solid blue line). The resulting distance to the transition state, $\Delta x_{rupture}/N$ = 1 ± 0.15 Å (Replicate I) and $\Delta x_{rupture}/N$ = 2.1 ± 0.15 Å (Replicate II), and the logarithm of the rate at the absence of force, $\ln(\alpha_0\ [s^{-1}])$ = -5.6 ± 1.3 (Replicate I) and $\ln(\alpha 0\ [s^{-1}])$=-14.7 ± 0.3 (Replicate II). For the reformation process, $\Delta x_{reformation}/N$ = 0.6 ± 0.2 Å (Replicate I) and $\Delta x_{reformation}/N$ = 1.8 ± 0.15 Å (Replicate II) while $\ln(\alpha_0\ [s^{-1}])$ = 10 ± 2 and $\ln(\alpha_0\ [s^{-1}])$ = 20 ± 1 for Replicate I and II, respectively.

3.5.6 1-undecanol layer #2 force-clamp

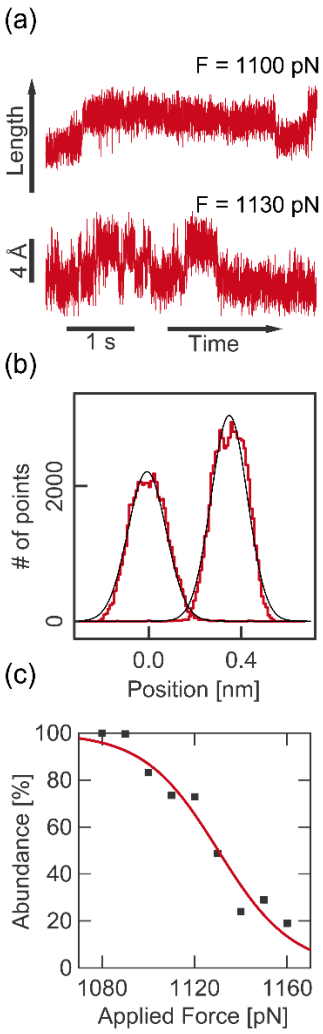

Fig. 3-10 Thermodynamics of the solvation layer #2 in 1-undecanol. (a) The rupture/reformation dynamic equilibrium of the solvation layer #2 of 1-undecanol shows fluctuation between two well-defined states. At an applied (low) force of 1100 pN (top trajectory), the system lies mainly in the reformed state. Slightly increasing the force to higher values (1130 pN, bottom trajectory) results in a shift of the equilibrium towards the ruptured state. (b) The histogram of the length channel of each trace exhibits two well-defined peaks corresponding to the ruptured and reformed states, respectively. Gaussian fitting (dark solid line) to each peak renders the average length position at each equilibrium state. Measuring the peak-to-peak distance provides a direct measurement of the layer thickness, Δl = 3.5 ± 1.5 Å. The relative abundance of each state can be calculated by integrating the area below the peaks. (c) Plot of the abundance of the reformed state as a function of the applied force for the layer #2 of 1-undecanol (dark squares). A sigmoidal function has been fitted (solid red line). The resulting distance between ruptured and reformed states, Δl = 2.6 ± 0.4 Å [thus close to that calculated in (b)] and the ΔG = 70 ± 10 kT.

3.5.7 Determination of *N* in 1-undecanol

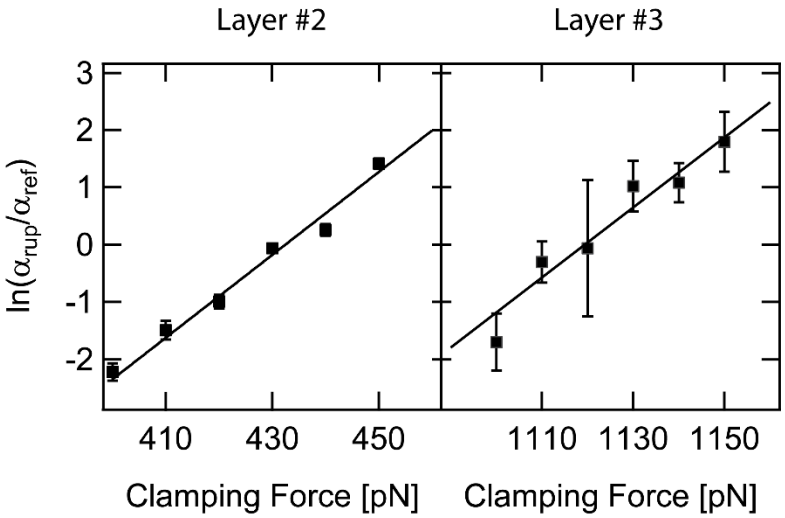

Fig. 3-11 Kinetics of the rupture/reformation of the solvation layer #2 and #3 in 1-undecanol. We measure the ln of the ratio between the rupture and reformation rates as a function of the applied pushing force for layers #2 and #3 in 1-undecanol. Fitting eq. (3.4) in the main text to the experimental data yields a value of $\Delta G = 68 \pm 12$ kT and $N = 1.1 \pm 0.3$ for layer #2 and $\Delta G = 31 \pm 2$ kT and $N = 0.9 \pm 0.1$ for layer #3. The data set consists of a total number of 15.525 transitions for layer #3 and 1131 transitions for layer #2.

3.5.8 Force-clamp of layer #1 in 1-undecanol

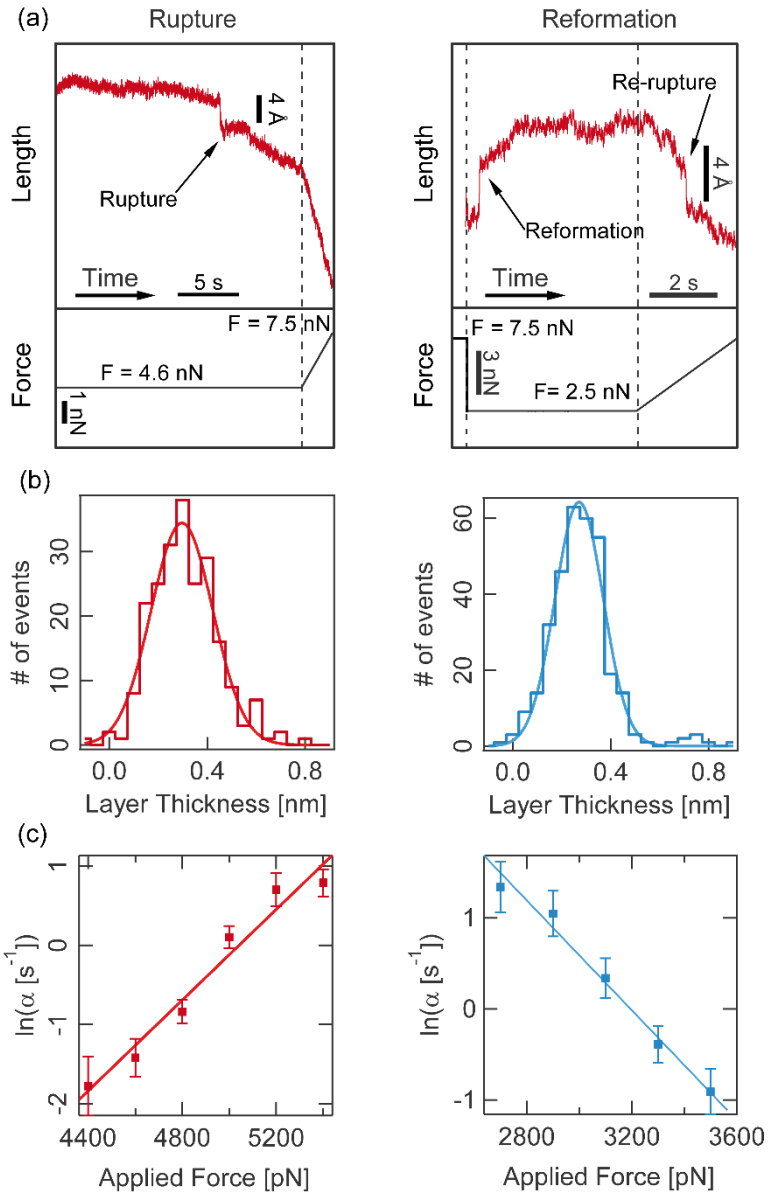

Fig. 3-12 Force-clamp experiments on the 'inner' solvation layer (#1) in 1-undecanol reveals a substrate effect. Probing of the kinetics of rupture (left column) and reformation (right column) of the 1-undecanol confined layer closer to the substrate. (a) (Left, bottom plot) A constant force (dark solid line) is applied to the layer #1 of 1-undecanol (7500 pN), which induces the rupture of the confined layer. The rupture event can be observed in the top graph as a sharp drop in the position of the piezoelectric actuator (red solid line), indicated by a solid red arrow. At the end of the Force-Clamp pulse, the applied force is quickly increased (up to 7500 pN) in order to check that there are no remaining layers. (Right) The reforming kinetics is studied by first applying a fast high force pulse (dark solid line in the bottom graph) of 7500 pN such that the 'inner' confined layer is ruptured. Then, the load is decreased to lower forces (2600 pN), where reforming transitions occur. These can be observed as a sharp rise in the position of the piezoelectric actuator (red solid line). At the end of the force-clamp pulse, the reformation of the layer is validated by quickly increasing the applied force back again at higher forces until the reformed layer is pierced again. (b) Histogram of the thickness of the confined layer #1 of 1-undecanol during the rupture

(left) and the reformation (right). Gaussian fits to the peaks (light coloured solid lines) displays a value of layer thickness of Δl = 2.9 ± 0.1 Å (rupture) and Δl = 3.0 ± 0.1 Å (reformation). (c) The rates of rupture (left) and reformation (right) of 1-undecanol layers depend exponentially on the applied force (square dots, respectively). Fitting of the Bell model to the rates of rupture (left plot, red solid line) and reformation (right plot, blue solid line) yield $\Delta x_{rupture}/N$ = 0.12 ± 0.01 Å and $\Delta x_{reformation}/N$ = 0.12 ± 0.07 Å. The logarithm of the rate at the absence of force, $\ln(\alpha_0\ [s^{-1}])$ = -14 ± 1 (rupture) and 10 ± 1 (reformation).

3.5.9 Force-extension of EAN

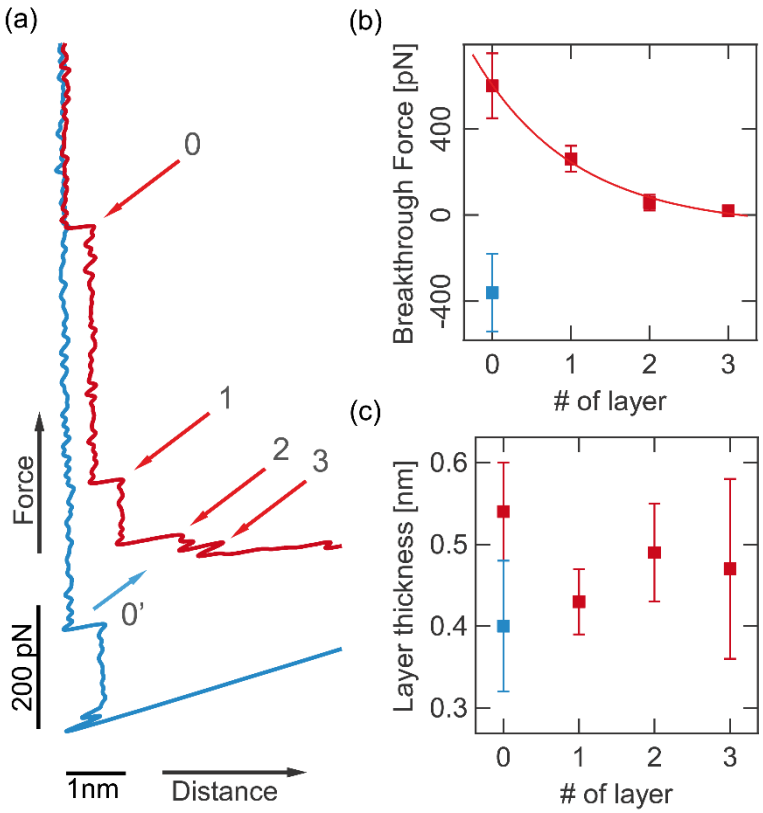

Fig. 3-13 The solvation properties of EAN on mica revealed by constant-velocity AFM experiments. (a) Force vs. Distance plot of the AFM tip approaching (red line) and subsequently retracting (blue line) from the Mica surface in EAN. In the close vicinity of the surface, a number of thin sharp discontinuities in the Force vs. Distance plot can be observed, corresponding to the rupture (red arrows) and reformation (blue arrow) of a single layer of EAN. The rupture of a total of four confined layers were detected for EAN. Note that in this case, the higher applied forces revealed a new layer closer to the substrate that was not observed in the range of forces probed in Fig. 3-3(a). (b). When this layer was ruptured, the reformation of any other confined layer was prevented. Rupturing and reforming forces of individual EAN solvation layers probed by force-distance AFM experiments. Data are obtained from a total of 48 individual trajectories. The mean force value and standard deviation has been plotted for each layer (red and blue squares, respectively). A periodically oscillating function has been fitted to the average rupturing force (the period of the oscillation is fixed to 1 layer). The obtained rate of decay is 1.13 (layers), very close to the theoretical value of 1 for confined layers consisting of non-deformable, apolar spheres. C) Measured thickness of each layer (red and blue squares for the rupture and reformation processes, respectively).

3.5.10 Layer thickness of EAN measured by force-clamp

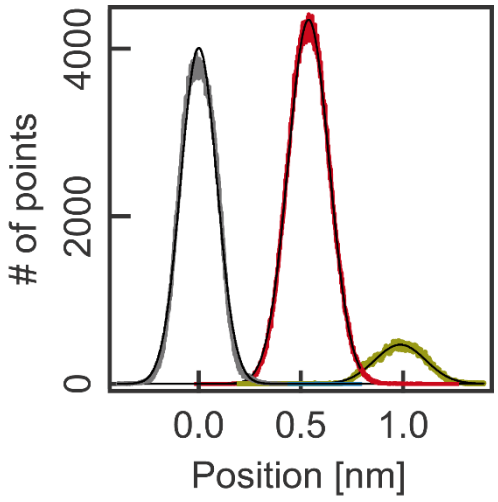

Fig. 3-14 The thickness of each EAN solvation layer measured with force-clamp experiments corresponds to the value obtained from analogous constant velocity measurements. Histogram of the length trace corresponding to the rupture/reformation dynamic equilibrium of confined EAN when pushed at a constant force of 50 pN. The histogram shows three well-defined peaks corresponding to the ruptured and reformed states of the layers #2 and #3 of EAN. Gaussian fits to each of the peaks allows measurement of the peak-to-peak distance, providing a direct estimation of the thickness of each layer: $\Delta l = 5 \pm 0.2$ Å (layer #1) and $\Delta l = 5 \pm 2$ Å (layer #2).

3.5.11 Compilation of all the determined parameters

	1-Undecanol			EAN	
	Layer #1	Layer #2	Layer #3	Layer #1	Layer #2
Δl (FX) [Å]	2.4 ± 1.3	2.5 ± 1	3.5 ± 0.6	4.3 ± 0.4	4.9 ± 0.6
Δl (FC) [Å]	2.9 ± 1	3.5 ± 2	3.3 ± 2	5 ± 2	5 ± 2
Δl (eq. (3)) [Å]		2.6 ± 0.4	2.6 ± 0.2	4.3 ± 0.4	6.2 ± 1.2
$\Delta x_{,rup} + \Delta x_{,ref}$ [Å]		2.7 ± 0.5	3 ± 0.1	5 ± 1.6	
$\Delta x_{,rup}$ [Å]	0.12 ± 0.01	1.9 ± 0.3	2.5 ± 0.05	2.5 ± 0.8	
$\Delta x_{,ref}$ [Å]	0.12 ± 0.07	0.8 ± 0.2	0.5 ± 0.05	2.5 ± 0.8	
N		1.1 ± 0.3	0.9 ± 0.1	2 ± 0.8	
ΔG (eq. (3)) [kT]		70 ± 10	27 ± 2	5.9 ± 0.6	4.5 ± 1
ΔG (eq. (4)) [kT]		68 ± 12	31 ± 2	2.3 ± 2	
ΔE [kT]		69 ± 10	44 ± 0.5	21 ± 0.5	

Table 3-1 Summary of all the results from the experiments aiming at characterizing the solvation properties of 1-undecanol on HOPG and EAN on mica.

4 The nanomechanics of lipid membranes

In this chapter, we investigate mechanical properties of lipid membranes by force spectroscopy. Firstly, we developed a new lipid membrane model system composed of stacked lipid membranes. By using force-extension, we find that stacked lipid membranes are not crucially affected by the substrate, as it happens with the single supported lipid membranes. Then, we investigate the rupture mechanism of lipid membranes by force-clamp. Our experimental results indicate for the first time that the rupture of lipid membranes is not a simple 2-state process, as it is currently thought to be the case. Instead, we propose that the rupture of lipid membrane occurs through the formation of a pore in the lipid membrane structure. Finally, we also report the existence of transient states likely corresponding to sub-structures of the lipid membrane. All in all, these experiments exhibit the complexity of the molecular mechanisms underpinning lipid pore rupture.

4.1 Introduction

Living organisms are constantly subjected to mechanical forces. These forces might stem from external fluctuations or from a variety of processes occurring in vivo — such as cell migration[212] and division[213]. If the resulting deformations lead to the formation of a pore in the cell membrane, the subsequent osmotic shock might lead to fatal damage to the cell. Thus, the pore formation is a determinant factor for cell integrity. Crucially, pore formation is also a key step in many cell processes occurring at the cell membrane. For example, during endo- and exocytosis, the hemi-fusion of two different lipid membranes is controlled by the formation of a pore[20]. Hemi-fusion is also a key step for virus infection of cells[62]. Further examples are the proteins Melittin[214][215] and Lipid-II[216][217], which form a pore in the lipid membrane to perform their physiological activity. Therefore, lipid membrane pore formation is also crucial for normal functioning of living organisms.

Perhaps the most successful approach to investigate the kinetics of lipid pore formation has been electroporation experiments, in which the formation of pores is induced by applying high electric voltages. Electroporation experiments have successfully identified the formation of small pre-pores as the necessary step for large scale lipid membrane rupture[61, p. theory of ele][60][218]. These pre-pores have also been captured in real time, observing their dynamics of expansion and contraction in the presence of a mild bias voltage[219]. In addition, the kink of lipid headgroups has been identified as a determinant step for the formation of critical pores that can lead to major lipid membrane rupture[220]. The dynamics of pore formation, however, are too fast at the high voltages applied to be precisely captured. In addition, such high voltages are not ubiquitous *in vivo*. As a result, the reported pore formation mechanism might be critically influenced by the high electrical fields, as computer simulations suggest[220].

An alternative technique is to bring into contact two giant unilamellar vesicles until they spontaneously merge together. This approach has revealed the detailed mechanism of vesicles hemi-fusion and has identified the shape

of conical lipids as a crucial parameter to explain spontaneous lipid pore formation[20]. Moreover, the application of selective forces at the nanoscale has been identified as crucial for the formation of protein-originated pores[20]. This experimental approach, however, lacks the ability to capture in real time the formation of a pore because it is detected through indirect capacitive or optical microscopic measurements. In addition, these experiments cannot control the crucial nanoscale forces exerted at the lipid membrane junction.

In this sense, force spectroscopy techniques offer a an attractve approach to the investigation of single pore kinetics under a calibrated force. By the use of the AFM in the force-extension mode, many key parameters for lipid membrane integrity have been identified. These encompass pH, temperature, cholesterol content, lipid chemistry, and lipid composition[221][222][135]. These advances notwithstanding, force-extension experiments have two main drawbacks. Firstly, the experimentally measured rupture forces in force-extension mode are difficult to interpret; they depend on several parameters which are still not well understood. Moreover, a 2-state simplistic models is used to interpret the rupture forces[163][164][223][224][225][226]. These models, however, provide no insight in the molecular mechanisms involved in the lipid fore formation, and hence fail to explain why lipid membrane mechanical stability depends so much in their surrounding environment. Secondly, force spectroscopy requires an underlying hard and smooth substrate to support the lipid membrane. The effect of the underlying substrate on the physicochemical properties of lipid membranes, however, remains still unknown. Many attempts have been devoted to obtain free standing membranes, such as pore-spanning[227][228] and polymer-cushioned[229] membranes. Obtaining the lipid intrinsic mechanical properties, however, has not been possible because these new lipid models cannot independently measure the elastic deformation of the membrane and the in-plane lipid-lipid interactions.

We have used here stacks of tens of lipid membranes to investigate the effect of the substrate. Initially developed for x-ray diffraction studies[49], this novel system has only recently been studied by means of optical microscopy[230] and AFM[231][226]. Furthermore, the stacked configuration

is representative of biological assemblies occurring i.e. in the human skin barrier[232], in lamellar bodies[232], or where energy transduction assemblies are present[233][234]. We have combined this novel model system with the use of force spectroscopy in force-clamp mode. Borrowed from the field protein pulling experiments, this technique has allowed to unveil a myriad of details of the kinetics and mechanisms underlying protein folding[235] and unfolding[236][237] not available with simple force-extension mode. In addition, force-clamp has successfully been used to investigate the rupture mechanism in solid-like solvation layers in confined liquids while pushing[187]. Taken together, our approach has successfully identified how the substrate effect influences the rupture mechanics. Furthermore, we have detected the complex kinetics of lipid membrane rupture for the first time and provided a novel conceptual framework to interpret lipid membrane rupture experiments. Finally, we have identified for the first time transient states of rupture likely corresponding to sub-structure of the lipid membrane.

4.2 Preparation of stacked lipid membranes

Stacked lipid membranes were formed following the Tristram-Nagle procedure[238]. In their method, the lipid membranes are directly formed on the substrate instead of deposited from liposome suspensions. Firstly, the lipids (Avanti Polar Lipids, Alabaster, AL) are dissolved in CH3Cl/MeOH (3:1) (>99% purity from Sigma-Aldrich, Saint Louis, MO). Then, a small aliquot (1-10 ul) is spread on top of a freshly cleaved Muscovite Mica substrate (Agar Scientific, Stansted, UK) and quickly dried under a gentle flow of nitrogen gas. Then, the nitrogen flow is maintained at lower pressures for forty minutes to evaporate any remaining organic solvent traces. After evaporation, the dried lipids have already structured into stacked membranes (Fig. 4-1). Our results are also in agreement with previous studies with dry DOPC lipid stacks[239][240].

Working with the lipid stacks in aqueous environment, however, proved to be more challenging. Hydrated stacked membranes have a great tendency to wash away or 'peel off'[241][242], especially with thin (0.1-8 um) lipid stacks. For this reason, lipid stacks are typically investigated in saturated humidity air environments where they cannot float in the aqueous medium[238]. Alternatively, very thick lipid stacks are employed to have a greater stock of stacked lipid membranes[243][230]. These solutions, however, are not well suited to study the effect of the substrate in biological conditions. Hence, we investigated the suitable hydration condition for a strong substrate attachment. We discovered that mild temperatures and longer resting time favour the attachment of lipids to the substrate. In our protocol, the samples are heated at low temperature (<50 C) in buffer solution (200 mM NaCl, HEPES 10 mM, pH=7.4) for at least two hours and then are left to settle overnight. During the experiments, the same buffer was kept without any rinsing to avoid the detachment of the lipid stacks due to turbulences. Even though this method still has a poor success rate (10% typically), it has allowed for the first time to study thin (< 0.1-8 um) liquid state lipid stacks in biological conditions.

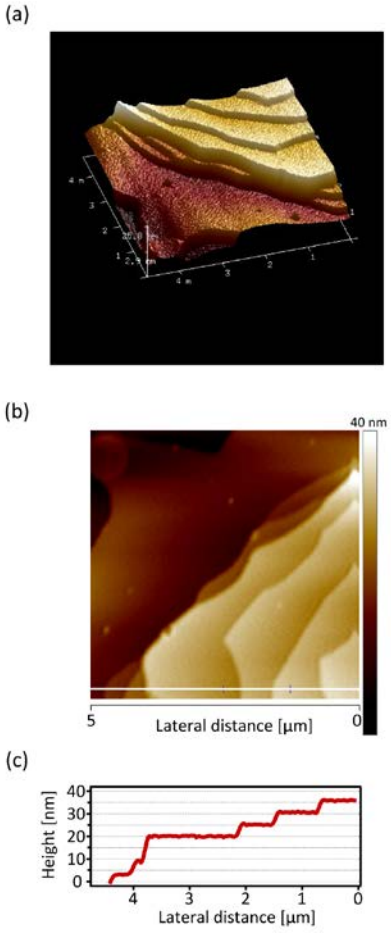

Fig. 4-1 AFM topographic images of a DPhPC lipid stack in dry conditions after deposition from an organic solution. (a) 3D reconstruction of the scanned area and (b) its corresponding 2D false colour map. Each of the plateaus correspond to a stacked lipid membrane (c) A profile of a scan line (white line) is displayed, showing that the height of each lines measures about 5nm, which is in agreement with the thickness of an individual lipid membrane.

4.3 Force-extension of lipid membranes

Stacks of lipid membranes composed of DPhPC (Diphytanoilphosphatidyl choline), DOPC (Dioleoylphosphatidylcholine), and DLPC (Dilaurylphosphatidylcholine) were indented using force-extension. The results for each lipid moiety are displayed, respectively, in Fig. 4-2(a-c). All the force vs. distance traces show a typical sawtooth pattern. Each of the spikes corresponds to the rupture of a single layer in the stack (red trace). When the AFM tip is subsequently retracted (blue trace) no spike is detected because the lipid membranes have already been broken. Force-extension thus permits to capture the thickness and mechanical stability — fingerprinted by the force of rupture — with single membrane resolution, which allows to precisely analyse the properties of the lipid membranes respect to their position in the stack.

4.3.1 The substrate-neighbouring lipid membrane displays critically different properties

The substrate-neighbouring lipid membrane [purple arrows in insets in [Fig. 4-2(a-c)] has very distinct properties than the rest of stacked membranes: the length required to break it is smaller than any of the preceding membranes. We have first quantified the thickness of stacked lipid membranes [red bars in Fig. 4-2(d)], which is in agreement with the literature[49]. The substrate-neighbouring lipid membrane, however, exhibits a significantly reduced thickness [purple bars in Fig. 4-2(d)], suggesting that it is significantly compressed. Indeed, considering that only the DPhPC lipid tails region measures 3.0 nm[244], more than the ca. 2 nm for the whole substrate-neighbouring membrane, the lipids in this layer should be highly tilted and packed to fit in such reduced space. Because only the first layer has a significantly different thickness, our results suggest that the tilting effect is caused by the direct contact to the substrate. Interestingly, supported lipid membranes (which also are in direct contact with the substrate) exhibit similar thicknesses [223], thus supporting our hypothesis.

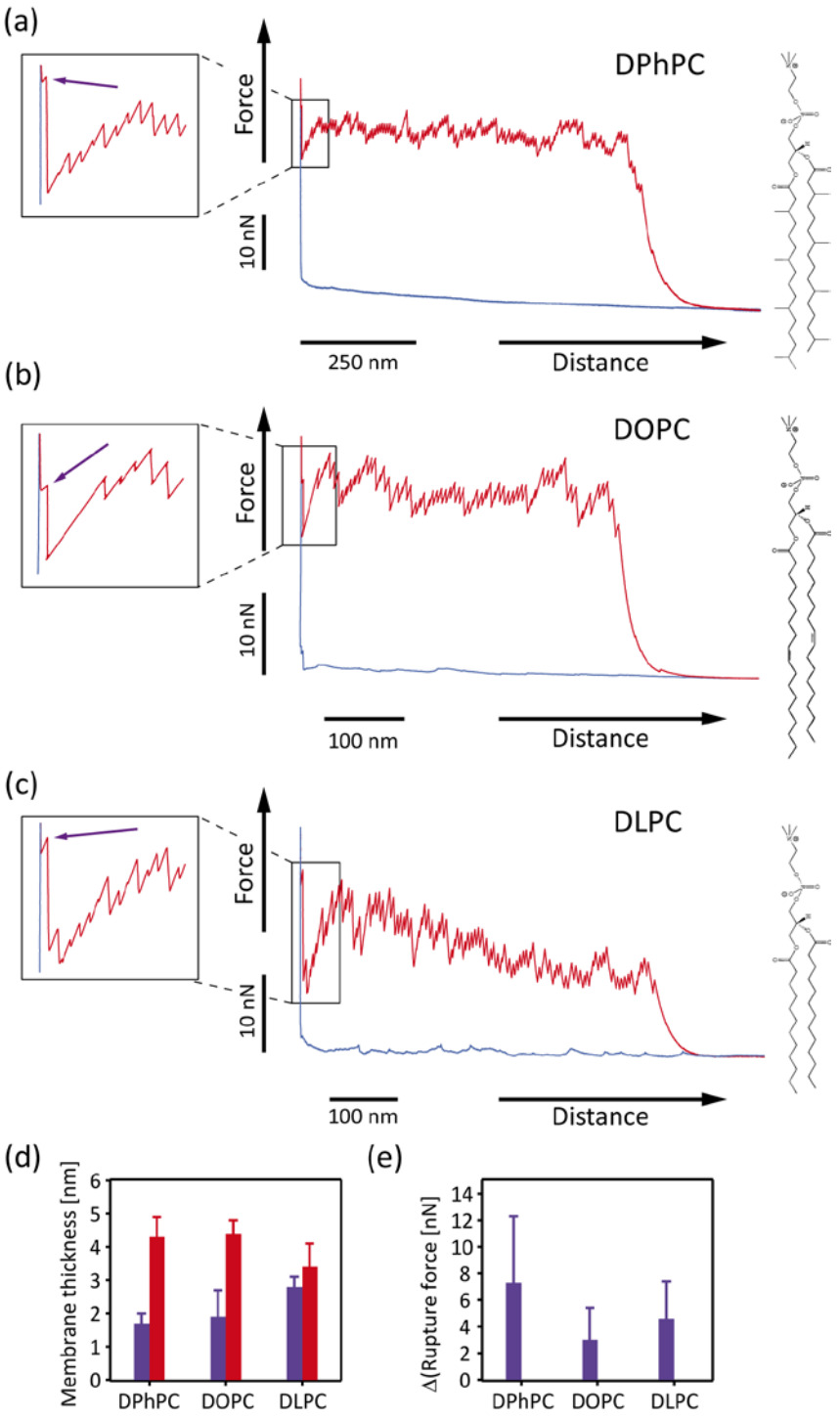

Fig. 4-2 Force-extension indentation traces of (a) DPhPC, (b) DOPC, and (c) DLPC stacked lipid membranes (their molecular structures are drawn on the left, respectively). The extension of the AFM tip (red trace) produces a sawtooth pattern in which each of the peaks corresponds to the rupture of a single lipid membrane. As the AFM tip is retracted (blue trace), no opposition is found by the previously broken lipid membranes. The lipid membrane in direct contact to the substrate (purple arrow in left inset) exhibits distinct mechanical properties. (d) The average thickness of the substrate-neighbouring (purple bars) and stacked membranes (red bars) is compared for each of the three studied lipids. (e) The difference between the rupture force of the substrate-neighbouring and the preceding lipid membranes is computed for all three lipids studied.

The proximity to the substrate also affects the mechanical stability of lipid membranes. The effect has two separate components. On the one hand, lipid membranes became decreasingly stable as the lie closer to the substrate, as will be discussed in the next section. On the other hand, the substrate-neighbouring lipid membrane always displays a significantly higher mechanical stability than its preceding membrane for the three lipids studied here, as shown in Fig. 4-2(e). These results indicate that stronger lipid-lipid interactions are taking place in the substrate-neighbouring layer, which is in agreement with a tilted, tight lipid molecular packing. Therefore, our experimental data indicates that the direct contact to the substrate tilts the configuration and reduces the mobility of lipid molecules, which is in agreement with the literature[245].

4.3.2 Lipid stacks display three mechanically distinct regions

The force required to rupture stacked lipid membranes depend on their relative position to the substrate, as shown in the DPhPC indentation trace displayed in Fig. 4-3(a). When the first membranes close to the top of the stack are indented (green area), the rupture force steadily increases. The rupture force then remains constant for most of the lipid stack (grey area). When the lipid membranes in the vicinity of the substrate are reached (purple area), the mechanical stability decreases with the distance to the substrate until the substrate-neighbouring lipid membrane is reached, which exhibits distinct properties due to the direct contact to the substrate. Therefore, the proximity to any of the edges of the DPhPC lipid stack reduces the observed mechanical stability. We have then proceeded to quantify these interface effects by measuring the rupture forces of 28 indentation traces of different lengths (4220 rupture events in total) for four independent days of experiment. We have separated them in three distinct regions:

AQUEOUS INTERFACE: Fig. 4-3(b) shows the rupture forces for the first membranes indented in the water-lipid interface (green area). By fitting an exponential function, we quantified that the six first layers are at least a 5% less mechanically stable than the average. A similar value has been measured for DOPC and DLPC (see appendix I, chapter 8), with six and nine affected layers, respectively. Hence, the depth of this region is roughly independent of the lipid chemistry for the three lipids studied here.

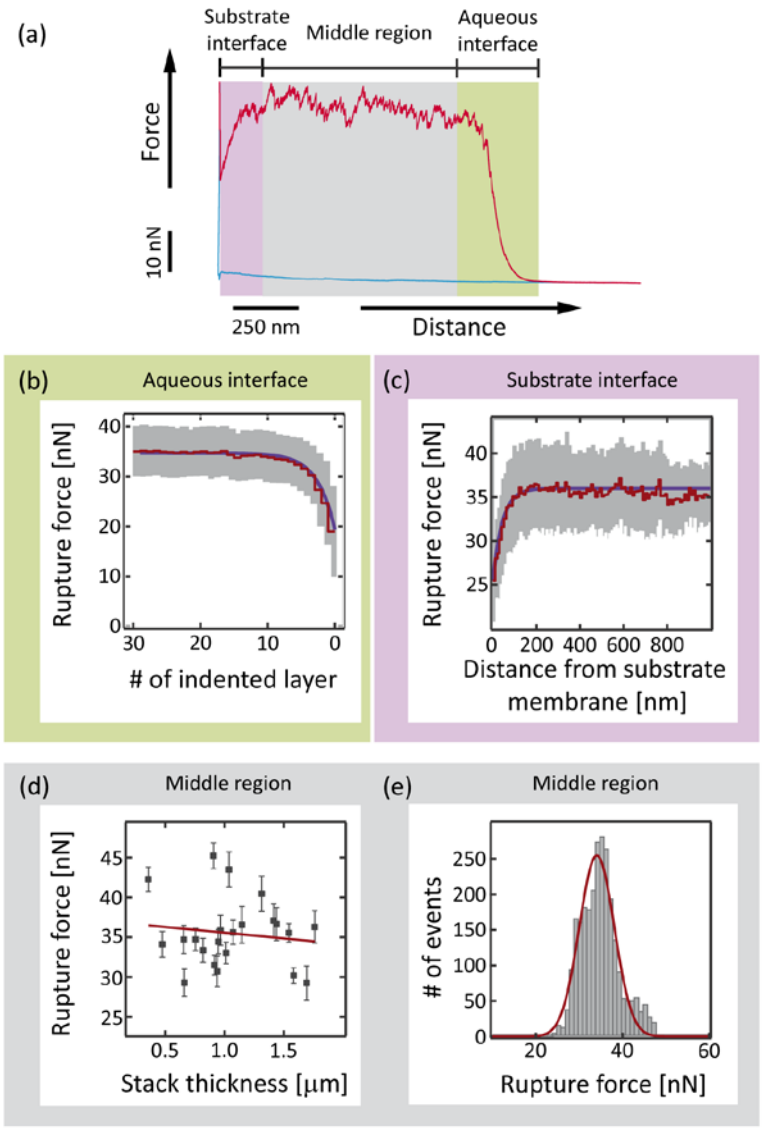

Fig. 4-3 DPhPC stacked lipid membranes display three mechanically distinct regions. (a) Force vs. separation indentation trace of the AFM tip advancing to (red trace), and subsequently retracting from (blue trace), a DPhPC lipid stack. The stacked lipid membranes show a distinct behaviour close to the top of the stack (aqueous interface, green box), to the substrate (substrate interface, purple box), and in-between (middle region, grey box). We have characterized the mechanical properties of each of these regions. (b) The average rupture force (red line) and its standard deviation (surrounding grey area) have been calculated for each indented layer, starting to count from the top of the stack. The increasing rupture force has been fitted (purple line) with an exponential function (τ = 0.38 ± 0.01 layers^{-1}) yielding that 6 layers are significantly different (<5%) than the average (those away from the substrate). (c) The average rupture force (red line) and its standard deviation (surrounding grey area) have been calculated at increasing separations from the substrate (bin size is ten nanometres). An exponential fitting function has been fitted (purple line, τ = 23 ± 1 pm^{-1}). The first ten top rupture events have been excluded from this analysis in order to avoid the effect of the aqueous interface. (d) The average rupture force in the middle region against the stack thickness for each lipid stack indented. (e) Histogram of all the events that are not affected by the proximity to the interfaces.

The increase of mechanical stability in the water-lipid interface might have two possible origins. On the one hand, the measured rupture force might increase due to memory effects: the rupture force depends on the initial applied force (see appendix I for further details). In our case, the small space between consecutive layers (ca. 5 nm) prevents the AFM tip to relax to zero force, which will produce an artificial increase in the measured rupture force even if all the layers have indistinguishable physical properties. On the other hand, we cannot discard that the proximity to the aqueous environment also affects the properties of the membranes. For example, it has been reported that lipid domains interact at long ranges in stacked membranes[230]. Thus, the proximity to the upper interface could have a long range destabilizing effect. Unfortunately, force-extension is incapable of quantitatively assessing the extent of each of the effects. In this sense, force-clamp should be performed at low applied forces for a variety of chemically distinct lipids to identify the exact origin of this effect.

SUBSTRATE INTERFACE: The destabilizing effect of the proximity to the substrate has been analysed following an analogous procedure. The results are shown in Fig. 4-3(c). For DPhPC, the first sixteen layers are significantly more labile (<5%). An almost identical value of fifteen layers has been measured for both DOPC and DLPC (see Fig. 8-1 and Fig. 8-2 in appendix I). The matching results here indicate that the substrate effect might likely have a common origin for the three lipids analysed. We hypothesize that it might be caused by a gradient of ion concentrations in the water layers confined between adjacent lipid membranes close to the substrate. Because water and ions diffuse in-between adjacent stacked membranes when hydrated[241][242], it is likely that the bottom stacked lipid membranes display a cation surplus to counteract the highly negatively charged Mica substrate, as in an electrical double layer. Given that the lipid-ion interactions are crucial for stacked lipid membrane mechanical stability[134][246], as well as attachment[247] and bending modulus[248][249], the postulated ion gradient could generate a variation on the measured mechanical stability. Unlike normal electrical double layers, however, the effect here would not depend on the distance but on the layers of separation because their only possible location is between adjacent lipid membranes. In any case, we still

hold a very limited knowledge on this destabilizing effect and more experiments should be performed to confirm any hypothesis. For instance, we propose that the extent of this effect should diminish with an increasing ionic strength, which is well-known for shielding electrostatic interactions.

MIDDLE REGION: Having identified the extent of the interface effects, we have proceeded to characterize the mechanical properties of the 'unaffected', stacked lipid membranes in the middle region (grey area). Fig. 4-3(d) shows that there is no correlation between the rupture force and the thickness of the stack. Moreover, no dependence has been detected between the rupture force and the distance to the substrate (data not shown). Hence, lipid membranes from different lipid stacks exhibit homologous mechanical properties, provided that they are in the middle region. This has been further confirmed by running a 1 factor ANOVA, which has showed that no significant difference exists between the different days of experiment (α<0.025). Hence, data from different experiments can also be added together to measure the average DPhPC mechanical properties. By calculating the histogram of rupture forces [Fig. 4-3 (e)], the resulting plot produces a bell-shaped distribution, just as expected. By fitting a Gaussian function, the DPhPC average rupture force yields 34 ± 4 nN.

Very similar results were encountered for DOPC. In this case, no dependency to the stack thickness was found (R^2=0.11) or to distance to the substrate. For DOPC, the average rupture force was 25 ± 5 nN. In the case of DLPC, even though there is no effect of lipid stack thickness, there is a clear increase in the measured rupture force as the stack is indented. The rupture force increase, however, it is unlikely to result from an increased intrinsic mechanical stability. Instead, we propose that it stems from the surface tension arising between the AFM tip and all the previously broken lipid membranes. It is still unclear why this effect only appears with DLPC and not in DPhPC and DOPC. It is possible that the instauration in their lipid tails decreases the surface tension with the AFM tip. Because our goal is to use lipid stacks to study the 'substrate-free' rupture kinetics, we have excluded DLPC from further analysis. From the two unsaturated lipids, we have chosen to use DPhPC for its higher deposition yield. Despite being less biologically

appealing than DOPC, we have previously demonstrated that both exhibit analogous mechanical properties.

4.3.3 Stacked lipid membranes break in a vertical hierarchy

A necessary condition for the previous conclusions is that the stacked lipid membranes break in vertical order: first breaking the stacked membrane at the top and the rest following subsequently. Despite being the most intuitive rupture hierarchy, we cannot discard the possibility that the force might transmit without dissipating to underlying membranes, thus allowing those to break before the upper one has. Indeed, this is the case in previously studied cases such as protein unfolding[250], where modules break in a mechanical hierarchy when pulled by the AFM tip. Thus, we decided to confirm the rupture hierarchy before proceeding.

In order to experimentally test the rupture hierarchy, we employed lipid stacks of DOPC/Sphyngomyelin (SM)/Cholesterol (Chol) (1:1:1). This mixture produces two mechanically distinct domains which, when indented, should reveal the rupture hierarchy as will be described later. Moreover, liquid-ordered domains in phase-segregated mixtures have been reported to 'pile up' when stacked in air conditions[230]. The same authors have proposed that the domain stacking is due to the line tension of the interlayer water leaflets occurring at the domain rims. In their model, the domains 'pile up' in separate areas, thus avoiding any interdigitation. Therefore, indenting DOPC/SM/Chol lipid stacks represents an attractive system to investigate both the rupture hierarchy and the interaction between neighbouring stacked lipid domains.

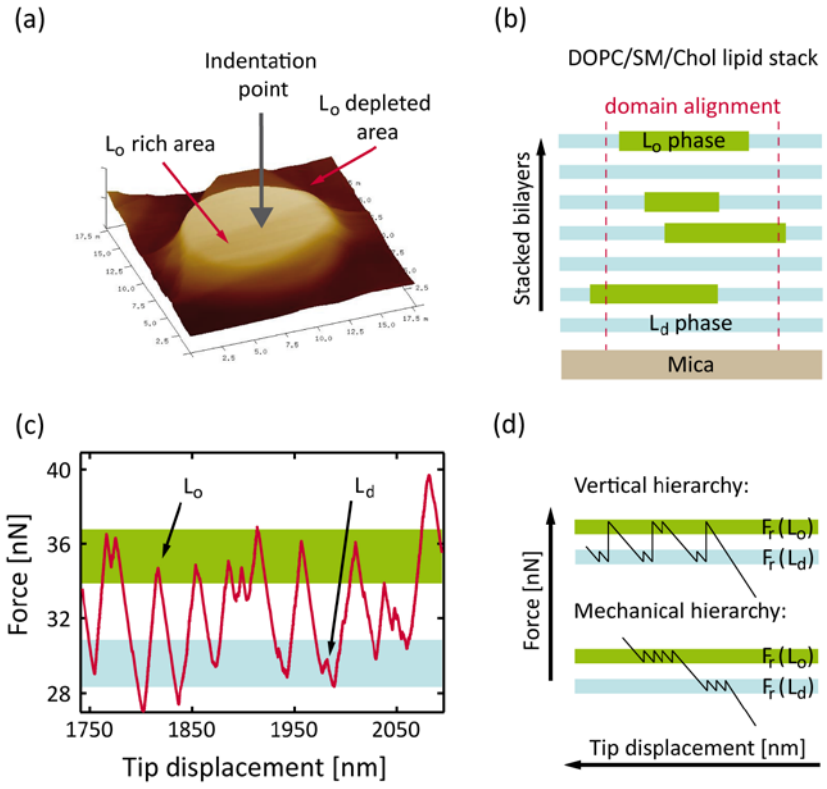

Fig. 4-4 DOPC/Sphingomyelin/Cholesterol (1:1:1) mixtures produces phase-segregated lipid stacks. (a) Dynamic mode AFM topographical image of the surface of a lipid stack in aqueous medium. (b) Given its large dimensions, the circular feature is proposed to originate in the partial stacking of liquid-ordered domains (green rectangles) intercalated with liquid-disordered phase layers (light blue rectangles). (c) By indenting at the middle of the circular feature, we obtain a force vs distance profile with alternating high and low mechanical stability layers corresponding to the indentation of the liquid-ordered and liquid-disordered layers (dark arrows), respectively. (d) Schematic diagram of the expected force-extension profile if the rupture follows a vertical hierarchy (top) or mechanical hierarchy (bottom).

By using our deposition method, we achieved for the first time to obtain stable lipid stacks of DOPC/SM/Chol lipid membrane in physiological conditions. Fig. 4-4(a) shows a non-contact AFM image of the DOPC/SM/Chol lipid stack surface, demonstrating that the 'piling up' effect also occur in aqueous conditions. The large dimensions of the circular object in the image (ca. 30 μm x 20 nm) indicates that it cannot correspond to a single membrane domain (typically 1-5 μm x 5-6 nm[251]). Instead, we propose that the larger domain dimensions correspond to the convolution of many smaller domains which are slightly misaligned in the horizontal dimensions, as shown in Fig. 4-4(b). As a consequence, both the ordered and disordered phases would

interdigitate, which contradicts the current model for domain piling. To confirm this hypothesis, we indented the piled-up domain in its central point. The indentation trace [Fig. 4-4(c)] shows two distinct rupture force trends. The liquid-ordered (high force, green area and liquid-disordered (low force, blue area) have been assigned in agreement with previous force spectroscopy studies[252]. Thus, our experimental data demonstrates that both phases interdigitate. Moreover, if the membranes broke in a mechanical hierarchy, the labile liquid-disordered phases (low force) should all break before any liquid-ordered domain (high force) was to be penetrated, as shown in the schematic in Fig. 4-4(d). Instead, we observe alternating rupture events which demonstrate the vertical hierarchy of stacked lipid membranes. The same result has also been replicated in our laboratory using force-clamp, where the time-window of experimentation is highly expanded (data not shown).

As a conclusion, the indentation of DOPC/SM/Chol lipid stacks demonstrates that stacked lipid membranes rupture in a vertical hierarchy, just as intuitively expected. Consequently, the applied force must quickly dissipate when it transmits to the underlying membranes. In addition, we have investigated for the first time the structure of phase segregated lipid stacks and the domain 'piling up' properties in physiological conditions. The observed interdigitation of domains clearly contradicts the current model. To construct a new model, however, the autocorrelation for domains of the same phase should be calculated. As well, the size and distribution of 'piled up' domains should be investigated for different proportions of DOPC/Chol and lipid stack thicknesses to understand better the origin of the piling effect.

4.4 Force-clamp of stacked lipid membranes

We performed force-clamp on DPhPC stacked lipid membranes in order to study the detailed kinetics of lipid membrane rupture. In this force spectroscopy mode, the AFM tip penetrates through the lipid stacks while applying a constant force. Fig. 4-5 displays a typical force-clamp trace (red trace in top graph). When the downwards path of the AFM tip is observed closely (inset in top graph), the irregular trajectory becomes a succession of single discrete steps. These transitions are also observed in the force channel (dark trace in bottom graph) as spike due to the non-instantaneous response of the feedback system driving the AFM tip.

Each discrete step corresponds to the rupture of a single stacked lipid membrane. Their thickness measure an average of 5.4 ± 0.2 nm, which is in agreement with previous force-extension results. Also, the time-to-rupture, or

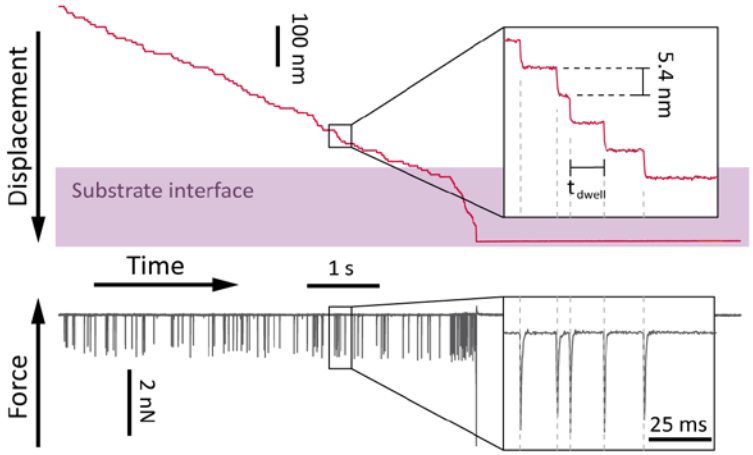

Fig. 4-5 Indentation profile acquired in force-clamp on a stack of DPhPC lipid membranes. The irregular profile followed by the AFM tip (red trace in upper graph) is composed by discrete steps. (Inset) Each step measures 5.4 ± 0.2 nm on average (# of events = 555) and occurs concurrently with the appearance of an spike in the force channel (dark trace in lower graph). The separation between consecutive steps is called the dwell time, or rupture time, and it is the fingerprint of the mehcnaical stability in force-clamp. The last indented region (purple box), closer to the underlying substrate, displays a higher rupture rate, which is in agreement with the destabilizing substrate effect.

dwell time, hallmarks the mechanical stability of the lipid membrane. In the middle region, the lipid membranes break at a constant rate because they are mechanically indistinguishable, as measured with force-extension. At the bottom of the trace, instead, the AFM tip advances at an increasing velocity due to the destabilizing effect of the lipid-substrate interface. The water-lipid interface, however, is not observed here because there is a small lag time before the indentation is recorded by the computer in our experiments. Therefore, force-clamp successfully reproduces the substrate features encountered in force-extension. Force-clamp, however, offers an expanded time window of experimentation which we will utilize to measure the detailed kinetics of rupture (see further details in chapter 2). In the next sections, all the analyses have been performed after discarding the sections affected by the substrate interface.

4.4.1 The rupture of stacked lipid membranes is a step-by-step memoryless process

If the rupture of adjacent lipid membranes is a step-by-step process, the total time required to indent a whole lipid stack will depend on its thickness. As a consequence, the resulting force-clamp traces cannot be averaged — as it is customary — despite having the same rupture rate, as shown in Fig. 4-6(a). Instead, we developed the software tools to pool the individual dwell times altogether. In order to test the correctness of the analysis, first we needed to demonstrate that the measured dwell times are independent of the indentation trace of origin and of preceding rupture events. To check both conditions, the dwell times were measured for 152 different traces performed at the same applied force. Then, their penetration trajectory was reconstructed from the measured dwell times, as shown in Fig. 4-6(b). To test the first hypothesis, the rupture rate was measured by fitting a linear function to its reconstructed indentation trajectory. Fig. 4-6(c) demonstrates that the rupture rate is independent of the thickness of the lipid stack ($R^2 = 0.0016$). To test the second hypothesis, the autocorrelation function was calculated for the rupture events in each indentation trace. As shown in Fig. 4-6(d), no significant correlation exists between successive rupture events. As a result, all the rupture events can be correctly pooled together. Moreover, these results

demonstrate that stacked lipid membranes behave like a chain of discrete memoryless stochastic events — as in a Poisson process.

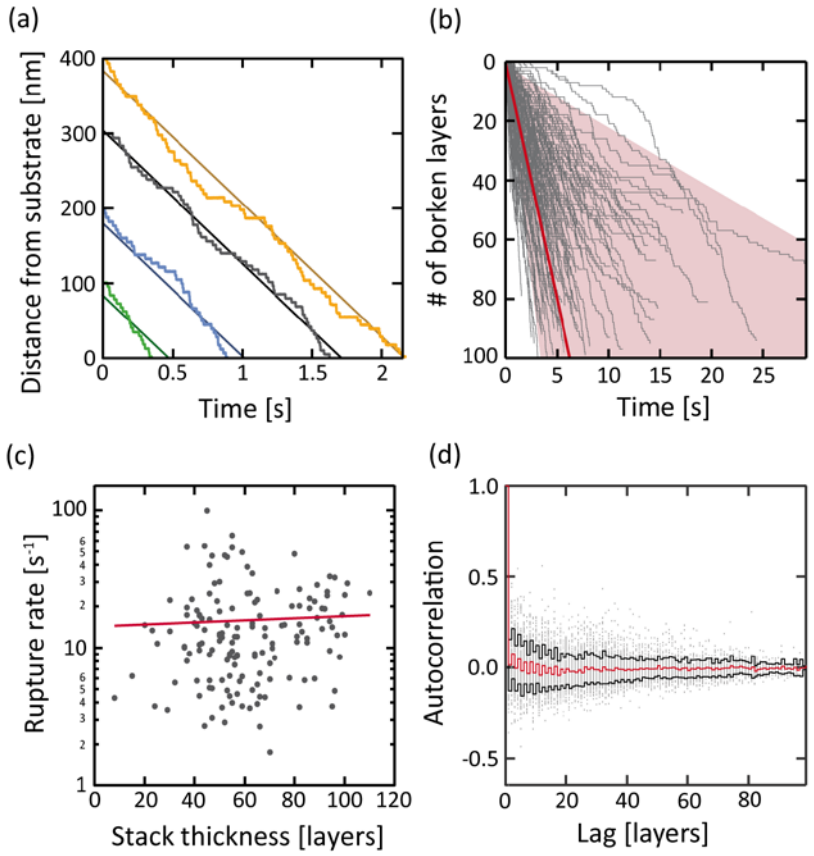

Fig. 4-6 The time course of a force-clamp indentation trace depends on the number of stacked lipid membranes. (a) Length vs. time indentation profiles of four different stack sections containing a decreasing number of layers (irregular coloured lines). A linear function has been fitted to each of them (straight coloured lines) to capture the rupture rate. (b) The rupture times of the middle region have been measured for a total of 152 traces and their time course has been reconstructed (grey thin lines). As previously, a linear function has been fitted to each individual time course and the average rupture rate calculated (solid dark red line. The light red area corresponds to one standard deviation from the mean). (c) The average rupture rate has been plotted against the stack thickness. The fitted trend line returns that no correlation exists between both variables (R^2=0.0016). (d) Autocorrelation function of the rupture times that are separate a number of layers (lag).

4.4.2 The rupture of lipid membranes happens through a common transition state

Once established the analysis method, we proceeded to analyse the effect of the applied force on the rupture kinetics. Fig. 4-7(a) displays three force-clamp indentation traces performed at increasing pushing forces. As the force is increased, the lipid membranes break quicker. We have quantified the force dependency by measuring the average rupture rate α – calculated as the inverse of the rupture times. Fig. 4-7(b) displays the $\ln(\alpha)$ against the applied force in stacked lipid membranes (red dots), showing that the rupture rate increases exponentially with the force. The exponential force dependency thus demonstrates that the rupture of lipid membranes is a force-activated barrier-crossing process.

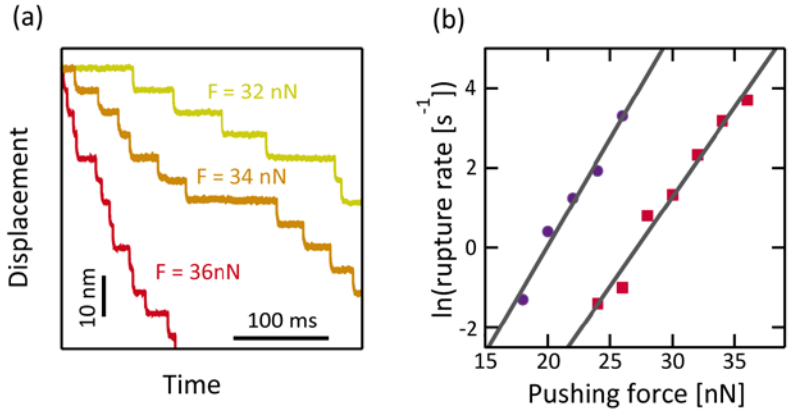

Fig. 4-7 (a) When a lipid membrane stack is indented (32 nN) it produces a typical staircase profile (yellow trace). When higher forces are applied, the time to rupture the lipid membranes is highly reduced (orange and red trace correspond to 34 and 36 nN, respectively). (b) By taking the inverse of the averages, the rupture rate has been calculated at several pushing forces (red dots). By fitting the Bell model, we obtain an exponential term $\Delta x/N = 1.87 \pm 0.04$ pm and $\ln(\alpha_0) = 12.2 \pm 0.9$. The same experiments were performed on single supported lipid membranes (purple dots). The fitting of the Bell model yields $\Delta x/N = 2.2 \pm 0.2$ pm and $\ln(\alpha_0) = 11 \pm 1$.

By using the Bell model described in chapter 2, the experimental data has been fitted using the following expression:

$$\alpha(F) \equiv \alpha(0) \exp\left(\frac{\Delta x}{N \cdot k_B T} F \right) \tag{4.1}$$

where $\alpha(0)$ is the rate in absence of force, Δx the distance to the energy barrier, and N the number of disrupted interactions. Fitting eq. (4.1) to the experimental data yields the exponential term $\Delta x / N$ = 1.87 ± 0.04 pm.

The measured exponential term has no direct physical meaning as long as $N \neq 1$. In this case, the lack of a rupture-reformation equilibrium, as with confined liquids (chapter 3), prevents us from directly measuring the number of disrupted interactions. An alternative is to estimate N by using mechanical contact models. Redondo-Morata and co-workers[224] used a simple indentation model to calculate the contact area, obtaining N = 58. This estimate, however, might be significantly biased because the indentation depth fitted was in the same range as the AFM resolution (< 1 nm, see chapter 2 for more details). Moreover, they discarded from the fitting the initial stages of deformation, which are crucial to discern between different contact models.

We thus decided to re-evaluate this estimate by fitting their model to the indentation traces of our lipid stacks, which offer an elastic deformation region orders of magnitude larger than that of single supported membranes. Their indentation model did not fit successfully our experimental data (data not shown). We also tried other indentation models such as Hertz (normal[253] and size-limited[254]), JKR[255], and DMT[255] with the same unsuccessful results. The lack of fitting might be originated in the limited and layered nature of lipid stacks, which none of these models account for. In a more general sense, the contact mechanics at the nanoscale are still poorly understood and might range from single atoms contacts — as with confined liquids — to much larger areas — as with whole live cells (chapter 5). Since we cannot know beforehand the threshold between both regimes, we have avoided using contact models to estimate the number of disrupted interactions, and hence we will evaluate the pair $\Delta x / N$ directly.

In order to compare our results to those of substrate-affected lipid membranes, we performed the same rupture experiments on deposited single lipid membranes [purple circles in Fig. 4-7(b), see appendix I (chapter 8) for the preparation method]. The resulting rate in the absence of force α_0 is significantly higher than that of stacked lipid membranes. By assuming that the attempt frequency is similar for both lipid membrane configurations, our results show that the rupture of single lipid membranes goes through a smaller energy barrier, which is in agreement with the previously reported effect of the substrate. Conversely, the value of $\Delta x / N$ = 2.2 ± 0.2 pm is almost identical for both lipid membrane configurations. Indeed, very similar $\Delta x / N$ parameters have been obtained in a variety of phophatidylcholine lipid membranes[224][226][231]. Assuming that the number of disrupted interactions is similar for all cases (the AFM tips used have the identical geometries), all these chemically distinct lipid membranes should then go through a common transition state, even if they are highly deformed by the underlying substrate.

Interpreting the origin of the common transition state is difficult for our case: the lipid membrane rupture must involve the creation of a pore that allows the AFM tip to break through, which likely involves the displacement of a vast quantity of molecules. Indeed, electroporation studies suggests that metastable pre-pores can exists up to 10 nm of radius[219], which corresponds to hundreds of lipid molecules. Hence, we identify two possible processes that might be the rate determining step of the rupture kinetics: the rupture of lipid-lipid bonds and the creation of a pore with a critical radius — like in a nucleation process. These two processes happen in entirely different time and length scales and draw a completely different picture of lipid membrane rupture. Hence, it is impossible to understand the nature of the common transition state without having a precise knowledge of the order of magnitude of Δx. Consequently, we find too uncertain to directly interpret force dependency results — the $\Delta x / N$ — without precisely measuring the number of disrupted interactions or a clearer theoretical framework.

4.4.3 The lipid membrane rupture times follow a lognormal distribution

In order to better understand the kinetics of lipid membrane rupture, we have analysed the time distribution of rupture events. Fig. 4-8(a) shows the histograms of rupture times for two different applied forces. Both distributions display a right-skewed unimodal distribution. This shape is far from the exponential distribution that the Bell model predicts. The lack of short rupture times, however, occurs in a time scale much larger than our PID feedback — up to two orders of magnitude — and thus cannot be attributed to an instrumental artefact. In addition, the unimodal distribution varies its shape and position with the applied force and it is also encountered in single lipid membranes (data not shown). Taken together, these findings demonstrate that the observed non-exponential distribution is an intrinsic property of the lipid membrane rupture kinetics.

We repeated the force-clamp experiments with a much larger number of rupture events to investigate the precise shape of the rupture time distribution. By recording a total of 9125 rupture events at a single applied force, we now realized that the distribution of rupture events expanded over several decades, encompassing events happening from a few milliseconds to the tens of seconds. In order to display the wide scattering of rupture times, we plotted the distribution of events, or probability density function (PDF), in terms of $ln(t)$. As shown in Fig. 4-8(b), the logarithmic PDF follows a normal distribution. Hence, the direct PDF follows a lognormal distribution.

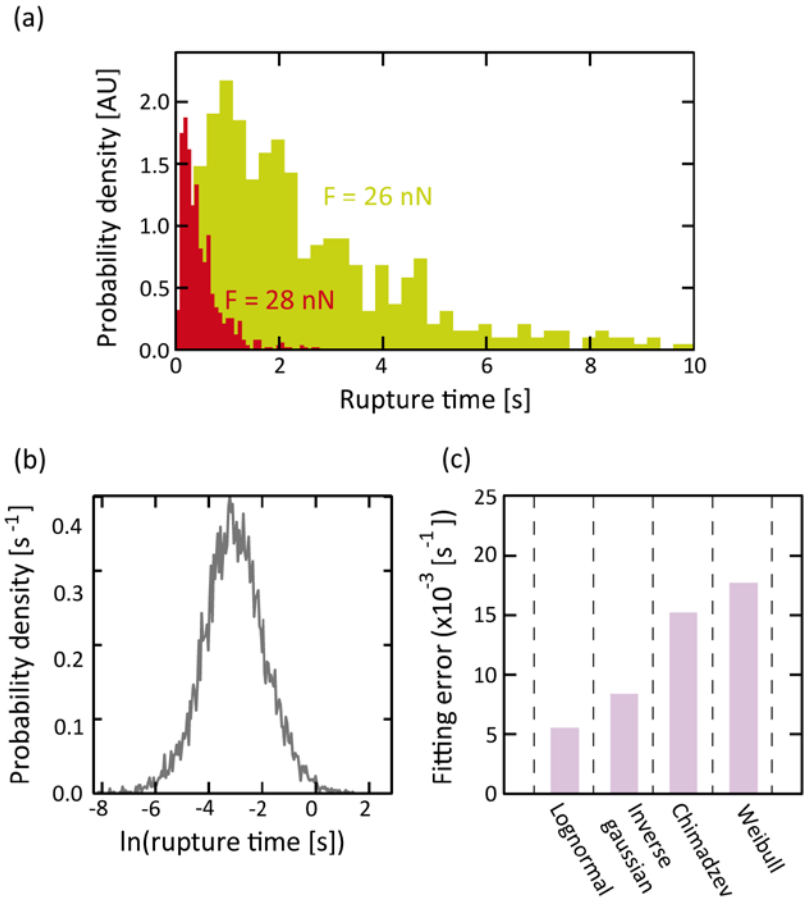

Fig. 4-8 The lipid membranes produces a complex distribution of rupture events. (a) Rupture time distribution of DPhPC stacked lipid membranes at a low (26 nN, green bars) and high forces (28 nN, red bars). The probability density has been re-scaled for visualization purposes (b) The indentation experiment has been measured with greater precision (N = 9125) at 32 nN. The graph displays the probability density function against the logarithm of the rupture time. (c) Four models have been fitted to the probability density function. The fitting error is displayed for each of the models considered.

This type of distribution has also been observed in the unfolding of proteins[256], which was later interpreted in terms of static disorder theory[257]. In the case of protein unfolding, however, the lognormal distribution showed a time-decreasing hazard rate — the probability of unfolding decreases with time. Conversely, lipid membranes display a time-increasing hazard rate, which is an important property because, as a consequence, our PDF cannot be explained either by static disorder theory or 2-state Kramers models as other previous cases. In short, these two models must result in a weighted sum of several exponentials, which cannot produce

a unimodal distribution typical of increasing hazard rate functions. Therefore, lipid membranes are the first example of non-Kramers rupture kinetics at the nanometre realm to our knowledge.

We assessed that the shape of the rupture time distribution follows a lognormal function by comparing its goodness of fit with alternative models available in the literature. We investigated among the reported models in patient survival analysis, material failure analysis, lipid membrane electroporation, and force spectroscopy. Among all the models, we selected those that could predict a time-increasing hazard rate. We then investigated the underlying rupture mechanism that leads to the given distribution, including the lognormal distribution. Finally, we discarded those distributions without a realistic underlying rupture mechanism (i.e. the Gamma distribution[258]) and those with an unrealistic one (i.e. Cox's multi-hazard approach[259]). A brief description of the four remaining models is provided below:

LOGNORMAL MODEL. Lognormal distributions are characteristic of multiplicative growth processes, such as bacterial growth, fatigue fracture, future stock market returns, computer file sizes or wealth distribution[260][261]. In these processes, the current instantaneous growth is proportional to the current size of the system. By following a simple argument, the size distribution at each moment can be deduced to follow a lognormal function. Despite the ubiquity of multiplicative growth processes, lognormal fracture models are seldom. To our knowledge, this is restricted to the efforts of Birnbaum and Saunders to construct a model to predict fatigue fracture[262][263]. The variables in their model, however, are empirical in nature and provide little information of the underlying molecular processes, thus yielding it unpractical. Nonetheless, the appearance of lognormal distributions is tightly bound to an underlying multiplicative process. In our case, it can be interpreted as the multiplicative rupture of inter-lipid bonds that, when reaching a certain critical number, will lead to the lipid membrane rupture. Its PDF in the logarithmic space, $y = \ln(t)$, is the Normal distribution:

$$F(y) = \frac{1}{\sqrt{2\pi\sigma^2}} \exp\left(\frac{-(x-\mu)^2}{2\sigma^2} \right) \quad (4.2)$$

where σ and μ are the standard deviation and the mean, respectively.

INVERSE GAUSSIAN MODEL. The Inverse Gaussian (IG) distribution defines the first passage time probability of a particle undergoing Brownian motion through a distant threshold[264]. Even though this distribution was initially employed without little mechanistic considerations in a variety of cases such the emptying of a dam[265], the inter-purchasing times[266], and the duration of strikes[267], it has recently been reconsidered in medical research for its 'process point of view' mechanism[268]: instead of an 'all-or-none' process, death is considered the consequence of a deterioration process. In our case, this model considers that a critical number of inter-lipid interactions will rupture and reform stochastically. When a certain threshold is reached, then the rupture will occur, similarly to the lognormal model. Its PDF in the logarithmic space is:

$$f(y) = \sqrt{\frac{\lambda}{2\pi}} \exp\left(\frac{-\lambda}{2\mu^2} \frac{\left(\exp(y) - \mu\right)^2}{exp(y)} - \frac{1}{2} y \right) \quad (4.3)$$

where λ is the scale parameter and μ the mean.

CHIMADZEV MODEL. Chimadzev and co-workers proposed in a series of papers that the rupture of lipid membrane occurs through a series of equilibrium steps[269][270][271][272][273][274][275]. In their model, first a 'hydrophobic' pre-pore is generated. Then, the pre-pore expands in a series of steps until becoming a stable 'hydrophilic' pore, which irreversibly expands forming large scale rupture of the lipid membrane. This model is a more complex and detailed version of a multiple step reaction. Also, it is similar to the lognormal one, with the exception that the pre-critical steps happen in a step-by-step (non-multiplicative) fashion. Its logarithmic PDF is:

$$f(y) = \frac{u}{\tau} \exp\left(y + \frac{k(\tau - 1)}{2} \exp(y) \right) \cdot \left[1 - \exp\left(-\tau k \exp(y) \right) \right] \quad (4.4)$$

where u, τ, and k are three aggregated time constants of the reaction chain.

WEIBULL MODEL. The Weibull distribution is one of the most widely applied distributions, mostly due to its mathematical flexibility[276]. This model states that a material is as strong as the weakest of its parts. Hence, the life expectancy of a material will depend only on the stability of its weakest links. By assuming that the weakest links break in an 'all-or-none' fashion the model results in a composition of exponentially decaying functions. A very similar model has been employed to predict protein unfolding[257]. Thus, if the process is governed by a 2-state rupture of one of its parts, the rupture time distribution should adapt to the following PDF:

$$f(y) = \frac{\lambda}{\alpha^{\lambda}} \exp\left(\lambda y - \frac{\exp(\lambda y)}{\alpha^{\lambda}} \right) \tag{4.5}$$

where λ and α are the scale and shape parameters, respectively.

Fig. 4-8(c) displays the Chi-Square scores for the four models. Even though Bayesian inference would provide a more precise answer, Chi-square comparison clearly shows that Chimadzev and Weibull models fits significantly worse than the lognormal and Inverse Gaussian models. An analysis of residuals shows that the former pair of models underestimate the probability of long rupture times. Thus, Chimadzev and Weibull models can be discarded. Discarding Weibull model strongly suggests that lipid membrane do not break as an 'all-or-none' fashion, which is in contradiction with the currently 2-state accepted view in our field. Interestingly, it is not either a finite sequence of reaction steps like Chimadzev model describes and as the electroporation field holds. Instead, the lognormal distribution is indicative of multiplicative rupture of inter-lipid bonds. Moreover, the better fitting of both IG and lognormal models suggests that a large number of interactions are involved in the rupture of lipid membranes. In any case, both models are far from Kramers models used to interpret a wide variety of force spectroscopy experiments, which yields the kinetics of lipid membrane rupture a unique case of study.

4.4.4 The rupture of the lipid membrane fits a pore growth model

We hypothesize that the lognormal (or IG) distribution of rupture events is caused by a pore growth mechanism. Our mechanism is shown in Fig. 4-9(a): when a defect in the lipid membrane structure is created, expansion through the adjacent molecules will be more energetically favourable because the boundary lipids have less neighbours to bond to. As more defects are created, the number of boundary lipids will increase proportionally to the effective perimeter of the pre-pore, thus generating a multiplicative growth process. When a critical pore size is reached, the pore will become stable — as electroporation experiments suggest[61] — and the lipid membrane will rupture.

Finding a mathematical expression for this problem requires solving the first passage time distribution of a branching Markov Chain. In principle, this problem is similar to solving a simple Markov Chain. Doing this transformation, however, requires a deep mathematical knowledge that we lack. In addition, there is no reported solution available in the literature to our knowledge. Therefore, we currently lack the tools to directly find a closed-form expression for our proposed model. Instead, we have developed two alternative mathematical methods to test that our model reproduces a lognormal distribution.

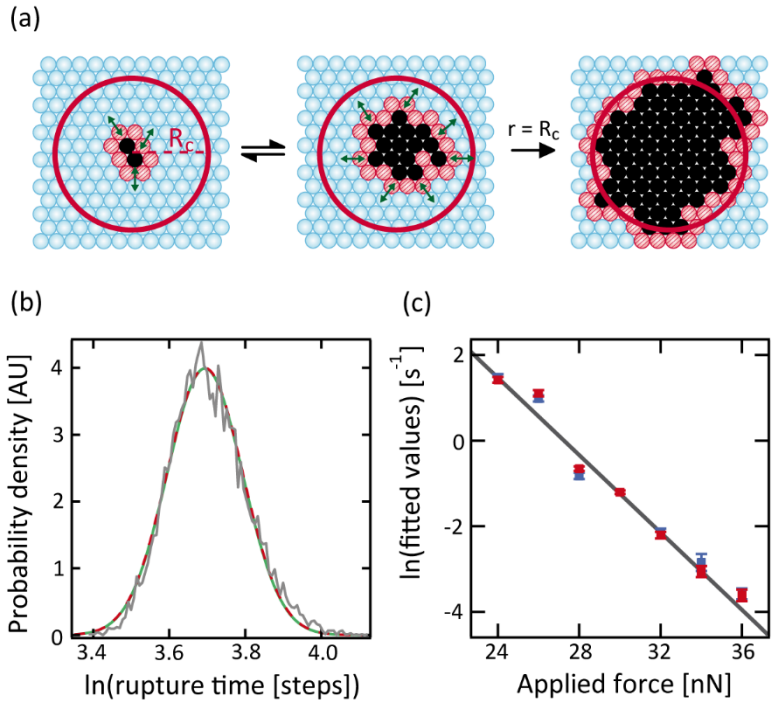

Fig. 4-9 (a) Schematic representation of the proposed model of rupture. The lipid membrane is composed of a densely packed 2D lipid-ion network (blue circles). When a vacancy is spontaneously generated (black circles), the hole will either expand, or reduce, (green arrows) through the boundary molecules (red circles). The number of boundary lipids will thus linearly depend on the number of broken lipid-ion interactions. When the effective radius r of the hole reaches the critical radius of poration R_c (thick red circular line), the hole will become a stable pore, which will produce the lipid membrane rupture. (b) Monte Carlo simulation of the previous model. The model assumed that the number of boundary molecules equals the current number of broken molecules. An arbitrary threshold of 100 broken interactions has been set as the effective critical radius. The simulation has been run for 10^5 iterations. The graph displays the resulting probability density function against the logarithm of the number of steps required to reach the threshold (the rupture time). A lognormal (green line) and Inverse Gaussian (discontinuous red line) functions have been fitted to the simulated PDF. (c) An Inverse Gaussian function has been fitted to the experimental DPhPC lipid membrane distributions of rupture times. The logarithm of the scale parameter λ (blue dots) and the mean μ (red dots) have been plotted for several applied forces. A linear function has been fitted to μ (dark line) yielding $\Delta x/N$ = 1.86 ± 0.1 pm and $\ln(\alpha_0)$ = 12.3 ± 0.2

We firstly tested the resulting rupture time distribution of our model by performing a stochastic simulation, following a procedure similar to the one Söderlund and co-workers[277] used to model nanoparticle nucleation. In this model, all the boundary sites have a probability to be broken at each computation step. We assumed that at $t = 0$ the lipid membrane exhibited no defects. As a defect is created, we assumed that two new sites become readily cleavable. This assumption is in agreement with the reported hexagonal packing of solid phase lipid membranes, even though it also applies for many other two-dimensional packing geometries. The resulting average probability density function is shown in Fig. 4-9(b). The logarithmic PDF clearly follows a Gaussian shape. Interestingly, both lognormal and IG models fit well the PDF. The mutual goodness of fit suggests that both distributions might model the same type of multiplicative process.

Secondly, we have developed a simple 'continuous' analytical model to fit the experimental data. In this case, we assume that the pre-pore will have an effective radius *r*. Along the perimeter of the pre-pore, a number of lipid 'active sites' will be available for cleavage. The total number of sites will depend on the current pre-pore perimeter, and thus the total growth will increase with the current pore radius in a multiplicative fashion. This can be expressed mathematically as:

$$\frac{dr}{dt} = 2\pi r \delta \nu \tag{4.6}$$

where δ is the density of cleavage sites per unit length and ν the pore growth rate. Since the cleavage sites in our model corresponds to the defect creation in the lipid-ion network, δ can be well approximated as the inverse of the lipid-lipid separation.

The rate of pore growth corresponds to the constant cleavage and reformation of lipid-lipid bonds. This constant process — happening at rates much faster than our time resolution — will produce a stochastic fluctuation of the pore perimeter. This fluctuation, however, will have a bias towards cleavage because of the applied force. Therefore, the rate of pore growth will correspond, as a first approximation, to a Brownian motion with positive drift. Thus, the pore growth will be described by the following expression:

$$\frac{dr}{dt} = 2\pi r\left(\alpha + \sigma B(t)\right) \tag{4.7}$$

where α is the force-dependant (thermally activated) net rate of bond cleavage [as in eq.(4.1)], $B(t)$ a Brownian motion term, and σ its standard deviation.

This equation is equivalent to a geometric Brownian motion. In order to solve this equation, we followed Black-Scholes procedure[278]. First, we converted the geometric into normal Brownian motion by making the variable change $X = \ln(r)$. As we commented above, the first passage time of Brownian motion over a threshold is described by the Inverse Gaussian distribution depicted in eq. (4.3). In this case, however, the previously unknown parameters are defined by:

$$\begin{cases} \mu = \dfrac{X_C}{2\pi\alpha} \\ \lambda = \dfrac{X_C^2}{4\pi^2\sigma^2} \end{cases}$$

where $X_C = \ln\left(R_C / R_0\right)$ is the ratio between the critical pore radius R_C and the pre-pore initial size R_0.

We have fitted the rupture time distributions at different applied forces to our model. The results are shown in Fig. 4-9(c). As expected, the term μ depends exponentially on the force. By fitting a linear function to the data (in logarithmic time scale), the exponential term yields 1.86 ± 0.1 pm. The current parameter exactly matches with the previously obtained $\Delta x / N$ because the mean of the Inverse Gaussian happens to equal e^{μ}. Our model, however, provides an extra piece of information: the rate of bond cleavage α, from which μ depends, corresponds to the cleavage of lipid-lipid interactions. Therefore, the distance to the transition state for a bond cleavage reaction can be approximated to half of the inter-lipid separation. By using the value of 5 Å for the lipid radius obtained from X-ray diffraction studies of DPhPC lipid stacks[279], the total number of disrupted molecules yields $N = 268$. The equivalent affected radius is 8 nm, which is in close agreement with the radius of the AFM tip and of the largest pre-pores observed in electroporation

experiments. It also is an order of magnitude bigger than the values estimated by mechanical contact models.

Beyond the accuracy in the estimation of N, the prediction that Δx corresponds to the lipid-lipid separation has an important implication: all lipids should display a similar transition state because most lipids have a similar lipid-lipid separations. Indeed, our prediction is in agreement with the literature[224][226][231] and with our previously reported common transition state. Despite the predicted similarity in the force dependency, however, different lipids might still exhibit different kinetics of lipid membrane pore formation, which depend on the critical pore radius R_C obtained from the rupture time distributions. Therefore, our results split the study of the lipid membrane rupture kinetics in two separate levels: the rupture and reformation of bonds — accessible through the force dependency plots — and the formation of a critical pore — described by the rupture time distribution. This new framework, if confirmed, would allow to gain an unprecedented insight in the mechanics of lipid membrane rupture. Most importantly, our results highlight the importance of analysing the rupture time distributions instead of the force dependency plots, as it is currently believed.

Validating these predictions, however, requires constructing a more robust model. Even though our model explains the variation of the fitting parameter μ, it fails to explain the force dependency of the parameter λ. This is likely because we have used an arbitrary constant σ to define variance in the stochastic lipid bond rupture/reformation equilibrium. Therefore, a better mathematical description might complete our model. In the future, we aim to directly solve the branching Markov Chain first passage time distribution, which would be the equivalent of analytically solving the stochastic simulation shown in Fig. 4-9(b).

4.4.5 Force-clamp captures the lipid membrane sub-structure

Until now, lipid membranes were indented at relatively high forces, which allow us to measure their rupture kinetics at lab-time affordable rates. If the pushing force is further decreased, however, the rupture of lipid membranes is no longer observed as a single transition. Instead, it splits into several smaller steps [upper graph in Fig. 4-10(a)], which is contrary to the current belief. These steps (dark arrows and coloured boxes) are assigned to rupture transitions because they also generate spikes in the force channel due to the non-instantaneous response of the feedback system [lower graph in Fig. 4-10(a)]. Moreover, the spikes permit to spot them even when they are smaller than a nanometre, which is particularly useful for the two transitions with longer rupture times (green and purple boxes).

For the lipid membrane shown, a total number of five transitions have been detected: three happening at very short time scales (a few milliseconds) and two happening at longer times (tens to hundreds of milliseconds). The total number of steps, however, varies for different lipid membranes; by analysing the rupture of 139 lipid membranes, we have detected various situations ranging from two to five steps per lipid membrane. We have separated each situation depending on the number of steps and the time scale of their rupture time. It is worth mentioning that whereas the long rupture-time events never overlap, the time scale of the initial ones is typically as fast as the instrument resolution (< 1 ms), which complicates their quantification. In total, we have identified five cases [Fig. 4-10(b)], which are listed below:

I. Three steps happen at very short times, with their corresponding spikes overlapping each other. The two initial steps are much thicker than the third one. The two long rupture-time steps, conversely, happen typically hundreds of milliseconds after the main rupture and are very small (< 1 nm)

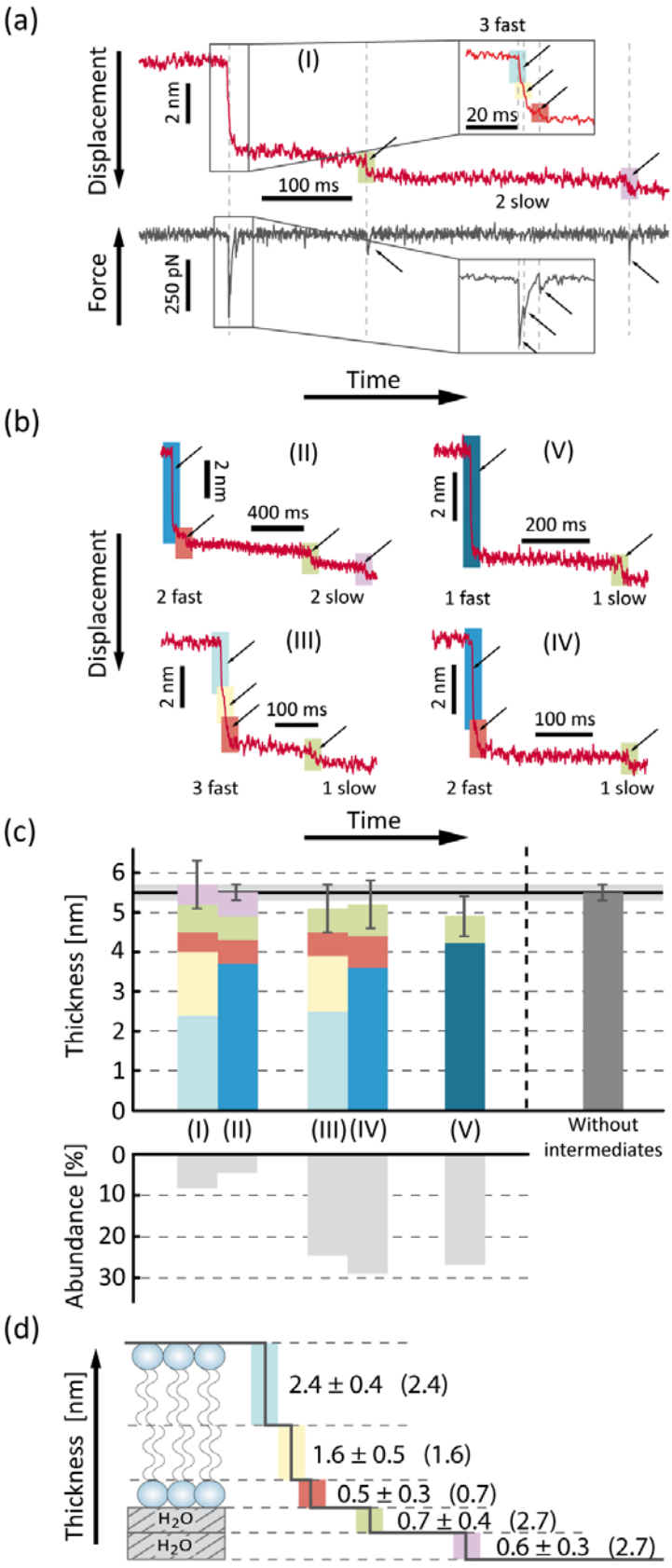

Fig. 4-10 DPhPC stacked lipid membranes display a complex rupture profile. (a) (Upper graph) when a stacked lipid membrane is broken at a low force (20 nN), the previous sharp transitions are observed (red trace) as a series of smaller transitions (dark arrows). (Continues in the next page)

(Continuation) These transitions happen in two different time scales. Two transitions happen at hundreds of milliseconds (green and purple boxes), whereas three happen at few milliseconds from the first transition (pale blue, pale yellow and red boxes in inset). (Lower graph) each transition can also be observed as a spike in the force channel (inset). (b) Four extra types of rupture profile have been identified (II-V) displaying a different combination of transitions. Every new type of transition has been assigned a new coloured box. (c) The average thickness has been measured for each type of transition. (Upper graph) cumulative bar plot displaying the thickness of each transitions for every situation. Each coloured bar corresponds to the transitions with the same colour. (Lower graph) Abundance for each situation. (d) Schematic representation of the sub-structure of the lipid membrane corresponding to each identified transition. The parameters in brackets correspond to x-ray values for DMPC stacked membranes[168].

II. A very thick step initially occurs, closely followed by a smaller one. The thick step typically has a spike in the force channel with a longer tail, suggesting that it is composed of two separate events that could not be resolved by our AFM. As before, the two long rupture-time steps happen hundreds of milliseconds from the main rupture and are very small.

III. This situation is like (I), except that only one step is detected at long rupture times.

IV. This situation is like (II), except that only one step is detected at long rupture times.

V. Only two transitions are detected, one at short and one at long times.

We have quantitatively analysed the fine structure of the lipid membranes by measuring the thickness of the sub-steps for each situation. As shown in Fig. 4-10(c), the sum of all the sub-step agrees with the thickness of a whole lipid membrane, thus indicating that the sub-steps correspond to sub-structures of the lipid membrane. Moreover, each of them exhibits a consistent thickness, with a deviation smaller than 1 nm and of the same size as the experimental error.

The sum of the short-lived states is also constant throughout the various cases. For instance, the overlapping first and second spikes in situations (I) and (III) sums up to the same height than the first transition in (II) and (IV). The matching thickness strongly suggests that our AFM resolves them as separate events when their life-times are long enough (> 1-2 ms), but cannot

resolve them when their ruptures are too close in time. The same argument can be extended to case (V), where the first step equals the sum of the height of all the short rupture-time steps. Therefore, our results indicate that the short-lived states are caused by the presence of three distinct labile sub-structures of the lipid membrane.

All situations exhibit at least one step featuring 0.7 ± 0.4 nm of thickness, which consistently occurs at longer rupture times. Situations (I) and (II), however, display an extra step. In this case, they break at times separate enough in time to be well resolved by the AFM. Thus, one of them might be escaping consistent detection. A possibility is that the second step breaks together with the first one of the next membrane. This is a likely possibility since the second step is detected not far from the next lipid membrane rupture. Another possibility is that we simply cannot detect it because its concurrent force spike is too small to be detected by the operator eye. A last possibility is that it is an impurity, which would be in agreement with the small abundance of ruptures with two long rupture-time steps. Because the length of the second long-lived state does not significantly change the total measured thickness, it is impossible to confirm the existence of this long-lived state. We believe that it is a sub-structure of the lipid membrane because it appears in several independent days of experiment with the same consistent thickness and rupture time scale, which would be very unlikely to occur if it were an impurity. Therefore, we confirm that at least one, but perhaps two, long-lived states correspond to the sub-structure of the lipid membrane.

The total 4-5 states captured with force-clamp, however, are not intermediates of the rupture process. As we aforementioned, the rupture process happens in the horizontal plane with the creation of a pore that permits the passage of the AFM tip. Instead, here we observe states that are at a different plane. Most importantly, the lognormal distribution of rupture events is kept even if these steps are taken into account. This result is in agreement with the fact that the multi-step Chimadzev model underestimates long rupture times. Furthermore, single supported lipid membranes do not display any long-lived sub-structure and still result in lognormal kinetics, which demonstrates that the observed long-lived states are not a condition for

complex kinetics to occur. Therefore, the transitions observed here are orthogonal to pore-forming kinetics.

We propose that these states are sub-structures of the lipid membrane pore transiently probed as the tip breaks through it. We tested this hypothesis by comparing the thickness of our detected transient states to that of the sub-structures of a lipid membrane [Fig. 4-10 (d)], obtained from x-ray diffraction data on DMPC stacked lipid membranes[280]. Even though DMPC is not our lipid of study, its headgroup is identical to that of DPhPC and its tail is of comparable size. The short-lived states closely match the size of the two lipid leaflets. The first transient state (light blue) closely matches the thickness of the proximal lipid leaflet. Being 0.8 nm shorter, the second transient state (pale yellow) matches the size of the lipid tail and the third one (red) the lipid headgroup. Interestingly, this sequence of rupture events suggests that both lipid leaflets are mechanically independent. On the other hand, the long-lived transient states are in close agreement with the water layers confined between the stacked lipid membranes, as molecular dynamics simulations suggest[281][282]. Their different nature would be in agreement also with their distinct rupture kinetics. To confirm their existence, experiments using different ionic buffer chemical moieties — such as Lithium and Cesium — should allow monitoring the change in thickness of the long-lived transient states with the ionic strength. Analogously, lipid membranes of different lipid chain and headgroup size could be employed to confirm the assignment of the short-lived transient states.

To sum up, force-clamp indentation experiments on stacked lipid membranes allow us to capture a plethora of transient states which do not exist in supported lipid membranes. Moreover, we have identified at least four such states, and possibly a fifth one, which have consistent thickness and mechanical stability. Finally, we have assigned each of these transient states to the different sub-structures of the lipid membrane. If confirmed, these experiments would allow for the first time to study the structural and mechanical properties of each part of the lipid membrane individually. Interestingly, we have also possibly identified for the first time confined water, which opens up the possibility to conduct similar experiments of those reported in chapter 3 in a solvent of higher interest. All in all, these

experiments demonstrate that the lipid membrane is a complex structure that now thanks to force-clamp can be studied in detail.

4.5 Conclusions

In this chapter we have first developed a new method to investigate lipid membranes by generating stacks of tens to hundreds of layers. Thanks to our protocol, we have been able to produce lipid stacks from a variety of lipid moieties in aqueous conditions. Moreover, it has allowed for the first time to compare the properties of substrate-neighbouring lipid membranes to 'substrate-free' stacked ones. As a result, we have determined that the substrate-neighbouring lipid membrane is highly deformed, displaying a much reduced thickness compared to the unaffected stacked ones. Our results suggest that the lipid tails tilt and pack in a tighter configuration. These results are in agreement with the properties of single membranes deposited from liposomes, indicating that the substrate-induced compression is caused by the direct contact with the mica substrate.

Then, we have identified three distinct mechanical regions within the stacked membranes: the substrate-lipid interface, the middle region, and the water-lipid interface. The mechanical stability in both interface regions depends on the distance to the lipid stack edge. In this case, however, their thickness remains unaffected. Conversely, the lipid membranes in the middle region of DPhPC lipid stacks break in an independent and consecutive fashion, which makes them suitable as a model to study lipid membrane rupture kinetics without the effect of the substrate.

By using force-clamp, we have captured for the first time the complex kinetics of lipid membrane rupture. By analysing the force dependency of the rupture rate, we have identified a common transition state shared by substrate-neighbouring and stacked lipid membranes. This common transition state is also in agreement with the previously reported data on chemically-distinct lipid membranes. Obtaining the distance to the transition state, however, has been prevented by the indeterminacy of the number of disrupted interactions.

A way to further investigate the number of disrupted interactions could be to indent lipid membranes using AFM tips of variable radius. This alternative, however, has two main drawbacks. Firstly, milling AFM tips to

obtain small radiuses (< 100 nm) is a difficult and imprecise process that might lead to significant experimental errors. Secondly, the contact between the tip and the lipid membrane are likely to remain outside the macroscopic Hertz regime even for blunt tips (> 100-300 nm) because the total deformation of the lipid membrane will remain the same (< 2 nm). In this sense, it is likely that only the last asperities of the tip apply the relevant force to form a critical pore, thus complicating the quantification of the exerted force.

We have analysed the detailed lipid membrane rupture kinetics in order to circumvent estimating the mechanical contact area. We have experimentally measured that the distribution of rupture times follows a lognormal distribution. The lognormally distributed kinetics demonstrates for the first time that the rupture of lipid membrane occurs through a large number of steps; unlike it is currently accepted in the force spectroscopy field. Furthermore, this specific distribution is in agreement with a multiplicative growth process. We have interpreted these results in terms of a multiplicative pore nucleation model, in which a pore expands through its perimeter until reaching a critical size where it irreversibly expands. We have developed two proof-of-principle models that demonstrate that our argument fits the experimental data. Under this approach, the kinetics of lipid-lipid rupture and lipid membrane poration would occur in two separate time and length scales. This model would be in agreement with the common transition state, which would correspond to the (widely conserved) cleavage of lipid-lipid bonds. Consequently, the critical pore radius would become the real determinant of lipid membrane rupture kinetics. This new perspective is highly beneficial because the critical pore radius can be accessed through the shape of the rupture time distribution, which is not affected by the way forces are transmitted between the AFM tip and the lipid membrane. Therefore, this innovative approach provides a completely new viewpoint on how to conceptualize and analyse the kinetics of lipid membrane poration.

Finally, we have identified at least four — and probably five — transient states occurring after the poration of the lipid membrane. These transient states have been correlated to the consecutive rupture of the proximal leaflet, distal leaflet, and the water layers confined between stacked membranes. If confirmed, this would allow for the first time to investigate the properties of

each lipid leaflet independently. Also, our findings open the possibility to study the kinetics of confined water under well controlled conditions

All in all, the combined efforts conducted towards obtaining better lipid preparation methods, instrumental techniques, and theoretical models have permitted us to investigate the properties of lipid membranes with an unprecedented level of detail. The resulting experimental data shifted the currently accepted simplistic point of view of two-state lipid membrane rupture to a very complex pore formation picture with a myriad of underlying processes happening during indentation at real time. We expect that this work will provide and experimental and theoretical platform to push further lipid research in the future.

5 The nanomechanics of cell membranes in live cells

In this chapter, we investigate the mechanical properties of live cells using force spectroscopy AFM. By indenting cells at high indentation forces, we observe the rupture of each individual lipid membrane in the nucleus and cytoplasm envelopes. Together with mechanical measurements performed in supported lipid membranes and with global lipid profiling, we demonstrate that the lipid composition changes are linked to an increased mechanical stability, pointing out to an undescribed biological role of lipids. Then, by indenting at low force regime, we demonstrate lipid composition also alters the mechanical properties of the underlying cytoskeleton.

This chapter is part of an article published 30th January 2014 in Cell[283] (attached in appendix IV)

5.1 Introduction

Lipid composition crucially defines the mechanical properties of the cell membrane. In red blood cells, for example, the lipid composition defines the bending rigidity of the cell, and thus their ability to adapt to external mechanical stresses[284]. Another example are the lipids interacting with proteins to form local signalling platforms in vesicles or at the plasma membrane, which possess distinct mechanical properties[285]. In a different context, membranes and membrane trafficking are important to stabilize changes in curvature and to provide membrane to alleviate tension caused by shape changes during cell division[286]. Membranes are also essential in signalling and are involved in the transport and modulation of key proteins at constriction and scission sites[287][288].

Until now, the mechanical properties of cell membranes have been mostly investigated in vivo by using the micropipette aspiration technique[284]. This approach has enabled the correlation in vivo and in vitro of the relationships between lipid composition and the bending rigidity of the lipid membrane. However, this approach cannot directly capture the nanoscale dynamics that underpin lipid membrane mechanical stability. On the other hand, Atomic Force Microscopy (AFM) experiments have provided a colourful picture of the relationship between lipid composition and mechanical stability, but only in vitro[13]. Many attempts have been made to construct model systems as close as possible to the cell environment such as polymer-cushioned[229], free-standing[227], and stacked lipid membranes. Despite these systems reproduce well the soft environment surrounding the cell membrane, we still ignore if the properties observed in vitro also occur in live cells.

Previous AFM indentation experiments have been mainly focused on analysing the low indentation force regime of cell deformation. In this regime, the predominant force is the compression of the underlying cytosol and cytoskeleton scaffold. Indeed, these elasticity measurements have been employed to investigate the role of the cytoskeleton during cell division and spreading[289][290]. These measurements, however, do not provide information of the lipid membrane mechanics. To circumvent this limitation,

Yokokawa and co-workers[291] pioneered the rise of higher indentation forces to indent living cells. By using this protocol, they identified for the first time the rupture of the cell membranes just after the cell is fully compressed. Their experiments, however, did not clearly resolve the number of indented cell membranes and, most importantly, did not correlate the observed lipid membrane mechanical stability to any biological changes.

By using high indentation forces, we aim to compare for the first time the mechanical stability of lipid membranes in vitro and in living cells. For this purpose, we have collaborated with Eggert group in order to investigate the link between the chemical composition and lipid membrane mechanical stability during cell division. As mentioned above, membranes have a key role during the massive changes undergoing during cell division. Although membranes are intimately connected to the cytoskeleton, and intact membranes are an absolute requirement after division has been completed, little is known about the role of membranes during cell division.

In this sense, Eggert group used liquid chromatography-mass spectrometry (LC-MS) based global lipid profiling to analyse the lipidome of cells synchronized at different stages of the cell cycle[283]. They compared total lipids extracted from HeLa cells at cytokinesis (a division stage) to cells at S-phase (a non-division stage). The lipid composition of cells in S-phase differed from cells in cytokinesis. Specifically, 11 lipid species out of the many thousand species synthesized (and detected by LC-MS) accumulated at least four-fold in dividing (measured in cytokinesis, but unchanged in mitosis) cells[283].

To get a better understanding of the lipids' potential biological roles, Eggert group also perturbed lipid levels in cells and evaluated the resulting phenotypes. They used RNAi to systematically perturb the biosynthesis of different lipid families. Knockdown of 23 genes caused cytokinesis failure[283]. They therefore analysed the three top RNAi hits: SMPD4, GALC and DGAT2. The overall cellular consequences of SMPD4, GALC and DGAT2 knockdown were similar and connected to defects in the cytoskeleton, the main driver of cell mechanics. To varying degrees, all three RNAi treatments caused a significant delay during metaphase in mitosis, followed by cell

division failure at different stages, mostly coupled with unusual membrane blebbing.

Here, we have first indented live cells at 37 ^{0}C in the high force regime to measure for the first time the distinct mechanical stability of dividing versus non-dividing cells. Then, we have correlated the in vivo results with indentation experiments conducted on supported lipid membranes from cell lipid extracts. Finally, we have correlated the observed lipid composition changes caused by RNAi knockdown to a variation in the mechanical response of the underlying cytoskeleton scaffold by using low indentation forces.

5.2 Results

5.2.1 Cell membranes display a higher mechanical stability during cell division

To investigate the full range of mechanical stabilities of dividing cells, we have expanded the sampled range of forces to higher values, spanning 10-250 nN, and compressed the cell, until the plasma membrane was penetrated just before the tip reached the hard substrate[292]. Applying such high forces deforms the entire cell, pushing the AFM probe through a variety of cellular structures and compartments until the membrane is broken. The rupture of the plasma membrane is recognized by a rupture or 'breakthrough' jump in the force-distance curve, representing a clear molecular fingerprint[293][57], which is similar in cells and in supported lipid bilayers (Fig. 5-1).

We found that much higher forces (3-fold increase) were required to reach this breaking point in dividing vs. non-dividing cells of comparable heights [Fig. 5-1(a-c)], suggesting that both the cell body and the plasma membrane have different mechanical properties in dividing cells. The same trend was observed in the nuclear regions [Fig. 5-2(a-b)], albeit shifted to higher force values. Much of the increased stiffness in dividing cells is undoubtedly due to the cytoskeleton, which has a well-documented and essential role in the division process. However, our experiments suggest that the properties of the plasma membrane also need to be different in dividing cells to be able to withstand substantially higher forces applied during force spectroscopy.

5.2.2 Lipids isolated from dividing cells have distinct morphological and mechanical properties

The mechanical resistance we found in the plasma membrane of dividing cells is likely due to the combined action of membrane proteins, cell surface glycans and lipids. The full complement of membrane proteins is not known, but we show here precisely which lipids change in dividing cells. If the lipids themselves have physical properties that might influence their function, these could include a predisposition to organize into different domains, possibly recruiting other lipids and/or proteins to these domains in cells. In an attempt to identify a potential contribution of lipids to the overall mechanical stability of S-phase and dividing cells, we again used AFM to test the topographic and mechanical properties of supported lipid bilayers from isolated lipids at very high spatial resolution[294][295] [Fig. 5-1(d-g)]. Because the different membrane compartments in cells are very dynamic and we have an incomplete understanding of the membrane proteins involved that could potentially be used as markers for a membrane fraction's origin especially in dividing vs. non-dividing cells, it is not possible to isolate only plasma membrane in sufficient purity to allow meaningful comparisons. We therefore analysed total lipids isolated from cells under the same conditions as the samples used for LC-MS, allowing a direct comparison between the identities of the lipid mixtures and their properties.

Although the differences in lipids that were observed by LC-MS were large for specific lipids, the total change was quite small relative to the cellular lipidome (for example, the total amount of ceramides doubled, but only ~2% of lipids in HeLa are ceramides). Surprisingly, such a small detected change in the lipid composition had a significant effect on the topographic properties of supported lipid bilayers formed from S-phase and cytokinesis derived membranes: supported lipid bilayers formed from S-phase cells were mostly uniform [presenting only the matrix phase 'P0', Fig. 5-1(d), Fig. 5-2(c)], while lipids from dividing cells were more likely to separate into three distinct phases (P0, P2 and P3)[Fig. 5-1(e)]. To test whether such distinct lateral molecular arrangement of the lipids also had an effect on the bilayers' mechanical properties, we conducted force spectroscopy experiments on both

samples [Fig. 5-1(f-g)][13]. While bilayers corresponding to S-phase cells (P0) exhibited moderate mechanical stability ~ 4 nN [Fig. 5-1(g)], the distinct phases found in the bilayers formed from cytokinesis cells exhibit increasingly larger forces required to puncture the membrane, culminating in the P3 phase [Fig. 5-1(e), see Fig. 5-2 for further description of the different phases). The P3 phase, which was observed in about 20% of samples [Fig. 5-2(d)], was dramatically stiffer, with an associated mechanical resistance of ~28.3 nN. These observations on supported lipid bilayers suggest that some of the mechanical properties we observed in cells could be related to the physical properties of the lipids themselves, functioning in conjunction with membrane proteins.

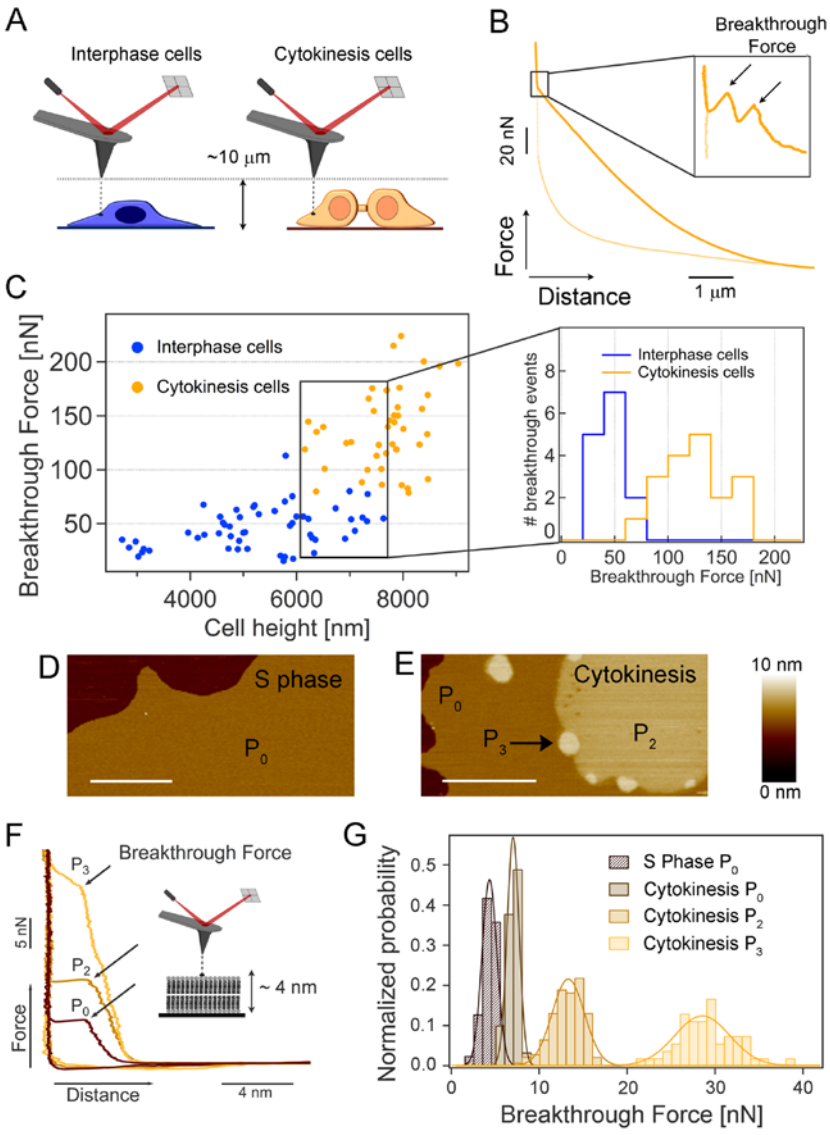

Fig. 5-1 The mechanical resistance of cytokinesis-associated lipid bilayers is higher both in live cells and in supported lipid bilayers measured in vitro. (a) Schematics of a force spectroscopy experiment on an interphase (non-dividing) and cytokinesis (dividing) live cell. (b) Typical force-distance curve conducted on a live HeLa cell during cytokinesis. In a typical cycle, the cantilever tip approaches the cell membrane and applies an increasingly higher pushing force that deforms the cytoplasm. Once the cantilever reaches a position close to the stiff substrate, it is able to penetrate through the two lipid membranes. This breakthrough event is marked by two consecutive discontinuities in the force-extension trace (arrows in inset). The cantilever is then retracted to the initial position (light yellow line). (c) Scatter-plot of the first membrane breakthrough force vs. the cell height for interphase (blue, 26 independent cells) and cytokinesis cells (yellow, 17 independent cells) in cytoplasmic areas. Similar experiments performed in the nuclear areas are shown in Fig. 5-2. (continues next page)

(continues from previous page) The plot shows that, while the breakthrough force increases with the cell height, dividing cells exhibit markedly higher breakthrough forces. Selecting a comparable range of cell heights (6-7.6 μm), the mechanical resistance of cytokinesis cells is significantly higher (inset in (c), 125 ± 30 nN and 48 ± 14 nN rupture force for dividing and interphase cells, respectively) with >99.99% confidence (Student's T-test). While the error in comparing values between dividing and non-dividing cells is small, there is an additional potential error in the absolute values reported due to limitations in the size of the cantilevers available for these experiments (see supplemental experimental procedures for a discussion). (d-e) Lipids derived from cells at S-phase and cytokinesis form supported lipid individual bilayers that exhibit distinct morphologies as revealed by tapping mode AFM topographical images. d) Supported lipid bilayers composed of S-phase lipids exhibit a continuous P0 phase. (e) By contrast, in the case of lipids extracted from cytokinesis cells, three main phases of increasing height are observed (respectively P0, P2 and P3). Scale bar = 1μm. (f) Force-distance curves on both supported lipid bilayers revealed distinct mechanical stabilities. (g) The mechanical resistance of lipid bilayers formed from S-phase cells (P0) yielded a mean breakthrough force of 3.87 ± 0.84 nN (n = 900), obtained by Gaussian fits to the data. In the case of the cytokinesis sample, both the P2 phase (12.93 ± 1.83 nN, n = 137) and the P3 phase (28.3 ± 3.17 nN, n = 54) revealed a much higher mechanical stability than the matrix bilayer phase, P0 (6.5 ± 0.68 nN, n = 90). For detailed descriptions of all phases and the height profile of (e), see Fig. 5-2.

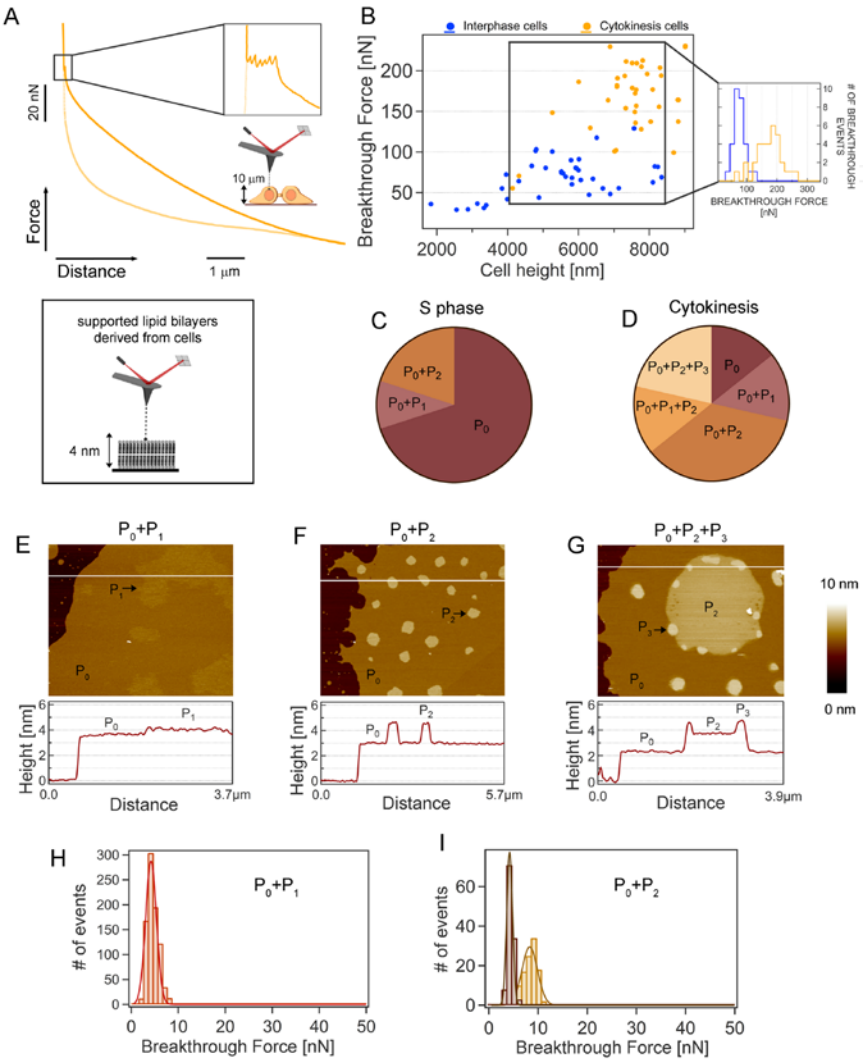

Fig. 5-2 Cytokinesis cells exhibit higher mechanical resistance than interphase cells in distinct cellular regions. (continues next page). High-resolution AFM images on supported lipid bilayers reveals a complex distribution of phases (related to Fig. 5-1). (a) Typical force-distance curve conducted on a live dividing HeLa cell in the nuclear area. This event is distinguishable by six consecutive discontinuities corresponding to the breakthrough of the plasma membrane (two events) in addition to those of the nuclear envelope (composed by two lipid bilayers and therefore showing four rupture events). (b) Scatter-plot of the upper membrane rupture force (first event) vs. the cell height for interphase (blue) and cytokinesis cells (yellow) in the nuclear area (19 cells per case). As in the case of the cytoplasmic region, the rupture force steadily increases with the cell height. When selecting a comparable range of cell heights (4.1-8.3 µm), the mechanical resistance of the nuclear region in cytokinesis membranes is clearly higher (174 ± 42 nN, n =34) than that of non-dividing cells (76 ± 19 nN, n=29) (inset in B) with a >99.99% confidence (Student's T-test). (c-i) Supported lipid bilayers isolated from live cells and analysed at high-spatial resolution by AFM imaging exhibit a complex distribution of phases and mechanical stabilities. While Fig. 5-1(d-e) reflects the most distinctive patterns of phase distribution in our supported lipid bilayer samples, in some of the preparations additional phase distributions were observed. (continues next page)

(continues from previous page) (c) Pie chart corresponding to S-phase preparations shows that, while samples showing only a P0 phase are predominant [Fig. 5-1(d)], in some cases P0 is accompanied by P1 or P2 phases. Note that the nomenclature defining each of the phases is arbitrary, yet self-consistent throughout the paper. (d) In the case of lipid bilayers formed from cytokinesis cells, a wider combination of the four distinct observed phases is encountered, as shown in the pie chart. The very stiff P3 phase was never observed in lipid bilayers isolated from S-phase cells. Each pie chart contains 10 and 14 sets of experiments for S-phase and cytokinesis cells, respectively. Particularly interesting phase combinations that are not discussed in the main text for cytokinesis preparations are shown in (e) and (f). (e) exhibits a P1 phase that is only slightly higher than the matrix P0 phase (< 0.2 nm) and readily apparent in the phase channel (not shown). (h) Notably, there is no measurable difference in the mechanical stability of the P0 and P1 phases (3.7 ± 1.7 nN). (f) Another common combination of phases is observed in F, whereby only P0 and P2 phase coexist. In this case, the height of the P2 phase is significantly higher (> 1.27 nm) than the matrix P0 phase. (i) The mechanical stability of the P2 phase is higher (8.0 ± 1.3 nN) than the P0 phase (3.7 ± 0.6 nN). A larger version of Fig. 5-1(e) with the associated height profile is shown in (g). In this case three main phases are observed: a first P0 phase exhibiting 2.86 ± 0.52 nm, a second phase (P2) showing a height of 4.13 ± 0.54 nm relative to the mica substrate, and a higher P3 phase, featuring 4.96 ± 0.16 nm. For S-phase cells, an average height of 2.63 ± 0.72 nm is observed for the matrix, continuous P0 phase (ref. to Fig. 5-1(d), height profile not shown).

5.2.3 RNAi knockdown of key lipid biosynthetic enzymes causes mechanical defects in cells

We measured the mechanical response of SMPD4 RNAi treated cells compared to control ones. Because the resulting phenotypes from SMPD4 knockdown suggest defective processing of mechanical signals, we tested if mechanical integrity was affected in cells. Using AFM at forces lower than 0.6 nN (as opposed to the high forces needed to break through membranes discussed above) to measure elasticity, we recorded the stiffness of cells in a N x N grid of equally spaced points [inset in Fig. 5-3]. The indentation method is described in appendix II (chapter 10) and the theoretical model and experimental technique used are explained in chapter 2. The nucleus possesses a distinctively higher stiffness than the cytoplasm for both SMPD4 RNAi and control cells (data not shown). When the stiffness of the cytosol region is pooled for many cells, we found that SMPD4 RNAi cells are 4-fold stiffer than control cells (Fig. 5-3). Analogous results were observed for the cell nucleus (data not shown). Interestingly, all cells display the same mean stiffness than its variance, which is typical of i.e. the Poisson distribution[296]. Finding a generating mechanism for the data distribution, in this case, will be left for future investigations. Most importantly, these data show a clear mechanical role for lipids, either directly or by causing changes to the cytoskeleton. Since SMPD4 RNAi was found to be accompanied by changes in the actin cytoskeleton, it is likely that the effects exerted by lipid composition changes cause cytoskeletal defects rather than structural roles of the lipids themselves.

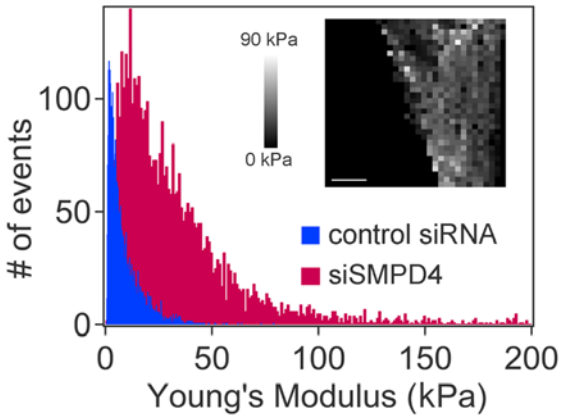

Fig. 5-3 F) Histogram of cell stiffness (Young's modulus values, see appendix II) measured on control and SMPD4 siRNA-treated cells. A total number of 4098 indentations (21 cells) and 4314 indentations (18 cells) were performed on SMPD4 and control siRNA treated cells, respectively. The average value for siSMPD4 cells is significantly higher (35 ± 8.8 kPa, average ± s.e.m.) than siRNA control cells (8.3 ± 1.9 kPa) with a >99.95% confidence. Inset: typical 32x32 force-volume map measured on a siSMPD4 cell. The topography of the force-volume corresponds to an arbitrary colour scale of the Young's Modulus. Scale bar = 10 μm.

5.3 Conclusions

By extending the range of indentation forces, we have quantified for the first time the mechanical properties of lipid membranes in living cells. The measured rupture forces are intrinsically linked to the previous indentation history, which precludes analysing the absolute value of the rupture forces. This notwithstanding, we have observed that dividing cells possess significantly stronger mechanical properties than non-dividing cells for the same indented depth. By extracting the cell lipids and depositing them on a flat substrate, we have observed a distinct phase behaviour in samples extracted during division. As well, the supported lipid membranes extracted during division have an overall higher mechanical stability than those extracted during S-phase. Together with the lipid composition changes obtained by LC-MS, our results indicate that lipid composition modulates the mechanical properties of the cell lipid membranes during cell division. Indeed, this change is not limited to the lateral packing of the lipids. By performing indentation experiments in the low force regime, we have observed that lipid composition also alters the mechanical properties of the underlying cytoskeleton. Taken together, our efforts highlight for the first time the crucial role that lipids directly play during cell division. Moreover, our efforts set new experimental protocols towards monitoring the precise rupture kinetics of lipid membranes in relevant biological environments. In this way, we hope that in the future the precise experiments performed in lipid stacks can be translated to living cells.

6 Conclusions

6.1 Work accomplished

During this PhD project, we have investigated the mechanical properties of materials at the nanoscale by applying force spectroscopy. In this vein, we have assembled a custom-built atomic force microscope with force-clamp capabilities. Moreover, we have developed the instrumental and software tools to perform indentation experiments in living cells at 37 ^{0}C with a commercial AFM. Then, we have used these tools to investigate the mechanical properties of three different materials. Firstly, we have investigated the rupture-reformation dynamic equilibrium in confined liquid layers. We have discovered that the rupture mechanism of confined layers occurs at the molecular level when indented by the AFM tip. Secondly, we have captured the complex kinetics of rupture of lipid membranes. By using stacked lipid membranes, we have measured the tightening of the lipid membrane when in direct contact with the hard underlying substrate. Most importantly, the non-exponential distributions of rupture times indicate that lipid membranes break through a multi-step pore formation mechanism, as opposed to the current single step viewpoint. Finally, we have developed the instrumental and analytical protocol to investigate the mechanical stability of lipid membranes in living cells. Together with the work from our collaborators, our results highlight the crucial role of lipid composition to modulate the mechanical properties of lipid membranes in vivo.

The following sections review the main accomplishments for each chapter and discuss them in the context of the value added in their respective fields. Then, we summarize how these different findings have improved our knowledge of the rupture mechanisms at the nanoscale.

6.1.1 Instrumentation

An atomic force microscope with force-clamp capabilities has been successfully built by adapting a previous existing model developed to pull single proteins. Correctly assembling it was a crucial step for my PhD project: the specific indentation force-clamp protocols employed would have been very difficult, if not impossible, to develop with a commercial AFM. It was also a personal feat given my complete lack of engineering skills at the beginning of the PhD project.

Another key step towards building the microscope has been thoroughly testing each individual component as well as the global behaviour. As a result, several issues affecting our microscope were spotted. One of them was originated in the model design rather than our specific built, which points out the ethical importance of thoroughly testing and benchmarking any custom-built equipment. Despite the simplicity of many designs, the probability that measurements biases are affecting our instruments is always relevant and if malfunctions are not detected at the testing stages, these biases and errors can be propagated for long times. In my personal opinion, public and stricter tests should be asked to scientific instrument developers when measuring new systems in order to avoid undetected instrumental errors. In this sense, we have made an effort in all the projects to give a detailed explanation of all the instrumental and analytical procedures employed. In any case, the tests performed clearly show that our particular instrument is well calibrated and can produce precise and accurate measurements.

We also adapted a commercial AFM to perform force spectroscopy at 37 ^{0}C. For this purpose, we have developed a home-made temperature controller and have adapted the protocols of our microscope to apply force spectroscopy. Developing our own controller was faster and cheaper than buying a commercial solution. Moreover, we have pushed a bit further the instrumental know-how of our laboratory in a field where very few commercial solutions are available. On the other hand, finding the conditions to perform force spectroscopy with Bruker Dimension Icon has not just been beneficial for this project, but also for later investigations in cell mechanical properties performed with the same instrument.

Finally, we have developed an extensive code to control force spectroscopy experiments and analyse the raw experimental data. Indeed, each individual project has required its own specific software analysis tools. Moreover, the code written can be easily translated to other projects within our research group, thus providing a support for future investigations i.e. in the protein pulling field. Therefore, learning to write working analytical procedures has been crucial towards providing higher quality research for me and my research group.

6.1.2 The nanomechanics of solvation layers in confined liquids

By using force spectroscopy, we have investigated quantitatively for the first time the rupture and reformation transitions of confined solid-like layers. Constant velocity experiments have shown that confined layers become thinner and exponentially increase their mechanical stability with the distance to the substrate, as reported in the literature. By applying force-clamp, we have captured the dynamic rupture-reformation equilibrium in real time — with exception of the substrate-neighbouring layer which displays a clearly different behaviour. Analysing the thermodynamic properties of the equilibrium provided the distance between the initial and final state as well as its energy difference. Thanks to obtaining these quantities, we have been able to experimentally measure both the distance to the transition state and the number of disrupted interactions. This is a great advantage compared to non-equilibrium rupture processes, such as with lipid membranes, where obtaining the two parameters independently is not possible. As a consequence, we have determined that molecular confined liquids break though one single interaction whereas ionic confined liquids break through two interactions. The different number of disrupted interactions in ionic liquids might be due to the cation-anion ionic radius mismatch. Most importantly, the discrete number of interactions disrupted by the cantilever tip is complementary with previous AFM evidence, but in opposition to the currently accepted point of view of the rupture process generated by surface force apparatus indentation experiments whereby the confined liquid layers are broken with a much blunter tip (radius > micrometre). Hence, our

experiments demonstrate that AFM indentation captures the single molecule rearrangements involved in the molecular scale rupture mechanism of confined liquid layers.

These discoveries are also exciting for our research field. This is the first evidence, to our knowledge, that AFM indentation can occur at the single molecule level. Our results seem reasonable in the light that the total deformation exerted for each layer is below the radius of a single silicon oxide ion, which constitutes the atom-scale termination of the AFM tip. Thus, it is unlikely that macroscopic contact models apply in this indentation depth regime. Instead, molecular-scale indentation contact models should be developed in order to account for these indentation depth scales. These results are of particular importance for measuring the stiffness of a variety of nanoscale materials, such as lipid membrane, whereby the Young modulus is extracted by fitting an indentation depth[254] that is also in the Angstrom scale. In this sense, Asylum Research, a leading AFM manufacturing company, recently developed dynamic indentation protocols that are independent of the AFM tip size in order to obtain relevant stiffness measurements at the atomic scale. Hence, our results indicate that a better understanding of the contact mechanics is required in order to obtain reliable mechanical measurements at molecular-scale.

We have also demonstrated the enticing properties of dynamic equilibriums to understand their rupture mechanism. Without experimentally determining the distance between the initial and the final state through the relative time abundances, it would have been impossible to determine the number of disrupted interactions. In this sense, correlating the broken to unbroken states distance to the thickness of a single confined layer set the direction of the reaction coordinate and thus helped us understand the breaking mechanism of the confined layers. These results thus pinpoint the intrinsic benefits of studying both the rupture and reformation processes, when available, in order to gain a deeper insight in the rupture mechanisms. A clear example where to apply this idea is in lipid membrane investigations, whereby the reformation mechanism has been greatly overlooked until now. Taken together, these results provide a better understanding of the dynamics

of confined solvation layers at the Angstrom scale and shows interesting ways to obtain more detailed pictures of the rupture energy landscape.

6.1.3 The nanomechanics of lipid membranes

We have developed a new method to investigate the nanomechanics of lipid membranes by generating stacks of tens to hundreds of layers. In this configuration, lipid membranes are maintained far away from the hard substrate while keeping an underlying support, thus avoiding the undesired effects of the substrate. Indeed, supported lipid membranes display a complex sequence of transient states that has not been reported to date. Furthermore, stacked DPhPC and DOPC lipid membranes in the middle region break in an independent and consecutive manner when indented. Hence, the rupture of a layer marks the start of a completely new experiment, which highly increases the throughput of our mechanical measurements. These two properties turn lipid stacks in a seducing lipid model system, obtaining an unprecedented compromise between accuracy and biological relevancy in mechanical measurements of the lipid membrane.

By comparing stacked versus substrate-neighbouring lipid membranes, we have quantitatively measured for the first time the effect of the substrate. We have observed two separate effects: in the long range, the substrate proximity decreases the mechanical stability of the lipid membranes, which might be caused by the ion gradient concentration close to the highly charged mica substrate; in the short range, the direct contact with the substrate thins the lipid membranes while increasing its mechanical stability. The latter effect suggests a molecular arrangement with lipid tails laying almost in parallel to the surface. Furthermore, the substrate-neighbouring lipid membranes do not display any transient states of rupture. All in all, we have demonstrated for the first time that the substrate crucially affects the structural properties of the lipid membrane in direct contact to it.

Despite these structural differences, both substrate-neighbouring and stacked lipid membranes break through the same transition state. As a consequence, we could not directly link the transition state to any structural part of the lipid membrane — namely the lipid heads or the tails. By analysing

the complete kinetics, we have proposed that the rupture of lipid membranes goes through the formation of a critical pore, which is subsequently expanded with very little energetic cost. In our model, the pore forms by expanding on its rim, which results in a multiplicative growth process in agreement with the measured lognormal distribution of rupture events. This novel approach clearly show the advantages of considering the full rupture time distributions instead of just considering these as small deviations from an ideal model. Most importantly, our results clearly indicate that the lipid membrane kinetics cannot be explained by a simple 'all-or-none', single-transition model, as it is currently accepted.

Considering the lipid membrane rupture as a pore formation process also shifts the focus of attention of force spectroscopy research from the current — and sometimes vague — idea of mechanical stability to a more concise physical process. In this new context, the rupture force variations occur because of a change in the energetics of the formation of the pore. Thus, those parameters changing the bonds at the rim of the pre-critical pore will be crucial to define lipid membrane stability. Hence, different parameters might affect lipid pore formation through different mechanisms: the pure increase of net lipid-lipid interactions, which would only affect the height of the energy barrier; and the variation in the critical pore size, which would also change its rupture time distribution. We speculate that ion concentration might strengthen lipid-lipid bonds while cholesterol, which crucially influences the type of lipid-lipid interactions, might also influence the critical pore radius. All in all, our results provide a clearer and more detailed picture of the lipid membrane rupture.

6.1.4 The nanomechanics of cell membranes in live cells

We have indented live cells using force spectroscopy AFM at two different indentation regimes to investigate the changes in the cell membrane during cell division. By applying low indentation forces, we have firstly accessed the properties of the cytoskeleton underlying the cell membrane. We observed a stiffening of the cytoskeleton during division. By applying higher forces, we have then quantified for the first time the lateral packing interactions of the cytosol and nuclear envelopes. By comparing dividing

versus non-dividing cells, we have observed that cell division increases the mechanical stability of the cell membrane. Finally, we have conducted experiments in supported lipid membrane from cell total lipid extracts, which produced analogous results. Our results are one of the first evidences that lipids play a direct role during cell division and, in a broader context, probably in other biological processes. Thus, these results strongly suggest that the lipid membrane is not a passive 'wall' in which biological processes just occur.

Our work has shown to be also appealing to our scientific field; in the last year, several researchers have published closely related works. For instance, Angle and co-workers have recently published a deeper investigation in the effect of the tip geometry to the measured rupture force of lipid membranes in live cells[297]. Another example is Aisling Williams, from my research group, who is currently investigating the changes in mechanostability of cells when we interrupt proteins in the LINC complex – a multiplex of proteins connecting the cytoskeleton to the nucleoskeleton. As well, there are currently efforts in my research group to apply force-clamp to the cell membrane, which would complement our previous investigations with stacked lipid membranes. Hence, it is likely that live cells will become in the following years a target lipid membrane system of study.

6.1.5 The molecular rupture mechanisms

The work accomplished in this project answers several crucial questions of how fracture occurs at the nanoscale. For instance, our investigations have determined that at the Angstrom scale, the contact might happen directly with the last asperities of the tip, in contradiction with the current viewpoint. Cell indentation experiments demonstrate, instead, that when the indention depth is in the micron scale, the contact between the tip and the sample occurs between the walls of the tip and the substrate, as predicted by Hertz theory. As a result, the nanoscale seems to be the turning point between continuous and molecular contact. Indeed, the estimated number of disrupted interactions for lipid membranes is bigger than that predicted by a point force model and lower that that calculated by the Hertz spherical contact model. The estimation of the contact area for lipid membranes, however, is precluded by confirming the application of our rupture mechanism model. In any case, all three sets of experiments have been performed with identical tips but resulted in completely different contact models. Thus, the defining element for contact seems to be the sample, not the AFM tip profile, at least for nanosharp tips.

Our experiments have also helped clarify the methods to interpret the force-clamp results while pushing. As previously said, it is impossible to know beforehand the reaction coordinate or its direction. In this sense, indenting confined liquids have revealed the usefulness of rupture-reformation dynamic equilibriums in order to experimentally determine the reaction coordinate. In the absence of reformation, the interpretation of the reaction coordinate requires of a rupture model. In a broader sense, our results clearly show that the reaction coordinate needs not to be in the vertical axis in which we are pushing. This counterintuitive conclusion points out the importance of interpreting the molecular mechanisms underlying the measured rupture events.

Finally, we have observed that distinct systems possess very different rupture mechanisms. Whereas the rupture of confined liquids involves the horizontal dislocation of an array of molecules, the rupture of lipid membranes requires the formation of a pore. The difference is not just limited

to the process itself, but also with the number of molecules involved in each of the processes. These differences notwithstanding, each of the processes require the formation of pore in the surface structure — composed of either a few or many molecules. Thus, despite its specific mechanistic differences and implications for each their respective fields, it is likely that they might follow the same pore formation kinetics, which might also be the case for many 'hard' materials whereby the first stages of indentation occur through the rupture of Angstrom-scale layers of materials such as sodium chloride, graphite, or graphene. Unfortunately, we have had no time to assess this possibility during the PhD time. But despite the specificities of each rupture mechanism, in all cases the rupture of 2D materials ultimately occurs at the molecular scale. Thus, our experiments are in agreement with the hypothesis stated in the introduction regarding the importance of understanding the rupture mechanisms at the nanoscale.

6.2 Future work

The next sections discuss some prospective projects based on the work developed in this PhD project.

6.2.1 To complete and translate the lipid pore formation model

As aforementioned, the next logical step is to complete the model to fit the rupture time distributions of lipid membranes. The most straightforward way to solve it is to find the first passage time distribution for a branching Markov Chain, which would provide a very straightforward solution to the pore nucleation problem. If no analytical closed form is available, we could also investigate the origin of the Brownian motion term in the stochastic 'continuous' model in terms of the generating model — the creation of lipid vacancy holes.

Afterwards, we propose to investigate the effect of various crucial parameters such as Cholesterol content and ionic strength in the pore forming kinetics. Following our model, we predict that the distance to the transition state should remain roughly equal, but the critical pore radius should sharply vary, at least for Cholesterol content. As well, we propose to re-examine the rupture time distributions of confined solvation layers under the light of this model. As a longer term project, the translation of this model to other systems such as the first stages of indentation of 'hard' solids or the unfolding proteins could help identify any possible common mechanism of rupture at the nanoscale.

6.2.2 Understanding the transient states

Despite we have identified a number of transient states during the indentation of lipid membranes and proposed that they correspond to the different constituting parts of a stacked lipid membrane, we still lack a complete experimental determination of their nature. To confirm their identity, we propose to conduct the same experiments with stacks of chemically distinct lipids. For instance, by changing the lipid tail length we

could identify which transient states also change their length. Following the same logic, the transient states corresponding to the inter-membrane water layers could be identified by changing the ionic strength or the buffer chemical moiety. Indeed, these experiments are currently being conducted by Amy Beedle in our laboratory.

6.2.3 Studying the reformation of lipid membranes

Despite all the efforts to better understand lipid membrane rupture, lipid membrane reformation has been mostly ignored until now. As confined liquids clearly showed, the reformation processes can greatly help understanding the rupture mechanism. Furthermore, it is reasonable to think that pores are eventually formed in living cells due to spurious external perturbations. Thus, the reformation of an already created pore might be even more crucial for biology than its formation mechanism. Investigating the reforming kinetics, however, has been precluded until now because of the effect of the substrate, which was thought to crucially influence the mobility of supported lipid membranes. We propose to use stacked lipid membranes, which are unaffected by the substrate, in order to investigate for the first time the reformation kinetics. Together with the previous investigations on lipid membrane rupture, these efforts could portray a detailed landscape of the dynamics of lipid pore formation and healing at the nanoscale.

6.2.4 Developing an open source analysis software

Studying biophysics by means of force spectroscopy requires to put together people with different backgrounds, from biology to engineering, which might sometimes be difficult to achieve. In particular, the lack of software programming skills might greatly delay relatively simple analysis. For example, just for the simple task of measuring rupture forces, in many laboratories still nowadays the process is conducted by taking hand notes, which then are manually transferred to virtual spreadsheets. As a result, measuring just hundreds of rupture forces might become a task even more time consuming than the experiments themselves. Most importantly, these time limitations decrease the amount of data analysed, which also might lead to involuntary cherry-picking. Moreover, many researchers frequently

require short programs to perform mathematical tasks that are otherwise very time consuming. These delays, however, could easily be reduced with an open source project. The core of the project would contain a rupture force analysis module which could be expanded with specific routines to perform i.e. indentation fittings or polyprotein WLC analyses. With the necessary collaboration of various research groups and given my software programming expertise, this project could quickly develop to contain the basic features to process most of the force spectroscopy analysis routines. Thus, the proposed software could be a small but important step towards adding value to force spectroscopy investigations worldwide.

…

‘We are the chick — the world is our egg.

If we don't crack the world's shell, we
will die without ever truly being born.’

— *Student council*

(Revolutionary Girl Utena)

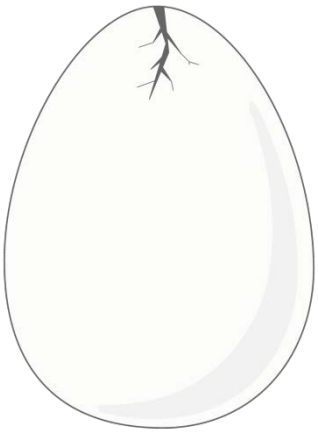

7 Bibliography

[1] A. A. Griffith, "The theory of rupture," *Proc. First Int. Congr. Appl. Mech.*, pp. 55–63, 1924.
[2] A. A. Griffith, "The phenomena of rupture and flow in solids," *Philos Trans R Soc*, no. A221, pp. 163–198, 1920.
[3] R. A. Sack, "Extension of Griffith's theory of rupture to three dimensions," *Proc. Phys. Soc.*, vol. 58, no. 6, p. 729, Nov. 1946.
[4] K. B. Broberg, "The foundations of fracture mechanics," *Eng. Fract. Mech.*, vol. 16, no. 4, pp. 497–515, 1982.
[5] K. B. Broberg, "Critical review of some theories in fracture mechanics," *Int. J. Fract. Mech.*, vol. 4, no. 1, pp. 11–19, Mar. 1968.
[6] T. L. Anderson, *Fracture Mechanics: Fundamentals and Applications, Third Edition*. .
[7] M. Jono, A. Sugeta, and Y. Uematsu, "Atomic force microscopy and the mechanism of fatigue crack growth," *Fatigue Fract. Eng. Mater. Struct.*, vol. 24, no. 12, pp. 831–842, Dec. 2001.
[8] K. Minoshima, Y. Oie, and K. Komai, "Nanoscopic fatigue and stress corrosion crack growth behaviour in a high-strength stainless steel visualized in situ by atomic force microscopy," *Fatigue Fract. Eng. Mater. Struct.*, vol. 28, no. 11, pp. 951–961, Nov. 2005.
[9] J. R. Kermode, T. Albaret, D. Sherman, N. Bernstein, P. Gumbsch, M. C. Payne, G. Csányi, and A. De Vita, "Low-speed fracture instabilities in a brittle crystal," *Nature*, vol. 455, no. 7217, pp. 1224–1227, Oct. 2008.
[10] L. M. Lee and A. P. Liu, "The Application of Micropipette Aspiration in Molecular Mechanics of Single Cells," *J. Nanotechnol. Eng. Med.*, vol. 5, no. 4, pp. 0408011–0408016, Nov. 2014.
[11] J. N. Israelachvili, *Intermolecular and Surface Forces: Revised Third Edition*. Academic Press, 2011.
[12] K. C. Neuman and A. Nagy, "Single-molecule force spectroscopy: optical tweezers, magnetic tweezers and atomic force microscopy," *Nat. Methods*, vol. 5, no. 6, pp. 491–505, Jun. 2008.
[13] S. Garcia-Manyes and F. Sanz, "Nanomechanics of lipid bilayers by force spectroscopy with AFM: A perspective," *Biochim. Biophys. Acta BBA - Biomembr.*, vol. 1798, no. 4, pp. 741–749, Apr. 2010.
[14] S. J. O'Shea, N. N. Gosvami, L. T. W. Lim, and W. Hofbauer, "Liquid Atomic Force Microscopy: Solvation Forces, Molecular Order, and Squeeze-Out," *Jpn. J. Appl. Phys.*, vol. 49, no. 8S3, p. 08LA01, Aug. 2010.
[15] C. Lee, X. Wei, J. W. Kysar, and J. Hone, "Measurement of the Elastic Properties and Intrinsic Strength of Monolayer Graphene," *Science*, vol. 321, no. 5887, pp. 385–388, Jul. 2008.
[16] J. Fraxedas, S. Garcia-Manyes, P. Gorostiza, and F. Sanz, "Nanoindentation: Toward the sensing of atomic interactions," *Proc. Natl. Acad. Sci.*, vol. 99, no. 8, pp. 5228–5232, Apr. 2002.
[17] S. Garcia-Manyes, J. Liang, R. Szoszkiewicz, T.-L. Kuo, and J. M. Fernández, "Force-activated reactivity switch in a bimolecular chemical reaction," *Nat. Chem.*, vol. 1, no. 3, pp. 236–242, Jun. 2009.
[18] M. Schlierf, H. Li, and J. M. Fernandez, "The unfolding kinetics of ubiquitin captured with single-molecule force-clamp techniques," *Proc. Natl. Acad. Sci. U. S. A.*, vol. 101, no. 19, pp. 7299–7304, May 2004.
[19] J. M. Fernandez and H. Li, "Force-Clamp Spectroscopy Monitors the Folding Trajectory of a Single Protein," *Science*, vol. 303, no. 5664, pp. 1674–1678, Mar. 2004.

[20] L. V. Chernomordik and M. M. Kozlov, "Mechanics of membrane fusion," *Nat. Struct. Mol. Biol.*, vol. 15, no. 7, pp. 675–683, Jul. 2008.
[21] P. A. Tipler and G. Mosca, *Physics for Scientists and Engineers, Volume 2: Electricity, Magnetism, Light, and Elementary Modern Physics*. W. H. Freeman, 2004.
[22] M. i S. Pere, M. C. Cadevall, N. L. i Isern, and J. V. Olià, *Ciència dels materials (2a edició)*. Edicions Universitat Barcelona, 2011.
[23] P. Atkins and J. de Paula, *Atkins' Physical Chemistry*. OUP Oxford, 2010.
[24] M. Grandbois, M. Beyer, M. Rief, H. Clausen-Schaumann, and H. E. Gaub, "How Strong Is a Covalent Bond?," *Science*, vol. 283, no. 5408, pp. 1727–1730, Mar. 1999.
[25] S. Garcia-Manyes, J. Liang, R. Szoszkiewicz, T.-L. Kuo, and J. M. Fernández, "Force-activated reactivity switch in a bimolecular chemical reaction," *Nat. Chem.*, vol. 1, no. 3, pp. 236–242, Jun. 2009.
[26] Y. Zhu, S. Murali, W. Cai, X. Li, J. W. Suk, J. R. Potts, and R. S. Ruoff, "Graphene and Graphene Oxide: Synthesis, Properties, and Applications," *Adv. Mater.*, vol. 22, no. 35, pp. 3906–3924, Sep. 2010.
[27] M. J. Allen, V. C. Tung, and R. B. Kaner, "Honeycomb Carbon: A Review of Graphene," *Chem. Rev.*, vol. 110, no. 1, pp. 132–145, Jan. 2010.
[28] D. R. Askeland, P. P. Fulay, and W. J. Wright, *The Science and Engineering of Materials*. Cengage Learning, 2010.
[29] T. Welton, "Ionic liquids in catalysis," *Coord. Chem. Rev.*, vol. 248, no. 21–24, pp. 2459–2477, Dec. 2004.
[30] T. P. Thuy Pham, C.-W. Cho, and Y.-S. Yun, "Environmental fate and toxicity of ionic liquids: A review," *Water Res.*, vol. 44, no. 2, pp. 352–372, Jan. 2010.
[31] K. N. Marsh, J. A. Boxall, and R. Lichtenthaler, "Room temperature ionic liquids and their mixtures—a review," *Fluid Phase Equilibria*, vol. 219, no. 1, pp. 93–98, May 2004.
[32] S. Pandey, "Analytical applications of room-temperature ionic liquids: A review of recent efforts," *Anal. Chim. Acta*, vol. 556, no. 1, pp. 38–45, Jan. 2006.
[33] "JPK Instruments AG - Image Gallery : Force Curves, Maps and Images - Atomic mica." [Online]. Available: http://usa.jpk.com/atomic-mica.771.us.html. [Accessed: 29-Apr-2016].
[34] T. Fukuma, M. J. Higgins, and S. P. Jarvis, "Direct Imaging of Lipid-Ion Network Formation under Physiological Conditions by Frequency Modulation Atomic Force Microscopy," *Phys. Rev. Lett.*, vol. 98, no. 10, p. 106101, Mar. 2007.
[35] H. Asakawa and T. Fukuma, "The molecular-scale arrangement and mechanical strength of phospholipid/cholesterol mixed bilayers investigated by frequency modulation atomic force microscopy in liquid," *Nanotechnology*, vol. 20, no. 26, p. 264008, 2009.
[36] T. Fukuma, "Subnanometer-Resolution Frequency Modulation Atomic Force Microscopy in Liquid for Biological Applications," *Jpn. J. Appl. Phys.*, vol. 48, no. 8, p. 08JA01, Aug. 2009.
[37] P. Ball, "Water: Water — an enduring mystery," *Nature*, vol. 452, no. 7185, pp. 291–292, Mar. 2008.
[38] S. Garcia-Manyes, G. Oncins, and F. Sanz, "Effect of Ion-Binding and Chemical Phospholipid Structure on the Nanomechanics of Lipid

Bilayers Studied by Force Spectroscopy," *Biophys. J.*, vol. 89, no. 3, pp. 1812–1826, Sep. 2005.
[39] "Lennard-Jones potential," *Wikipedia, the free encyclopedia*. 09-Mar-2016.
[40] K. Autumn and A. M. Peattie, "Mechanisms of Adhesion in Geckos," *Integr. Comp. Biol.*, vol. 42, no. 6, pp. 1081–1090, Dec. 2002.
[41] R. J. Hunter, *Introduction to Modern Colloid Science*. Oxford University Press, 1993.
[42] D. Myers, *Surfaces, interfaces, and colloids: principles and applications*. Wiley-VCH, 1999.
[43] A. L. Lehninger, D. L. Nelson, and M. M. Cox, *Lehninger Principles of Biochemistry*. W. H. Freeman, 2005.
[44] R. A. Böckmann and H. Grubmüller, "Multistep Binding of Divalent Cations to Phospholipid Bilayers: A Molecular Dynamics Study," *Angew. Chem. Int. Ed.*, vol. 43, no. 8, pp. 1021–1024, Feb. 2004.
[45] S. Mabrey and J. M. Sturtevant, "Investigation of phase transitions of lipids and lipid mixtures by sensitivity differential scanning calorimetry," *Proc. Natl. Acad. Sci.*, vol. 73, no. 11, pp. 3862–3866, Nov. 1976.
[46] R. L. Biltonen and D. Lichtenberg, "The use of differential scanning calorimetry as a tool to characterize liposome preparations," *Chem. Phys. Lipids*, vol. 64, no. 1, pp. 129–142, Sep. 1993.
[47] H. Reinl, T. Brumm, and T. M. Bayerl, "Changes of the physical properties of the liquid-ordered phase with temperature in binary mixtures of DPPC with cholesterol," *Biophys. J.*, vol. 61, no. 4, pp. 1025–1035, Apr. 1992.
[48] W. Curatolo, B. Sears, and L. J. Neuringer, "A calorimetry and deuterium NMR study of mixed model membranes of 1-palmitoyl-2-oleylphosphatidylcholine and saturated phosphatidylcholines," *Biochim. Biophys. Acta BBA - Biomembr.*, vol. 817, no. 2, pp. 261–270, Jul. 1985.
[49] J. F. Nagle and S. Tristram-Nagle, "Structure of lipid bilayers," *Biochim. Biophys. Acta BBA - Rev. Biomembr.*, vol. 1469, no. 3, pp. 159–195, Nov. 2000.
[50] T. P. W. McMullen and R. N. McElhaney, "New aspects of the interaction of cholesterol with dipalmitoylphosphatidylcholine bilayers as revealed by high-sensitivity differential scanning calorimetry," *Biochim. Biophys. Acta BBA - Biomembr.*, vol. 1234, no. 1, pp. 90–98, Mar. 1995.
[51] S. Karmakar, V. A. Raghunathan, and S. Mayor, "Phase behaviour of dipalmitoyl phosphatidylcholine (DPPC)-cholesterol membranes," *J. Phys. Condens. Matter*, vol. 17, no. 14, p. S1177, 2005.
[52] Y.-W. Chiang, A. J. Costa-Filho, and J. H. Freed, "Dynamic Molecular Structure and Phase Diagram of DPPC−Cholesterol Binary Mixtures: A 2D-ELDOR Study," *J. Phys. Chem. B*, vol. 111, no. 38, pp. 11260–11270, Sep. 2007.
[53] D. Marsh, "Liquid-ordered phases induced by cholesterol: A compendium of binary phase diagrams," *Biochim. Biophys. Acta BBA - Biomembr.*, vol. 1798, no. 3, pp. 688–699, Mar. 2010.
[54] C. Eggeling, C. Ringemann, R. Medda, G. Schwarzmann, K. Sandhoff, S. Polyakova, V. N. Belov, B. Hein, C. von Middendorff, A. Schönle, and S. W. Hell, "Direct observation of the nanoscale dynamics of

membrane lipids in a living cell," *Nature*, vol. 457, no. 7233, pp. 1159–1162, Feb. 2009.

[55] K. Simons and D. Toomre, "Lipid rafts and signal transduction," *Nat. Rev. Mol. Cell Biol.*, vol. 1, no. 1, pp. 31–39, Oct. 2000.

[56] K. Jacobson, O. G. Mouritsen, and R. G. W. Anderson, "Lipid rafts: at a crossroad between cell biology and physics," *Nat. Cell Biol.*, vol. 9, no. 1, pp. 7–14, Jan. 2007.

[57] S. Garcia-Manyes, L. Redondo-Morata, G. Oncins, and F. Sanz, "Nanomechanics of Lipid Bilayers: Heads or Tails?," *J. Am. Chem. Soc.*, vol. 132, no. 37, pp. 12874–12886, Sep. 2010.

[58] L. Bo and R. E. Waugh, "Determination of bilayer membrane bending stiffness by tether formation from giant, thin-walled vesicles," *Biophys. J.*, vol. 55, no. 3, pp. 509–517, Mar. 1989.

[59] L. Picas, M. T. Montero, A. Morros, M. E. Cabañas, B. Seantier, P.-E. Milhiet, and J. Hernández-Borrell, "Calcium-Induced Formation of Subdomains in Phosphatidylethanolamine−Phosphatidylglycerol Bilayers: A Combined DSC, 31P NMR, and AFM Study," *J. Phys. Chem. B*, vol. 113, no. 14, pp. 4648–4655, Apr. 2009.

[60] A. Barnett and J. C. Weaver, "Electroporation: A unified, quantitative theory of reversible electrical breakdown and mechanical rupture in artificial planar bilayer membranes," *Bioelectrochem. Bioenerg.*, vol. 25, no. 2, pp. 163–182, Apr. 1991.

[61] J. C. Weaver and Y. A. Chizmadzhev, "Theory of electroporation: A review," *Bioelectrochem. Bioenerg.*, vol. 41, no. 2, pp. 135–160, Dec. 1996.

[62] L. V. Chernomordik, V. A. Frolov, E. Leikina, P. Bronk, and J. Zimmerberg, "The Pathway of Membrane Fusion Catalyzed by Influenza Hemagglutinin: Restriction of Lipids, Hemifusion, and Lipidic Fusion Pore Formation," *J. Cell Biol.*, vol. 140, no. 6, pp. 1369–1382, Mar. 1998.

[63] J. C. Rasaiah, S. Garde, and G. Hummer, "Water in Nonpolar Confinement: From Nanotubes to Proteins and Beyond," *Annu. Rev. Phys. Chem.*, vol. 59, no. 1, pp. 713–740, 2008.

[64] R. G. Horn and J. N. Israelachvili, "Direct measurement of structural forces between two surfaces in a nonpolar liquid," *J. Chem. Phys.*, vol. 75, no. 3, pp. 1400–1411, Aug. 1981.

[65] R. G. Horn, D. F. Evans, and B. W. Ninham, "Double-layer and solvation forces measured in a molten salt and its mixtures with water," *J. Phys. Chem.*, vol. 92, no. 12, pp. 3531–3537, Jun. 1988.

[66] R. Lim and S. J. O'Shea, "Solvation Forces in Branched Molecular Liquids," *Phys. Rev. Lett.*, vol. 88, no. 24, p. 246101, May 2002.

[67] N. N. Gosvami, S. K. Sinha, and S. J. O'Shea, "Squeeze-Out of Branched Alkanes on Graphite," *Phys. Rev. Lett.*, vol. 100, no. 7, p. 076101, Feb. 2008.

[68] V. Franz and H.-J. Butt, "Confined Liquids: Solvation Forces in Liquid Alcohols between Solid Surfaces," *J. Phys. Chem. B*, vol. 106, no. 7, pp. 1703–1708, Feb. 2002.

[69] R. Atkin and G. G. Warr, "Structure in Confined Room-Temperature Ionic Liquids," *J. Phys. Chem. C*, vol. 111, no. 13, pp. 5162–5168, Apr. 2007.

[70] R. Hayes, G. G. Warr, and R. Atkin, "At the interface: solvation and designing ionic liquids," *Phys. Chem. Chem. Phys.*, vol. 12, no. 8, pp. 1709–1723, Feb. 2010.

[71] J. I. Kilpatrick, S.-H. Loh, and S. P. Jarvis, "Directly Probing the Effects of Ions on Hydration Forces at Interfaces," *J. Am. Chem. Soc.*, vol. 135, no. 7, pp. 2628–2634, Feb. 2013.

[72] B. V. Derjaguin, A. S. Titijevskaia, I. I. Abricossova, and A. D. Malkina, "Investigations of the forces of interaction of surfaces in different media and their application to the problem of colloid stability," *Discuss. Faraday Soc.*, vol. 18, no. 0, pp. 24–41, Jan. 1954.

[73] B. V. Derjaguin, I. I. Abrikosova, and E. M. Lifshitz, "Direct measurement of molecular attraction between solids separated by a narrow gap," *Q. Rev. Chem. Soc.*, vol. 10, no. 3, pp. 295–329, Jan. 1956.

[74] J. N. Israelachvili and D. Tabor, "The Measurement of Van Der Waals Dispersion Forces in the Range 1.5 to 130 nm," *Proc. R. Soc. Lond. Math. Phys. Eng. Sci.*, vol. 331, no. 1584, pp. 19–38, Nov. 1972.

[75] D. Tabor and R. H. S. Winterton, "The Direct Measurement of Normal and Retarded van der Waals Forces," *Proc. R. Soc. Lond. Math. Phys. Eng. Sci.*, vol. 312, no. 1511, pp. 435–450, Sep. 1969.

[76] G. Binnig, H. Rohrer, C. Gerber, and E. Weibel, "Surface Studies by Scanning Tunneling Microscopy," *Phys. Rev. Lett.*, vol. 49, no. 1, pp. 57–61, Jul. 1982.

[77] G. Binnig, C. F. Quate, and C. Gerber, "Atomic Force Microscope," *Phys. Rev. Lett.*, vol. 56, no. 9, pp. 930–933, Mar. 1986.

[78] A. Ashkin, J. M. Dziedzic, J. E. Bjorkholm, and S. Chu, "Observation of a single-beam gradient force optical trap for dielectric particles," *Opt. Lett.*, vol. 11, no. 5, p. 288, May 1986.

[79] K. C. Neuman and A. Nagy, "Single-molecule force spectroscopy: optical tweezers, magnetic tweezers and atomic force microscopy," *Nat. Methods*, vol. 5, no. 6, pp. 491–505, Jun. 2008.

[80] H. Chen, G. Yuan, R. S. Winardhi, M. Yao, I. Popa, J. M. Fernandez, and J. Yan, "Dynamics of Equilibrium Folding and Unfolding Transitions of Titin Immunoglobulin Domain under Constant Forces," *J. Am. Chem. Soc.*, vol. 137, no. 10, pp. 3540–3546, Mar. 2015.

[81] D. Tabor and R. H. S. Winterton, "The Direct Measurement of Normal and Retarded van der Waals Forces," *Proc. R. Soc. Lond. Math. Phys. Eng. Sci.*, vol. 312, no. 1511, pp. 435–450, Sep. 1969.

[82] J. N. Israelachvili and D. Tabor, "The Measurement of Van Der Waals Dispersion Forces in the Range 1.5 to 130 nm," *Proc. R. Soc. Lond. Math. Phys. Eng. Sci.*, vol. 331, no. 1584, pp. 19–38, Nov. 1972.

[83] J. B. Sykes and D. ter Haar, *Perspectives in Theoretical Physics: The Collected Papers of E\M\Lifshitz*. Newnes, 2012.

[84] I. E. Dzyaloshinskii, E. M. Lifshitz, and L. P. Pitaevskii, "GENERAL THEORY OF VAN DER WAALS' FORCES," *Sov. Phys. Uspekhi*, vol. 4, no. 2, pp. 153–176, Feb. 1961.

[85] J. Israelachvili, Y. Min, M. Akbulut, A. Alig, G. Carver, W. Greene, K. Kristiansen, E. Meyer, N. Pesika, K Rosenberg, and H. Zeng, "Recent advances in the surface forces apparatus (SFA) technique," *Rep. Prog. Phys.*, vol. 73, no. 3, p. 036601, 2010.

[86] R. M. Pashley and J. N. Israelachvili, “Dlvo and hydration forces between mica surfaces in Mg2+, Ca2+, Sr2+, and Ba2+ chloride solutions,” *J. Colloid Interface Sci.*, vol. 97, no. 2, pp. 446–455, Feb. 1984.

[87] R. Tadmor, E. Hernández-Zapata, N. Chen, P. Pincus, and J. N. Israelachvili, “Debye Length and Double-Layer Forces in Polyelectrolyte Solutions,” *Macromolecules*, vol. 35, no. 6, pp. 2380–2388, Mar. 2002.

[88] J. N. Israelachvili and P. M. McGuiggan, “Forces Between Surfaces in Liquids,” *Science*, vol. 241, no. 4867, pp. 795–800, Aug. 1988.

[89] “Molecular mechanisms and forces involved in the adhesion and fusion of amphiphilic bilayers | Science.” [Online]. Available: http://science.sciencemag.org/content/246/4932/919. [Accessed: 12-Mar-2016].

[90] C. A. Helm, J. N. Israelachvili, and P. M. McGuiggan, “Role of hydrophobic forces in bilayer adhesion and fusion,” *Biochemistry (Mosc.)*, vol. 31, no. 6, pp. 1794–1805, Feb. 1992.

[91] [Online]. Available: https://scholar.google.co.uk/scholar.bib?q=info:bVmyeoNNEpwJ:scholar.google.com/&output=citation&scisig=AAGBfm0AAAAAVuO_Py5X2Q-pSupCCwhnP7pY28Y135d-&scisf=4&hl=ca. [Accessed: 12-Mar-2016].

[92] H. Yoshizawa, C. You-Lung, and J. Israelachvili, “Recent advances in molecular level understanding of adhesion, friction and lubrication,” *Wear*, vol. 168, no. 1–2, pp. 161–166, Sep. 1993.

[93] R. G. Horn, D. R. Clarke, and M. T. Clarkson, “Direct measurement of surface forces between sapphire crystals in aqueous solutions,” *J. Mater. Res.*, vol. 3, no. 03, pp. 413–416, Jun. 1988.

[94] R. G. Horn, D. T. Smith, and W. Haller, “Surface forces and viscosity of water measured between silica sheets,” *Chem. Phys. Lett.*, vol. 162, no. 4, pp. 404–408, Oct. 1989.

[95] N. Maeda, N. Chen, M. Tirrell, and J. N. Israelachvili, “Adhesion and Friction Mechanisms of Polymer-on-Polymer Surfaces,” *Science*, vol. 297, no. 5580, pp. 379–382, Jul. 2002.

[96] W. Helfrich and R.-M. Servuss, “Undulations, steric interaction and cohesion of fluid membranes,” *Il Nuovo Cimento D*, vol. 3, no. 1, pp. 137–151, Jan. 1984.

[97] null Evans and null Rawicz, “Entropy-driven tension and bending elasticity in condensed-fluid membranes,” *Phys. Rev. Lett.*, vol. 64, no. 17, pp. 2094–2097, Apr. 1990.

[98] W. Helfrich and R.-M. Servuss, “Undulations, steric interaction and cohesion of fluid membranes,” *Il Nuovo Cimento D*, vol. 3, no. 1, pp. 137–151, Jan. 1984.

[99] W. Rawicz, K. C. Olbrich, T. McIntosh, D. Needham, and E. Evans, “Effect of chain length and unsaturation on elasticity of lipid bilayers,” *Biophys. J.*, vol. 79, no. 1, pp. 328–339, Jul. 2000.

[100] K. J. Tierney, D. E. Block, and M. L. Longo, “Elasticity and phase behavior of DPPC membrane modulated by cholesterol, ergosterol, and ethanol,” *Biophys. J.*, vol. 89, no. 4, pp. 2481–2493, Oct. 2005.

[101] M. Goulian, O. N. Mesquita, D. K. Fygenson, C. Nielsen, O. S. Andersen, and A. Libchaber, “Gramicidin channel kinetics under tension,” *Biophys. J.*, vol. 74, no. 1, pp. 328–337, Jan. 1998.

[102] R. M. Hochmuth, "Micropipette aspiration of living cells," *J. Biomech.*, vol. 33, no. 1, pp. 15–22, Jan. 2000.
[103] W. R. Jones, H. P. Ting-Beall, G. M. Lee, S. S. Kelley, R. M. Hochmuth, and F. Guilak, "Alterations in the Young's modulus and volumetric properties of chondrocytes isolated from normal and osteoarthritic human cartilage," *J. Biomech.*, vol. 32, no. 2, pp. 119–127, Feb. 1999.
[104] D. P. Theret, M. J. Levesque, M. Sato, R. M. Nerem, and L. T. Wheeler, "The application of a homogeneous half-space model in the analysis of endothelial cell micropipette measurements," *J. Biomech. Eng.*, vol. 110, no. 3, pp. 190–199, Aug. 1988.
[105] T. Luo, K. Mohan, P. A. Iglesias, and D. N. Robinson, "Molecular mechanisms of cellular mechanosensing," *Nat. Mater.*, vol. 12, no. 11, pp. 1064–1071, Nov. 2013.
[106] S. E. Chesla, P. Selvaraj, and C. Zhu, "Measuring two-dimensional receptor-ligand binding kinetics by micropipette," *Biophys. J.*, vol. 75, no. 3, pp. 1553–1572, Sep. 1998.
[107] E. Evans, A. Leung, V. Heinrich, and C. Zhu, "Mechanical switching and coupling between two dissociation pathways in a P-selectin adhesion bond," *Proc. Natl. Acad. Sci. U. S. A.*, vol. 101, no. 31, pp. 11281–11286, Aug. 2004.
[108] J. E. Molloy and M. J. Padgett, "Lights, action: Optical tweezers," *Contemp. Phys.*, vol. 43, no. 4, pp. 241–258, Jul. 2002.
[109] S. M. Block, L. S. Goldstein, and B. J. Schnapp, "Bead movement by single kinesin molecules studied with optical tweezers," *Nature*, vol. 348, no. 6299, pp. 348–352, Nov. 1990.
[110] K. Svoboda and S. M. Block, "Force and velocity measured for single kinesin molecules," *Cell*, vol. 77, no. 5, pp. 773–784, Jun. 1994.
[111] K. Svoboda, C. F. Schmidt, B. J. Schnapp, and S. M. Block, "Direct observation of kinesin stepping by optical trapping interferometry," *Nature*, vol. 365, no. 6448, pp. 721–727, Oct. 1993.
[112] M. Mammen, K. Helmerson, R. Kishore, S. K. Choi, W. D. Phillips, and G. M. Whitesides, "Optically controlled collisions of biological objects to evaluate potent polyvalent inhibitors of virus-cell adhesion," *Chem. Biol.*, vol. 3, no. 9, pp. 757–763, Sep. 1996.
[113] R. I. Litvinov, H. Shuman, J. S. Bennett, and J. W. Weisel, "Binding strength and activation state of single fibrinogen-integrin pairs on living cells," *Proc. Natl. Acad. Sci. U. S. A.*, vol. 99, no. 11, pp. 7426–7431, May 2002.
[114] M. D. Wang, M. J. Schnitzer, H. Yin, R. Landick, J. Gelles, and S. M. Block, "Force and velocity measured for single molecules of RNA polymerase," *Science*, vol. 282, no. 5390, pp. 902–907, Oct. 1998.
[115] K. C. Neuman, E. A. Abbondanzieri, R. Landick, J. Gelles, and S. M. Block, "Ubiquitous transcriptional pausing is independent of RNA polymerase backtracking," *Cell*, vol. 115, no. 4, pp. 437–447, Nov. 2003.
[116] K. M. Herbert, A. La Porta, B. J. Wong, R. A. Mooney, K. C. Neuman, R. Landick, and S. M. Block, "Sequence-resolved detection of pausing by single RNA polymerase molecules," *Cell*, vol. 125, no. 6, pp. 1083–1094, Jun. 2006.
[117] J. W. Shaevitz, E. A. Abbondanzieri, R. Landick, and S. M. Block, "Backtracking by single RNA polymerase molecules observed at near-base-pair resolution," *Nature*, vol. 426, no. 6967, pp. 684–687, Dec. 2003.

[118] E. A. Abbondanzieri, W. J. Greenleaf, J. W. Shaevitz, R. Landick, and S. M. Block, "Direct observation of base-pair stepping by RNA polymerase," *Nature*, vol. 438, no. 7067, pp. 460–465, Nov. 2005.
[119] M. S. Kellermayer, S. B. Smith, H. L. Granzier, and C. Bustamante, "Folding-unfolding transitions in single titin molecules characterized with laser tweezers," *Science*, vol. 276, no. 5315, pp. 1112–1116, May 1997.
[120] J. Liphardt, B. Onoa, S. B. Smith, I. Tinoco, and C. Bustamante, "Reversible unfolding of single RNA molecules by mechanical force," *Science*, vol. 292, no. 5517, pp. 733–737, Apr. 2001.
[121] C. Bustamante, Z. Bryant, and S. B. Smith, "Ten years of tension: single-molecule DNA mechanics," *Nature*, vol. 421, no. 6921, pp. 423–427, Jan. 2003.
[122] "Atomic-force microscopy," *Wikipedia, the free encyclopedia*. 01-May-2016.
[123] J. Domke and M. Radmacher, "Measuring the Elastic Properties of Thin Polymer Films with the Atomic Force Microscope," *Langmuir*, vol. 14, no. 12, pp. 3320–3325, Jun. 1998.
[124] B. Du, O. K. C. Tsui, Q. Zhang, and T. He, "Study of Elastic Modulus and Yield Strength of Polymer Thin Films Using Atomic Force Microscopy," *Langmuir*, vol. 17, no. 11, pp. 3286–3291, May 2001.
[125] M. R. Angle, A. Wang, A. Thomas, A. T. Schaefer, and N. A. Melosh, "Penetration of Cell Membranes and Synthetic Lipid Bilayers by Nanoprobes," *Biophys. J.*, vol. 107, no. 9, pp. 2091–2100, Nov. 2014.
[126] E. Moeendarbary, L. Valon, M. Fritzsche, A. R. Harris, D. A. Moulding, A. J. Thrasher, E. Stride, L. Mahadevan, and G. T. Charras, "The cytoplasm of living cells behaves as a poroelastic material," *Nat. Mater.*, vol. 12, no. 3, pp. 253–261, Mar. 2013.
[127] F. L. Leite and P. S. P. Herrmann, "Application of atomic force spectroscopy (AFS) to studies of adhesion phenomena: a review," *J. Adhes. Sci. Technol.*, vol. 19, no. 3–5, pp. 365–405, Jan. 2005.
[128] M. Rief, M. Gautel, F. Oesterhelt, J. M. Fernandez, and H. E. Gaub, "Reversible Unfolding of Individual Titin Immunoglobulin Domains by AFM," *Science*, vol. 276, no. 5315, pp. 1109–1112, May 1997.
[129] M. Schlierf, H. Li, and J. M. Fernandez, "The unfolding kinetics of ubiquitin captured with single-molecule force-clamp techniques," *Proc. Natl. Acad. Sci. U. S. A.*, vol. 101, no. 19, pp. 7299–7304, May 2004.
[130] S. Garcia-Manyes, J. Brujić, C. L. Badilla, and J. M. Fernández, "Force-Clamp Spectroscopy of Single-Protein Monomers Reveals the Individual Unfolding and Folding Pathways of I27 and Ubiquitin," *Biophys. J.*, vol. 93, no. 7, pp. 2436–2446, Oct. 2007.
[131] D. J. Müller and A. Engel, "Atomic force microscopy and spectroscopy of native membrane proteins," *Nat. Protoc.*, vol. 2, no. 9, pp. 2191–2197, Sep. 2007.
[132] S. Garcia-Manyes, J. Liang, R. Szoszkiewicz, T.-L. Kuo, and J. M. Fernández, "Force-activated reactivity switch in a bimolecular chemical reaction," *Nat. Chem.*, vol. 1, no. 3, pp. 236–242, Jun. 2009.
[133] S. Garcia-Manyes, G. Oncins, and F. Sanz, "Effect of pH and ionic strength on phospholipid nanomechanics and on deposition process onto hydrophilic surfaces measured by AFM," *Electrochimica Acta*, vol. 51, no. 24, pp. 5029–5036, Jul. 2006.

[134] L. Redondo-Morata, G. Oncins, and F. Sanz, "Force Spectroscopy Reveals the Effect of Different Ions in the Nanomechanical Behavior of Phospholipid Model Membranes: The Case of Potassium Cation," *Biophys. J.*, vol. 102, no. 1, pp. 66–74, Jan. 2012.
[135] L. Redondo-Morata, M. I. Giannotti, and F. Sanz, "Influence of Cholesterol on the Phase Transition of Lipid Bilayers: A Temperature-Controlled Force Spectroscopy Study," *Langmuir*, vol. 28, no. 35, pp. 12851–12860, Sep. 2012.
[136] S. Garcia-Manyes, G. Oncins, and F. Sanz, "Effect of Temperature on the Nanomechanics of Lipid Bilayers Studied by Force Spectroscopy," *Biophys. J.*, vol. 89, no. 6, pp. 4261–4274, Dec. 2005.
[137] L. Picas, F. Rico, and S. Scheuring, "Direct Measurement of the Mechanical Properties of Lipid Phases in Supported Bilayers," *Biophys. J.*, vol. 102, no. 1, pp. L01–L03, Jan. 2012.
[138] P. A. Tipler and G. Mosca, *Physics for Scientists and Engineers, Volume 1: Mechanics, Oscillations and Waves; Thermodynamics*, Fifth Edition edition. New York: W. H. Freeman, 2003.
[139] R. W. Stark, T. Drobek, and W. M. Heckl, "Thermomechanical noise of a free v-shaped cantilever for atomic-force microscopy," *Ultramicroscopy*, vol. 86, no. 1–2, pp. 207–215, Jan. 2001.
[140] "Equipartition theorem," *Wikipedia, the free encyclopedia*. 31-Mar-2016.
[141] J. M. Fernandez and H. Li, "Force-Clamp Spectroscopy Monitors the Folding Trajectory of a Single Protein," *Science*, vol. 303, no. 5664, pp. 1674–1678, Mar. 2004.
[142] S. Garcia-Manyes, J. Liang, R. Szoszkiewicz, T.-L. Kuo, and J. M. Fernández, "Force-activated reactivity switch in a bimolecular chemical reaction," *Nat. Chem.*, vol. 1, no. 3, pp. 236–242, Jun. 2009.
[143] S. Garcia-Manyes, G. Oncins, and F. Sanz, "Effect of Ion-Binding and Chemical Phospholipid Structure on the Nanomechanics of Lipid Bilayers Studied by Force Spectroscopy," *Biophys. J.*, vol. 89, no. 3, pp. 1812–1826, Sep. 2005.
[144] "Young's modulus," *Wikipedia, the free encyclopedia*. 30-Mar-2016.
[145] K. L. Johnson and K. L. Johnson, *Contact Mechanics*. Cambridge University Press, 1987.
[146] K. L. Johnson and K. L. Johnson, *Contact Mechanics*. Cambridge University Press, 1987.
[147] J. Fraxedas, S. Garcia-Manyes, P. Gorostiza, and F. Sanz, "Nanoindentation: Toward the sensing of atomic interactions," *Proc. Natl. Acad. Sci.*, vol. 99, no. 8, pp. 5228–5232, Apr. 2002.
[148] L. Redondo-Morata, M. I. Giannotti, and F. Sanz, "AFM-Based Force-Clamp Monitors Lipid Bilayer Failure Kinetics," *Langmuir*, vol. 28, no. 15, pp. 6403–6410, Apr. 2012.
[149] C. Lee, X. Wei, J. W. Kysar, and J. Hone, "Measurement of the Elastic Properties and Intrinsic Strength of Monolayer Graphene," *Science*, vol. 321, no. 5887, pp. 385–388, Jul. 2008.
[150] E. Moeendarbary, L. Valon, M. Fritzsche, A. R. Harris, D. A. Moulding, A. J. Thrasher, E. Stride, L. Mahadevan, and G. T. Charras, "The cytoplasm of living cells behaves as a poroelastic material," *Nat. Mater.*, vol. 12, no. 3, pp. 253–261, Mar. 2013.

[151] K. L. Johnson, K. Kendall, and A. D. Roberts, “Surface Energy and the Contact of Elastic Solids,” *Proc. R. Soc. Lond. Math. Phys. Eng. Sci.*, vol. 324, no. 1558, pp. 301–313, Sep. 1971.
[152] B. V. Derjaguin, V. M. Muller, and Y. P. Toporov, “Effect of contact deformations on the adhesion of particles,” *J. Colloid Interface Sci.*, vol. 53, no. 2, pp. 314–326, Nov. 1975.
[153] V. M. Muller, B. V. Derjaguin, and Y. P. Toporov, “On two methods of calculation of the force of sticking of an elastic sphere to a rigid plane,” *Colloids Surf.*, vol. 7, no. 3, pp. 251–259, Aug. 1983.
[154] E. Evans and K. Ritchie, “Dynamic strength of molecular adhesion bonds,” *Biophys. J.*, vol. 72, no. 4, pp. 1541–1555, Apr. 1997.
[155] S. Garcia-Manyes and F. Sanz, “Nanomechanics of lipid bilayers by force spectroscopy with AFM: A perspective,” *Biochim. Biophys. Acta BBA - Biomembr.*, vol. 1798, no. 4, pp. 741–749, Apr. 2010.
[156] S. J. O’Shea, N. N. Gosvami, L. T. W. Lim, and W. Hofbauer, “Liquid Atomic Force Microscopy: Solvation Forces, Molecular Order, and Squeeze-Out,” *Jpn. J. Appl. Phys.*, vol. 49, no. 8S3, p. 08LA01, Aug. 2010.
[157] G. I. Bell, “Models for the specific adhesion of cells to cells,” *Science*, vol. 200, no. 4342, pp. 618–627, May 1978.
[158] H. A. Kramers, “Brownian motion in a field of force and the diffusion model of chemical reactions,” *Physica*, vol. 7, no. 4, pp. 284–304, Apr. 1940.
[159] P. Hänggi, P. Talkner, and M. Borkovec, “Reaction-rate theory: fifty years after Kramers,” *Rev. Mod. Phys.*, vol. 62, no. 2, pp. 251–341, Apr. 1990.
[160] M. Schlierf, H. Li, and J. M. Fernandez, “The unfolding kinetics of ubiquitin captured with single-molecule force-clamp techniques,” *Proc. Natl. Acad. Sci. U. S. A.*, vol. 101, no. 19, pp. 7299–7304, May 2004.
[161] A. P. Wiita, S. R. K. Ainavarapu, H. H. Huang, and J. M. Fernandez, “Force-dependent chemical kinetics of disulfide bond reduction observed with single-molecule techniques,” *Proc. Natl. Acad. Sci.*, vol. 103, no. 19, pp. 7222–7227, May 2006.
[162] W. E. Thomas, V. Vogel, and E. Sokurenko, “Biophysics of Catch Bonds,” *Annu. Rev. Biophys.*, vol. 37, no. 1, pp. 399–416, 2008.
[163] H.-J. Butt and V. Franz, “Rupture of molecular thin films observed in atomic force microscopy. I. Theory,” *Phys. Rev. E*, vol. 66, no. 3, p. 031601, Sep. 2002.
[164] S. Loi, G. Sun, V. Franz, and H.-J. Butt, “Rupture of molecular thin films observed in atomic force microscopy. II. Experiment,” *Phys. Rev. E*, vol. 66, no. 3, p. 031602, Sep. 2002.
[165] O. K. Dudko, G. Hummer, and A. Szabo, “Intrinsic Rates and Activation Free Energies from Single-Molecule Pulling Experiments,” *Phys. Rev. Lett.*, vol. 96, no. 10, p. 108101, Mar. 2006.
[166] O. K. Dudko, G. Hummer, and A. Szabo, “Theory, analysis, and interpretation of single-molecule force spectroscopy experiments,” *Proc. Natl. Acad. Sci.*, vol. 105, no. 41, pp. 15755–15760, Oct. 2008.
[167] L. B. Freund, “Characterizing the resistance generated by a molecular bond as it is forcibly separated,” *Proc. Natl. Acad. Sci.*, vol. 106, no. 22, pp. 8818–8823, Jun. 2009.

[168] Y. Suzuki and O. K. Dudko, "Single-Molecule Rupture Dynamics on Multidimensional Landscapes," *Phys. Rev. Lett.*, vol. 104, no. 4, p. 048101, Jan. 2010.

[169] R. B. Best, E. Paci, G. Hummer, and O. K. Dudko, "Pulling Direction as a Reaction Coordinate for the Mechanical Unfolding of Single Molecules†," *J. Phys. Chem. B*, vol. 112, no. 19, pp. 5968–5976, May 2008.

[170] F. Rico, L. Gonzalez, I. Casuso, M. Puig-Vidal, and S. Scheuring, "High-Speed Force Spectroscopy Unfolds Titin at the Velocity of Molecular Dynamics Simulations," *Science*, vol. 342, no. 6159, pp. 741–743, Nov. 2013.

[171] J. Brujić, R. I. Z. Hermans, S. Garcia-Manyes, K. A. Walther, and J. M. Fernandez, "Dwell-Time Distribution Analysis of Polyprotein Unfolding Using Force-Clamp Spectroscopy," *Biophys. J.*, vol. 92, no. 8, pp. 2896–2903, Apr. 2007.

[172] T.-L. Kuo, S. Garcia-Manyes, J. Li, I. Barel, H. Lu, B. J. Berne, M. Urbakh, J. Klafter, and J. M. Fernández, "Probing static disorder in Arrhenius kinetics by single-molecule force spectroscopy," *Proc. Natl. Acad. Sci.*, vol. 107, no. 25, pp. 11336–11340, Jun. 2010.

[173] I. Popa, J. M. Fernández, and S. Garcia-Manyes, "Direct Quantification of the Attempt Frequency Determining the Mechanical Unfolding of Ubiquitin Protein," *J. Biol. Chem.*, vol. 286, no. 36, pp. 31072–31079, Sep. 2011.

[174] H. Lannon, E. Vanden-Eijnden, and J. Brujic, "Force-Clamp Analysis Techniques Give Highest Rank to Stretched Exponential Unfolding Kinetics in Ubiquitin," *Biophys. J.*, vol. 103, no. 10, pp. 2215–2222, Nov. 2012.

[175] S. National Institute of Standrads and Technology, "NIST/SEMATECH Engineering Statistics Handbook," *8.2.1. How do you choose an appropriate life distribution model?*, 27-Apr-2015. [Online]. Available: http://www.itl.nist.gov/div898/handbook/apr/section2/apr21.htm. [Accessed: 27-Apr-2015].

[176] S. National Institute of Standrads and Technology, "NIST/SEMATECH Engineering Statistics Handbook," *1.3.6.6.8. Weibull Distribution*, 27-Apr-2015. [Online]. Available: http://www.itl.nist.gov/div898/handbook/eda/section3/eda3668.htm. [Accessed: 27-Apr-2015].

[177] M. Wiggin, C. Tropini, V. Tabard-Cossa, N. N. Jetha, and A. Marziali, "Nonexponential Kinetics of DNA Escape from α-Hemolysin Nanopores," *Biophys. J.*, vol. 95, no. 11, pp. 5317–5323, Dec. 2008.

[178] F. Bezanilla, E. Perozo, and E. Stefani, "Gating of Shaker K+ channels: II. The components of gating currents and a model of channel activation," *Biophys. J.*, vol. 66, no. 4, pp. 1011–1021, Apr. 1994.

[179] D. Chatterjee and B. J. Cherayil, "Anomalous reaction-diffusion as a model of nonexponential DNA escape kinetics," *J. Chem. Phys.*, vol. 132, no. 2, p. 025103, Jan. 2010.

[180] D. Colquhoun and A. G. Hawkes, "On the Stochastic Properties of Bursts of Single Ion Channel Openings and of Clusters of Bursts," *Philos. Trans. R. Soc. Lond. B Biol. Sci.*, vol. 300, no. 1098, pp. 1–59, Dec. 1982.

[181] I. Goychuk and P. Hänggi, "Fractional diffusion modeling of ion channel gating," *Phys. Rev. E*, vol. 70, no. 5, p. 051915, Nov. 2004.

[182] F. Ritort, "Single-molecule experiments in biological physics: methods and applications," *J. Phys. Condens. Matter*, vol. 18, no. 32, p. R531, Aug. 2006.
[183] R. Liu, S. Garcia-Manyes, A. Sarkar, C. L. Badilla, and J. M. Fernández, "Mechanical Characterization of Protein L in the Low-Force Regime by Electromagnetic Tweezers/Evanescent Nanometry," *Biophys. J.*, vol. 96, no. 9, pp. 3810–3821, May 2009.
[184] S. Garcia-Manyes, L. Dougan, C. L. Badilla, J. Brujić, and J. M. Fernández, "Direct observation of an ensemble of stable collapsed states in the mechanical folding of ubiquitin," *Proc. Natl. Acad. Sci.*, vol. 106, no. 26, pp. 10534–10539, Jun. 2009.
[185] R. Berkovich, S. Garcia-Manyes, J. Klafter, M. Urbakh, and J. M. Fernández, "Hopping around an entropic barrier created by force," *Biochem. Biophys. Res. Commun.*, vol. 403, no. 1, pp. 133–137, Dec. 2010.
[186] A. F. Oberhauser, P. K. Hansma, M. Carrion-Vazquez, and J. M. Fernandez, "Stepwise unfolding of titin under force-clamp atomic force microscopy," *Proc. Natl. Acad. Sci.*, vol. 98, no. 2, pp. 468–472, Jan. 2001.
[187] J. Relat-Goberna and S. Garcia-Manyes, "Direct Observation of the Dynamics of Self-Assembly of Individual Solvation Layers in Molecularly Confined Liquids," *Phys. Rev. Lett.*, vol. 114, no. 25, p. 258303, Jun. 2015.
[188] B. Cappella and G. Dietler, "Force-distance curves by atomic force microscopy," *Surf. Sci. Rep.*, vol. 34, no. 1–3, pp. 1–104, 1999.
[189] H.-J. Butt and R. Stark, "Atomic force microscopy in structured liquids: remark on the interpretation of jumps in force curves," *Colloids Surf. Physicochem. Eng. Asp.*, vol. 252, no. 2–3, pp. 165–168, Jan. 2005.
[190] F. Liu, S. de Beer, D. van den Ende, and F. Mugele, "Atomic force microscopy of confined liquids using the thermal bending fluctuations of the cantilever," *Phys. Rev. E*, vol. 87, no. 6, p. 062406, Jun. 2013.
[191] R. Lim and S. J. O'Shea, "Solvation Forces in Branched Molecular Liquids," *Phys. Rev. Lett.*, vol. 88, no. 24, p. 246101, May 2002.
[192] N. N. Gosvami, S. K. Sinha, and S. J. O'Shea, "Squeeze-Out of Branched Alkanes on Graphite," *Phys. Rev. Lett.*, vol. 100, no. 7, p. 076101, Feb. 2008.
[193] V. Franz and H.-J. Butt, "Confined Liquids: Solvation Forces in Liquid Alcohols between Solid Surfaces," *J. Phys. Chem. B*, vol. 106, no. 7, pp. 1703–1708, Feb. 2002.
[194] R. Hayes, G. G. Warr, and R. Atkin, "At the interface: solvation and designing ionic liquids," *Phys. Chem. Chem. Phys.*, vol. 12, no. 8, pp. 1709–1723, Feb. 2010.
[195] R. Atkin and G. G. Warr, "Structure in Confined Room-Temperature Ionic Liquids," *J. Phys. Chem. C*, vol. 111, no. 13, pp. 5162–5168, Apr. 2007.
[196] M. Antognozzi, A. D. L. Humphris, and M. J. Miles, "Observation of molecular layering in a confined water film and study of the layers viscoelastic properties," *Appl. Phys. Lett.*, vol. 78, no. 3, pp. 300–302, Jan. 2001.
[197] J. I. Kilpatrick, S.-H. Loh, and S. P. Jarvis, "Directly Probing the Effects of Ions on Hydration Forces at Interfaces," *J. Am. Chem. Soc.*, vol. 135, no. 7, pp. 2628–2634, Feb. 2013.

[198] M. Schlierf, H. Li, and J. M. Fernandez, "The unfolding kinetics of ubiquitin captured with single-molecule force-clamp techniques," *Proc. Natl. Acad. Sci. U. S. A.*, vol. 101, no. 19, pp. 7299–7304, May 2004.
[199] K. Morishige and T. Kato, "Chain-length dependence of melting of n-alcohol monolayers adsorbed on graphite: n-hexanol, n-heptanol, n-octanol, and n-nonanol," *J. Chem. Phys.*, vol. 111, no. 15, pp. 7095–7102, Oct. 1999.
[200] F. Mugele, S. Baldelli, G. A. Somorjai, and M. Salmeron, "Structure of Confined Films of Chain Alcohols†," *J. Phys. Chem. B*, vol. 104, no. 14, pp. 3140–3144, Apr. 2000.
[201] T. Hiasa, K. Kimura, and H. Onishi, "Interfacial Structure of Primary and Tertiary Liquid Alcohols over Hydrophilic Thiolate Monolayers," *J. Phys. Chem. C*, vol. 117, no. 11, pp. 5730–5735, Mar. 2013.
[202] G. I. Bell, "Models for the specific adhesion of cells to cells," *Science*, vol. 200, no. 4342, pp. 618–627, May 1978.
[203] C. Cecconi, E. A. Shank, C. Bustamante, and S. Marqusee, "Direct Observation of the Three-State Folding of a Single Protein Molecule," *Science*, vol. 309, no. 5743, pp. 2057–2060, Sep. 2005.
[204] S. Garcia-Manyes, L. Dougan, C. L. Badilla, J. Brujić, and J. M. Fernández, "Direct observation of an ensemble of stable collapsed states in the mechanical folding of ubiquitin," *Proc. Natl. Acad. Sci.*, vol. 106, no. 26, pp. 10534–10539, Jun. 2009.
[205] L. Y. Low, "Review," *J. Am. Stat. Assoc.*, vol. 78, no. 384, p. 987, Dec. 1983.
[206] I. Popa, J. M. Fernández, and S. Garcia-Manyes, "Direct Quantification of the Attempt Frequency Determining the Mechanical Unfolding of Ubiquitin Protein," *J. Biol. Chem.*, vol. 286, no. 36, pp. 31072–31079, Sep. 2011.
[207] L. T. W. Lim, A. T. S. Wee, and S. J. O'Shea, "Temperature dependence of solvation forces as measured in atomic force microscopy," *J. Chem. Phys.*, vol. 130, no. 13, p. 134703, Apr. 2009.
[208] D. Wakeham, R. Hayes, G. G. Warr, and R. Atkin, "Influence of Temperature and Molecular Structure on Ionic Liquid Solvation Layers," *J. Phys. Chem. B*, vol. 113, no. 17, pp. 5961–5966, Apr. 2009.
[209] S. J. O'Shea and M. E. Welland, "Atomic Force Microscopy at Solid−Liquid Interfaces," *Langmuir*, vol. 14, no. 15, pp. 4186–4197, Jul. 1998.
[210] W. Hofbauer, R. J. Ho, H. R., N. N. Gosvami, and S. J. O'Shea, "Crystalline structure and squeeze-out dissipation of liquid solvation layers observed by small-amplitude dynamic AFM," *Phys. Rev. B*, vol. 80, no. 13, p. 134104, Oct. 2009.
[211] T. Hiasa, K. Kimura, and H. Onishi, "Cross-Sectional Structure of Liquid 1-Decanol over Graphite," *J. Phys. Chem. C*, vol. 116, no. 50, pp. 26475–26479, Dec. 2012.
[212] V. Vogel and M. Sheetz, "Local force and geometry sensing regulate cell functions," *Nat. Rev. Mol. Cell Biol.*, vol. 7, no. 4, pp. 265–275, Apr. 2006.
[213] G. E. Atilla-Gokcumen, E. Muro, J. Relat-Goberna, S. Sasse, A. Bedigian, M. L. Coughlin, S. Garcia-Manyes, and U. S. Eggert, "Dividing Cells Regulate Their Lipid Composition and Localization," *Cell*, vol. 156, no. 3, pp. 428–439, Jan. 2014.

[214] G. van den Bogaart, J. V. Guzmán, J. T. Mika, and B. Poolman, "On the Mechanism of Pore Formation by Melittin," *J. Biol. Chem.*, vol. 283, no. 49, pp. 33854–33857, Dec. 2008.

[215] A. S. Ladokhin, M. E. Selsted, and S. H. White, "Sizing membrane pores in lipid vesicles by leakage of co-encapsulated markers: pore formation by melittin.," *Biophys. J.*, vol. 72, no. 4, pp. 1762–1766, Apr. 1997.

[216] E. Breukink, I. Wiedemann, C. van Kraaij, O. P. Kuipers, H.-G. Sahl, and B. de Kruijff, "Use of the Cell Wall Precursor Lipid II by a Pore-Forming Peptide Antibiotic," *Science*, vol. 286, no. 5448, pp. 2361–2364, Dec. 1999.

[217] I. Wiedemann, R. Benz, and H.-G. Sahl, "Lipid II-Mediated Pore Formation by the Peptide Antibiotic Nisin: a Black Lipid Membrane Study," *J. Bacteriol.*, vol. 186, no. 10, pp. 3259–3261, May 2004.

[218] J. Teissie, M. Golzio, and M. P. Rols, "Mechanisms of cell membrane electropermeabilization: A minireview of our present (lack of ?) knowledge," *Biochim. Biophys. Acta BBA - Gen. Subj.*, vol. 1724, no. 3, pp. 270–280, Aug. 2005.

[219] M. Kotulska, "Natural Fluctuations of an Electropore Show Fractional Lévy Stable Motion," *Biophys. J.*, vol. 92, no. 7, pp. 2412–2421, Apr. 2007.

[220] D. P. Tieleman, H. Leontiadou, A. E. Mark, and S.-J. Marrink, "Simulation of Pore Formation in Lipid Bilayers by Mechanical Stress and Electric Fields," *J. Am. Chem. Soc.*, vol. 125, no. 21, pp. 6382–6383, May 2003.

[221] S. Garcia-Manyes and F. Sanz, "Nanomechanics of lipid bilayers by force spectroscopy with AFM: A perspective," *Biochim. Biophys. Acta BBA - Biomembr.*, vol. 1798, no. 4, pp. 741–749, Apr. 2010.

[222] R. M. A. Sullan, J. K. Li, and S. Zou, "Quantification of the Nanomechanical Stability of Ceramide-Enriched Domains," *Langmuir*, vol. 25, no. 22, pp. 12874–12877, Nov. 2009.

[223] S. Garcia-Manyes, L. Redondo-Morata, G. Oncins, and F. Sanz, "Nanomechanics of Lipid Bilayers: Heads or Tails?," *J Am Chem Soc*, vol. 132, no. 37, pp. 12874–12886, 2010.

[224] L. Redondo-Morata, M. I. Giannotti, and F. Sanz, "AFM-Based Force-Clamp Monitors Lipid Bilayer Failure Kinetics," *Langmuir*, vol. 28, no. 15, pp. 6403–6410, Apr. 2012.

[225] R. M. A. Sullan, J. K. Li, C. Hao, G. C. Walker, and S. Zou, "Cholesterol-Dependent Nanomechanical Stability of Phase-Segregated Multicomponent Lipid Bilayers," *Biophys. J.*, vol. 99, no. 2, pp. 507–516, Jul. 2010.

[226] B. D. Almquist and N. A. Melosh, "Fusion of biomimetic stealth probes into lipid bilayer cores," *Proc. Natl. Acad. Sci.*, vol. 107, no. 13, pp. 5815–5820, Mar. 2010.

[227] S. Steltenkamp, M. M. Müller, M. Deserno, C. Hennesthal, C. Steinem, and A. Janshoff, "Mechanical Properties of Pore-Spanning Lipid Bilayers Probed by Atomic Force Microscopy," *Biophys. J.*, vol. 91, no. 1, pp. 217–226, Jul. 2006.

[228] I. Mey, M. Stephan, E. K. Schmitt, M. M. Müller, M. Ben Amar, C. Steinem, and A. Janshoff, "Local Membrane Mechanics of Pore-

Spanning Bilayers," *J. Am. Chem. Soc.*, vol. 131, no. 20, pp. 7031–7039, May 2009.

[229] J. Majewski, J. Y. Wong, C. K. Park, M. Seitz, J. N. Israelachvili, and G. S. Smith, "Structural Studies of Polymer-Cushioned Lipid Bilayers," *Biophys. J.*, vol. 75, no. 5, pp. 2363–2367, Nov. 1998.

[230] L. Tayebi, Y. Ma, D. Vashaee, G. Chen, S. K. Sinha, and A. N. Parikh, "Long-range interlayer alignment of intralayer domains in stacked lipid bilayers," *Nat. Mater.*, vol. 11, no. 12, pp. 1074–1080, Dec. 2012.

[231] B. D. Almquist, P. Verma, W. Cai, and N. A. Melosh, "Nanoscale patterning controls inorganic–membrane interface structure," *Nanoscale*, vol. 3, no. 2, pp. 391–400, Feb. 2011.

[232] I. Iwai, H. Han, L. den Hollander, S. Svensson, L.-G. Öfverstedt, J. Anwar, J. Brewer, M. Bloksgaard, A. Laloeuf, D. Nosek, S. Masich, L. A. Bagatolli, U. Skoglund, and L. Norlén, "The Human Skin Barrier Is Organized as Stacked Bilayers of Fully Extended Ceramides with Cholesterol Molecules Associated with the Ceramide Sphingoid Moiety," *J. Invest. Dermatol.*, vol. 132, no. 9, pp. 2215–2225, Sep. 2012.

[233] K. Keegstra and K. Cline, "Protein Import and Routing Systems of Chloroplasts," *Plant Cell*, vol. 11, no. 4, pp. 557–570, Apr. 1999.

[234] D. Bald, J. Kruip, and M. Rögner, "Supramolecular architecture of cyanobacterial thylakoid membranes: How is the phycobilisome connected with the photosystems?," *Photosynth. Res.*, vol. 49, no. 2, pp. 103–118, Aug. 1996.

[235] J. M. Fernandez and H. Li, "Force-Clamp Spectroscopy Monitors the Folding Trajectory of a Single Protein," *Science*, vol. 303, no. 5664, pp. 1674–1678, Mar. 2004.

[236] M. Schlierf, H. Li, and J. M. Fernandez, "The unfolding kinetics of ubiquitin captured with single-molecule force-clamp techniques," *Proc. Natl. Acad. Sci. U. S. A.*, vol. 101, no. 19, pp. 7299–7304, May 2004.

[237] I. Popa, P. Kosuri, J. Alegre-Cebollada, S. Garcia-Manyes, and J. M. Fernandez, "Force dependency of biochemical reactions measured by single-molecule force-clamp spectroscopy," *Nat. Protoc.*, vol. 8, no. 7, pp. 1261–1276, Jul. 2013.

[238] S. A. Tristram-Nagle, "Preparation of Oriented, Fully Hydrated Lipid Samples for Structure Determination Using X-Ray Scattering," in *Methods in Membrane Lipids*, vol. 400, A. M. Dopico, Ed. Totowa, NJ: Humana Press, 2007, pp. 63–75.

[239] M. Hishida, H. Seto, P. Kaewsaiha, H. Matsuoka, and K. Yoshikawa, "Stacking structures of dry phospholipid films on a solid substrate," *Colloids Surf. Physicochem. Eng. Asp.*, vol. 284–285, pp. 444–447, Aug. 2006.

[240] M. Hishida, H. Seto, and K. Yoshikawa, "Smooth/rough layering in liquid-crystalline/gel state of dry phospholipid film, in relation to its ability to generate giant vesicles," *Chem. Phys. Lett.*, vol. 411, no. 1–3, pp. 267–272, Aug. 2005.

[241] M. Hishida, H. Seto, N. L. Yamada, and K. Yoshikawa, "Hydration process of multi-stacked phospholipid bilayers to form giant vesicles," *Chem. Phys. Lett.*, vol. 455, no. 4–6, pp. 297–302, Apr. 2008.

[242] D. D. Lasic, "The mechanism of vesicle formation.," *Biochem. J.*, vol. 256, no. 1, pp. 1–11, Nov. 1988.

[243] A. Schäfer, T. Salditt, and M. C. Rheinstädter, “Atomic force microscopy study of thick lamellar stacks of phospholipid bilayers,” *Phys. Rev. E*, vol. 77, no. 2, p. 021905, Feb. 2008.
[244] K. Hristova and S. H. White, “Determination of the hydrocarbon core structure of fluid dioleoylphosphocholine (DOPC) bilayers by x-ray diffraction using specific bromination of the double-bonds: effect of hydration.,” *Biophys. J.*, vol. 74, no. 5, pp. 2419–2433, May 1998.
[245] J. T. Groves, N. Ulman, P. S. Cremer, and S. G. Boxer, “Substrate−Membrane Interactions: Mechanisms for Imposing Patterns on a Fluid Bilayer Membrane,” *Langmuir*, vol. 14, no. 12, pp. 3347–3350, Jun. 1998.
[246] S. Garcia-Manyes, G. Oncins, and F. Sanz, “Effect of Ion-Binding and Chemical Phospholipid Structure on the Nanomechanics of Lipid Bilayers Studied by Force Spectroscopy,” *Biophys. J.*, vol. 89, no. 3, pp. 1812–1826, Sep. 2005.
[247] M. Manghi and N. Destainville, “Statistical Mechanics and Dynamics of Two Supported Stacked Lipid Bilayers,” *Langmuir*, vol. 26, no. 6, pp. 4057–4068, Mar. 2010.
[248] H. I. Petrache, S. Tristram-Nagle, D. Harries, N. Kučerka, J. F. Nagle, and V. A. Parsegian, “Swelling of phospholipids by monovalent salt,” *J. Lipid Res.*, vol. 47, no. 2, pp. 302–309, Feb. 2006.
[249] N. Chu, N. Kučerka, Y. Liu, S. Tristram-Nagle, and J. F. Nagle, “Anomalous swelling of lipid bilayer stacks is caused by softening of the bending modulus,” *Phys. Rev. E*, vol. 71, no. 4, p. 041904, Apr. 2005.
[250] A. F. Oberhauser, C. Badilla-Fernandez, M. Carrion-Vazquez, and J. M. Fernandez, “The mechanical hierarchies of fibronectin observed with single-molecule AFM,” *J. Mol. Biol.*, vol. 319, no. 2, pp. 433–447, May 2002.
[251] C. Yuan, J. Furlong, P. Burgos, and L. J. Johnston, “The Size of Lipid Rafts: An Atomic Force Microscopy Study of Ganglioside GM1 Domains in Sphingomyelin/DOPC/Cholesterol Membranes,” *Biophys. J.*, vol. 82, no. 5, pp. 2526–2535, May 2002.
[252] R. M. A. Sullan, J. K. Li, C. Hao, G. C. Walker, and S. Zou, “Cholesterol-Dependent Nanomechanical Stability of Phase-Segregated Multicomponent Lipid Bilayers,” *Biophys. J.*, vol. 99, no. 2, pp. 507–516, Jul. 2010.
[253] K. L. Johnson and K. L. Johnson, *Contact Mechanics*. Cambridge University Press, 1987.
[254] L. Picas, F. Rico, and S. Scheuring, “Direct Measurement of the Mechanical Properties of Lipid Phases in Supported Bilayers,” *Biophys. J.*, vol. 102, no. 1, pp. L01–L03, Jan. 2012.
[255] “Contact mechanics,” *Wikipedia, the free encyclopedia*. 04-Jun-2015.
[256] S. Garcia-Manyes, J. Brujić, C. L. Badilla, and J. M. Fernández, “Force-Clamp Spectroscopy of Single-Protein Monomers Reveals the Individual Unfolding and Folding Pathways of I27 and Ubiquitin,” *Biophys. J.*, vol. 93, no. 7, pp. 2436–2446, Oct. 2007.
[257] T.-L. Kuo, S. Garcia-Manyes, J. Li, I. Barel, H. Lu, B. J. Berne, M. Urbakh, J. Klafter, and J. M. Fernández, “Probing static disorder in Arrhenius kinetics by single-molecule force spectroscopy,” *Proc. Natl. Acad. Sci.*, vol. 107, no. 25, pp. 11336–11340, Jun. 2010.
[258] “Gamma distribution,” *Wikipedia, the free encyclopedia*. 24-Jun-2015.

[259] D. R. Cox, "Regression Models and Life-Tables," *J. R. Stat. Soc. Ser. B Methodol.*, vol. 34, no. 2, pp. 187–220, Jan. 1972.
[260] M. Mitzenmacher, "A Brief History of Generative Models for Power Law and Lognormal Distributions," *Internet Math.*, vol. 1, no. 2, pp. 226–251, Jan. 2004.
[261] C. Park and W. J. Padgett, "Accelerated Degradation Models for Failure Based on Geometric Brownian Motion and Gamma Processes," *Lifetime Data Anal.*, vol. 11, no. 4, pp. 511–527, Dec. 2005.
[262] Z. W. Birnbaum and S. C. Saunders, "A Statistical Model for Life-Length of Materials," *J. Am. Stat. Assoc.*, vol. 53, no. 281, pp. 151–160, Mar. 1958.
[263] Z. W. Birnbaum and S. C. Saunders, "A New Family of Life Distributions," *J. Appl. Probab.*, vol. 6, no. 2, pp. 319–327, Aug. 1969.
[264] J. L. Folks and R. S. Chhikara, "The Inverse Gaussian Distribution and Its Statistical Application--A Review," *J. R. Stat. Soc. Ser. B Methodol.*, vol. 40, no. 3, pp. 263–289, Jan. 1978.
[265] A. M. Hasofer, "A dam with inverse Gaussian input," *Math. Proc. Camb. Philos. Soc.*, vol. 60, no. 04, pp. 931–933, Oct. 1964.
[266] A. K. Banerjee and G. K. Bhattacharyya, "A Purchase Incidence Model with Inverse Gaussian Interpurchase Times," *J. Am. Stat. Assoc.*, vol. 71, no. 356, pp. 823–829, Dec. 1976.
[267] T. Lancaster, "A Stochastic Model for the Duration of a Strike," *J. R. Stat. Soc. Ser. Gen.*, vol. 135, no. 2, pp. 257–271, Jan. 1972.
[268] O. O. Aalen and H. K. Gjessing, "Understanding the shape of the hazard rate: a process point of view (With comments and a rejoinder by the authors)," *Stat. Sci.*, vol. 16, no. 1, pp. 1–22, Feb. 2001.
[269] I. G. Abiror, V. B. Arakelyan, L. V. Chernomordik, Y. A. Chizmadzhev, V. F. Pastushenko, and M. R. Tarasevich, "246 - Electric breakdown of bilayer lipid membranes I. The main experimental facts and their qualitative discussion," *Bioelectrochem. Bioenerg.*, vol. 6, no. 1, pp. 37–52, Mar. 1979.
[270] V. F. Pastushenko, Y. A. Chizmadzhev, and V. B. Arakelyan, "247 - Electric breakdown of bilayer lipid membranes II. Calculation of the membrane lifetime in the steady-state diffusion approximation," *Bioelectrochem. Bioenerg.*, vol. 6, no. 1, pp. 53–62, Mar. 1979.
[271] Y. A. Chizmadzhev, V. B. Arakelyan, and V. F. Pastushenko, "248 - Electric breakdown of bilayer lipid membranes III. Analysis of possible mechanisms of defect origination," *Bioelectrochem. Bioenerg.*, vol. 6, no. 1, pp. 63–70, Mar. 1979.
[272] V. F. Pastushenko, Y. A. Chizmadzhev, and V. B. Arakelyan, "249 - Electric breakdown of bilayer lipid membranes IV. Consideration of the kinetic stage in the case of the single-defect membrane," *Bioelectrochem. Bioenerg.*, vol. 6, no. 1, pp. 71–79, Mar. 1979.
[273] V. B. Arakelyan, Y. A. Chizmadzhev, and V. F. Pastushenko, "250 - Electric breakdown of bilayer lipid membranes V. Consideration of the kinetic stage in the case of the membrane containing an arbitrary number of defects," *Bioelectrochem. Bioenerg.*, vol. 6, no. 1, pp. 81–87, Mar. 1979.
[274] V. F. Pastushenko, V. B. Arakelyan, and Y. A. Chizmadzhev, "251 - Electric breakdown of bilayer lipid membranes VI. A stochastic theory taking into account the processes of defect formation and death:

Membrane lifetime distribution function," *Bioelectrochem. Bioenerg.*, vol. 6, no. 1, pp. 89–95, Mar. 1979.

[275] V. F. Pastushenko, V. B. Arakelyan, and Y. A. Chizmadzhev, "251 bis - Electric breakdown of bilayer lipid membranes VII. A stochastic theory taking into account the processes of defect formation and death: Statistical properties," *Bioelectrochem. Bioenerg.*, vol. 6, no. 1, pp. 97–104, Mar. 1979.

[276] W. Weibull, "A statistical distribution function of wide applicability," *J. Appl. Mech.*, vol. 18, pp. 293–297, 1951.

[277] J. Söderlund, L. B. Kiss, G. A. Niklasson, and C. G. Granqvist, "Lognormal Size Distributions in Particle Growth Processes without Coagulation," *Phys. Rev. Lett.*, vol. 80, no. 11, pp. 2386–2388, Mar. 1998.

[278] F. Black and M. Scholes, "The Pricing of Options and Corporate Liabilities," *J. Polit. Econ.*, vol. 81, no. 3, pp. 637–654, May 1973.

[279] S. Tristram-Nagle, D. J. Kim, N. Akhunzada, N. Kučerka, J. C. Mathai, J. Katsaras, M. Zeidel, and J. F. Nagle, "Structure and water permeability of fully hydrated diphytanoylPC," *Chem. Phys. Lipids*, vol. 163, no. 6, pp. 630–637, Jun. 2010.

[280] N. Kučerka, Y. Liu, N. Chu, H. I. Petrache, S. Tristram-Nagle, and J. F. Nagle, "Structure of Fully Hydrated Fluid Phase DMPC and DLPC Lipid Bilayers Using X-Ray Scattering from Oriented Multilamellar Arrays and from Unilamellar Vesicles," *Biophys. J.*, vol. 88, no. 4, pp. 2626–2637, Apr. 2005.

[281] K. Murzyn, W. Zhao, M. Karttunen, M. Kurdziel, and T. Róg, "Dynamics of water at membrane surfaces: Effect of headgroup structure," *Biointerphases*, vol. 1, no. 3, pp. 98–105, Sep. 2006.

[282] M. Sega, R. Vallauri, and S. Melchionna, "Diffusion of water in confined geometry: The case of a multilamellar bilayer," *Phys. Rev. E*, vol. 72, no. 4, p. 041201, Oct. 2005.

[283] G. E. Atilla-Gokcumen, E. Muro, J. Relat-Goberna, S. Sasse, A. Bedigian, M. L. Coughlin, S. Garcia-Manyes, and U. S. Eggert, "Dividing Cells Regulate Their Lipid Composition and Localization," *Cell*, vol. 156, no. 3, pp. 428–439, Jan. 2014.

[284] N. Mohandas and E. Evans, "Mechanical Properties of the Red Cell Membrane in Relation to Molecular Structure and Genetic Defects," *Annu. Rev. Biophys. Biomol. Struct.*, vol. 23, no. 1, pp. 787–818, 1994.

[285] D. Lingwood and K. Simons, "Lipid Rafts As a Membrane-Organizing Principle," *Science*, vol. 327, no. 5961, pp. 46–50, Jan. 2010.

[286] G. van Meer, D. R. Voelker, and G. W. Feigenson, "Membrane lipids: where they are and how they behave," *Nat. Rev. Mol. Cell Biol.*, vol. 9, no. 2, pp. 112–124, Feb. 2008.

[287] R. Albertson, B. Riggs, and W. Sullivan, "Membrane traffic: a driving force in cytokinesis," *Trends Cell Biol.*, vol. 15, no. 2, pp. 92–101, Feb. 2005.

[288] U. S. Eggert, A. A. Kiger, C. Richter, Z. E. Perlman, N. Perrimon, T. J. Mitchison, and C. M. Field, "Parallel Chemical Genetic and Genome-Wide RNAi Screens Identify Cytokinesis Inhibitors and Targets," *PLoS Biol*, vol. 2, no. 12, p. e379, Oct. 2004.

[289] R. Matzke, K. Jacobson, and M. Radmacher, "Direct, high-resolution measurement of furrow stiffening during division of adherent cells," *Nat. Cell Biol.*, vol. 3, no. 6, pp. 607–610, Jun. 2001.

[290] A. Pietuch and A. Janshoff, "Mechanics of spreading cells probed by atomic force microscopy," *Open Biol.*, vol. 3, no. 7, p. 130084, Jul. 2013.
[291] M. Yokokawa, K. Takeyasu, and S. h. Yoshimura, "Mechanical properties of plasma membrane and nuclear envelope measured by scanning probe microscope," *J. Microsc.*, vol. 232, no. 1, pp. 82–90, Oct. 2008.
[292] A. Hategan, R. Law, S. Kahn, and D. E. Discher, "Adhesively-Tensed Cell Membranes: Lysis Kinetics and Atomic Force Microscopy Probing," *Biophys. J.*, vol. 85, no. 4, pp. 2746–2759, Oct. 2003.
[293] S. Garcia-Manyes, G. Oncins, and F. Sanz, "Effect of Ion-Binding and Chemical Phospholipid Structure on the Nanomechanics of Lipid Bilayers Studied by Force Spectroscopy," *Biophys. J.*, vol. 89, no. 3, pp. 1812–1826, Sep. 2005.
[294] K. El Kirat, S. Morandat, and Y. F. Dufrêne, "Nanoscale analysis of supported lipid bilayers using atomic force microscopy," *Biochim. Biophys. Acta BBA - Biomembr.*, vol. 1798, no. 4, pp. 750–765, Apr. 2010.
[295] E. Sackmann, "Supported Membranes: Scientific and Practical Applications," *Science*, vol. 271, no. 5245, pp. 43–48, Jan. 1996.
[296] "Poisson distribution," *Wikipedia, the free encyclopedia*. 22-Jun-2015.
[297] M. R. Angle, A. Wang, A. Thomas, A. T. Schaefer, and N. A. Melosh, "Penetration of Cell Membranes and Synthetic Lipid Bilayers by Nanoprobes," *Biophys. J.*, vol. 107, no. 9, pp. 2091–2100, Nov. 2014.
[298] E. Moeendarbary, L. Valon, M. Fritzsche, A. R. Harris, D. A. Moulding, A. J. Thrasher, E. Stride, L. Mahadevan, and G. T. Charras, "The cytoplasm of living cells behaves as a poroelastic material," *Nat. Mater.*, vol. 12, no. 3, pp. 253–261, Mar. 2013.
[299] A. R. Harris and G. T. Charras, "Experimental validation of atomic force microscopy-based cell elasticity measurements," *Nanotechnology*, vol. 22, no. 34, p. 345102, Aug. 2011.
[300] T. Kihara, T. Yoshida, S. M. A. Haghparast, and J. Miyake, "Elasticity Mapping Analysis of Apical Cell Periphery Actin Structures of Normal Fibroblasts and Cervical Cancer Cells," *J. Anal. Sci. Methods Instrum.*, vol. 03, no. 02, pp. 124–129, 2013.

8 Appendix I: nanomechanics of lipid membranes

8.1 Preparation of single lipid membranes

Single supported lipid membranes were prepared following the liposome deposition method[223]. In this method, DPhPC was dissolved in chloroform/methanol (3:1) to give a final concentration of 3 mM. Chloroform and Methanol were purchased from Aldrich (>99% purity from Sigma-Aldrich, Saint Louis, MO). A small aliquot of DPhPC solution (tens of microliters) was poured into a falcon tube, and it was evaporated under a nitrogen flow, obtaining a film covering the walls of the tube. The falcon tube was then kept under a stronger nitrogen stream for forty extra minutes to evaporate any remaining organic solvent traces. Then, buffer solution (200 mM NaCl, 10 mM and HEPES/NaOH 10 mM at pH = 7.4) was added to obtain a lipid concentration of 500 μM. The falcon tube was then subjected to five vortexing cycles of 40 s each at high temperature (ca. 60˚C) to generate giant multilamellar lipid vesicles. The solution was then sonicated for 30 min to obtain small unilamellar vesicles. Prior to experiments, a Muscovite Mica substrate (Agar Scientific, Stansted, UK) was glued onto Teflon discs with an epoxy-based adhesive, rinsed, and cleaved with adhesive tape. A total of 60 μl of the vesicle-containing solution were deposited on the mica substrate and let deposit for 30 min at a temperature of ca. 70 ºC. Afterwards, the remaining lipid vesicles floating in the aqueous solution were rinsed away by washing three times with buffer solution.

8.2 Supplementary figures

8.2.1 Force-extension analysis in DOPC lipid stacks

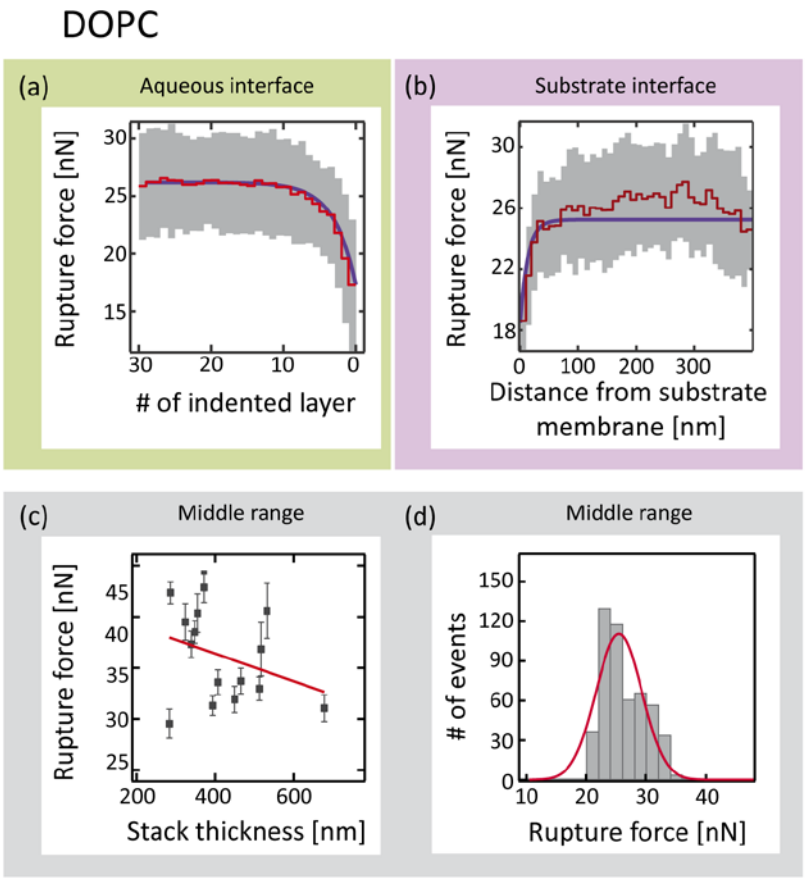

Fig. 8-1 DOPC stacked lipid membranes display three mechanically distinct regions. The stacked lipid membranes show a distinct behaviour close to the top of the stack (aqueous interface, green colour), to the substrate (substrate interface, purple colour), and in-between (middle region, grey colour). We have characterized the mechanical properties of each of these regions. (a) The average rupture force (red line) and its standard deviation (surrounding grey area) have been calculated for each indented layer, starting to count from the top of the stack. The increasing rupture forcer has been fitted (purple line) with an exponential function ($\tau = 0.33 \pm 0.01$ layers^{-1}) yields that 6 layers are significantly different (<5%) than the average away from it. (b) The average rupture force (red line) and its standard deviation (surrounding grey area) have been calculated at increasing separations from the substrate (bin size is ten nanometres). An exponential fitting function has been fitted (purple line, $\tau = 74 \pm 3$ pm^{-1}). The first ten top rupture events have been excluded from this analysis in order to avoid the effect of the aqueous interface. (c) The average rupture force in the middle region against the stack thickness for each lipid stack indented show no significant dependency ($R^2 = 0.11$) (d) Histogram of all the events that are not affected by the proximity to the interfaces (# of events = 507).

8.2.2 Force-extension analysis in DLPC lipid stacks

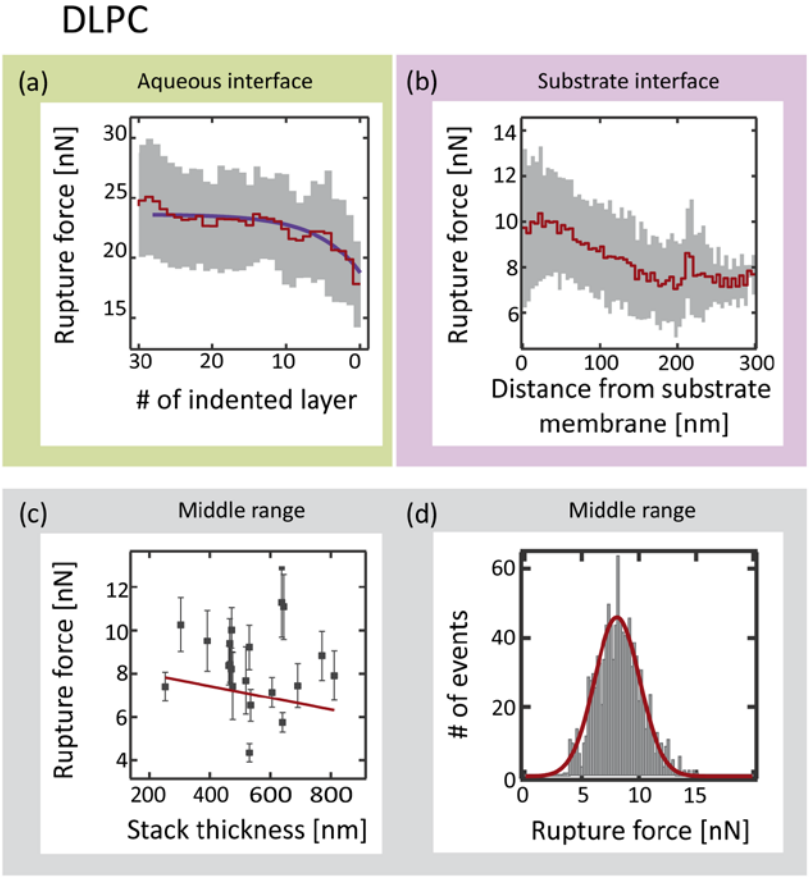

Fig. 8-2 DLPC stacked lipid membranes display three mechanically distinct regions. The stacked lipid membranes show a distinct behaviour close to the top of the stack (aqueous interface, green colour), to the substrate (substrate interface, purple colour), and in-between (middle region, grey colour). We have characterized the mechanical properties of each of these regions. (a) The average rupture force (red line) and its standard deviation (surrounding grey area) have been calculated for each indented layer, starting to count from the top of the stack. The increasing rupture forcer has been fitted (purple line) with an exponential function ($\tau = 0.17 \pm 0.03$ layers^{-1}) yields that 9 layers are significantly different (<5%) than the average away from it. (b) The average rupture force (red line) and its standard deviation (surrounding grey area) have been calculated at increasing separations from the substrate (bin size is ten nanometres). In this case, the mechanical stability is not constant throughout the lipid stack, which prevented using the same approach as before. We then calculated the extent of the substrate effect by taking the distance at which the mechanical stability is higher. The distinct measurement protocol used here should introduce only a small bias because the effect of the substrate is much more pronounced than the gentle mechanical stability decrease observed at longer distances. (c) Indeed, the average rupture force in the middle region against the stack thickness for each lipid stack indented only show no significant dependency ($R^2 = 0.031$). (d) Histogram of all the events that are not affected by the proximity to the interfaces (# of events = 1149)

9 Appendix II: nanomechanics of cell membranes

9.1 Materials and methods

9.1.1 Force spectroscopy measurements on cells using high indenting forces

HeLa cells (150,000) were seeded in a 60 mm plastic cell culture dish (Greiner bio-one) 24h prior the AFM experiment. Force Spectroscopy experiments were performed using a commercial AFM (Dimension Icon, Bruker AXS, Karlsruhe, Germany) equipped with a custom-made temperature controller. The controller is composed of a 16x6x0.5 cm aluminium plate with two silicone heating mats located at each of its ends (detailed in chapter 2). The dish containing the cells is located at the centre of the plate and a type K thermocouple probe (Fluke, WA, USA) is immersed near the edge of the dish making contact with its bottom surface. This design has a temperature resolution of ±0.1 ºC and a set point stability of ±1 ºC.

Prior to experiments, the spring constant of the AFM cantilevers (MLCT tip F, k=0.6 N/m, Bruker AXS, Karlsruhe, Germany) was individually calibrated against a freshly cleaved mica surface in MilliQ water. Then, the heater was turned on, let stabilize, and the HeLa cells were transferred to the AFM and let equilibrate for around 30 min. In the absence of CO2, media was buffered with 50mM HEPES during the experiment. Target cells were identified with the use of the AFM's built-in optical microscope. Only cells that were sitting far apart from other neighbouring cells were indented, in order to avoid indenting regions with overlapping cytoplasms from adjacent cells. Dividing cells were identified according to their morphology following the criteria of E. Muro.

Once a target cell was identified, the AFM probe was allowed to indent the entire cell at a constant velocity of 1 m sec^{-1} until the culture dish substrate was encountered (applying forces in the range of 10-250 nN), and the probe was subsequently retracted. The resulting force-extension trace features a steady increase in force, as a result of the complex combined effect of deforming the cytoplasm (consisting of a porous elastic solid meshwork (cytoskeleton, organelles, macromolecules) bathed in an interstitial fluid

(cytosol)) [298]. The complexity of these force-extension traces, where a variety of cellular structures are plastically deformed, precludes the fitting of purely elastic deformation models to the entire force-indentation curve. Once the cell has completely deformed, and just before the AFM cantilever tip reaches the hard substrate, a discontinuity (or rip) in the force vs. extension trace can be easily identified[291]. Each discontinuity corresponds to the breakthrough of an individual lipid bilayer, featuring an average thickness of 2.5 ± 0.9 nm (N = 189). Crucially, the number of 'jumps' or discontinuities varies according to the cell region. These observations concur with the results previously reported by Yokokawa et al.[298], where it was clearly demonstrated that the 'rips' or discontinuities observed in the indentation curves on live cells just before contacting the hard substrate and occurring at high applied forces correspond to the penetration of the AFM probe through the plasma membrane. In the Yokokawa et al. experiments, the number of 'rips' varied with the region of the cell being indented. Pushing through the cell peripheries mainly gave rise to one rip (with a second rip being rarely observed), raising the possibility that both the upper and bottom membranes were simultaneously penetrated. In contrast, when indenting the nuclear envelope region, a second rip was observed, which was composed of several small rips, suggesting that the different nuclear membranes were penetrated by the AFM probe. These results were further confirmed by indenting isolated nuclei, revealing multiple rips. In the present study, while indentation on the cytoplasm region clearly reveals two breakthrough events (corresponding to the penetration of the cell's 'dorsal' membrane and the substrate-attached 'ventral' membrane, respectively), when indenting the cell's nucleus we observe 6 breakthrough events (which correspond to the outer and inner cell membranes (2) plus the indentation of the outer and inner nuclear membrane, each of which is a double bilayer (4)). Altogether, our observations agree with the results reported by Yokokawa et al. in that we observe rips when indenting live cells at higher forces, and also that the number of rips increases when the indentations are carried out on the cell nucleus rather than on the cytoplasm. Our findings have also been recently confirmed by Angle et al. using custom-made AFM tips[297]. A key point in our experiments is that each rip or discontinuity is typically formed by a single membrane (confirmed

by the length associated with each particular discontinuity). In the experiments reported by Yokokawa et al., many of the observed rips where larger (although the total length of each rip was unfortunately not measured in these experiments), corresponding to the simultaneous breakthrough of a few individual bilayers. Interestingly, in our experiments we show that the thickness of the lipid membranes of live cells closely corresponds to the values measured when such lipid bilayers are supported on a solid substrate[293][57] [Fig. 5-1(e-g)], thus providing further confidence that each rupture event corresponds to the indentation of a single lipid bilayer by the AFM probe. The force at which the tip penetrates the bilayer, the rupture force or 'breakthrough force', is hence the maximum force that the membrane is able to withstand before breaking (plastic deformation), and hence it can be regarded as a true molecular fingerprint[57][13].

For each individual cell, about 5-6 indentations were performed to avoid the effects of cell damage through consecutive force-extension traces. The breakthrough force of live cell membranes depends on the cell thickness, as reported before elsewhere[291]. This is probably due to a large contact area between the probe and the cell surface in the case of a deep indentation. Crucially, the breakthrough force also depends on the region of the cell being indented (cytoplasm or nucleus) and the state of division of the cell (dividing or non-dividing). Due to the mechanism of cell division, dividing cells are, on average, thicker than non-dividing cells, thus leaving a window of cell thickness spanning from 6-7.6 μm (cytoplasm region) (Fig. 5-1) and 4.1-8.3 μm (nucleus) (Fig. 5-2) amenable for comparison. In each case, for comparable cell thickness values, dividing cells are always more mechanically stable (>99.99%, t-test) than non-dividing cells.

The cantilevers used for these experiments (MLCT tip F, k=0.6 N/m, Bruker AXS, Karlsruhe, Germany) were imaged using SEM (HITACHI S4000, Tokyo, Japan). The Bruker MLCT cantilever has a length of 5.7 μm, and thus somewhat shorter than the thickness of some of the probed cells. Since the shape of the deformed cells as they are being indented by the pyramidal tip is unknown, it is plausible that, at large forces, the contact area between the cell and the cantilever can have contributions both from the pyramidal tip and the cantilever underside[299]. We attempted to address this potential issue by

performing the experiments with cantilevers having longer tips. Unfortunately, most of them (e.g. Bruker OLTESPA and FESPA) were found non-suitable for measurements in liquid environment, due to the inadequacy of their aluminium coating. Therefore, in this work, some caution should be taken with the absolute values in breakthrough force recorded for cells exhibiting very large heights. However, it must be emphasized that this potential bias does not affect our conclusions, which are based on the large differences in the relative (not absolute) values of breakthrough forces obtained for dividing vs. non-diving cells that exhibit similar cell heights.

9.1.2 Preparation of lipid bilayers for Atomic Force Microscopy (AFM):

HeLa S3 cell pellets synchronized in S-phase or cytokinesis were re-suspended in 1 mL PBS. In order to reduce potential protein contamination, the samples were subjected to two cycles of Dounce-homogenization in 1:1:2 PBS:MeOH:CHCl3 and centrifugation at 500xg for 10 min followed by separation of the chloroform layer. This solution was used to prepare small unilamellar vesicles following the method described previously[57]. Briefly, a 100 μL aliquot of the chloroform solution was evaporated under nitrogen flow for 40 min to ensure the absence of organic solvents. After adding 1 mL of buffer solution (150 mM NaCl, 20 mM MgCl2, 10 mM HEPES pH=7.4), samples were subjected to 5 cycles of 40 s vortexing at 60 ºC. The solution was finally sonicated for 30 min and then deposited for 30 min onto freshly cleaved Muscovite Mica (Ted Pella, Redding, CA). Before observation with AFM, the samples were thoroughly rinsed with buffer.

9.1.3 Observation of lipid bilayers using Atomic Force Microscopy (AFM):

Samples were imaged with a commercial Dimension Icon (Bruker, Karlsruhe, Germany) in tapping mode using V-shaped Si3N4 tips (Bruker, Karlsruhe, Germany) of 0.35 N/m nominal spring constant. Each cantilever was individually calibrated using the equipartition theorem (thermal noise) method before force-distance curves were recorded. Right after imaging a lipid patch, Force-extension curves were performed to a set of chosen

locations at a constant velocity of 1000 nm/s. All experiments were performed at room temperature ranging from 20-24 ºC. AFM images were analysed and processed with Nanoscope Software (Bruker, Karlsruhe, Germany). In order to measure the height of each independent phase from the tapping mode images, we flattened each particular image and made a histogram of the height corresponding to all pixels of the image. The height of each individual phase was measured by taking the central value of each distinct peak in the histogram with respect to the mica surface. Force Spectroscopy data was analysed using a custom-made routine written in Igor Pro Software (Wavemetrics, Portland, OR). The distribution of breakthrough force data shown in Fig. 5-1(f) corresponds to the sample area shown in Fig. 5-1(d) and Fig. 5-1(e), respectively. The same trend in the mechanical stability of each phase is reproducibly observed when using cantilever tips and samples within independent days of experiment.

9.1.4 Force spectroscopy measurements on cells at low indenting forces. Measurement of cell elasticity (Young's modulus):

SiRNA treated cells were prepared similarly as described in the RNAi screen section and grown in 60 mm culture dishes. Cells were maintained at controlled temperature and in buffered medium during the measurements as described here in the previous AFM section. In order to test the elasticity (Young's modulus) of SMPD4 siRNA treated cells as opposed to cells treated with control siRNA, we conducted force-volume experiments whereby the cell surface was regularly indented at 4 μm sec^{-1} applying forces lower than 1.5 nN in the X and Y directions in maps of 16x16 or 32x32 points. In this study, the scan size was set, for most cases, in the range 10-30 μm, depending on the size and shape of the cell cytoplasm, with a resolution between 0.3-2 μm/pixels. For these studies, a cantilever with a lower spring constant (Bruker MLCT, tip C, k=0.01 N/m, Bruker AXS, Karlsruhe, Germany) was used. We developed our own computational tools, written in Igor Pro (Wavemetrics, Portland, OR), to extract the sample stiffness from the raw force-volume files. In this analysis, once the contact point between the tip and the sample is detected by finding the intersection point that best fits the change in trend

between a linear and a quadratic function, the stiffness of the contacting region is computed by using the Hertz model for a pyramidal geometry, which allows to calculate the Young's modulus of the sample cell, E, from the evolution of the force, F, as a function of the indentation depth, δ, according to the equation[299]:

$$F = \frac{1.4096E \tan\varphi}{2(1-\upsilon)^2}\delta^2 \qquad (10.1)$$

Where υ is the Poisson ratio and φ, the opening angle of the pyramid. We imaged by SEM the tip used during the experiments (Bruker MLCT tip C, Bruker AXS, Karlsruhe, Germany), and measured the tip height of 5.74 μm, φ = 29.8 ˚and R = 50 nm. Assuming a υ = 0.5, the value of the Young's Modulus was obtained by fitting the Hertz equation to each of the 5537 (siSMPD4 cells) and 5070 (control cells) individual force-extension traces. The Hertz model is derived for an infinitely thick sample. Hence, data should be fitted if the indentation is small compared with the thickness of the sample. Each trace was fitted within the force range below 600 pN, which corresponds to a tip indentation of 500 nm at most, which is small compared to the average height of dividing cells, about 5-10 μm.[300]. Therefore, the E values obtained were not significantly affected by the underlying stiff substrate. Each individual trace was manually inspected to ensure that no plastic deformation of any sort (discontinuity in the force-distance trace) occurred within the fitted force range. Each indentation force-volume map was individually inspected in order to discard any possible outliers that might mistakenly appear in the rims of the cell and corresponding instead to the substrate.

Individual Force Volumes presented local differences of stiffness depending on the sampled region of the cytoplasm. In any case, these differences are rather small compared to the cell to cell differences in mechanical properties. Each force volume can be defined by a single stiffness histogram. Each distinct histogram shows a unimodal distribution of stiffness values with a positive skew. The overall histogram that includes the results of all individual force volume datasets shows a distribution of stiffness values that cannot be accounted for variability within experimental days or used AFM probes.

The values of Young's modulus that we obtained (kPa for both dividing and non-dividing cells) are similar to those observed by others for a variety of different cells, including HeLa cells[291], and ranging between ~ 1-30 kPa.

10 Appendix III:

PRL article

Direct Observation of the Dynamics of Self-Assembly of Individual Solvation Layers in Molecularly Confined Liquids

Josep Relat-Goberna and Sergi Garcia-Manyes*
Department of Physics and Randall Division of Cell and Molecular Biophysics, King's College London, Strand, WC2R 2LS London, United Kingdom
(Received 11 March 2015; published 25 June 2015)

Confined liquids organize in solidlike layers at the liquid-substrate interface. Here we use force-clamp spectroscopy AFM to capture the equilibrium dynamics between the broken and reformed states of an individual solvation layer in real time. Kinetic measurements demonstrate that the rupture of each individual solvation layer in structured liquids is driven by the rupture of a single interaction for 1-undecanol and by two interactions in the case of the ionic liquid ethylammonium nitrate. Our results provide a first description of the energy landscape governing the molecular motions that drive the packing and self-assembly of each individual liquid layer.

DOI: 10.1103/PhysRevLett.114.258303 PACS numbers: 82.37.Gk, 68.08.De, 68.37.Ps, 82.65.+r

Understanding the structural properties of liquids at the solid interface is fundamental to many applications in the fields of nanotribology, wetting, or molecular biophysics [1]. When confined between two flat surfaces separated by a few nanometers, liquids exhibit properties that cannot be described by the continuum theories based on van der Waals and electrostatic interactions characterizing the bulk properties. Instead, the molecules forming the liquid order into well-defined solvation layers, giving rise to oscillatory forces described by radial distribution functions with a periodicity of about one molecular diameter [1].

The discrete oscillation forces were first experimentally measured by pioneering surface force apparatus (SFA) experiments, in which liquids are confined between two opposing macroscopic flat mica plates of $R \sim 10\ \mu$m [2]. These observations were later complemented by atomic force microscopy (AFM) measurements, where the confined liquid is compressed by the AFM tip, with a much smaller contact radius ($R \sim 10$ nm) [3]. In the latter case, the deflection of the AFM cantilever is measured as it approaches a rigid, flat substrate [typically highly oriented pyrolytic graphite (HOPG) or mica] at constant velocity. The layered nature of the probed liquids is hallmarked by the presence of discrete jumps in the resulting force-distance curves. Each discontinuity or jump occurs when an individual layer of confined liquid is suddenly squeezed out from below the AFM tip [4]. Crucially, the distance between two consecutive jumps informs on the precise orientation of each molecular layer with respect to the surface. This experimental approach has revealed invaluable information about the molecular packing properties of a variety of chemically distinct liquids, encompassing nonpolar liquids with spherical structure such as octamethylcyclotetrasiloxane (OMCTS) [5], linear and branched alkanes [6,7], polar liquids such as short alcohols [8], a variety of ionic liquids [9,10], and even water [11,12], all exhibiting *a priori* similar force-induced rupture mechanisms. This progress notwithstanding, the reverse process encompassing the reversible reformation of each individual molecular layer, together with the quantification of the number of interactions involved in the rupture and reformation processes, remained completely elusive.

In this Letter, we make use of force-clamp spectroscopy AFM to directly capture the forced-induced rupture and reformation of each of the individual solidlike ordered layers populating the alcohol-HOPG and ethylammonium nitrate (EAN)-mica interface. These measurements enable us to map out the complete energy landscape of a confined liquid, providing (sub)molecular insight into the mechanisms underpinning the rupture and reformation dynamics of packing and self-assembly of an individual liquid layer according to its particular chemical structure.

Using a homemade AFM spectrometer [13], we measured individual force distance curves [Fig. 1(a)] on 1-undecanol, whereby the cantilever was approached towards (red trace) and, subsequently, retracted from (blue trace) a HOPG surface at a constant velocity of 200 nm s^{-1}. Upon approaching the surface, the cantilever penetrated 5 well-defined 1-undecanol layers (red arrows), each of them requiring an exponentially higher force to be indented [Fig. 1(b)]. As the cantilever was withdrawn from the sample, each previously broken layer was reversibly reformed (blue arrows). The distribution of breakthrough forces can be fitted with an exponentially decaying function [4],

$$F = F_0 \cos(2\pi d) \exp(-\tau d) \quad (1)$$

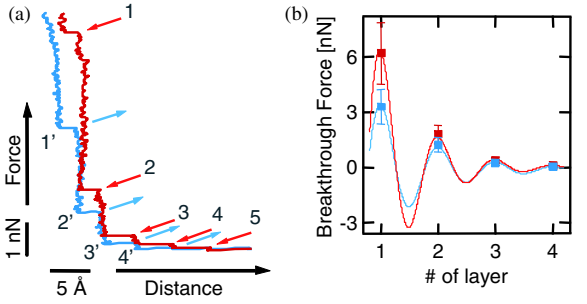

FIG. 1 (color online). Solvation layers in 1-undecanol revealed by constant velocity AFM. (a) Force vs distance plot of the AFM tip approaching towards (red line) and, subsequently, retracting from (blue line) the HOPG surface in 1-undecanol at constant velocity, showing the rupture and reversible reformation of a total of 5 confined layers. (b) Rupturing and reforming forces ($n = 90$ individual trajectories) for the first four measurable solvation layers.

(where d is the thickness of the confined layers and τ stands for the decay length), further confirming the periodic packing properties of 1-undecanol. The average jump-in distance (~3 Å) is significantly shorter than the 1-undecanol length (~14.7 Å) [14], thus suggesting an almost flat layering of the 1-undecanol layers on the HOPG surface. These results are in full agreement with previous x-ray [15], SFA [14], force [8], and imaging [16] AFM studies. The direct observation of the discrete reformation events in the force-extension traces [Fig. 1(a), blue arrows] suggests that the rupturing process is reversible and that, by holding the applied force constant throughout the experiment at an "average" set-point value between the rupturing and reformation force, the equilibrium dynamics between the broken and reformed states should be captured. In fact, applying a constant force of 430 pN with the force-clamp setup displayed bistability [Fig. 2(a)]; the layer 3 hopped between the broken and reformed states in real time, with a concomitant change in length $\Delta l = 3.3 \pm 2$ Å, corresponding to the length of an individual layer (Fig. S2 in the Supplemental Material [18]). Changing the applied force to lower (410 pN) and higher (450 pN) values dramatically altered the equilibrium between the reformed and broken states. The thermodynamics of the reformed ⇄ ruptured transition can be evaluated by measuring the relative time abundance of the reformed state $N_{\mathrm{ref}}/N_{\mathrm{total}}$ for each distinct constant force value according to the Boltzmann distribution:

$$\frac{N_{\mathrm{ref}}}{N_{\mathrm{total}}} = 1 - \frac{1}{1 + \exp(\frac{\Delta G - \Delta l F}{kT})}, \qquad (2)$$

where ΔG is the difference in free energy between the broken and reformed states and Δl is the physical length distance separating them. Fitting this equation to the experimental

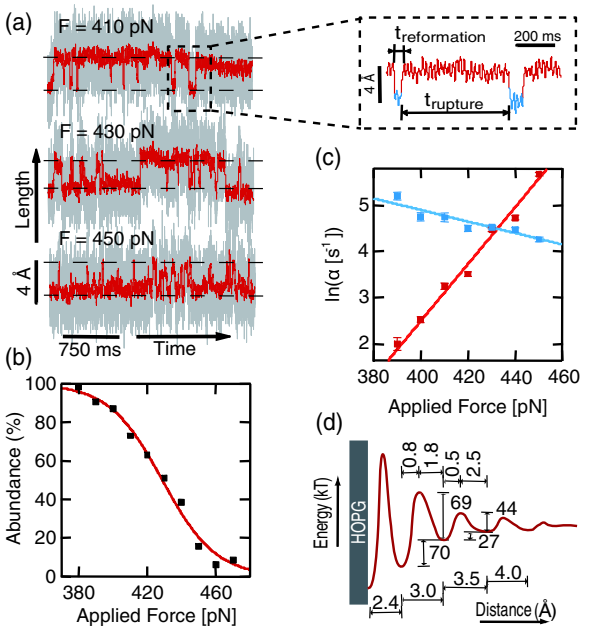

FIG. 2 (color online). The equilibrium dynamics of an individual solvation layer in 1-undecanol captured by force-clamp AFM. (a) Applying a constant force of 430 pN samples the rupture and reformation dynamics of layer 3. The equilibrium is readily displaced upon changing the applied force. (b) Plot of the abundance of the reformed state as a function of the applied force. (c) The dwell times of rupture and reformation [(a), inset] depend exponentially on the applied force (red and blue dots, respectively). The error has been calculated using the bootstrap method [17]. (d) Repeating the process for each individual layer (Figs. S6–S8) allows the full 1D reconstruction of the energy landscape of confined 1-undecanol.

data corresponding to the rupture and reformation of layer 3 [Fig. 2(b)] yields $\Delta G = (27 \pm 2)kT$ and $\Delta l = 2.6 \pm 0.2$ Å. Notably, the measured value of Δl is consistent with the thickness of one individual 1-undecanol layer and in agreement with the results obtained from force-extension (Fig. S1, [18]) and force-clamp (Fig. S2, [18]) measurements. The force dependent rates of breakthrough and reformation have been measured by extracting the dwell time for each individual transition occurring at a fixed force (Fig. S3 [18]), assuming that, as a first approximation, the distribution of dwell times at a particular force follows a single exponential (Fig. S4, [18]). Our observations demonstrate that, both for the rupturing and reformation processes, the measured rates depend exponentially on the applied force following a simple Bell formalism [19]:

$$\alpha(F) = A_0 \exp\left(-\frac{\Delta E}{kT} + \frac{\Delta x}{NkT} F\right), \qquad (3)$$

where $\alpha(F)$ is the rate of the process as a function of force, A_0 the preexponential factor, ΔE stands for the height of the

energy barrier, Δx is the width of the energy barrier governing the process (normally known as "distance to the transition state") and N is the number of bonds (or interactions) that withstand mechanical force. This approach has been used to interpret a wide variety of single molecule pulling experiments [13,20,21] for which $N = 1$. Figure 2(c) shows the graph plotting the $\ln[\alpha(F)]$ as a function of the pushing force, for both the rupturing (red) and reformation (blue) processes. Fitting Eq. (3) for both processes results in $\Delta x_{\text{rupture}}/N = 2.5 \pm 0.1$ Å for the rupturing process $\Delta x_{\text{reformation}}/N = 0.5 \pm 0.1$ Å for the reverse reforming reaction. By assuming an arbitrary value $A_0 = 4 \times 10^9$ s^{-1} [22], we obtain $\Delta E = 44kT$.

Dividing the expressions for the rates of rupturing α_{rup} and reformation α_{ref} and assuming that $A_{0,\text{rup}} \sim A_{0,\text{ref}}$ it follows that

$$\ln\left(\frac{\alpha_{\text{rup}}}{\alpha_{\text{ref}}}\right) = \frac{\Delta G}{kT} + \frac{\Delta l}{NkT} F. \tag{4}$$

Fitting Eq. (4) to the experimental data, and using the previously obtained value of $\Delta l = 2.6 \pm 0.2$ Å, we obtain $\Delta G = (31 \pm 2)kT$ and $N = 0.9 \pm 0.1$. Remarkably, the ΔG values obtained through kinetic and thermodynamic measurements are in close agreement, thus strongly suggesting that the hopping process occurs through a single barrier. Most importantly, our experiments revealed that $N \approx 1$ (by definition N must be an integer ≥ 1). This has fundamental implications, entailing that the applied force is transmitted through an "individual" interaction within a very narrow space. These conclusions complement recent findings suggesting that the force does not distribute through the whole cantilever tip in contact with the liquid (which would imply that a larger number of bonds are effectively broken, yielding a large N) but rather through the last microasperities of the AFM cantilever tip [23]. The same approach used to uncover the kinetic and thermodynamic properties of layer 3 was extended and applied to layers 1 and 2 (Figs. S6–S8 in the Supplemental Material [30]). Combined, these results allowed us to reconstruct the energy landscape of the first confined layers of 1-undecanol in the 1D direction perpendicular to the graphite surface [Fig. 2(d)]. Interestingly, and as expected in light of the large hysteresis between the breakthrough and reformation events observed in Fig. 1(a), the layer closer to the surface does not exhibit signatures of dynamic equilibrium between the ruptured and reformed states. Moreover, in this case, N is an order of magnitude bigger than in the rest of the confined layers (Table SI, [18]). The markedly different behavior of this first layer suggests that the underlying solid substrate is likely to have a large effect on the conformation and dynamics of the layer.

The dynamic properties of a long, nonbranched alcohol, such as 1-undecanol, lying flat on a HOPG surface sets the ground to study the molecular self-assembly mechanism of chemically more complex solvents. Because of their sterically mismatched anion-cation pairs, ionic liquids exhibit fascinating properties that lie in-between those of a liquid and a solid [9,10]. In this context, ethylammonium nitrate (EAN) has revealed oscillatory forces in the vicinity of a flat mica substrate. Using constant velocity experiments [Fig. 3(a)], we recorded force-distance traces showing the initial 3 clear discontinuities hallmarking the rupture (red) and reformation (blue) processes. In this case, each jump measures 4.3 ± 0.4 Å in excellent agreement with the predicted ion pair diameter of EAN and with previous

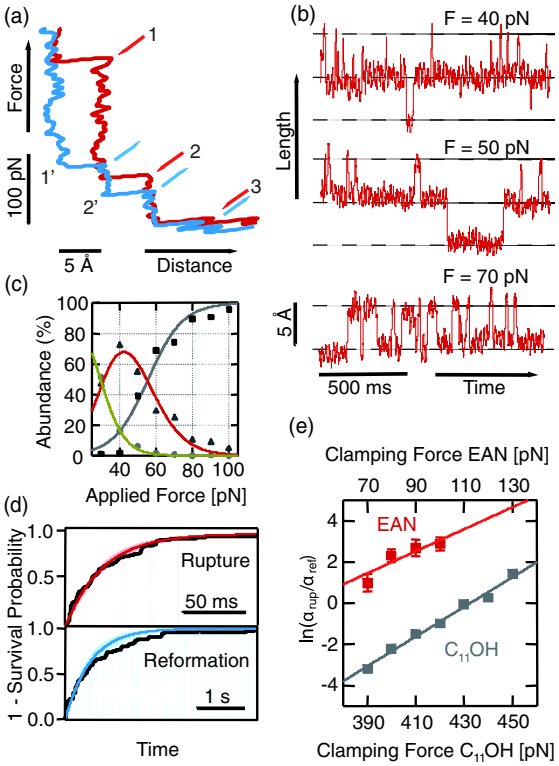

FIG. 3 (color online). The solvation dynamics of EAN. (a) Force extension trajectories showing the rupture and reformation of 3 confined EAN solvation layers. (b) The system hops between layers 1 and 2 as the applied constant force varies from 70–40 pN. (c) Relative abundances of the reformed (green) and ruptured state (red) of layer 1 and the ruptured state of layer 2 as a function of the applied force. Global fit of Eq. (2) yields $\Delta l = 4.3 \pm 0.4$ Å and $\Delta G = (5.9 \pm 0.6)kT$ (layer 2, red line); $\Delta l = 6.2 \pm 0.1$ Å and $\Delta G = (4.5 \pm 1)kT$ (layer 3, gray line). (d) The cumulative density function reconstructed from the transition dwell times is fitted, as a first approximation, to an exponential function to obtain the rates of rupture (red line, $\tau = 29 \pm 4$ ms) and reformation (blue line, $\tau = 500 \pm 100$ ms) for $F = 100$ pN. (e) Fitting of Eq. (4) yields $\Delta G = (4.5 \pm 1)kT$ and $N = 2.0 \pm 0.8$ (EAN, red solid line). For comparison, the same equation was fitted to 1-undecanol results (gray solid line) yielding $\Delta G = (31 \pm 2)kT$ and $N = 0.9 \pm 0.1$.

SFA [24] and AFM results [9,25]. This suggests that the EA^+ and the nitrate ions facing the bulk liquid are perpendicularly adsorbed onto the mica substrate. Because of the similar forces between consecutive solvation layers in EAN [Fig. 3(a)], applying a constant pushing force of 50 pN to the EAN-mica interface results in an equilibrium situation where the system hops between three well-defined states (layers 1–2) in discrete jumps of $\sim 5 \pm 2$ Å [Fig. 3(b)]. Slightly changing the applied force to lower (40 pN) or higher (70 pN) values dramatically shifts the equilibrium properties of the system. The relative time abundance of each state as a function of the applied force is shown in Fig. 3(c). Fitting Eq. (2) for each state provides a direct measurement of the associated ΔG and Δl values for the studied layers 1 and 2. Crucially, the obtained Δl values are ~ 5 Å, thus corresponding to the actual measurement obtained from force-extension [Fig. 3(a) and Fig. S9 in [18]] and force-clamp (Fig. S10, [18]). As before, the dwell times for each individual transition can be used to compute the cumulative probability density function for the rupturing and reformation processes, the time course of which can be in both cases captured by a single exponential [Fig. 3(d)]. The resulting rates at each particular force are fitted to Eq. (4) yielding in this case $N = 2.0 \pm 0.8 \approx 2$ [Fig. 3(e)]. The observed $N = 2$ indicates that 2 interactions are disrupted in parallel, most likely suggesting that the ions have to be dislocated in pairs in order to avoid configurations where two ions of the same sign are in close contact.

While qualitatively similar, AFM solvation force measurements quantitatively differ from SFA results [23]. The main important difference lies in the massively different ($\sim 10^6$ fold) contact radius, which affects the liquid confinement area and hence the mechanisms of liquid squeeze-out. Briefly, the nanometer confinement below the AFM tip has allowed measurement of solvation forces in branched liquid molecules lacking molecular symmetry [6], and the packing properties can be analysed even for surfaces that are not atomically flat (such as self-assembled monolayers, SAMs) [23], both being important prerequisites in SFA measurements [1]. Moreover, the large temperature effect of the solvation forces observed with AFM [26] and the lack of correlation between the measured forces and the tip radius [27]—indicating that the nanometer-scale microasperities of the tip dominate the short-range interaction—suggest novel molecular mechanisms underlying the squeezing out of liquids confined in the gap between the cantilever tip and the substrate [23]. These observations have been recently complemented by AFM and STM imaging [16,28,29], directly demonstrating the semisolid behavior of the liquid layers. Our results using force-clamp spectroscopy add a new dimension to the study of the solvation phenomena, providing precise quantification of the equilibrium rupture-reformation dynamics, which allow, for the first time, the reconstruction of the solvation free-energy landscape. Moreover, these experiments provide new insights into the (molecular) mechanisms underlying liquid disruption; (i) using the Bell formalism, borrowed from antigen-antibody and single molecule mechanics pulling experiments, we gained access to the number of key interactions disrupted (and reformed) under force. (ii) For 1-undecanol, molecules lie parallel to the HOPG surface. Our experiments reveal that a unique interaction ($N = 1$) needs to be broken to induce the rupture of the layer. We speculate that the pore created in the structure of the confined liquid induces the lateral shift of a whole row of molecules pushed to the sides [Fig. 4(a)]. However, our experiments cannot tell whether the lateral displacement corresponds to 1 or more molecular positions. (iii) In the case of EAN, molecules are oriented upright from the mica normal direction. The EA^+ moiety measures 3 Å, while the nitrate measures 1.7 Å [30]. Since the barrier is highly symmetric ($\Delta x = 2.5$ Å), and probably located in the plane where electrostatic interactions take place, we speculate that there is a slight molecular mismatch between the position of contiguous ion pairs in order to better accommodate their charges. Our experiments show that in this case $N = 2$. Since N *only* corresponds to the number of molecules or interactions being disrupted in parallel with the tip, we hypothesise that individual anion-cation pairs need to be displaced together in tandem [Fig. 4(b)], which is easy to rationalize due to their electrostatic nature. These results demonstrate the surprisingly short-range dependence of the interaction between the last atom of the AFM probe and the solvation layer. Altogether, our experiments directly capture the molecular motions involved in the rupturing and self-assembly processes of individual solidlike liquid layers and highlight the single molecule nature of the squeeze-out mechanism when the confinement area lies in the nanometer realm.

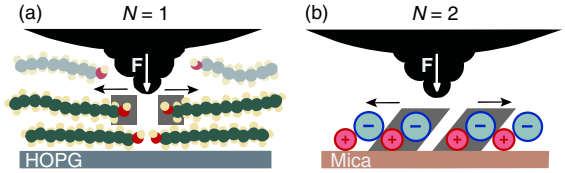

FIG. 4 (color online). Schematics of the rupturing process for (a) 1-undecanol ($N = 1$) and (b) EAN ($N = 2$).

We thank Amy Beedle and Aisling Williams for critical reading of the manuscript. J. R.-G. was recipient of a "La Caixa" fellowship. This work was supported by the Marie Curie CIG (293462), BBSRC (J00992X/1), and Royal Society (RG120038) Grants, and by the EPSRC Fellowship (K00641X/1), all to S. G.-M.

*Corresponding author.
sergi.garcia-manyes@kcl.ac.uk

[1] J. N. Israelachvili, 3rd ed. *Intermolecular and Surface Forces* (Academic Press, Elsevier, New York, 2011).

[2] R. G. Horn and J. N. Israelachvili, J. Chem. Phys. **75**, 1400 (1981).
[3] B. Cappella and G. Dietler, Surf. Sci. Rep. **34**, 1 (1999).
[4] H. H. Butt and R. Stark, Colloids Surf. A **252**, 165 (2005).
[5] F. Liu, S. de Beer, D. van den Ende, and F. Mugele, Phys. Rev. E **87**, 062406 (2013).
[6] R. Lim and S. J. O'Shea, Phys. Rev. Lett. **88**, 246101 (2002).
[7] N. N. Gosvami, S. K. Sinha, and S. J. O'Shea, Phys. Rev. Lett. **100**, 076101 (2008).
[8] V. Franz and H. J. Butt, J. Phys. Chem. B **106**, 1703 (2002).
[9] R. Atkin and G. G. Warr, J. Phys. Chem. C **111**, 5162 (2007).
[10] R. Hayes, G. G. Warr, and R. Atkin, Phys. Chem. Chem. Phys. **12**, 1709 (2010).
[11] J. I. Kilpatrick, S. H. Loh, and S. P. Jarvis, J. Am. Chem. Soc. **135**, 2628 (2013).
[12] M. Antognozzi, A. D. L. Humphris, and M. J. Miles, Appl. Phys. Lett. **78**, 300 (2001).
[13] M. Schlierf, H. B. Li, and J. M. Fernandez, Proc. Natl. Acad. Sci. U.S.A. **101**, 7299 (2004).
[14] F. Mugele, S. Baldelli, G. A. Somorjai, and M. Salmeron, J. Phys. Chem. B **104**, 3140 (2000).
[15] K. Morishige and T. Kato, J. Chem. Phys. **111**, 7095 (1999).
[16] T. Hiasa, K. Kimura, and H. Onishi, J. Phys. Chem. C **117**, 5730 (2013).
[17] L. Y. Low, J. Am. Stat. Assoc. **78**, 987 (1983).
[18] See Supplemental Material at http://link.aps.org/supplemental/10.1103/PhysRevLett.114.258303 for a full description of the materials and methods employed, and plots displaying the results of the supporting experiments.
[19] G. I. Bell, Science **200**, 618 (1978).
[20] C. Cecconi, E. A. Shank, C. Bustamante, and S. Marqusee, Science **309**, 2057 (2005).
[21] S. Garcia-Manyes, L. Dougan, C. L. Badilla, J. Brujic, and J. M. Fernandez, Proc. Natl. Acad. Sci. U.S.A. **106**, 10534 (2009).
[22] I. Popa, J. M. Fernandez, and S. Garcia-Manyes, J. Biol. Chem. **286**, 31072 (2011).
[23] S. J. O'shea, N. N. Gosvami, L. T. W. Lim, and W. Hofbauer, Jpn. J. Appl. Phys. **49**, 08LA01 (2010).
[24] R. G. Horn, D. F. Evans, and B. W. Ninham, J. Phys. Chem. **92**, 3531 (1988).
[25] D. Wakeham, R. Hayes, G. G. Warr, and R. Atkin, J. Phys. Chem. B **113**, 5961 (2009).
[26] L. T. Lim, A. T. Wee, and S. J. O'Shea, J. Chem. Phys. **130**, 134703 (2009).
[27] S. J. O'shea and M. E. Welland, Langmuir **14**, 4186 (1998).
[28] W. Hofbauer, R. J. Ho, R. Hairulnizam, N. N. Gosvami, and S. J. O'Shea, Phys. Rev. B **80**, 134104 (2009).
[29] T. Hiasa, K. Kimura, and H. Onishi, J. Phys. Chem. C **116**, 26475 (2012).
[30] Y. Umebayashi, W.-L. Chung, T. Mitsugi, S. Fukuda, M. Takeuchi, K. Fujii, T. Takamuku, R. Kanzaki, and S. Ishiguro, J. Comput. Chem., Jpn. **7**, 125 (2008).

11 Appendix IV:

Cell article

Cell

Dividing Cells Regulate Their Lipid Composition and Localization

G. Ekin Atilla-Gokcumen,[1,6,7] Eleonora Muro,[2,6] Josep Relat-Goberna,[3] Sofia Sasse,[1,4] Anne Bedigian,[1] Margaret L. Coughlin,[5] Sergi Garcia-Manyes,[3] and Ulrike S. Eggert[1,2,*]
[1]Department of Biological Chemistry and Molecular Pharmacology and Dana-Farber Cancer Institute, Harvard Medical School, Boston, MA 02115, USA
[2]Department of Chemistry and Randall Division of Cell and Molecular Biophysics, King's College London, London SE1 1UL, UK
[3]Department of Physics and Randall Division of Cell and Molecular Biophysics, King's College London, London WC2R 2LS, UK
[4]Institute for Neurobiology, Westfälische Wilhelms-Universität Münster, 48149 Münster, Germany
[5]Department of Systems Biology, Harvard Medical School, Boston, MA 02115, USA
[6]These authors contributed equally to this work
[7]Present address: Department of Chemistry, The State University of New York, Buffalo, NY 14260, USA
*Correspondence: ulrike.eggert@kcl.ac.uk
http://dx.doi.org/10.1016/j.cell.2013.12.015

SUMMARY

Although massive membrane rearrangements occur during cell division, little is known about specific roles that lipids might play in this process. We report that the lipidome changes with the cell cycle. LC-MS-based lipid profiling shows that 11 lipids with specific chemical structures accumulate in dividing cells. Using AFM, we demonstrate differences in the mechanical properties of live dividing cells and their isolated lipids relative to nondividing cells. In parallel, systematic RNAi knockdown of lipid biosynthetic enzymes identified enzymes required for division, which highly correlated with lipids accumulated in dividing cells. We show that cells specifically regulate the localization of lipids to midbodies, membrane-based structures where cleavage occurs. We conclude that cells actively regulate and modulate their lipid composition and localization during division, with both signaling and structural roles likely. This work has broader implications for the active and sustained participation of lipids in basic biology.

INTRODUCTION

As a cell divides, it undergoes massive shape changes, culminating in the formation of a small structure, the midbody, where cleavage between daughter cells occurs (Eggert et al., 2006b). Traditionally, cell division research has focused primarily on the actin and microtubule cytoskeletons as determinants of cell shape and as drivers of cell division. Although membranes are intimately connected to the cytoskeleton and intact membranes are an absolute requirement after division has been completed, little is known about the role of membranes during cell division. For example, starting at the most basic level, we do not know whether cells change their lipid composition as they go through the cell cycle. We report here a comprehensive and systematic analysis of changes in the lipid composition and localization during cell division.

Membranes and membrane trafficking are important to stabilize changes in curvature and to provide membrane to alleviate tension caused by shape changes during division. Membranes are also essential in signaling and are involved in the transport and modulation of key proteins at constriction and scission sites (Albertson et al., 2005; Echard, 2008; Eggert et al., 2004; Montagnac et al., 2008; Zhang et al., 2012). A recent report showed that, in dividing sea urchin eggs, new membrane addition is also required at the poles (Gudejko et al., 2012). Membrane lipids can achieve these different outcomes through different interactions with their binding partners, which are mostly proteins and/or other lipids. For example, some lipid species might interact with proteins to form local signaling platforms in vesicles or at the plasma membrane, whereas other lipid species might provide mechanical support for membrane architectures such as curved structures (van Meer et al., 2008). Local transport and/or synthesis and turnover of different lipid species are likely to be essential in regulating their varied functions. Except for a few examples of well-studied lipids, we are only beginning to appreciate the critical and diverse roles that lipids play during many biological processes.

Cells express hundreds of enzymes that synthesize lipids and produce tens of thousands of different lipids. Except for a few specific cases, it is unclear why cells invest energy into producing such complex and diverse lipidomes. Compared to other biological macromolecules, we have a poor understanding of the roles of specific lipids in biological processes. One of the reasons why it has been difficult to study lipids in their biological context is that, compared to proteins, there are fewer standard methods to visualize and manipulate lipid levels and localizations in cells (Saario et al., 2012; Schultz, 2010). There have been hints that a few different lipids might be involved in cell division (Atilla-Gokcumen et al., 2011; reviewed in Atilla-Gokcumen et al., 2010)

mostly by showing that fluorescent markers for these lipids localize to cytokinesis structures (Emoto et al., 2005; Ng et al., 2005). Only phosphatidylinositol 4,5-bisphosphate (PIP2) (Field et al., 2005) and the related phosphatidylinositol 3,4,5-triphosphate (PIP3) (Sagona et al., 2010), well-known signaling lipids that regulate actin polymerization and membrane trafficking (Echard, 2012), have been studied extensively. Here, we use mass spectrometry to identify which lipid species change as cells divide and dissect localized contributions at the midbody. We systematically perturb lipid levels in cells by knocking down lipid biosynthetic enzymes and use atomic force microscopy (AFM) to analyze biophysical properties of dividing and perturbed cells. Having determined the lipid complement of dividing cells, our combined approach is now allowing us to form hypotheses about the biological roles of the lipids that we identified.

RESULTS

A Lipidomic Comparison of Dividing and Nondividing Cells Reveals Cell-Cycle-Dependent Lipid Composition

We used liquid chromatography-mass spectrometry (LC-MS)-based global lipid profiling, an unbiased approach that does not require lipid perturbations (Saghatelian et al., 2004), to analyze the lipidome of cells synchronized at different stages of the cell cycle. Lipids are a broad class of metabolites that vary in structure and size. Based on this diversity, different ionization techniques can be used to analyze different classes and subgroups of lipids. For lipidomic studies, the use of ionization methods that do not cause extensive fragmentation is preferred because it enables the detection of a wide range of lipids within complex mixtures. We used electrospray ionization (ESI) (Han and Gross, 2003), which allows the analysis of different lipids from total lipid extracts over a range of mass-to-charge (m/z) ratios. We compared total lipids extracted from HeLa cells at cytokinesis to cells at S phase or the metaphase stage of mitosis and confirmed the identity of predicted lipid species by tandem MS (Table 1, Figure 1, and Table S1 available online). The lipid composition of cells in mitosis was similar to cells in cytokinesis. The timing of division relative to other stages of the cell cycle is rapid, suggesting that there may not be enough time for the global synthesis of new lipids, similar to protein translation not playing a major role during cell division (Stumpf et al., 2013).

The lipid composition of cells in S phase differs from cells in cytokinesis. Specifically, 11 lipid species out of the many thousand species synthesized (and detected by LC-MS) accumulate at least 4-fold in dividing (measured in cytokinesis but unchanged in mitosis) cells (Table 1 and Figure 1). Remarkably, all of these lipids are very specific species within different families. This specificity is exciting because it shows that cells are highly precise in their lipid regulation, but it also presents analytical challenges because tools are barely available to study lipid families, let alone specific species within these families. Biological roles have not been reported for two species that we identified: an unusual sterol derivative and an ether/ester-linked phosphatidic acid (rather than a traditional diester). The geometry and hydrophobic profile of the sterol derivative (hydroxy cholestane) is different from traditional sterols, such as cholesterol, due to the absence of a double bond in the B ring and the additional hydroxyl groups. Ether-linked phospholipids are rare structures (Ivanova et al., 2010). Their biosynthesis varies significantly from traditional glycerolipids, and it involves the esterification of acetyl CoA as the first step. These lipids, with a more lipophilic head group due to the ether linkage, can cause changes in the arrangement of lipids within membranes (Braverman and Moser, 2012). The upregulation of both of these lipid species during cell division suggests previously undescribed functions.

Eight of the lipids that we identified are specific subspecies within the sphingolipid family. Sphingolipids are a large lipid family based around a sphingosine base. They often include a fatty acid (then called ceramide) and can be highly glycosylated. Sphingolipids have been implicated in several biological processes, including regulation of apoptosis, inflammatory response, autophagy, and motility (Hannun and Obeid, 2011; Meivar-Levy et al., 1997). The first clues for a role for ceramides

Table 1. Specific Lipids Accumulate in Dividing Cells and at Midbodies

LIPID	Fold Increase during Cytokinesis[a]	Fold Increase at the Midbody[b]
Sterol derivative	>27	unchanged
Phosphatidic acid ether/ester (O-18:0/16:0)	40	unchanged
Phosphatidylinositol (16:0/18:0)	10	unchanged
C16 diH-ceramide	>11	unchanged
C18 diH-ceramide	accumulated[c]	unchanged
C20 diH-ceramide	accumulated[c]	unchanged
C22 diH-ceramide	accumulated[c]	accumulated[c]
C24 diH-ceramide	accumulated[c]	accumulated[c]
C22 ceramide	4	4
C24 ceramide	4	14
C16 hexosylceramide	>16	13
C24 hexosylceramide	unchanged	>36
Phosphatidic acid (16:0/16:0)	unchanged	14
Triacylglycerol (16:1, 12:0, 18:1)	unchanged	54
Phosphatidylserine (18:0/20:4)	unchanged	6

Results of LC-MS lipidomic analysis of S phase versus cytokinesis cells (middle column) and midbodies versus mock midbody purification from asynchronous lysate (right column). Lipids and their corresponding fold increases are shown (averages of three independent profiling experiments). The chemical structures of these lipids are shown in Figure 1. See Table S1 and Figures 5D and S1 for additional details.

[a]Fold increase in S phase versus cytokinesis cells is determined by [$Abundance_{cytokinesis}$] / [$Abundance_{S\text{-}phase}$] for each lipid. Abundance is the total ion count for a given ion. Each ion corresponds to a mass-to-charge ratio (m/z), which is used to assign the lipid species.

[b]Fold increase in midbody versus cytokinesis cells is determined by [$Abundance_{midbody}$] / [$Abundance_{purified\ lysate}$] for each lipid.

[c]A numeric value for fold increase could not be calculated due to the low abundance of these species in S phase or cytokinesis cells.

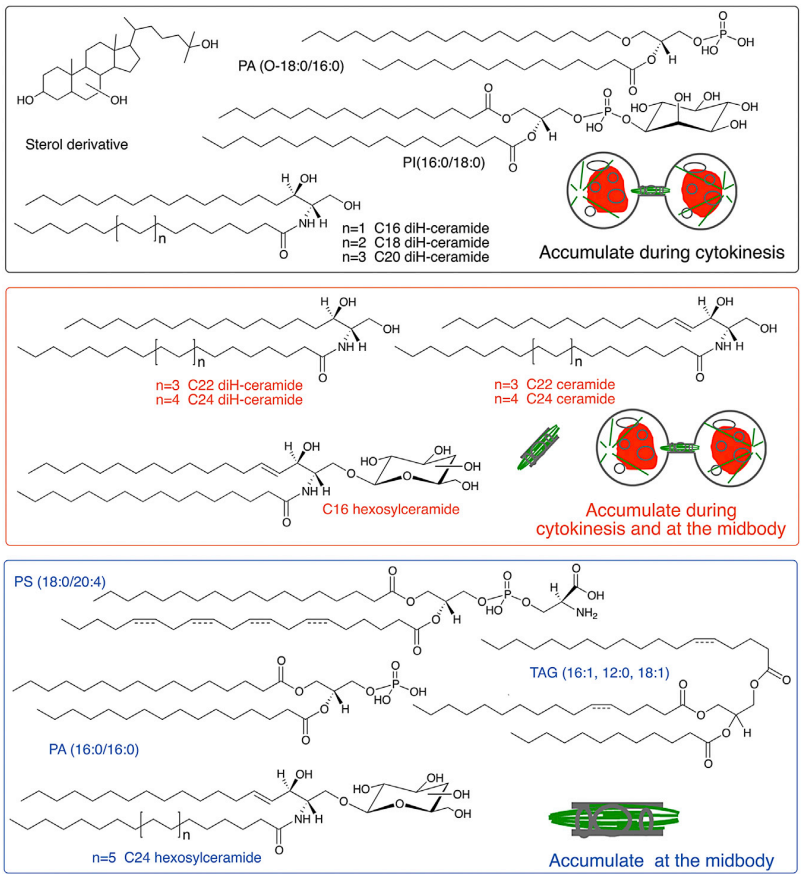

Figure 1. Chemical Structures of Lipids that Change during Cytokinesis and at the Midbody

Chemical structures of the lipids listed in Table 1 are shown. Lipids that accumulate from S phase to cytokinesis are shown in black and red. Lipids that accumulate at the midbody are shown in red and blue. Note that the *sn*-1 and *sn*-3 positions and the positions of the double bonds in TAG (16:1, 12:0, 18:1) and PS (18:0/20:4) and the position of the third hydroxyl group on the B ring of the trihydroxycholestane could not be determined. Targeted MS analysis of the ceramide and diH-ceramide content of cytokinesis cells and midbodies is shown in Figure S1.

in mammalian cell division were provided in our previous report that inhibition of glucosylceramide synthase (GCS) causes cytokinesis failure. Chemical inhibition of GCS versus RNAi knockdown resulted in changes in different lipid species, highlighting the high plasticity of lipid regulation in response to different perturbation methods (Atilla-Gokcumen et al., 2011; Eggert et al., 2006a; Castoreno and Eggert, 2011). The specific ceramides changed upon GCS inhibition, however, mostly differ from the species upregulated in dividing cells, which are ceramides with long fatty acid side chains. Some of the largest relative lipid accumulations in dividing cells were dihydroceramides (diH-ceramides, Table 1 and Figure S1). These lipids are expressed at very low levels in nondividing cells and have been studied little because it was assumed that they were inert precursors during ceramide synthesis. Our findings suggest a broader role. Our study links several specific and unusual lipids to cell division and, more broadly, reports a cell-cycle-dependent regulation of the global lipidome during a basic biological process.

Dividing Cells Have Distinct Mechanical Properties

Having uncovered the high precision that cells use to regulate their lipidomes, we wanted to better understand whether the lipids that we identified had any particular physical properties that might give us hints about their biological functions. In cells, lipids function in complex environments that include different proteins and, if in the plasma membrane, extracellular matrix and cell surface carbohydrates, making it challenging to dissect the contributions of membranes and the lipids themselves. We used atomic force microscopy (AFM) in its force spectroscopy mode to first investigate the mechanical properties of live cells at 37°C. At relatively low forces and low indentation depths, force-spectroscopy AFM has been used successfully to measure the elasticity of a range of different cell types and experimental environments (Harris and Charras, 2011; Kasas et al., 2013; Stewart et al., 2012). For example, elasticity measurements have been applied to study cell division and spreading (Matzke et al., 2001; Pietuch and Janshoff, 2013), and we use this approach here to investigate the properties of cells in which lipid biosynthesis has been perturbed (see below and Figure 3F). To gain more insight into the full range of mechanical stabilities of dividing cells, we turned to a less common approach: we expanded the traditionally sampled range of forces to higher values, spanning 10–250 nN and compressed the cell until the plasma membrane was penetrated just before the tip reached the hard substrate (Hategan et al., 2003). Applying such high forces deforms the entire cell, pushing the AFM probe through a variety of cellular structures and compartments until the membrane is broken. The rupture of the plasma membrane is recognized by a breakthrough jump in the force-distance curve, representing a clear molecular fingerprint (Garcia-Manyes et al., 2005a, 2010), which is similar in cells and in supported lipid bilayers (Figure 2). We based this work on a precedent (Yokokawa et al., 2008), wherein it was demonstrated that the "rip" encountered at high forces during indentation corresponds to the real penetration of the probe through the plasma membrane (see Extended Experimental Procedures for more details). We found that much higher forces (3-fold increase) were required to reach this breaking point in

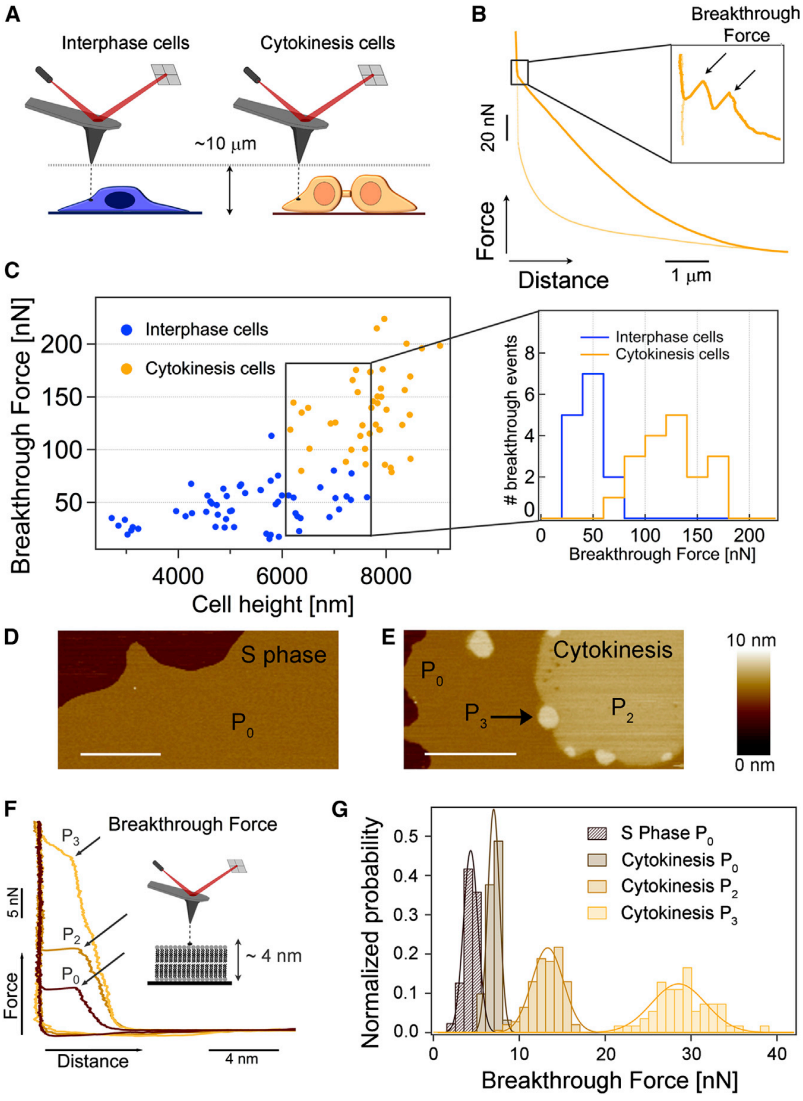

Figure 2. The Mechanical Resistance of Cytokinesis-Associated Membranes Is Higher Both in Live Cells and in Supported Lipid Bilayers Measured In Vitro

(A) Schematics of a force spectroscopy experiment on an interphase (nondividing) and cytokinesis (dividing) live cell.

(B) Typical force-distance curve conducted on a live HeLa cell during cytokinesis. In a typical cycle, the cantilever tip approaches the cell membrane and applies an increasingly higher pushing force that deforms the cytoplasm. Once the cantilever reaches a position close to the stiff substrate, it is able to penetrate through the two lipid membranes. This breakthrough event is marked by two consecutive discontinuities in the force-extension trace (arrows in inset). The cantilever is then retracted to the initial position (light-yellow line).

(C) Scatterplot of the first membrane breakthrough force versus the cell height for interphase (blue, 26 independent cells) and cytokinesis cells (yellow, 17 independent cells) in cytoplasmic areas. Similar experiments performed in the nuclear areas are shown in Figure S2. The plot shows that, although the breakthrough force increases with the cell height, dividing cells exhibit markedly higher breakthrough forces. Selecting a comparable range of cell heights (6–7.6 μm), the mechanical resistance of cytokinesis cells is significantly higher (inset in C, 125 ± 30 nN and 48 ± 14 nN breakthrough force for dividing and interphase cells, respectively) with >99.99% confidence (Student's t test). Though the error in comparing values between dividing and nondividing cells is small, there is an additional potential error in the absolute values reported due to limitations in the size of the cantilevers available for these experiments (see Extended Experimental Procedures for a discussion).

(D and E) Lipids derived from cells at S phase and cytokinesis form supported lipid individual bilayers that exhibit distinct morphologies as revealed by tapping mode AFM topographical images.

(D) Supported lipid bilayers composed of S phase lipids exhibit a continuous P_0 phase.

(E) By contrast, in the case of lipids extracted from cytokinesis cells, three main phases of increasing height are observed (respectively, P_0, P_2, and P_3). Scale bar, 1 μm.

(F) Force-distance curves on both supported lipid bilayers revealed distinct mechanical stabilities.

(G) The mechanical resistance of lipid bilayers formed from S phase cells (P_0) yielded a mean breakthrough force of 3.87 ± 0.84 nN (n = 900), obtained by Gaussian fits to the data. In the case of the cytokinesis sample, both the P_2 phase (12.93 ± 1.83 nN, n = 137) and the P_3 phase (28.3 ± 3.17 nN, n = 54) revealed a much higher mechanical stability than the matrix bilayer phase, P_0 (6.5 ± 0.68 nN, n = 90).

Note that the nomenclature defining each of the phases is arbitrary yet consistent throughout the paper. For detailed descriptions of all phases and the height profile of (E), see Figure S2.

dividing versus nondividing cells of comparable heights (Figures 2A–2C), suggesting that both the cell body and the plasma membrane have different mechanical properties in dividing cells. The same trend was observed in the nuclear regions (Figure S2A and S2B), albeit shifted to higher force values. Much of the increased stiffness in dividing cells is undoubtedly due to the cytoskeleton, which has well-documented and essential roles in the division process. However, our experiments suggest that the properties of the plasma membrane also need to be different in dividing cells to be able to withstand substantially higher forces applied during force spectroscopy.

Lipids Isolated from Dividing Cells Have Distinct Morphological and Mechanical Properties

The mechanical resistance that we found in the plasma membrane of dividing cells is likely due to the combined action of membrane proteins, cell surface glycans, and lipids. The full complement of membrane proteins is not known, but we show

Table 2. Cytokinesis Hits from an RNAi Screen of Lipid Biosynthetic Enzymes

Gene Symbol	Predicted Lipid Product	% Multinucleated
SMPD4	*ceramide*	*51.7 ± 4.9*
CERS4	*diH-ceramide/ceramide*	*24.2 ± 2.8*
GALC	*ceramide*	*22.5 ± 6.3*
DGAT2	*triacylglycerol*	*21.9 ± 6.6*
SERINC4	*phosphatidylserine/* 3-ketodihydrosphingosine	*17.7 ± 2.8 (96h)*
LSS	lanosterol	17.6 ± 1.9
SMPDL3A	*ceramide*	*16.1 ± 3.2 (96h)*
CH25H	*25-hydroxycholesterol*	*14.9 ± 3.4 (96h)*
SERINC1	*phosphatidylserine/* 3-ketodihydrosphingosine	*14.4 ± 0.3 (96h)*
ACSL5	acyl-CoA	13.9 ± 2.3
ALOX12B	12(R)-HPETE	13.8 ± 5.6
PIKFYVE	PI(5)P/PI(3,5)P2	13.4 ± 1.4
GLB1	*glucosylceramide*/GM2	*13.3 ± 4.0*
LYPLA2	glycerophosphocholine/ glycerophosphoethanolamine	13.2 ± 2.8
GAL3ST1	sulfatide/ digalactosylceramidesulfate	13.0 ± 0.8
SCD	oleoyl-CoA/ oleoyl-[acyl-carrier protein]	12.2 ± 0.7
ABHD5	*phosphatidic acid*	*11.6 ± 2.0*
MTM1	*PI* /PIP/I(1)P	*11.5 ± 3.1 (96h)*
ST6GALNAC6	GD1α/GQ1bα/GT1aα	11.4 ± 2.7 (96h)
ST8SIA5	GD1c/GT1a/GQ1b/GT3	11.1 ± 3.8
LCAT	1-acylglycerophosphocholine/ cholesteryl ester	10.8 ± 1.9
PTPLB	VLC trans-2,3-dehydroacyl-[acyl-carrier protein]/trans-2, 3-dehydroacyl-CoA	10.2 ± 0.9
CERS2	*diH-ceramide/ceramide*	*10.0 ± 1.0*
Nontargeting siRNA control		2.3 ± 0.8

Enzymes shown in *italics* are predicted to process lipid families that accumulate in cytokinesis and/or midbody samples (Table 1). Predicted lipid products were identified using the KEGG database (http://www.genome.jp/kegg/). See Table S2 for a full list of the RNAi library and the RNAi screen section in the Extended Experimental Procedures for additional details. The average percentage of multinucleated cells, as well as the standard deviation between the four experiments, is shown (two independent experiments with two time points each: 72 and 96 hr). A minimum of 100 cells per case were counted.

here precisely which lipids change in dividing cells. If the lipids themselves have physical properties that might influence their function, these could include a predisposition to organize into different domains, possibly recruiting other lipids and/or proteins to these domains in cells. In an attempt to identify a potential contribution of lipids to the overall mechanical stability of S phase and dividing cells, we again used AFM to test the topographic and mechanical properties of supported lipid bilayers from isolated lipids at very high spatial resolution (El Kirat et al., 2010; Sackmann, 1996) (Figures 2D–2G). Because the different membrane compartments in cells are very dynamic and we have an incomplete understanding of the membrane proteins involved that could potentially be used as markers for a membrane fraction's origin especially in dividing versus nondividing cells, it is not possible to isolate only plasma membrane in sufficient purity to allow meaningful comparisons. We therefore analyzed total lipids isolated from cells under the same conditions as the samples used for LC-MS, allowing a direct comparison between the identities of the lipid mixtures and their properties.

Although the differences in lipids that we observed by LC-MS were large for specific lipids, the total change was quite small relative to the cellular lipidome (for example, the total amount of ceramides doubled, but only ~2% of lipids in HeLa are ceramides). Surprisingly, such a small detected change in the lipid composition had a significant effect on the topographic properties of supported lipid bilayers formed from S-phase- and cytokinesis-derived membranes: supported lipid bilayers formed from S phase cells were mostly uniform (presenting only the matrix phase "P_0"; Figures 2D and S2C), whereas lipids from dividing cells were more likely to separate into three distinct phases (P_0, P_2, and P_3) (Figure 2E). To test whether such a distinct lateral molecular arrangement of the lipids also had an effect on the bilayers' mechanical properties, we conducted force spectroscopy experiments on both samples (Figures 2F and 2G) (Garcia-Manyes and Sanz, 2010). Whereas bilayers corresponding to S phase cells (P_0) exhibited moderate mechanical stability of ~4 nN (Figure 2G), the distinct phases found in the bilayers formed from cytokinesis cells exhibit increasingly larger forces required to puncture the membrane, culminating in the P_3 phase (Figures 2E and 2G; see Figure S2 for further description of the different phases). The P_3 phase, which was observed in about 20% of samples (Figure S2D), was dramatically stiffer, with an associated mechanical resistance of ~28 nN. These observations on supported lipid bilayers suggest that some of the mechanical properties that we observed in cells could be related to the physical properties of the lipids themselves, functioning in conjunction with membrane proteins.

RNAi Knockdown of Lipid Biosynthetic Enzymes Causes Cell Division Defects

To get a better understanding of the lipids' potential biological roles, we perturbed lipid levels in cells and evaluated the resulting phenotypes. In the absence of techniques for lipids comparable to genetic knockouts or knockdowns, inhibition of lipid biosynthesis is one of the few ways in which lipid levels in cells can be manipulated. We used RNAi to systematically perturb the biosynthesis of different lipid families. We designed a custom library targeting 244 lipid biosynthetic enzymes and screened this library for cytokinesis inhibition in HeLa cells. Knockdown of 23 genes caused cytokinesis failure (Tables 2 and S2). Although there was a range across different lipid classes, 11 out of 23 are involved in sphingolipid metabolism, which is in excellent agreement with our LC-MS data. Some of these enzymes are predicted to process highly glycosylated sphingolipids (GLB1, ST6GALNAC6, and ST8SIA5), which were not detected in our lipidomic analysis using

standard LC-MS parameters. These data partially correlate with the literature. It was shown in sea urchin eggs that cholesterol and the glycosphingolipid GM1 accumulate in an equatorial band coupled to contractile ring formation and assembly (Ng et al., 2005). GM1 is one of GLB1's substrates, and both ST6GALNAC6 and ST8SIA5 process GD1a, a direct derivative of GM1.

The broad importance of different lipids and membrane compartments in the cell division process is highlighted by our identification of enzymes associated with a variety of different pathways and predicted functions and localizations. For example, two enzymes are predicted to process sterol derivatives (LSS, CH25H). Other enzymes are implicated in the glycerophospholipid and glycerolipid pathways (LYPLA2, LCAT, SERINC1 and 4, DGAT2, and ABHD5), and two enzymes (PIKFYVE and MTM1) process phosphatidylinositols, which are known to be involved in cytokinesis (Echard, 2012). In addition, we identified enzymes predicted to be involved in the biosynthesis, metabolism, or elongation of fatty acids: ACSL5, ALOX12B, SCD, and PTPLB. Some of these enzymes may be involved in the synthesis of precursors of the lipids that we identified by LC-MS.

Several of the most penetrant RNAi phenotypes are caused by single enzymes that are part of multimember families, for example, ceramide synthases (six enzymes) or neutral sphingomyelinases (four enzymes in mammals). The field is only just beginning to appreciate the complexity of lipid biosynthesis and the level of crosstalk between different biosynthetic routes and enzymes. Many biosynthetic enzymes have predicted substrate and product families, but the nature of specific lipids involved and the factors regulating the enzymes and therefore lipid production are only known in very few cases (Hannun and Obeid, 2011). For example, a biochemical analysis of different ceramide synthases showed that different enzymes preferentially process different side-chain-length ceramides and that their expression is tightly connected (Mullen et al., 2011). We therefore used LC-MS to analyze the lipid composition of three top RNAi hits: SMPD4, GALC, and DGAT2 (Figure S3A and Table S3). DGAT2 is an acyltransferase that catalyzes the terminal step in triacylglycerol synthesis, GALC catalyzes the conversion of galactosylceramide into ceramide, and SMPD4 is predicted to convert sphingomyelin into ceramide (Figure S3B). Unexpectedly, knockdown of SMPD4 did not result in accumulation of substrate or depletion of product, as would be predicted by classical enzymology, but instead caused accumulation of specific side-chain ceramides (product) and glycosylated ceramides. This is likely due to cells adjusting their substrate specificities and activating alternative lipid biosynthesis feedback loops over the 3 day duration of the RNAi experiment. GALC RNAi also caused accumulation of specific side-chain hexosylceramides. DGAT2's lipid profile is discussed further in the section on midbodies because we found that it is involved in the metabolism of a lipid accumulated at the midbody.

RNAi Knockdown of Key Lipid Biosynthetic Enzymes Causes Mechanical Defects in Cells

The overall cellular consequences of SMPD4, GALC, and DGAT2 knockdown were similar and connected to defects in the cytoskeleton, the main driver of cell mechanics. To varying degrees, all three RNAi treatments caused a significant delay during metaphase in mitosis (Figures 3A and 3B), followed by cell division failure at different stages, mostly coupled with unusual membrane blebbing (Figures 3A and S3D). The morphologies of interphase cells as well as the actin cytoskeleton were also changed, including an increase in the footprint of cells (Figures 3D and 3E). Because these phenotypes suggest defective processing of mechanical signals, we tested whether mechanical integrity was affected in cells in which our top hit SMPD4 was knocked down. Using AFM at forces lower than 0.6 nN (as opposed to the high forces needed to break through membranes discussed above) to measure elasticity, we found that SMPD4 RNAi cells are 4-fold stiffer than control cells (Figure 3F). These data show a clear mechanical role for lipids, either directly or by causing changes to the cytoskeleton. Because SMPD4 RNAi is accompanied by changes in the actin cytoskeleton (Figure 3D), in this case it is likely that the effects exerted by lipid changes cause cytoskeletal defects rather than structural roles of the lipids themselves.

Dividing Cells Regulate the Lipid Composition of the Midbody

Membranes are particularly important in the midbody, where final cleavage takes place, because they are needed to seal the plasma membrane after fission. Super-resolution imaging shows that ceramide-positive vesicles and the glycosylated sphingolipid GM1 localize to different regions of the midbody (Figure 4A). Ceramide vesicles do not substantially overlap with endosomal proteins known be involved in cytokinesis (FIP3-RAB11 and ESCRTIII; Figures 4B and 4C), suggesting that they participate in an as yet unknown mechanism. Membrane trafficking is reduced during mitosis and is thought to increase again during cytokinesis. Thus, a specific lipid composition at the midbody might be regulated both by specific trafficking and by local synthesis. We therefore tested whether cells regulate their lipid composition at the midbody. Midbody-rich fractions can be purified biochemically, and their proteome has been determined. To isolate midbodies with intact membranes, we adapted previous protocols (Mullins and McIntosh, 1982; Skop et al., 2004) and compared lipids extracted from cells in cytokinesis and midbodies (Figure 5). To control for the copurification of nonmidbody lipid structures, we also compared the lipidome of midbodies to lysate from nonsynchronized cells that was subjected to the same purification protocol (Figure 5D). As with dividing cells, we found that a small number of lipids with very specific structures strongly accumulated in midbodies (Tables 1 and S1 and Figure 1). Five out of nine lipids that accumulate at midbodies also accumulate during division, and all five lipids are sphingolipid derivatives with specific fatty acid chains, suggesting that long-chain dihydroceramides' and ceramides' effects are specific to the abscission site.

Several lipid species, including a rare TAG (16:1, 12:0, 18:1) (Figure S4), accumulate in midbodies but were not upregulated in dividing cells, suggesting that they are always present in cells and specifically localize to the midbody. TAGs are the primary unit of energy storage in eukaryotic cells. Whereas the lengths of fatty acid chains in TAGs vary significantly based on the cells'

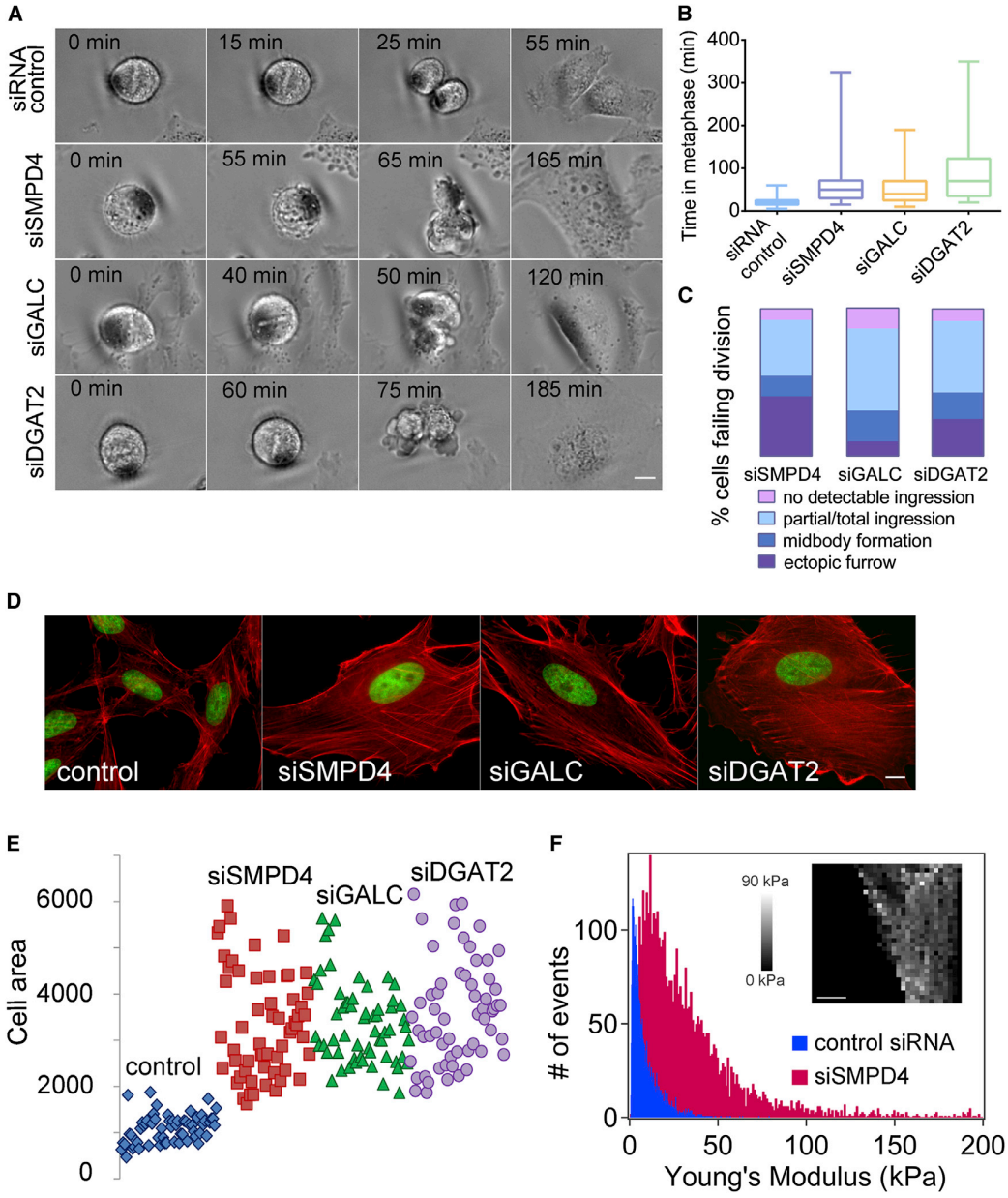

Figure 3. RNAi Knockdown of Lipid Biosynthetic Enzymes Causes Cell Division Defects and Cytoskeletal Changes in Interphase Cells

(A) Still images from time-lapse movies of dividing cells for control, SMPD4, GALC, and DGAT2 siRNA treatments. Movies are available in the Supplemental Information. Scale bar, 10 μm.

(B) Box plots of metaphase delays caused by siSMPD4, siGALC, and siDGAT2 treatments, respectively (average ± SEM), 58 ± 4.6, 56.5 ± 5.4, and 90.6 ± 9 min. The time in metaphase for all RNAi-treated cells was significantly higher than the control (20.4 ± 1 min) with a > 99.99% confidence (t test). A minimum of 70 cells from 3 independents experiments for each case were analyzed.

(C) SMPD4, GALC, and DGAT2 siRNA treatments result in different cytokinesis failure phenotypes. Examples for each phenotype are shown in Figure S3D. Ectopic furrow refers to both successful and unsuccessful abscissions. A minimum of 70 cells from three independent experiments for each case were analyzed.

(D–F) SMPD4, GALC, and DGAT2 siRNA treatments result in altered cell shape and actin morphology.

(D) Representative images are shown for control and siRNA-treated cells. F-actin is shown in red (phalloidin staining) and DNA in green (DAPI staining). Scale bar, 10 μm.

(E) Quantification of the cell area for control cells (1088 ± 39 μm^2, average ± SEM) and different siRNA-treated cells (respectively, for siSMPD4, siGALC, and siDGAT2: 3331 ± 143, 3386 ± 113, and 3617 ± 144 μm^2). The area was measured in at least 60 mononucleated cells per treatment and was significantly higher in

(legend continued on next page)

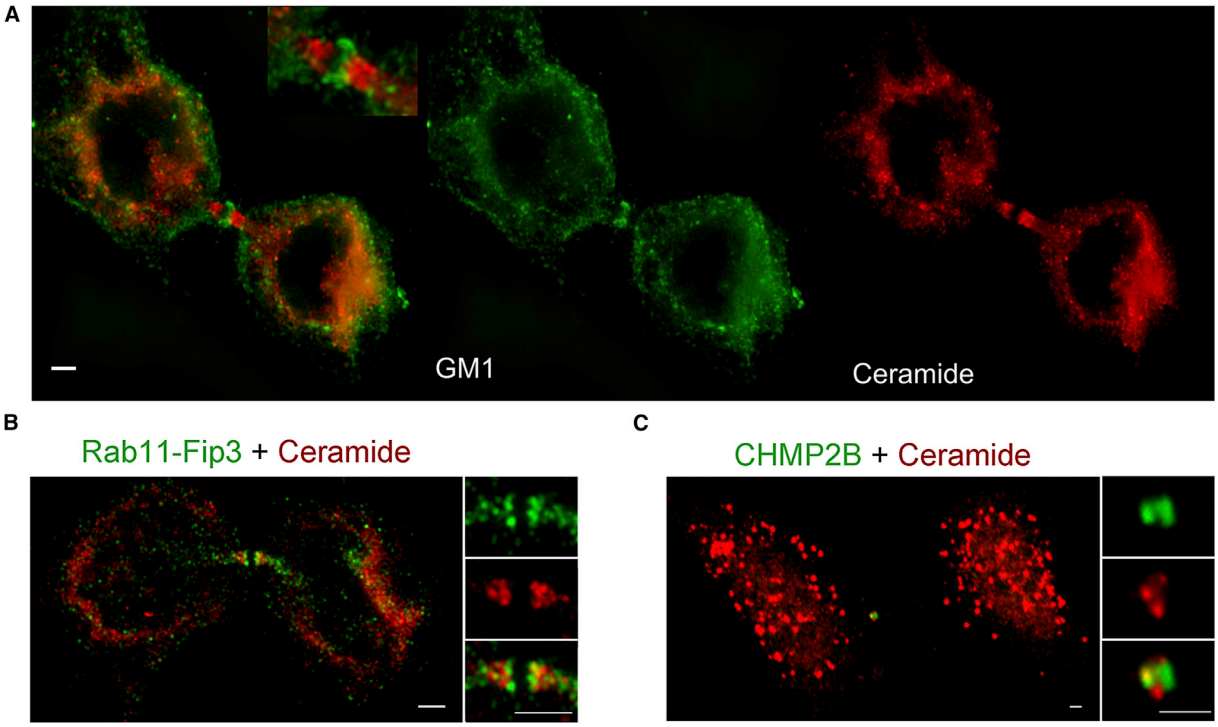

Figure 4. Ceramide-Containing Vesicles Localize to the Midbody

(A) Different lipids show differential localization to division sites. The glycosphingolipid GM1 (green, visualized by cholera toxin) and ceramide (red, pan-ceramide antibody staining) at the midbody are shown. Images are Z projections and were acquired with a N-SIM super-resolution microscope. Inset shows 2× zoom of the midbody area. Scale bar, 2 μm.

(B and C) Ceramide antibody staining only partially overlaps with endosomal proteins known to be involved in cytokinesis: FIP3-RAB11 (B) and CHMP2B (C). The images are Z projections acquired with an N-SIM super-resolution microscope (B) and a confocal microscope (C). Scale bars, 2 μm.

repertoire, longer-chain fatty acids (14–20 carbons) are usually preferred in eukaryotic cells. Our TAG species is unusual because it contains a 12 carbon chain. Although cells make thousands of different TAGs, the biological functions of individual species are not well studied and neither are the selectivity or specificity of several different enzymes that synthesize TAGs (Coleman and Mashek, 2011). DGAT2, a TAG-synthesizing enzyme (Figure S3C), was a top hit in our RNAi screen (Figures 3A–3C). MS analysis showed that several lipids were changed in DGAT2 RNAi cells, including TAG (16:1, 12:0, 18:1) (Figure S3A), suggesting that DGAT2 is involved in the metabolism of this lipid.

A specific phosphatidylserine also accumulated at midbodies. Phosphatidylserines mostly reside in the plasma membrane and are present in the inner leaflet in the resting state of the cell. Synthesized in the endoplasmic reticulum, phosphatidylserines are transported through different organelles and to the plasma membrane and can also be flipped from the inner leaflet to the outer leaflet of the plasma membrane when necessary. This dynamic nature is important for biological processes, including apoptosis and autophagy (Kay and Grinstein, 2011). Biological functions for specific unsaturated long-chain phosphatidylserine species, such as the one that we identified, have not been reported.

In addition to the more unusual lipid species that we observed in dividing cells and at midbodies, we also found two common lipids: (16:0/16:0) phosphatidic acid accumulated in midbodies and (16:0/18:0) phosphatidylinositol in dividing cells. Both fatty acid configurations represent major subspecies within these lipid families. As a major constituent of the plasma

all RNAi-treated cells compared to control, with a >99.99% confidence (t test). Targeted lipid analyses of the RNAi samples are reported in Table S3 and Figure S3A.

(F) Histogram of cell stiffness (Young's modulus values, see Extended Experimental Procedures) measured on control and SMPD4 siRNA-treated cells. A total number of 4,098 indentations (21 cells) and 4,314 indentations (18 cells) were performed on control siRNAi and siSMPD4-treated cells, respectively. The average value for siSMPD4 cells is significantly higher (35 ± 8.8 kPa, average ± SEM) than siRNA control cells (8.3 ± 1.9 kPa), with a >99.95% confidence. (Inset) Typical 32 × 32 force-volume map measured on a siSMPD4 cell. The topography of the force-volume corresponds to an arbitrary color scale of the Young's Modulus. Scale bar, 10 μm.

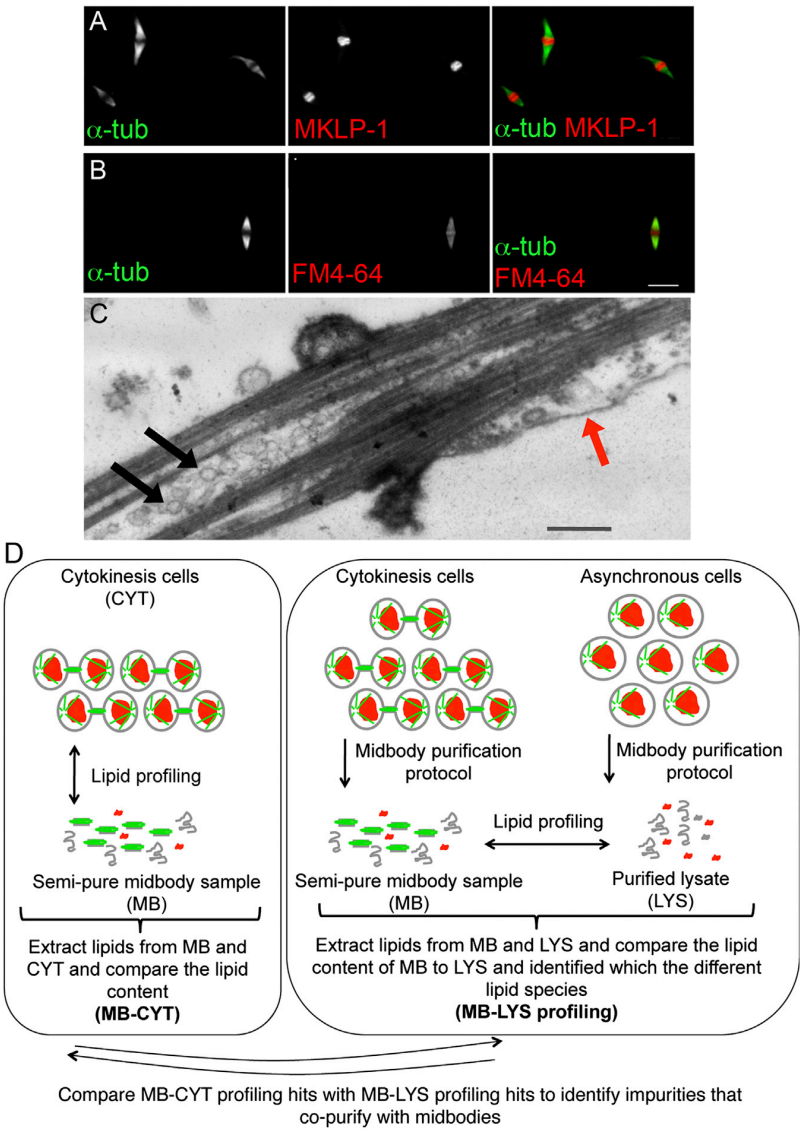

Figure 5. Midbody and Membrane Markers Are Correctly Localized in Isolated Intact Midbodies

(A and B) Isolated midbodies were stained with α-tubulin, MKLP-1, a marker for midbodies (A), and FM4-64, a membrane marker (B). Scale bar, 5 μm.

(C) Representative electron micrograph shows an isolated midbody with intact membrane structures. Black arrows show vesicles inside, and red arrow shows plasma membrane that surrounds the midbody. Scale bar, 500 nm.

(D) Schematic of the experiments that we conducted to exclude from our LC-MS analysis membrane impurities that copurify with midbodies. We obtained and compared the profiles of midbodies versus cytokinesis (MB-CYT) and midbody versus purified lysate (MB-LYS). The hits from MB-CYT and MB-LYS profiling were compared. MB-CYT hits were checked in MB-LYS profiling. Lipids that were unchanged in MB-LYS profiling (i.e., found in lysate from asynchronous cells in equal amounts) were eliminated, as they are most likely impurities that copurified in both samples. Membrane structures, microtubules, and DNA are cartooned in gray, green, and red, respectively.

membrane, phosphatidic acids are important signaling molecules and precursors for a diverse group of lipids, including phosphatidylserines and phosphatidylinositols. Phosphatidylinositols are a constituent of the inner leaflet of the plasma membrane. They can be glycosylated and form glycosylphosphatidylinositol (GPI) anchors, which are important post-translational protein modifications. They are also precursors for phosphatidylinositol phosphates, important signaling molecules that actively participate in cell division (Echard, 2012). Much of lipid signaling is regulated through localization of lipids to specific membrane structures, often vesicles. Our data show that cells not only specifically regulate when they synthesize specific lipids, but also where they are localized within larger structures of the cell.

There Is High Correlation between Lipid Species Identified by LC-MS and RNAi Screening

It has become clear in recent years that the lipid composition of different cell types can vary substantially for reasons that are only beginning to be understood (Gerl et al., 2012). The work that we report here was done in HeLa, and we expect that the extent and/or identity of lipid changes in other dividing cells may vary depending on the physiology of the cell type. We show, however, excellent agreement between the lipid families targeted by the biosynthetic enzymes that scored in our RNAi screen and the lipids identified in the unperturbed LC-MS analysis (overlap is shown in italics in Table 2). Twelve out of 23 enzymes identified in our RNAi screen are predicted to process lipids found accumulated in cytokinesis cells and/or at the midbody, eight of which belong to the nine strongest RNAi hits. Reaching the same results by two complementary approaches strongly suggests that the lipids we identified by both approaches have biological significance.

DISCUSSION

We have shown here that HeLa cells actively regulate the production and localization of lipids during cell division and that cells display high specificity in the chemical structures of these lipids. Our analysis methods were comparative

(cytokinesis versus S phase cells and midbody versus purified lysate), allowing us to observe dynamic changes between the different states we analyzed. Several of the lipids that had previously been reported to play a role during cytokinesis, including the phosphatidylinositol phosphates (Emoto et al., 2005; Field et al., 2005), did not score in our LC-MS analysis. This is, in part, due to our inability to detect large lipids like PIP3 with the extraction conditions and the MS ionization method that we used (ESI). We could, however, detect PIP2, which was unchanged, likely due to its constant presence during the cell cycle, as would be expected for a signaling lipid that regulates multiple processes. Along this continuum and as with many proteins involved in cell division, some of the lipids reported here appear to also be involved in other cytoskeletal processes; for example, GALC, SMPD4, and DGAT2 RNAi interphase cells have altered actin morphologies (Figures 3D and 3E). The required presence of some lipids throughout the cell cycle explains why we observed very good, but not complete, correlation between the dynamic lipid changes identified by LC-MS and the biosynthetic enzymes scored in our RNAi screen. It is likely that several of the biosynthetic enzymes that did not have matching lipid changes are involved in the metabolism of lipids that are constantly present.

Our analyses showed not only that cells precisely regulate the timing of when they synthesize specific lipids, but also that they specifically regulate their localizations to the midbody. It is beginning to be appreciated that different membrane compartments such as some endosome species, for example, have distinct lipid compositions (Bissig and Gruenberg, 2013). We focused our analysis on the lipid composition of midbodies, both because they are crucial sites of cell fission and because we could purify them, and appropriate controls, in sufficient quantity and acceptable purity. We were interested to note that there was only partial overlap between the lipids accumulated in dividing cells and at midbodies, suggesting that several of the lipids accumulated in dividing cells have functions that are independent of the final division site, possibly during earlier steps of division. Conversely, several midbody lipids did not accumulate in dividing cells, suggesting that they have additional roles during the cell cycle. A finer dissection of the regulation of lipid localization, for example to the plasma membrane or to different vesicle types, would provide further functional information, but is currently limited by the ability to biochemically fractionate different compartments with sufficient purity. As our understanding of the protein requirements of different membrane compartments grows, it should become possible to use the protein markers as guides for more detailed lipidomic studies.

Despite decades of intense study predominantly focused on the proteins of the actin cortex located just beneath the plasma membrane (Eggert et al., 2006b), we still do not have a comprehensive understanding of the mechanics underlying the cell division process. For example, local tension changes of the actin cortex both at the cleavage furrow and at the opposing poles are important for successful division (Guha et al., 2005; Murthy and Wadsworth, 2005; Sedzinski et al., 2011). A recent report showed that a release of membrane tension triggered the assembly of the ESCRT fission complex during abscission (Lafaurie-Janvore et al., 2013). These intriguing observations suggest that there may well also be mechanical roles for membranes. These roles could be structural or could involve signaling to the cytoskeleton. We present here evidence suggesting that both occur, and we begin to tease apart the contributions made by lipids and membrane proteins. Lipids are involved in signaling by affecting specific membrane proteins or by assembling multiprotein and multilipid signaling platforms. We show that SMPD4 RNAi makes cells stiffer and causes defects in the actin cytoskeleton, likely because changes in the lipid composition cause the transmission of signals to the cytoskeleton.

We also present evidence for possible structural roles of lipids during division. Dividing cells are substantially more resistant to high forces applied by force spectroscopy than are nondividing cells, suggesting that their membranes have changed to adapt to mechanical stress during division. Although some of these properties are no doubt due to membrane proteins or lipid/protein signaling platforms, we now know precisely which lipids change in dividing cells, allowing us to consider whether the lipids themselves also might contribute. As it is not possible to use measurements in live cells to dissect the contributions of lipids versus membrane proteins, the cytoskeleton, or the cytoplasm (Moeendarbary et al., 2013), we used force spectroscopy on supported lipid bilayers isolated from dividing cells. We found an increased tendency toward more rigid domain formation, including the extraordinarily rigid P_3 phase. High-resolution AFM studies on lipid phase behavior are usually performed with carefully controlled synthetic membranes (Sullan et al., 2009a, 2009b). Here, though we know which lipids differ between the two samples, both are complex mixtures of total lipids extracted from cells. This allows interactions between lipids normally segregated in different cellular membrane compartments. Despite this dilution of possible naturally occurring interactions in both samples, we observe an increased tendency to form distinct phases in lipids extracted from dividing cells (Figures S2A and S2B), and we were intrigued by the surprisingly distinct change in the physicochemical properties of the supported lipid membranes. Due to the artificial conditions of the AFM experiment on supported lipid bilayers, we would not expect to observe identical domains in cells. However, in the absence of other techniques to study the role of lipids, it is tempting to speculate that the ability of cytokinesis lipids to form rigid phases in vitro could contribute to the extraordinary mechanical resistance that we observed in live dividing cells under high forces. In parallel with the development of methods to study the functions of lipids directly in the cell membrane, advances in biophysical techniques to study cell mechanics with enhanced resolution will be needed to conclusively understand the mechanical roles of different cellular and membrane compartments during division.

The order of magnitude of lipid diversity (10,000 s) approaches that of proteins, but the field is only beginning to appreciate this diversity. We show that dividing cells display exquisite specificity in their lipid composition, and many of the lipids that we identify are quite rare species that have not been assigned biological functions. Our discovery of the high precision that cells use to regulate their lipidome during the cell cycle suggests that these lipids play key roles in the division process. Although understanding the detailed roles of the lipids that we identified will

require further technological advances in lipid biology, we have made a start by showing that lipids contribute to the structural integrity of dividing cells and are involved in the transmission of signals. We have also identified strategies to perturb lipid levels by using RNAi to identify which biosynthetic enzymes are required for division, and we have described the cellular consequences of lipid perturbations. This work makes it clear that lipids play active and essential roles in a fundamental biological process and significantly strengthens the newly emerging paradigm that specific lipids within lipid families have specific functions.

EXPERIMENTAL PROCEDURES

Detailed information on the materials used can be found in the Extended Experimental Procedures section, as well as detailed procedures for cell culture methods and the RNAi screen.

S Phase Arrest

HeLa S3 cells were arrested at S phase by using thymidine. Cells were plated into complete DMEM containing 4 mM thymidine at a final concentration of 4×10^5 cells/ml in 10 cm dishes for 24 hr (in 10 ml). Cells were then washed twice with 5 ml PBS and were harvested using a cell scraper in 5 ml PBS. Cells were pelleted by centrifugation at 200 × *g*, and the pellets were stored at −80°C for S phase cells.

Cytokinesis Arrest

For a full description of the cytokinesis arrest, see the Extended Experimental Procedures. In brief, 100 nM nocodazole treatment for 12 hr yielded a highly mitotic population of HeLa S3 cells. Mitotic cells were collected by mitotic shake-off, and cells were replated after several washing steps. Cells were incubated for 2 hr, allowing them to synchronously release to cytokinesis, and Taxol was added prior to harvesting if cells were carried forward for midbody isolation.

Midbody Isolation

For a full description of the cytokinesis arrest, see the Extended Experimental Procedures. In brief, the first step of the isolation is the mechanical lysis of cytokinesis cells in Mb buffer using a 27 G1/2 needle. The resulting solution was vortexed in the presence of glass beads followed by the addition of micrococcal nuclease. Next, the solution was clarified by consecutive short spins to remove unlysed cells and larger structures in the lysate. The concentrated midbody-containing solution was subjected to a brief immunoprecipitation step by using integrin β3 antibody to remove nonmidbody-related membranes. The resulting supernatant was enriched in midbody structures and was used for midbody lipid profiling.

Preparation of Lipid Extracts for LC-MS and Data Analysis

Lipids were prepared according to a previously reported protocol (Saghatelian et al., 2004). A full description of the LC-MS method and lipid species assignments can be found in the Extended Experimental Procedures.

Atomic Force Microscopy

Force spectroscopy measurements using low (~0.6 nN) or high forces (10–250 nN) on cells as well as imaging and force spectroscopy on isolated lipid bilayers were performed using a commercial Dimension Icon AFM instrument (Bruker, Karlsruhe, Germany). Sample preparation, measurement details, and statistical analyses are discussed in the Extended Experimental Procedures.

SUPPLEMENTAL INFORMATION

Supplemental Information includes Extended Experimental Procedures, four figures, three tables, and four movies and can be found with this article online at http://dx.doi.org/10.1016/j.cell.2013.12.015.

ACKNOWLEDGMENTS

We thank Alan Saghatelian, Tim Mitchison, and Xin Zhang for helpful discussions. LC-MS data was acquired on an Agilent 6520 Q-TOF spectrometer supported by the Taplin Funds for Discovery Program at Harvard Medical School (PI, Suzanne Walker). We thank the Nikon Imaging Centres at King's College London and Harvard Medical School for help with light microscopy. We also thank the facilities of the EBN group of the Physics Department of King's College London. This work was funded by NIH grant R01 GM082834, Human Frontier Science Program Young Investigator Award, Marie Curie CIG grant 304137, ERC Starting Grant 306659 (to U.S.E.), the Heinrich Hertz Foundation (to S.S.), a "La Caixa" PhD fellowship (to J.R.-G.), NIH grant R01 GM39565 (M.L.C., awarded to T.J. Mitchison), and Marie Curie CIG grant 293462, BBSRC grant J00992X/1, and EPSRC Fellowship K00641X/1 (to S.G.-M.).

Received: May 16, 2013
Revised: October 16, 2013
Accepted: December 4, 2013
Published: January 23, 2014

REFERENCES

Albertson, R., Riggs, B., and Sullivan, W. (2005). Membrane traffic: a driving force in cytokinesis. Trends Cell Biol. *15*, 92–101.

Atilla-Gokcumen, G.E., Castoreno, A.B., Sasse, S., and Eggert, U.S. (2010). Making the cut: the chemical biology of cytokinesis. ACS Chem. Biol. *5*, 79–90.

Atilla-Gokcumen, G.E., Bedigian, A.V., Sasse, S., and Eggert, U.S. (2011). Inhibition of glycosphingolipid biosynthesis induces cytokinesis failure. J. Am. Chem. Soc. *133*, 10010–10013.

Bissig, C., and Gruenberg, J. (2013). Lipid sorting and multivesicular endosome biogenesis. Cold Spring Harb. Perspect. Biol. *5*, a016816.

Braverman, N.E., and Moser, A.B. (2012). Functions of plasmalogen lipids in health and disease. Biochim. Biophys. Acta *1822*, 1442–1452.

Castoreno, A.B., and Eggert, U.S. (2011). Small molecule probes of cellular pathways and networks. ACS Chem. Biol. *6*, 86–94.

Coleman, R.A., and Mashek, D.G. (2011). Mammalian triacylglycerol metabolism: synthesis, lipolysis, and signaling. Chem. Rev. *111*, 6359–6386.

Echard, A. (2008). Membrane traffic and polarization of lipid domains during cytokinesis. Biochem. Soc. Trans. *36*, 395–399.

Echard, A. (2012). Phosphoinositides and cytokinesis: the "PIP" of the iceberg. Cytoskeleton (Hoboken) *69*, 893–912.

Eggert, U.S., Kiger, A.A., Richter, C., Perlman, Z.E., Perrimon, N., Mitchison, T.J., and Field, C.M. (2004). Parallel chemical genetic and genome-wide RNAi screens identify cytokinesis inhibitors and targets. PLoS Biol. *2*, e379.

Eggert, U.S., Field, C.M., and Mitchison, T.J. (2006a). Small molecules in an RNAi world. Mol. Biosyst. *2*, 93–96.

Eggert, U.S., Mitchison, T.J., and Field, C.M. (2006b). Animal cytokinesis: from parts list to mechanisms. Annu. Rev. Biochem. *75*, 543–566.

El Kirat, K., Morandat, S., and Dufrêne, Y.F. (2010). Nanoscale analysis of supported lipid bilayers using atomic force microscopy. Biochim. Biophys. Acta *1798*, 750–765.

Emoto, K., Inadome, H., Kanaho, Y., Narumiya, S., and Umeda, M. (2005). Local change in phospholipid composition at the cleavage furrow is essential for completion of cytokinesis. J. Biol. Chem. *280*, 37901–37907.

Field, S.J., Madson, N., Kerr, M.L., Galbraith, K.A., Kennedy, C.E., Tahiliani, M., Wilkins, A., and Cantley, L.C. (2005). PtdIns(4,5)P2 functions at the cleavage furrow during cytokinesis. Curr. Biol. *15*, 1407–1412.

Garcia-Manyes, S., and Sanz, F. (2010). Nanomechanics of lipid bilayers by force spectroscopy with AFM: a perspective. Biochim. Biophys. Acta *1798*, 741–749.

Garcia-Manyes, S., Oncins, G., and Sanz, F. (2005a). Effect of ion-binding and chemical phospholipid structure on the nanomechanics of lipid bilayers studied by force spectroscopy. Biophys. J. *89*, 1812–1826.

Garcia-Manyes, S., Redondo-Morata, L., Oncins, G., and Sanz, F. (2010). Nanomechanics of lipid bilayers: heads or tails? J. Am. Chem. Soc. *132*, 12874–12886.

Gerl, M.J., Sampaio, J.L., Urban, S., Kalvodova, L., Verbavatz, J.M., Binnington, B., Lindemann, D., Lingwood, C.A., Shevchenko, A., Schroeder, C., and Simons, K. (2012). Quantitative analysis of the lipidomes of the influenza virus envelope and MDCK cell apical membrane. J. Cell Biol. *196*, 213–221.

Gudejko, H.F., Alford, L.M., and Burgess, D.R. (2012). Polar expansion during cytokinesis. Cytoskeleton (Hoboken) *69*, 1000–1009.

Guha, M., Zhou, M., and Wang, Y.L. (2005). Cortical actin turnover during cytokinesis requires myosin II. Curr. Biol. *15*, 732–736.

Han, X., and Gross, R.W. (2003). Global analyses of cellular lipidomes directly from crude extracts of biological samples by ESI mass spectrometry: a bridge to lipidomics. J. Lipid Res. *44*, 1071–1079.

Hannun, Y.A., and Obeid, L.M. (2011). Many ceramides. J. Biol. Chem. *286*, 27855–27862.

Harris, A.R., and Charras, G.T. (2011). Experimental validation of atomic force microscopy-based cell elasticity measurements. Nanotechnology *22*, 345102.

Hategan, A., Law, R., Kahn, S., and Discher, D.E. (2003). Adhesively-tensed cell membranes: lysis kinetics and atomic force microscopy probing. Biophys. J. *85*, 2746–2759.

Ivanova, P.T., Milne, S.B., and Brown, H.A. (2010). Identification of atypical ether-linked glycerophospholipid species in macrophages by mass spectrometry. J. Lipid Res. *51*, 1581–1590.

Kasas, S., Longo, G., and Dietler, G. (2013). Mechanical properties of biological specimens explored by atomic force microscopy. J. Phys. D *46*.

Kay, J.G., and Grinstein, S. (2011). Sensing phosphatidylserine in cellular membranes. Sensors (Basel) *11*, 1744–1755.

Lafaurie-Janvore, J., Maiuri, P., Wang, I., Pinot, M., Manneville, J.B., Betz, T., Balland, M., and Piel, M. (2013). ESCRT-III assembly and cytokinetic abscission are induced by tension release in the intercellular bridge. Science *339*, 1625–1629.

Matzke, R., Jacobson, K., and Radmacher, M. (2001). Direct, high-resolution measurement of furrow stiffening during division of adherent cells. Nat. Cell Biol. *3*, 607–610.

Meivar-Levy, I., Sabanay, H., Bershadsky, A.D., and Futerman, A.H. (1997). The role of sphingolipids in the maintenance of fibroblast morphology. The inhibition of protrusional activity, cell spreading, and cytokinesis induced by fumonisin B1 can be reversed by ganglioside GM3. J. Biol. Chem. *272*, 1558–1564.

Moeendarbary, E., Valon, L., Fritzsche, M., Harris, A.R., Moulding, D.A., Thrasher, A.J., Stride, E., Mahadevan, L., and Charras, G.T. (2013). The cytoplasm of living cells behaves as a poroelastic material. Nat. Mater. *12*, 253–261.

Montagnac, G., Echard, A., and Chavrier, P. (2008). Endocytic traffic in animal cell cytokinesis. Curr. Opin. Cell Biol. *20*, 454–461.

Mullen, T.D., Spassieva, S., Jenkins, R.W., Kitatani, K., Bielawski, J., Hannun, Y.A., and Obeid, L.M. (2011). Selective knockdown of ceramide synthases reveals complex interregulation of sphingolipid metabolism. J. Lipid Res. *52*, 68–77.

Mullins, J.M., and McIntosh, J.R. (1982). Isolation and initial characterization of the mammalian midbody. J. Cell Biol. *94*, 654–661.

Murthy, K., and Wadsworth, P. (2005). Myosin-II-dependent localization and dynamics of F-actin during cytokinesis. Curr. Biol. *15*, 724–731.

Ng, M.M., Chang, F., and Burgess, D.R. (2005). Movement of membrane domains and requirement of membrane signaling molecules for cytokinesis. Dev. Cell *9*, 781–790.

Pietuch, A., and Janshoff, A. (2013). Mechanics of spreading cells probed by atomic force microscopy. Open Biol. *3*, 130084.

Saario, S.M., McKinney, M.K., Speers, A.E., Wang, C., and Cravatt, B.F. (2012). Clickable, photoreactive inhibitors to probe the active site microenvironment of fatty acid amide hydrolase(). Chem. Sci. *3*, 77–83.

Sackmann, E. (1996). Supported membranes: scientific and practical applications. Science *271*, 43–48.

Saghatelian, A., Trauger, S.A., Want, E.J., Hawkins, E.G., Siuzdak, G., and Cravatt, B.F. (2004). Assignment of endogenous substrates to enzymes by global metabolite profiling. Biochemistry *43*, 14332–14339.

Sagona, A.P., Nezis, I.P., Pedersen, N.M., Liestøl, K., Poulton, J., Rusten, T.E., Skotheim, R.I., Raiborg, C., and Stenmark, H. (2010). PtdIns(3)P controls cytokinesis through KIF13A-mediated recruitment of FYVE-CENT to the midbody. Nat. Cell Biol. *12*, 362–371.

Schultz, C. (2010). Challenges in studying phospholipid signaling. Nat. Chem. Biol. *6*, 473–475.

Sedzinski, J., Biro, M., Oswald, A., Tinevez, J.Y., Salbreux, G., and Paluch, E. (2011). Polar actomyosin contractility destabilizes the position of the cytokinetic furrow. Nature *476*, 462–466.

Skop, A.R., Liu, H., Yates, J., 3rd, Meyer, B.J., and Heald, R. (2004). Dissection of the mammalian midbody proteome reveals conserved cytokinesis mechanisms. Science *305*, 61–66.

Stewart, M.P., Toyoda, Y., Hyman, A.A., and Müller, D.J. (2012). Tracking mechanics and volume of globular cells with atomic force microscopy using a constant-height clamp. Nat. Protoc. *7*, 143–154.

Stumpf, C.R., Moreno, M.V., Olshen, A.B., Taylor, B.S., and Ruggero, D. (2013). The translational landscape of the Mammalian cell cycle. Mol. Cell *52*, 574–582.

Sullan, R.M., Li, J.K., and Zou, S. (2009a). Direct correlation of structures and nanomechanical properties of multicomponent lipid bilayers. Langmuir *25*, 7471–7477.

Sullan, R.M., Li, J.K., and Zou, S. (2009b). Quantification of the nanomechanical stability of ceramide-enriched domains. Langmuir *25*, 12874–12877.

van Meer, G., Voelker, D.R., and Feigenson, G.W. (2008). Membrane lipids: where they are and how they behave. Nat. Rev. Mol. Cell Biol. *9*, 112–124.

Yokokawa, M., Takeyasu, K., and Yoshimura, S.H. (2008). Mechanical properties of plasma membrane and nuclear envelope measured by scanning probe microscope. J. Microsc. *232*, 82–90.

Zhang, X., Wang, W., Bedigian, A.V., Coughlin, M.L., Mitchison, T.J., and Eggert, U.S. (2012). Dopamine receptor D3 regulates endocytic sorting by a Prazosin-sensitive interaction with the coatomer COPI. Proc. Natl. Acad. Sci. USA *109*, 12485–12490.